

EFFICIENT FLAPPING FLIGHT OF PTEROSAURS

A DISSERTATION

SUBMITTED TO THE DEPARTMENT OF AERONAUTICS AND

ASTRONAUTICS

AND THE COMMITTEE ON GRADUATE STUDIES

OF STANFORD UNIVERSITY

IN PARTIAL FULFILLMENT OF THE REQUIREMENTS

FOR THE DEGREE OF

DOCTOR OF PHILOSOPHY

Karl Axel Sträng

September 2009

UMI Number: 3382955

Copyright 2009 by
Strang, Karl Axel

INFORMATION TO USERS

The quality of this reproduction is dependent upon the quality of the copy submitted. Broken or indistinct print, colored or poor quality illustrations and photographs, print bleed-through, substandard margins, and improper alignment can adversely affect reproduction.

In the unlikely event that the author did not send a complete manuscript and there are missing pages, these will be noted. Also, if unauthorized copyright material had to be removed, a note will indicate the deletion.

UMI[®]


UMI Microform 3382955
Copyright 2009 by ProQuest LLC
All rights reserved. This microform edition is protected against
unauthorized copying under Title 17, United States Code.

ProQuest LLC
789 East Eisenhower Parkway
P.O. Box 1346
Ann Arbor, MI 48106-1346

© Copyright by Karl Axel Sträng 2009

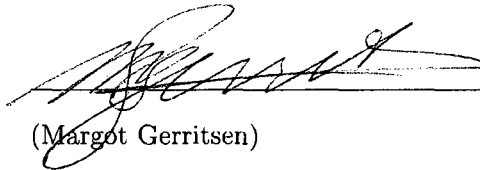
All Rights Reserved

I certify that I have read this dissertation and that, in my opinion, it is fully adequate in scope and quality as a dissertation for the degree of Doctor of Philosophy.



(Ilan Kroo) Principal Adviser

I certify that I have read this dissertation and that, in my opinion, it is fully adequate in scope and quality as a dissertation for the degree of Doctor of Philosophy.



(Margot Gerritsen)

(Energy Resources Engineering Department)

I certify that I have read this dissertation and that, in my opinion, it is fully adequate in scope and quality as a dissertation for the degree of Doctor of Philosophy.



(Scott Delp)

(Bioengineering Department)

Approved for the University Committee on Graduate Studies.



Abstract

In the late eighteenth century, humans discovered the first pterosaur fossil remains and have been fascinated by their existence ever since. Pterosaurs exploited their membrane wings in a sophisticated manner for flight control and propulsion, and were likely the most efficient and effective flyers ever to inhabit our planet. The flapping gait is a complex combination of motions that sustains and propels an animal in the air. Because pterosaurs were so large with wingspans up to eleven meters, if they could have sustained flapping flight, they would have had to achieve high propulsive efficiencies. Identifying the wing motions that contribute the most to propulsive efficiency is key to understanding pterosaur flight, and therefore to shedding light on flapping flight in general and the design of efficient ornithopters.

This study is based on published results for a very well-preserved specimen of *Coloborhynchus robustus*, for which the joints are well-known and thoroughly described in the literature. Simplifying assumptions are made to estimate the characteristics that can not be inferred directly from the fossil remains. For a given animal, maximizing efficiency is equivalent to minimizing power at a given thrust and speed. We therefore aim at finding the flapping gait, that is the joint motions, that minimize the required flapping power.

The power is computed from the aerodynamic forces created during a given wing

motion. We develop an unsteady three-dimensional code based on the vortex-lattice method, which correlates well with published results for unsteady motions of rectangular wings. In the aerodynamic model, the rigid pterosaur wing is defined by the position of the bones. In the aeroelastic model, we add the flexibility of the bones and of the wing membrane. The nonlinear structural behavior of the membrane is reduced to a linear modal decomposition, assuming small deflections about the reference wing geometry. The reference wing geometry is computed for the membrane subject to glide loads and pretension from the wing joint positions.

The flapping gait is optimized in a two-stage procedure. First the design space is explored using a binary genetic algorithm. The best design points are then used as starting points in a sequential quadratic programming optimization algorithm. This algorithm is used to refine the solutions by precisely satisfying the constraints. The refined solutions are found in generally less than twenty major iterations and constraints are violated generally by less than 0.1%.

We find that the optimal motions are in agreement with previous results for simple wing motions. By adding joint motions, the required flapping power is reduced by 7% to 17%. Because of the large uncertainties for some estimates, we investigate the sensitivity of the optimized flapping gait. We find that the optimal motions are sensitive mainly to flight speed, body accelerations, and to the material properties of the wing membrane. The optimal flight speed found correlates well with other studies of pterosaur flapping flight, and is 31% to 37% faster than previous estimates based on glide performance. Accounting for the body accelerations yields an increase of 10% to 16% in required flapping power. When including the aeroelastic effects, the optimal flapping gait is only slightly modified to accommodate for the deflections of stiff membranes. For a flexible membrane, the motion is significantly modified and

the power increased by up to 57%.

Finally, the flapping gait and required power compare well with published results for similar wing motions. Some published estimates of required power assumed a propulsive efficiency of 100%, whereas the propulsive efficiency computed for *Coloborhynchus robustus* ranges between 54% and 87%.

Acknowledgements

First, I would like to express my greatest gratitude to Professors Ilan Kroo, Margot Gerritsen and Scott Delp for their continuous guidance and enthusiasm in my work. Margot's excitement to solve unusual problems is contagious and I thank her deeply for initiating my career in paleo-aerodynamics. Ilan had also collaborated on a pterosaur replica project, namely on the QN Replica, and I am privileged to have benefited from his experience on pterosaur flapping flight. I thank him for welcoming me in his research group and for guiding me throughout my graduate studies. With his biological background, Scott has enriched the questions addressed in this study by addressing not only the fundamentals of flapping flight but also the key unsolved questions about pterosaur flight. Working closely with the three of them has been a fulfilling experience and I have learned greatly from their complimentary approaches. I would also like to thank Professor Juan Alonso to be part of the defense committee and Professor Mark Cutkosky for chairing my defense committee.

I would like to thank the National Geographic Society and Stanford University for providing funding for the Stanford University - National Geographic Pterosaur Replica Project. The replica project lead to this research on flapping flight of pterosaurs, which has been funded by the Stanford Bio-X Interdisciplinary Initiatives Program (IIP). Optimization runs were performed on the Stanford Bio-X2 cluster acquired

under the NSF award CNS-0619926 for computer resources.

In the course of the replica project, I have met fascinating people who all share a passion for pterosaur flight. I would like to thank all the team members and advisors of the replica project including, in alphabetical order, Dr. Chris Bennett, Dr. Steve Collie, John Conway, Peter Colpitts, James Cunningham, Peter Heppel, Marie-Anne Letourneux, Michael Luvara, Reinout vander Meulen, Paul MacCready, John McMasters, Steve Morris, Thuy Nguyen, Dr. Kevin Padian, Bob Parks, John Rubin, and Hall Train, among others. I am grateful to have shared this great experience with such accomplished and motivated individuals.

I have remained in close contact with several of the team members, especially with Dr. Chris Bennett, Peter Heppel, John McMasters, Dr. Kevin Padian and Bob Parks. They have helped me define the key questions when I transitioned the study from gliding flight to flapping flight. I greatly appreciate Peter's guidance and advice in defining a suitable model for the unsteady membrane aeroelasticity.

In the course of this research, I have been fortunate to share insights and data on pterosaur and on flapping flight in general. I would like to thank Steve Morris for providing the data on his ornithopter experiments and for lending one of his ornithopter wings for measurements. I look forward to continue our discussions and to follow his development of an efficient ornithopter. I would also like to thank Dr. Matthias Neef and Dr. Kevin Jones for sharing their data for the unsteady code comparisons which helped refine the UVLM code. I would also like to thank Desktop Aeronautics for providing a copy of LinAir for steady-state comparisons and AeroLogic for providing the wing geometry for calculations using CMARC. I would also like to thank Michael Habib and Eberhard "Dino" Frey for sharing their insights and data on pterosaur bone thickness and membrane properties respectively.

I would like to thank the staff of the Humes Writing Center for organizing “Dissertation Bootcamps”. I have attended several of these sessions and it has helped me greatly in the writing process. I subsequently formed a writing group with then fellow Ph.D. candidates Arthur Rallu and David Amsallem and I would like to thank them for reading, commenting and proof-reading this thesis.

I would also like to thank my family and friends for their support and for sharing their excitement about pterosaur flight which has really fueled my motivation. My parents Jan and Agneta Sträng have always pushed me to pursue my dreams and to seek endeavors that I am passionate about. My brother Eric Sträng finished his Ph.D. one year before me and I am thankful for his advice and comments. Last but not least, I would like to thank Marie-Anne Haour who has been my pillar during my years as a Ph.D. student. She has helped me maintain my forward momentum during frustrating moments and gain confidence upon reaching a milestone. All this work would have been impossible without her unfailing love and support.

As I close this chapter of my life and look forward to the next ones, I am grateful to have been granted the opportunity to work on these fascinating animals. Pterosaur flight is a truly interdisciplinary topic and, from my experience, has the ability to capture the imagination of people of all ages and background. I wish that this thesis will inspire many others to contribute to solving this great mystery.

Nomenclature

Wing constants

b_{ref} Reference wingspan, m

\bar{c} Average chord length, m

q_{∞} Freestream dynamic pressure, N.m^{-2} , $= \frac{1}{2}\rho U_{\infty}^2$

S_{ref} Reference area, m^2 , $= b.\bar{c}$

U_{∞} Freestream velocity, m.s^{-1}

m Mass, kg

W Weight, N

I_{xx} Moment of inertia about x -axis, with respect to center of gravity, kg.m^2

I_{yy} Moment of inertia about y -axis, with respect to center of gravity, kg.m^2

I_{zz} Moment of inertia about z -axis, with respect to center of gravity, kg.m^2

Fluid constants

μ Fluid viscosity, $\text{kg.m}^{-1}.\text{s}^{-1}$

ρ Fluid density, kg.m^{-3}

Dimensionless aerodynamic quantities

AR Aspect ratio, $= \frac{b}{\bar{c}}$

M Mach number, $= \frac{U_{\infty}}{a}$, for air at sea-level, $a = 340 \text{ m.s}^{-1}$

Re Reynolds number, $= \frac{U_{\infty}\bar{c}\rho}{\mu}$

St Strouhal number, $= \frac{fA}{U_\infty}$ with A the full motion amplitude

k Reduced frequency, $= \frac{\omega \bar{c}}{2U_\infty}$

Wing motion parameters

ϕ Rotation angle about x -axis, as defined in figure 1

θ Rotation angle about y -axis, as defined in figure 1

ψ Rotation angle about z -axis, as defined in figure 1

φ Motion phase angle

ω Circular frequency, rad.s^{-1} , $= 2\pi f = \frac{2\pi}{T}$

f Flapping frequency, Hz

t time, s

T_{period} motion period, s

Subscript

0 Center of gravity of animal

1 Shoulder joint

2 Elbow joint

3 Wrist joint

4 Knuckle joint

5 Joint between phalange I and II of fourth digit

6 Joint between phalange II and III of fourth digit

7 Joint between phalange III and IV of fourth digit

Forces and moments integrated over the wing in UVLM

$F_{X_{\text{inv}}}$ Inviscid net horizontal force, defined in the X -axis, N

F_Y Side force, defined in the Y -axis, N

F_Z Vertical force, defined in the Z -axis, N

L Total lift, chosen to be equal to F_Z , N

T Total thrust, N

M_x Moment about the x -axis, N.m⁻¹

M_y Moment about the y -axis, N.m⁻¹

M_z Moment about the z -axis, N.m⁻¹

Drag forces and power

D_{body} Body parasite drag, N

D_{tail} Tail parasite drag, N

D_{wing} Wing parasite drag, N

$D_{i_{\text{inv}}}$ Lift-induced inviscid drag, also called vortex drag, N

$D_{i_{\text{visc}}}$ Lift-induced viscous drag, N

D_{viscous} Viscous drag, N

D_{total} Total drag, N

P Mechanical power, W

Force and moment coefficients

C_l Section lift coefficient, $= \frac{\text{section lift force}}{q_{\text{local}} S_{\text{ref}}} \frac{\bar{c}}{\text{section chord}}$

$C_{l_{\text{max}}}$ Maximum section lift coefficient, $= \max [|C_l|]$

C_F Dimensionless coefficient for force F , $= \frac{F}{q_{\infty} S_{\text{ref}}}$

C_M Dimensionless coefficient for moment M , $= \frac{M}{q_{\infty} S_{\text{ref}} \bar{c}}$

C_P Mechanical power coefficient, $= \frac{P}{q_{\infty} S_{\text{ref}} U_{\infty}}$

$\overline{C_F}$ Force F coefficient averaged over one period, $= \frac{1}{T_{\text{period}}} \int_0^{T_{\text{period}}} C_F dt$

$\bar{\eta}$ Time-averaged propulsive efficiency, $= \frac{\overline{C_T}}{\overline{C_P}}$

Structural objects

ν Poisson's ratio

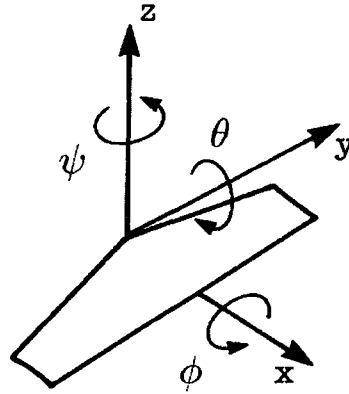


Figure 1: Definition of wing axes and angles in the frame attached to the body. Picture redrawn from Katz and Plotkin [1].

- E Young's modulus, Pa
- ϵ_0 Structural pre-strain
- $\{\mathbf{y}\}$ Vector of generalized nodal displacement of the structure
- $[\mathbf{M}]$ Generalized mass matrix
- $[\mathbf{D}]$ Generalized damping matrix
- $[\mathbf{K}]$ Generalized stiffness matrix
- $\{\mathbf{F}\}$ Vector of generalized nodal forces

Contents

Abstract	iv
Acknowledgements	vii
Nomenclature	x
1 Introduction	1
1.1 Challenges posed by the study of pterosaur flight	1
1.2 Scope of this study	3
1.3 Previous studies on pterosaur flight	4
1.3.1 Analytical results	4
1.3.2 Pterosaur reconstructions	5
1.4 Approach	6
1.5 Outline	8
2 Building the pterosaur model	10
2.1 Introduction	10
2.2 Description of pterosaurs and of <i>Coloborhynchus robustus</i>	11
2.2.1 Comparison of the wing structure of pterosaurs, birds and bats	13
2.2.2 Membrane attachment on the body	17

2.2.3	Approximations for the properties of the wing membrane . . .	17
2.2.4	Wing bones of pterosaurs	19
2.2.5	Estimates for the lengths and cortical thicknesses of the bones in the wing	21
2.2.6	Nomenclature for the wing geometry	23
2.2.7	Range of motions of the movable joints in the wing	24
2.2.8	Atmosphere in the Mezosoic and Lower Cretaceous	26
2.3	Estimates for the total mass and mass distribution	28
2.3.1	Inertial properties of the wings of birds and bats	30
2.3.2	Mass of the wing bones	31
2.3.3	Mass distribution of the wing membrane	33
2.3.4	Overall mass distribution in the wing	35
2.3.5	Distribution of soft tissue mass and volume on the wing	38
2.3.6	Overall mass distribution of <i>Coloborhynchus robustus</i>	38
2.4	Estimates of propulsive efficiency of migratory birds	41
2.4.1	Definition of propulsive efficiency	42
2.4.2	Methods to measure metabolic power	47
2.4.3	Method to estimate drag	49
2.4.4	Estimate of propulsive efficiency for migratory birds	51
2.5	Summary	52
3	Aerodynamic Model	55
3.1	Introduction	55
3.2	Flow assumptions for <i>Coloborhynchus robustus</i>	56
3.3	Unsteady three-dimensional vortex-lattice code (UVLM)	60
3.3.1	Choice of aerodynamic method	60

3.3.2	General description of UVLM	66
3.3.3	Adaptations to the method for pterosaur flapping flight	67
3.3.4	Definition of forces	69
3.3.5	Definition of power and propulsive efficiency	72
3.3.6	Code convergence	73
3.4	Comparison with published results	75
3.4.1	Comparison with steady results	78
3.4.2	Sudden acceleration of flat plate airfoil	78
3.4.3	Heaving and pitching motion of a flat plate airfoil	80
3.4.4	Heaving, pitching, flapping and twisting motions of a rectangular wing	82
3.4.5	Discussion of results	84
3.5	Aerodynamic model for <i>Coloborhynchus robustus</i>	87
3.5.1	Wing model of <i>Coloborhynchus robustus</i> used in the aerodynamic study	87
3.5.2	Estimates of the drag components	98
3.5.3	Model for the body accelerations	102
3.5.4	Grid convergence for the pterosaur wing	105
3.6	Summary	107
4	Aeroelastic Model	108
4.1	Introduction	108
4.2	Choice of unsteady aeroelastic model	109
4.2.1	Relevant studies in unsteady aeroelasticity	109
4.2.2	Relevant membrane studies	113
4.2.3	Methods chosen	115

4.3	Fluid-structure interaction model for pterosaur wings	117
4.3.1	General dynamic equations of motion	117
4.3.2	Modal decomposition of the wing structure	118
4.3.3	Fluid-structure interaction coupling	121
4.4	Comparison with measured wing motion of an ornithopter	124
4.4.1	Choice of ornithopter used for comparison	124
4.4.2	Description of the ornithopter tested	125
4.4.3	Computational model of the ornithopter wing	127
4.4.4	Comparison of computed and observed wing motions	130
4.5	Aeroelastic model for <i>Coloborhynchus robustus</i>	136
4.5.1	Approximations for the wing bones	136
4.5.2	Approximations for the wing membrane	138
4.6	Verification of the membrane model in the finite-element analysis . .	141
4.6.1	Details of the FEA model for the pterosaur wing	141
4.6.2	Deflections of two-dimensional membrane subject to uniform pressure	144
4.6.3	Deflections of circular membrane subject to uniform pressure .	150
4.6.4	Comparison with automated grid	153
4.7	Aeroelastic deformations of the pterosaur wing	155
4.7.1	Membrane tensioning from the joint motions	156
4.7.2	Modal decomposition of the tensioned wing	160
4.8	Summary	165
5	Optimization	168
5.1	Introduction	168
5.2	Mechanical power as an optimization goal	168

5.2.1	Optimization of vertebrate flight in biology	169
5.2.2	Optimization of flapping flight in aerodynamics	170
5.2.3	Choice of optimization goal	172
5.3	Formulation of the constrained optimization problem	174
5.3.1	Choice of optimization variables	174
5.3.2	Choice of sensitivity studies	176
5.3.3	Bounds of the variables	178
5.3.4	Definition of constraints	178
5.3.5	Formulation of the constrained optimization problem	182
5.4	Optimization algorithms used	184
5.4.1	Genetic algorithm	185
5.4.2	Sequential quadratic programming methods	188
5.4.3	Combined optimization procedure	192
5.5	Optimization results	195
5.5.1	Impact of each joint motion	195
5.5.2	Impact of average lift coefficient	199
5.5.3	Impact of wing geometry	203
5.5.4	Impact of animal weight	205
5.5.5	Impact of body accelerations	205
5.5.6	Impact of atmospheric density	206
5.5.7	Impact of membrane stiffness	207
5.6	Comparison with published results	209
5.6.1	Comparison with published results for pterosaurs	209
5.6.2	Comparison with estimates computed with 100% propulsive ef- ficiency	219

5.7	Summary	223
6	Conclusion	225
6.1	Summary of results	225
6.2	Discussion of the methods and results	227
6.2.1	Mass estimates	227
6.2.2	Aerodynamic model	228
6.2.3	Aeroelastic model	229
6.2.4	Optimization convergence	229
6.2.5	Results	230
6.3	Future work	231
6.3.1	Model of the pterosaur wing	231
6.3.2	Other flight conditions	233
6.3.3	High-fidelity refinements	235
	Bibliography	236

List of Tables

2.1	List of published material properties of bone	20
2.2	Lengths of the main wing bones of <i>Coloborhynchus robustus</i> . The lengths listed have been reported by Kellner and Tomida[2], or estimated by Cunnigham[3], or using the regression laws derived for ornithocheirids by Wilkinson[4]. We also include, for reference, the lengths in mm of the bones of <i>Pteranodon ingens</i> reported by Bramwell and Whitfield[5].	22
2.3	Cortical thicknesses of the main wing bones of <i>Coloborhynchus robustus</i> . The bone cortical thicknesses listed have been reported by Bramwell and Whitfield[5] for <i>Pteranodon ingens</i> , or estimated from the anterior-posterior or dorso-ventral widths at the bone mid-length from the data provided by Habib[6] and Bramwell and Whitfield[5]. The chosen thicknesses are also listed. All dimensions are given in mm. Abbreviations: AP, anterior-posterior ; DV: dorso-ventral. . . .	23

2.4	Angular range (in degrees) of movable joint motions for <i>Pteranodon</i> , <i>Anhanguera</i> , and ornithocheirids, as inferred by Bramwell and Whitfield[5], Bennett[7], Wellnhofer[8], Chatterjee and Templin[9], Wilkinson[4]. The values of allowed range of motion have been formulated in the nomenclature defined in section 2.2.6.	27
2.5	Maximum amplitudes of joint motion about glide position (in degrees) for <i>Coloborhynchus robustus</i>	27
2.6	Mass estimates of the main wing bones of <i>Coloborhynchus robustus</i> . The bones are assumed to be elliptic tubes of uniform cross-section and cortical thickness. We also list the mass estimates for the wing bones of <i>Pteranodon ingens</i> , derived from Bramwell and Whitfield[5] assuming an average tissue density of 1000 kg.m^{-3} . All dimensions are given in mm, the mass in g. Abbreviations: AP, anterior-posterior ; DV: dorso-ventral.	33
2.7	Mass estimates between the joints of the main wing bones of <i>Coloborhynchus robustus</i> . The area between the joints is estimated from the chord distribution of the wing in glide position.	34
2.8	Estimates of distribution of mass, expressed in g, for the wing of <i>Coloborhynchus robustus</i>	36
2.9	Estimates of distribution of moment of inertia I_{xx} about wing root axis x , expressed in g.m^2 , for the wing of <i>Coloborhynchus robustus</i>	36
2.10	Estimates of the dimensions for the soft tissue volume for the wing of <i>Coloborhynchus robustus</i> . All dimensions are expressed in mm.	38

2.11	Estimates for the distribution of mass, center of gravity x_{CG} and moments of inertia I_{yy} of each component of <i>Coloborhynchus robustus</i> . The estimates include the position of one wing's center of gravity y_{CG} , and moment of inertia I_{xx} about the root axis x . The masses are expressed in kg, distances in m, and moments of inertia (kg.m^2). . .	41
2.12	Key flight characteristics for four species of migratory birds. The dimensions are provided by Flight 1.20[10]. The flight conditions are computed by Flight 1.20[10] at the flight speed for minimum total drag calculated at sea-level. The propulsive efficiency is estimated for the European Starling with values of mechanical power given by Ward and Rayner[11].	53
3.1	Estimates of key flow parameters for a specimen of <i>Coloborhynchus robustus</i> , weighing 160 N, flying at an average $\overline{C_L}$ of 0.7. The reference length are taken from the glide position as specified in table 3.4. ($\rho = 1.23 \text{ kg.m}^{-3}$ and $\mu = 1.82 \times 10^{-5} \text{ kg.m}^{-1}.\text{s}^{-1}$)	59
3.2	Amplitudes and reduced frequencies considered for the comparison of the lift and thrust forces for a two-dimensional airfoil subject to heaving motion.	81
3.3	Amplitudes and reduced frequencies with the product $k \times \frac{z_0}{c}$ held constant, for the case of a two-dimensional airfoil subject to heaving motion.	82
3.4	Joint angles (in degrees) of right wing in glide position for the curved geometry. The abbreviations Sh., Elb., Wri., Knu., and Ph. refer to the shoulder, elbow, wrist, knuckle and interphalangeal joint.	97

3.5	Joint angles (in degrees) of right wing in glide position assuming a planar geometry. The abbreviation Ph. refers to an interphalangeal joint.	97
3.6	Estimates of the viscous drag for a 160 N specimen of <i>Coloborhynchus robustus</i> gliding at a steady lift coefficient $\overline{C_L} = 0.70$	101
3.7	Mass and moment of inertia I_{yy} of the right wing estimated for a 160 N specimen of <i>Coloborhynchus robustus</i> . We also list the corresponding position of the wing center of gravity relative to the body center of gravity.	105
3.8	Variation of time-averaged quantities for different number of periods N_{periods} , and of time steps per period $N_{\text{steps/period}}$. The time-averaged quantities correspond to the curved wing geometry of <i>Coloborhynchus robustus</i> , modeled with 20 panels chordwise and 14 panels spanwise, with flapping motion parameters: $k = 0.10$, $\bar{\theta} = 5.0$, $\phi_1 = 10.0$, $\theta_3 = 4.0$, $\varphi_{\theta_3} = 90.0$	106
3.9	Variation of time-averaged quantities for different number of panels N_{chord} in the chordwise direction. The time-averaged quantities correspond to the curved wing geometry of <i>Coloborhynchus robustus</i> , modeled for 2 periods with 50 time steps per period, with flapping motion parameters: $k = 0.10$, $\bar{\theta} = 5.0$, $\phi_1 = 10.0$, $\theta_3 = 4.0$, $\varphi_{\theta_3} = 90.0$	106
3.10	Variation of time-averaged quantities for different number of panels N_{span} in the spanwise direction. The time-averaged quantities correspond to the curved wing geometry of <i>Coloborhynchus robustus</i> , modeled for 2 periods with 50 time steps per period, with flapping motion parameters: $k = 0.10$, $\bar{\theta} = 5.0$, $\phi_1 = 10.0$, $\theta_3 = 4.0$, $\varphi_{\theta_3} = 90.0$	107

4.1	Main characteristic of the ornithopter designed and built by Steve Morris[12].	127
4.2	Mechanical properties of two composite materials and the orthotropic material used for the ornithopter wing model. The two composite materials are AS4/3501-6 Carbon-epoxy and S2-Glass-epoxy, with values given by Sun[13]. Longitudinal refers to the direction of the fiber. In the model for the ornithopter wing, the longitudinal properties are in the y -direction, and transverse corresponds to the x and z -directions.	129
4.3	Comparison of the wing mass and position of the center of gravity measured on the ornithopter wing and the finite-element model.	130
4.4	Parameters of the chosen flight test for comparison.	132
4.5	Dimensions of the bone used in the structural model of the pterosaur wing. To estimate the mass in section 2.3.2, the bones were assumed to be elliptic tubes of uniform cross-section and cortical thickness. In the aeroelastic model, the bone are assumed to be circular tube of uniform diameter and tickness. All dimensions are given in mm. Abbreviations: AP, anterior-posterior ; DV: dorso-ventral.	138
4.6	Chosen values of material properties for the three membrane models considered for the pterosaur wing.	140
4.7	Estimates for the total mass and position of the center of gravity about the root axis x for one wing. The masses are expressed in kg, distances in m.	144

4.8	Membrane deflections, Weber numbers and pressure differences for three values of Young's modulus. In these cases, the membrane is not subject to pre-strain ($\epsilon_0 = 0.0$). The maximum deflections $\frac{z_{\max}}{c}$ are chosen such that the pressure difference Δp is in the 100-200 Pa range.	146
4.9	Membrane deflections, Weber numbers and pressure differences for three values of Young's modulus. In these cases, the membrane is subject to a pre-strain of $\epsilon_0 = 0.05$. The maximum deflections $\frac{z_{\max}}{c}$ are set at $\frac{z_{\max}}{c} = 0.010$ and the pressure difference Δp are computed accordingly from the Weber number We	147
4.10	Computed maximum membrane deflections for three values of Young's modulus. In these cases, the membrane is not subject to pre-strain ($\epsilon_0 = 0.0$). The maximum deflections $\frac{z_{\max}}{c}$ are computed from the analytical results and the finite-element analysis (FEA).	148
4.11	Computed maximum membrane deflections for three values of Young's modulus. In these cases, the membrane is subject to a pre-strain of $\epsilon_0 = 5\%$. The maximum deflections $\frac{z_{\max}}{c}$ are computed from the analytical results and the finite-element analysis (FEA):	148
4.12	Pressure differences (in Pa) for three values of Young's modulus. The values of dimensionless pressure q of $q = 0.001$ and $q = 0.010$ are chosen such that the deflections under the uniform pressure loading case are the same as under the uniform lateral loading case.	152

4.13	Dimensionless vertical deflections computed using Hencky's solution and the finite-element analysis (FEA) for three values of Young's modulus. The deflections are computed at the center of the circular ring. The values of dimensionless pressure q of $q = 0.001$ and $q = 0.010$ are chosen such that the deflections under the uniform pressure loading case are the same as under the uniform lateral loading case.	152
4.14	Maximum deflections (in m) of the membrane under a uniform load of 10 Pa. The maximum deflection occurs on the trailing edge near the mid-span. The comparison is done for the three membrane models. .	154
4.15	Chosen values of material properties for the three membrane models considered in this study.	156
4.16	Imposed lateral displacements (in mm) imposed at the joints. These displacements aim at applying uniform tension in the y -direction. The total displacements at the tip are chosen to be 20 mm.	161
4.17	Frequencies (in Hz) of the first five modes computed for the pterosaur wing with three membrane models.	162
4.18	Maximum trailing edge deflections z_{\max} and lift coefficients $\overline{C_L}$ in gliding flight at at set angle of attack $\bar{\theta} = 7.0$ degrees. The results are computed for the pterosaur wing with three membrane models, and with the rigid wing defined of the aerodynamic model.	164
4.19	Motion parameters for the optimized flapping gait for motion J2, which includes motions of shoulder flapping ϕ_1 , sweeping ψ_1 and wrist pitching θ_3 . All angles are expressed in degrees.	165

4.20	Average lift, inviscid net horizontal force and power coefficients ($\overline{C_L}$, $\overline{C_{F_{x_{inv}}}}$, $\overline{C_P}$) in flapping flight. The motion parameters are listed in table 4.19. The results are computed for the pterosaur wing with three membrane models, and with the rigid wing defined of the aerodynamic model.	166
5.1	Definitions of active joint motions during flapping flight	175
5.2	The seven cases of joint motions considered in the optimization study.	176
5.3	Seven cases of average $\overline{C_L}$ conditions considered in the sensitivity study.	177
5.4	Three cases of animal weight considered in the sensitivity study. . .	177
5.5	Five cases of atmospheric density considered in the sensitivity study. ρ	177
5.6	List of flapping gait parameters (angles in degrees)	178
5.7	Seven cases of joint motions considered in the optimization study. . .	198
5.8	Comparison of time-averaged quantities between the planar and curved pterosaur wing geometry. The time-averaged quantities correspond to the curved wing geometry of <i>Coloborhynchus robustus</i> with flapping motion parameters: $k = 0.10$, $\bar{\theta} = 5.0$, $\phi_1 = 10.0$, $\theta_3 = 4.0$, $\varphi_{\theta_3} = 90.0$.	204
5.9	Optimization results for the study on the impact of the joint motions. These results apply to a 160 N specimen of <i>Coloborhynchus robustus</i> flying at an average $\overline{C_L}$ of 0.5 and 0.7. The body accelerations are not included in these cases. All angles are expressed in degrees.	210
5.10	Optimization results for the study on average lift coefficient. The reference results apply to a 160 N specimen of <i>Coloborhynchus robustus</i> flying at an average $\overline{C_L}$ of 0.7, considering the motion case J2. The body accelerations are not included in these cases. All angles are expressed in degrees.	211

5.11	Optimization results for the study on the impact of the curved geometry and of the wing extent. The reference results apply to a 160 N specimen of <i>Coloborhynchus robustus</i> flying at an average $\overline{C_L}$ of 0.7, considering the motion case J2, with the planar geometry. All angles are expressed in degrees.	212
5.12	Optimization results for the study on the impact of the animal weight. The reference results apply to a 160 N specimen of <i>Coloborhynchus robustus</i> flying at an average $\overline{C_L}$ of 0.7, considering the motion case J2, without body accelerations. All angles are expressed in degrees. .	213
5.13	Optimization results for the study on the impact of the body accelerations. The reference results apply to a 160 N specimen of <i>Coloborhynchus robustus</i> flying at an average $\overline{C_L}$ of 0.7, considering the motion case J2. The body accelerations are not included unless specified. All angles are expressed in degrees. We abbreviate body accelerations with body acc.	214
5.14	Optimization results for the study on the impact of the atmospheric density. The reference results apply to a 160 N specimen of <i>Coloborhynchus robustus</i> flying at an average $\overline{C_L}$ of 0.7, considering the motion case J2, without body accelerations, with the atmospheric density taken at sea level ($\rho=1.23 \text{ kg.m}^{-3}$). All angles are expressed in degrees. . . .	215
5.15	Optimization results for the study on the impact of the membrane flexibility. These results apply to a 160 N specimen of <i>Coloborhynchus robustus</i> flying at an average $\overline{C_L}$ of 0.7. The body accelerations are not included in these cases. All angles are expressed in degrees. . . .	216

5.16	Published estimates for minimum flapping power of pterosaurs of similar size and weight to <i>Coloborhynchus robustus</i> . Our estimates are for a 160 N specimen of <i>Coloborhynchus robustus</i> with the wing membrane attached to the ankle, flying at an average $\overline{C_L}$ of 0.7, considering the motion case J2, without body accelerations, with the atmospheric density taken at sea level ($\rho = 1.23 \text{ kg.m}^{-3}$). <i>Coloborhynchus robustus</i> , Average and Minimum are abbreviated <i>Colobor.</i> , Ave. and Min. respectively.	219
5.17	Comparison of required mechanical power at different values of average lift coefficient $\overline{C_L}$ estimated for the optimal flapping motion and for 100% efficiency. We also list the propulsive efficiency $\overline{\eta}$ calculated for the optimal wing motion. The reference results apply to a 160 N specimen of <i>Coloborhynchus robustus</i> flying at an average $\overline{C_L}$ of 0.7, considering the motion case J2, without body accelerations, with the atmospheric density taken at sea level ($\rho = 1.23 \text{ kg.m}^{-3}$). All angles are expressed in degrees.	221

List of Figures

1	Definition of wing axes and angles in the frame attached to the body. Picture redrawn from Katz and Plotkin [1].	xiii
1.1	Outline of <i>Coloborhynchus robustus</i> skeleton, with preserved bones of specimen NSM-PV 19892 in black. Picture adapted from Kellner and Tomida[2]. This top view shows the right wing bones in flight position and the left wing bones in folded position. We have pointed out the bones and joints of interest for this study. We note that this specimen was initially classified as <i>Anhanguera piscator</i>	2
2.1	Outline of <i>Coloborhynchus robustus</i> skeleton, with preserved bones of specimen NSM-PV 19892 in black. Picture adapted from Kellner and Tomida[2]. This top view shows the right wing bones in flight position and the left wing bones in folded position. We have pointed out the bones and joints of interest for this study. We note that this specimen was initially classified as <i>Anhanguera piscator</i>	12
2.2	Comparison of the structures and sizes in bat, bird and pterosaur wings. Pictures adapted with permission from Wellnhofer[8].	14

2.3	Diagram of a right pterosaur wing based on the fossils of the pterosaur <i>Rhamphorhynchus</i> described by Zittel[14]. The brachioptagium is be divided into two parts - the tenopatagium and the actinopatagium. The actinopatagium, stretching from the wrist to the tip, is reinforced by actinofibrils illustrated by the pattern of lines. The lines shown represent the orientations of the actinofibrils and not their actual spacing. The tenopatagium, like the propatagium and the uropatagium, do not display these structures. We also show the range of possible locations for the center of gravity, as estimated by Bennett[15]. Figure adapted from Bennett[16].	16
2.4	Illustration of the internal structure of pterosaur wing bones. These were hollow with a very thin wall and were reinforced by internal struts, making them light yet strong. The cortical thickness is relatively homogeneous along the length of the bone, except near the joints where it is thicker.	20
2.5	Top view of the orientation of the frames attached to the bones, superimposed on the skeleton from Tomida and Kellner[2]. The wing geometry is defined by the rotation of each bone relative to the joint at its proximal end. A frame, noted by its corresponding subscript, is attached to each bone with the origin at the proximal joint. The y -axis of each bone frame is defined by the length of the bone. The joint angles ϕ , θ , and ψ correspond to rotations about the x , y , and z -axes respectively as defined in figure 1. The orientation of the x_0 and y_0 axes is such that the view matches the outline in figure 2.1. . . .	24

2.6	Distribution of mass and moment of inertia from root to tip for the wings of a bird, <i>Turdus merula</i> , and of a bat, <i>Pipistrellus pipistrellus</i> . In birds, the mass is concentrated towards the root of the wing, and the moment of inertia varies in a bell-shaped curve along the span. Figures adapted with permission from van der Berg and Rayner[17].	32
2.7	Distribution of wing mass and moment of inertia from root to tip. For <i>Turdus merula</i> (figure 2.7(a)), the mass is concentrated towards the root of the wing and the moment of inertia varies in a bell-shaped curve along the span. For <i>Coloborhynchus robustus</i> (figure 2.7(b)), we estimated the soft tissue mass such that the total mass and inertia match these trends.	37
2.8	Diagram of an airfoil section of a wing (grey line) subject to horizontal and vertical forces (black arrows). The wing is moving at speed U_∞ from right to left. In cruise flight, the horizontal force (coefficients of thrust \overline{C}_T and drag $C_{D_{\text{total steady-state}}}$) and vertical forces (coefficients of lift \overline{C}_L and weight $W/(q_\infty S_{\text{ref}})$) are balanced on average during a period of the wing motion.	45

3.1	Description of main wing motions studied : heaving (left), pitching (middle), flapping (right). Picture reproduced with permission from Neef[18]. Heaving corresponds to a vertical translation of the wing along the z -axis. When pitched, the wing is rotated by the angle θ about an axis parallel to the y -axis at the center of rotation located at x_D . In this study, the rectangular wing is pitched about the leading edge of the wing. Neef also studied twisting the wing linearly by α_1 but these results are not included here. Flapping corresponds to rotating the wing about the x -axis by the angle ϕ	64
3.2	Flow chart of the UVLM code. The position of the joints is recalculated at each time step and defines the wing geometry. The wing-induced and wake-induced velocities are then calculated at every panel which are used in the influence matrix. The velocities induced by the wing kinematics are calculated to create the right-hand side vector. The vorticity distribution is the solution of this linear system. Using the unsteady Bernoulli equation, the code calculates the pressure jump across the wing which lead to force and moment calculations.	68
3.3	Comparison of the lift and inviscid net horizontal forces for several wing panel sizes. We consider here the case of a rectangular wing of $AR=8$ under combined heaving and pitching motion ($\frac{z_0}{c} = 0.52$, $\theta_0 = 2$ degrees, $\varphi_{\theta_0} = 90$ degrees, $k = 0.1$). In figures 3.3(a) and 3.3(b), the blue, green, red and black lines correspond to 10, 20 and 30 chordwise panels respectively. In figures 3.3(c) and 3.3(d), the blue, green, red and black lines correspond to 7, 14, 21 and 28 spanwise panels respectively.	76

3.4	Comparison of the lift and inviscid net horizontal forces for 50, 100 and 150 of time steps per period, in blue, green and red lines respectively. We consider here the case of a rectangular wing of $AR=8$ under combined heaving and pitching motion ($\frac{z_0}{c} = 0.52$, $\theta_0 = 2$ degrees, $\varphi_{\theta_0} = 90$ degrees, $k = 0.1$).	77
3.5	Comparison of the unsteady vortex-lattice code UVLM with lifting-line code LinAir for the distribution of section lift coefficient C_l for the planar pterosaur wing geometry, with five spanwise panels per bone. The plot shows the right wing at a steady angle attack $\overline{\theta}_0$ of five degrees.	87
3.6	Comparison of the unsteady vortex-lattice method code UVLM with the unsteady panel code CMARC for the case of a rectangular wing of $AR=8$ in heaving motion. Figures 3.6(a) and 3.6(b) correspond to the heaving motion defined by $\frac{z_0}{c} = 0.4$, $k = 0.2$. Figures 3.6(c) and 3.6(d) correspond to the heaving motion defined by $\frac{z_0}{c} = 0.4$, $k = 0.5$. The blue and green lines correspond to the results from CMARC, as computed by Jones[19], and UVLM respectively.	88
3.7	Comparison of the unsteady vortex-lattice method code UVLM with the unsteady panel code CMARC for the case of a rectangular wing of $AR=8$ in heaving motion ($\frac{z_0}{c} = 0.4$, $k = 1.0$). The blue and green lines correspond to the results from CMARC, as computed by Jones[19], and UVLM respectively. This choice of reduced frequency and amplitude is not appropriate for a meaningful comparison.	89

3.8	Comparison of the unsteady vortex-lattice method code UVLM with the unsteady panel code CMARC for the case of a rectangular wing of $AR=8$ in heaving motion ($\frac{z_0}{c} = 0.5, k = 0.2, \frac{z_0}{c} \times k = 0.1$). The blue and green lines correspond to the results from CMARC and UVLM respectively.	89
3.9	Comparison of the unsteady vortex-lattice method code UVLM with the unsteady panel code CMARC for the case of a rectangular wing of $AR=8$ in heaving motion. Figures 3.9(a) and 3.9(b) correspond to the heaving motion defined by $\frac{z_0}{c} = 0.2, k = 0.5, \frac{z_0}{c} \times k = 0.1$. Figures 3.9(c) and 3.9(d) correspond to the heaving motion defined by $\frac{z_0}{c} = 0.1, k = 1.0, \frac{z_0}{c} \times k = 0.1$. The blue and green lines correspond to the results from CMARC and UVLM respectively.	90
3.10	Comparison of the unsteady vortex-lattice code UVLM with the Euler code developped by Neef[18] for the case of a rectangular wing of $AR=8$ under heaving motion ($\frac{z_0}{c} = 0.52, k = 0.1$), for a steady angle-of-attack $\overline{\theta}_0 = 0$ degrees. The blue and green lines correspond to results from Neef and UVLM respectively.	91
3.11	Comparison of the unsteady vortex-lattice code UVLM with the Euler code developped by Neef[18] for the case of a rectangular wing of $AR=8$ under combined heaving and pitching motion ($\frac{z_0}{c} = 0.52, \theta_0 = 2$ degrees, $\varphi_{\theta_0} = 90$ degrees, $k = 0.1$), for a steady angle-of-attack $\overline{\theta}_0 = 0$ degrees. The blue and green lines correspond to results from Neef and UVLM respectively.	92

3.12	Comparison of the unsteady vortex-lattice code UVLM with the Euler code developed by Neef[18] for the case of a rectangular wing of $AR=8$ under flapping motion ($\phi_0 = 15$ degrees, $k = 0.1$), for a steady angle-of-attack $\overline{\theta}_0 = 0$ degrees (figures 3.12(a) and 3.12(b)) and $\overline{\theta}_0 = 4$ degrees. The blue and green lines correspond to results from Neef and UVLM respectively.	93
3.13	Top view and front view of the joint positions for the planar and curved glide geometries of <i>Coloborhynchus robustus</i> . The markers represent the joints, the lines represent the bones.	98
3.14	Illustration of the approximations in the wing geometry of <i>Coloborhynchus robustus</i> . We show here the example of the glide geometry. From the position of the joints (figure 3.14(a)), we define the leading-edge and trailing-edge of the wing (figure 3.14(b)), using the geometric assumptions in section 3.5.1. We then define the wing panels (figure 3.14(c)), used in the vortex-lattice code UVLM, by choosing the number of chordwise panels and the number of spanwise panels per bone. For numerical stability reasons, the paneling needs a finite chord at the tip, so the geometry is truncated near the tip.	99

3.15	At every time step, we apply the equations of motion of a rigid body, at the center of gravity to evaluate the accelerations induced by the variation of aerodynamic forces and moments. The gray line represents a side view of the wing at an angle of attack. The lift force coefficient C_L and inviscid net horizontal force coefficient $C_{F_{X_{inv}}}$ are calculated by the unsteady vortex-lattice code UVLM. If the wing motion creates thrust, $C_{F_{X_{inv}}}$ is negative. The weight estimate $W/(q_{\infty}S_{ref})$ is chosen and the viscous drag coefficient $C_{D_{viscous}}$ is calculated as described in section 3.3.4.	103
4.1	Picture of the general ornithopter design with foam wing 3. Picture taken by Steve Morris[12].	127
4.2	Comparison of the lift and inviscid net horizontal forces for different number of modes included in the structural model of the ornithopter wing. The red, blue, green and black lines correspond to the cases with respectively three, five, seven and ten modes.	133
4.3	Pictures of the ornithopter wing motion during one period. Picture taken by Steve Morris[12]. Videos of the flights are available on YouTube.	
	134	

4.4	Comparison of the computed and observed tip motion for the or- nithopter wing. The observed values are plotted in black. The green line corresponds the closest computed motion ($k = 0.29$, $U_\infty = 9.0$ m.s^{-1}) within the estimated bounds of flight speed U_∞ and reduced frequency k . The blue line corresponds to the computed motion with $k = 0.45$ and $U_\infty = 12.0 \text{ m.s}^{-1}$, yielding a motion frequency of 5.6 Hz. The computed values are plotted for the third period of the motion. Angular values are given in degrees.	135
4.5	Structural mesh of the pterosaur wing based on the nodal positions specified by the aerodynamic code UVLM.	144
4.6	Normalized vertical displacements $\frac{z_{\max}}{c}$ of a two-dimensional mem- brane as a function of pressure loads in the form of the dimensionless Weber number We for four values of pre-strain ϵ_0 . The membrane is assumed of uniform thickness and with linear elastic material proper- ties. The pressure loads are applied uniformly. The case for values of pre-strain $\epsilon_0 = 0\%$, $\epsilon_0 = 1\%$, $\epsilon_0 = 5\%$ are plotted respectively in blue, green and red lines.	147

4.7	Normalized vertical displacements $\frac{z_{\max}}{c}$ as a function of chordwise position $\frac{x}{c}$ of a two-dimensional membrane for different cases of Young's modulus E with pre-strain $\epsilon_0 = 5\%$. The applied pressure is scaled with the Young's modulus to yield the same vertical displacements. The membrane is assumed of uniform thickness and with linear elastic material properties. The pressure loads are applied uniformly. The blue line represents the analytical results. The black crosses, squares and triangles represent the nodal displacements of the FEA model for the case of $E=37$ MPa, 100 MPa, 1000 MPa respectively as described in table 4.9.	149
4.8	Comparison of the structural mesh generated by ANSYS with the mesh created manually based on the grid of the aerodynamic code UVLM.	154
4.9	Stress distributions of the wing membrane in the x -direction (left column) and in the y -direction (right column) for different displacements of the joints and for a uniform gradient of lateral displacements. The values of stresses correspond to the flexible membrane model ($E = 37$ MPa). In each case, we specify the range of the stress values. The dark blue color refers to the lowest value and the red color to the highest value.	159
4.10	Stress distributions of the wing membrane in the x -direction (left column) and in the y -direction (right column) for a uniform gradient of lateral displacements. The values of stresses correspond to the flexible membrane model ($E = 37$ MPa). The dark blue color refers to the lowest value and the red color to the highest value.	161

4.11	Comparison of the trailing-edge deflections in steady gliding flight for the three cases of membrane model. The vertical deflection normalized by the average chord $\frac{z}{c}$ is plotted against the spanwise position normalized by the semi span $\frac{y}{b_{\text{ref}}}$. The deflections for the stiff membrane ($E = 1000$ MPa), the pterosaur approximation ($E = 100$ MPa) and for the flexible membrane ($E = 37$ MPa) are plotted in red, green and blue respectively. The wing is held at a steady angle attack $\overline{\theta}_0 = 7$ degrees.	164
4.12	Comparison of the lift and inviscid net horizontal force variations in flapping flight. The motion parameters are specified in table 4.19. The forces computed in the third period are plotted. The black line represents the rigid wing of the aerodynamic model. The forces for the stiff membrane ($E = 1000$ MPa), the pterosaur approximation ($E = 100$ MPa) and for the flexible membrane ($E = 37$ MPa) are plotted in red, green and blue respectively.	166
5.1	Variation of propulsive efficiency with pitching amplitude $\Delta\alpha$ at different values of reduced frequency k for the case of a heaving and pitching airfoil. Calculations used an unsteady two-dimensional panel code. Figure from Jones[20].	174
5.2	In cruise level flight, the time-averaged horizontal forces (average inviscid net horizontal force $\overline{C_{F_{X_{\text{inv}}}}}$ and average viscous drag $\overline{C_{D_{\text{viscous}}}}$) and vertical forces (average lift $\overline{C_L}$ and weight $W/(q_{\infty}S_{\text{ref}})$) are balanced during a period of the wing motion.	179
5.3	Flow chart of the binary genetic algorithm coupled to the aerodynamic code UVLM.	187

5.4	Plots of the required average thrust $\overline{C_T}$ and product $k \times \phi_1$ for the optimal wing motion as a function of average lift coefficient $\overline{C_L}$	201
5.5	Plots of the propulsive efficiency $\eta_{\text{propulsive}}$ and mechanical power \overline{P} for the optimal wing motion as a function of average lift coefficient $\overline{C_L}$. .	202
5.6	Mechanical power and propulsive efficiency for the optimal flapping motion as a function of average thrust coefficient.	222

Chapter 1

Introduction

1.1 Challenges posed by the study of pterosaur flight

The origin of pterosaurs remained a mystery until 1801 when George Cuvier[21] discovered that fossils discovered earlier belonged to a flying reptile. Pterosaurs were the first vertebrates to evolve powered flight and were long thought to be primitive flyers inferior to birds and bats.

Recent findings and studies have completely changed this perspective. It is now believed that pterosaurs evolved for 150 million years and dominated the skies when they coexisted with birds. Pterosaurs evolved into extreme designs with wingspans exceeding ten meters, complex membrane wings and large heads and necks. They probably used subtle and sophisticated flight control mechanisms for flight control and propulsion. They probably actively controlled the geometry of their wings, and exploited the aeroelasticity of the wing membrane. Subtle changes in membrane tension could have produced significant changes in the distribution of lift over a

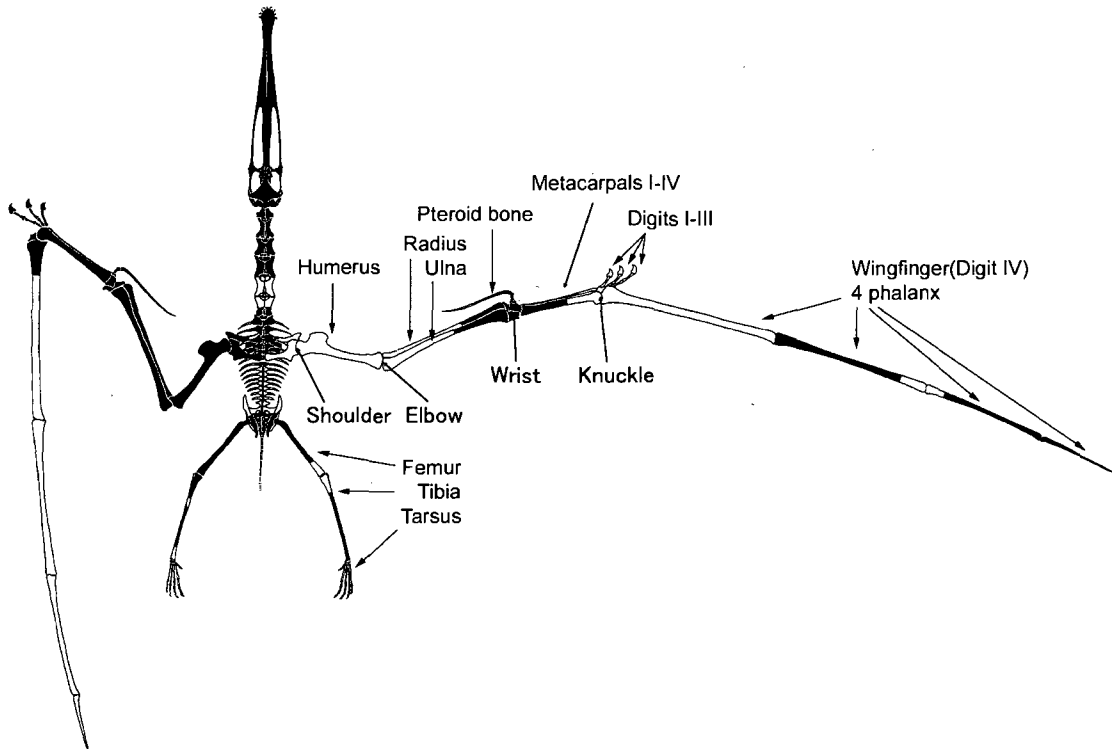


Figure 1.1: Outline of *Coloborhynchus robustus* skeleton, with preserved bones of specimen NSM-PV 19892 in black. Picture adapted from Kellner and Tomida[2]. This top view shows the right wing bones in flight position and the left wing bones in folded position. We have pointed out the bones and joints of interest for this study. We note that this specimen was initially classified as *Anhanguera piscator*.

pterosaur wing. The adaptive load redistribution was likely used to reduce bending moments in the pterosaur structure during maneuvers and gusts.

It is because of these challenging flight configurations that, perhaps, pterosaurs have the most to teach us regarding possible future aircraft development, not just in adaptive wing designs, but also in the design of effective membrane wings, advances in flight control mechanisms, and designs of effective flapping flight mechanisms, particularly in flying animals of great size.

1.2 Scope of this study

We aim to improve our understanding of the flapping flight of pterosaurs. Because pterosaurs are extinct and their wing structure is so distinct from birds and bats, this understanding cannot rely on observations. The current study is a detailed investigation of pterosaur flapping flight combining recent paleontological findings and computational tools that are more advanced than in previous pterosaur studies.

Although the wing motions can be inferred from the fossils, little is known about the weight distribution of the animal and the wing membrane properties. Furthermore, little is known about their ecology, and whether pterosaurs migrated or were mainly soarers adapted to their local environment, but they would have evolved to be the most adapted species to their environment and feeding patterns.

The key questions we will attempt to address in this study are:

- What are the probable bone, muscle and membrane properties related to flight?
- What was the likely optimal wing motions for flapping flight ?
- What energy expenditures were likely needed to sustain flight?
- How did pterosaurs possibly exploit aeroelasticity for propulsion?
- How do the uncertainties in parameters and modeling choices affect these results?

1.3 Previous studies on pterosaur flight

Most of the many studies on pterosaurs describe the fossil remains, and discuss how a new specimen updates the current knowledge base. Several authors have also investigated the flight performance of pterosaurs, and flapping flight. Most of those studies are based on analytical considerations. Several projects of pterosaur reconstructions have investigated flapping flight and the role of the membrane in flight. However, computational studies on pterosaur flapping flight have so far been limited, with past analyses conducted by Brooks et al.[22] and de Laurier[23].

1.3.1 Analytical results

Among the studies discussing the flight performance of pterosaurs, Bramwell and Whitfield[5] proposed a comprehensive reconstruction of *Pteranodon*. They proposed a method to estimate the weight of the animal from the fossil remains. They also inferred the range of joint motions, as well as the required strength of the wing bones and membrane. They estimated the required and available power for flapping flight. The required flapping power was estimated from the glide performance, and more particularly estimates of the minimum sinking speed and of the best glide ratio. The available power was estimated from the muscle volume. Brower[24] conducted a similar analysis. Chatterjee and Templin[9] later estimated the weight and glide performance for different species of pterosaurs using updated results. They also compared estimates of available and required flapping power for these species.

However most of these estimates on required flapping power were done using classical aerodynamic results derived for steady-level flight of fixed-wing aircrafts. These analytical results do not therefore account for the unsteady aerodynamic effects

of flapping flight.

1.3.2 Pterosaur reconstructions

QN replica built by Aerovironment

In 1984 the Smithsonian's Air and Space Museum commissioned Paul MacCready and his firm Aerovironment, Inc. to build a half scale flapping replica of *Quetzalcoatlus northropi* described by Brooks et al.[22] based on the paleontological knowledge of the time.

Flying without an aerodynamic tail structure, the replica relied on the use of forward sweep with wash-in at the wing finger joint to achieve pitch stability. Additional yaw control, described by Jex[25], was added by using the head as a steerable forward fin, and by using the three small finger digits as drag devices. The replica also flapped its wings and used passive aeroelasticity to dynamically twist the wings. The flights of the QN replica were a tremendous achievement by successfully resolving all of these challenging issues.

Although the flapping motion had been designed to be very efficient, the actual flapping performance of the replica underlined the difficulty of achieving efficient flapping flight. Indeed, the replica could not gain altitude even at full power. It is apparent that aeroelasticity of the wing is a key feature of pterosaur flight that was exploited to provide efficient flight control and propulsion. High quality fossil finds have recently shed new light on the functional morphology and aerodynamic potential of pterosaurs, and shown that the shortcoming of the QN replica could be due to the gaps in the paleontological information at the time.

Stanford University - National Geographic Pterosaur Replica Project

The Stanford University-National Geographic (SUNG) Pterosaur Replica Project[26] aimed to design and build a mechanical flying replica of *Coloborhynchus robustus*. It was the second of its kind after Paul MacCreadys project. The focus of the replica project was mainly to investigate the wing controls during gliding flight. The replica was featured in the National Geographic documentary Sky Monsters[27].

Building a flyable and controllable replica of the agile pterosaur was challenging. The tail was designed as a high speed pitch stabilizer, and wing sweep as a pilot-induced pitch control. The head was destabilizing in yaw primarily, and was computer controlled during flight. Asymmetric drag distributions were used to control turns. The wing membrane was designed to emulate the presence of actinofibrils, structural fibers in the wing membrane that helped transfer loads from the outer wing to the stronger inner wing, and had an important function in camber control.

Flight tests provided improved knowledge of the interactions among the wing finger, wing membrane, and other joints during gliding flight. However these interactions remained to be investigated for flapping flight.

1.4 Approach

This study builds on the knowledge acquired during the development of the SUNG Pterosaur Replica Project. From the available paleontological data available, we infer the characteristics required to build the model for the wing of *Coloborhynchus robustus*. Available data include the range of motions of the wing joints and the dimensions of the bones. Missing elements, such as weight or wing area, are estimated from other pterosaurs or other flying vertebrates.

Flapping flight encompasses take-off, cruise and landing. However the unsteady non-linear effects involved in take-off and landing are beyond the capabilities of most computational tools. For this reason we focus on the cruise flight of pterosaurs, which correspond to the animal maintaining its average altitude and speed constant. In cruise flight, the main performance criteria is efficiency. Although large pterosaurs were believed to be soarers or motor-gliders, if they were able to sustain flapping flight, they had to do so very efficiently. We therefore consider that the best wing motion in cruise flapping flight maximizes propulsive efficiency.

Because we seek to optimize the flapping gait, we need to choose computational tools that provide reasonable accuracy while maintaining the optimization time low. Furthermore, high-fidelity methods can potentially provide high accuracy, but also require detailed model representations, which are not generally available for pterosaurs. When choosing computational methods, we therefore consider these trade-offs in light of the available paleontological information and the approximations made.

For this study, we aim to find methods that capture the main effects of the wing motion while keeping the computational costs low. The method chosen to compute the aerodynamic loads is based on the unsteady three-dimensional vortex-lattice method. This method captures the main unsteady aerodynamic effects for the three-dimensional wing, with typical unsteady computations in the order of several minutes. For the aeroelastic model of the wing, we constrain the non-linear structural problem to conditions where the membrane has a linear behaviour. In these conditions, we can use a reduced-order model, such as a modal decomposition, to solve for the structural displacements. This limits the additional computational cost to several seconds, while capturing the main effects of the wing flexibility during the motion. The choice of these methods limits the domain of flight that we can study, but is adequate for the

study of cruise flapping flight.

1.5 Outline

In chapter 2, we describe the current knowledge on the wings of pterosaurs, and in particular for the specimen of *Coloborhynchus robustus* that we study. We also estimate the missing information required to model flapping flight, in particular the mass distribution. We also define the aerodynamic quantities used to define propulsive efficiency. Because migratory birds are examples of extreme efficiency, we estimate the propulsive efficiency of several species of migratory birds, from available data.

In chapter 3, we describe the unsteady three-dimensional aerodynamic model developed for the calculation of forces during the motion. Because the detailed wing shape of pterosaurs remains unknown, we describe the model used to define the wing geometry during the motion. We compare the aerodynamic code with published results for unsteady wing motions of rectangular wings.

In chapter 4.1, we describe the fluid-structure interaction model, which we add to the aerodynamic code in order to investigate the role of the flexible wing membrane. Membranes are non-linear structures, but can be treated as linear structures under specific conditions. We therefore describe the assumptions used to treat the pterosaur wing as a linear structure. We compare the results from this method with measurements from experiments on an ornithopter. We also compare the finite-element model with analytical results. We discuss the effects of the membrane flexibility for given wing motion, and discuss the effects of the material properties of the membrane.

In chapter 5, we describe the optimization procedure used to infer the flapping gait. We define the objective function and the constraints using the optimization

problem. The constraints correspond to the conditions for level flight averaged over a period of the motion. We then describe the two algorithms used in this study, binary genetic algorithm and the sequentially quadratic programming method, and how they are combined. We finally show the results of the optimal flapping gaits for the joint motions and for the sensitivity studies considered.

Chapter 6 summarizes the findings from the optimization results. We also discuss the limitations of the methods we use, and the implications of the findings. Finally we propose topics for future studies to refine the findings of this study.

Chapter 2

Building the pterosaur model

2.1 Introduction

This study on flapping flight of pterosaurs follows the development of a pterosaur replica within the Stanford University-National Geographic Pterosaur Replica Project, which we refer to as the SUNG Replica Project[26]. The goal of that project was to design and fly a replica of a pterosaur as close as possible to what the real animal was believed to be. A similar effort was conducted between 1982 and 1984, during which Aerovironment[22] built and flew a replica, called QN, of *Quetzalcoatlus northropi*, believed to be the largest pterosaur ever. Since the QN replica project, numerous fossil remains of pterosaurs have been found, and several with almost complete skeletons and with very well-preserved joints. Among these specimens, NSM-PV 19892 had an almost complete wing and the main wing joints had maintained their three dimensional shape during the fossilization process. With these exceptional findings, the understanding of pterosaur flight leaped forward, and the goal of the SUNG Replica Project was to test and verify new results, based on a reconstitution of the specimen

NSM-PV 19892, believed to belong to the species *Anhanguera piscator*, now classified as *Coloborhynchus robustus*. The SUNG Replica especially explored the wing controls of the pterosaur membrane wing during glide using the possible wing joint motions as control mechanisms. The replica was also used for a preliminary study on flapping flight. However the analysis and subsequent flight tests were limited, as the implementation of the analysis tools was not a priority of the replica project.

In this study, we aim to understand the role of the motion of each wing joint motion for flapping flight. In particular, we compare the effect of each joint motions on corresponding propulsive efficiency and required mechanical power. In this chapter, we describe the model of a pterosaur specimen used to study the wing motions. We first give a general background on pterosaurs comparing them to other flying vertebrates, describe the available information from the specimen NSM-PV 19892, and detail the assumptions made to infer missing information.

We then motivate our choice of selection criteria for the joint motions. Because of their very large sizes, derived pterosaurs were very close to the achievable limit of flapping flight, thus they had to have high propulsive efficiencies. Migratory birds have a similar need for very high propulsive efficiency, and we therefore estimate the efficiencies for several species of migratory birds, that we will compare with values computed for the most efficient pterosaur wing motion.

2.2 Description of pterosaurs and of *Coloborhynchus robustus*

Kellner and Tomida[2] described the exceptionally well-preserved fossils of the specimen NSM-PV 19892 shown in figure 2.1. Although not the largest pterosaur, its

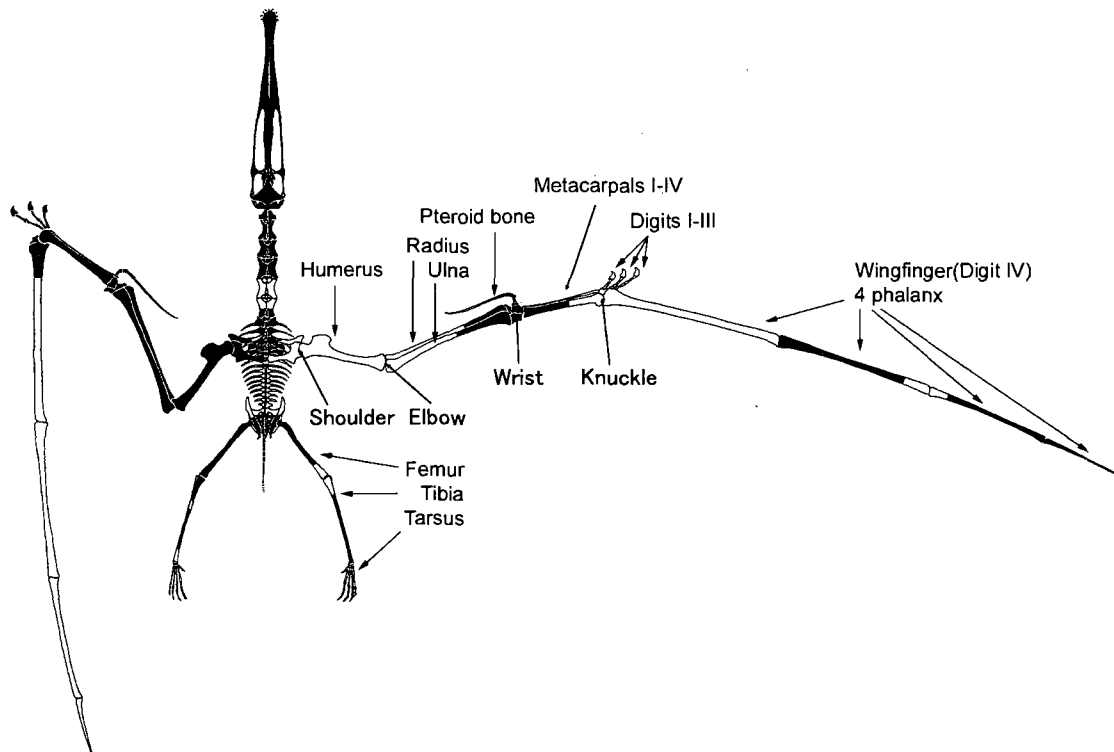


Figure 2.1: Outline of *Coloborhynchus robustus* skeleton, with preserved bones of specimen NSM-PV 19892 in black. Picture adapted from Kellner and Tomida[2]. This top view shows the right wing bones in flight position and the left wing bones in folded position. We have pointed out the bones and joints of interest for this study. We note that this specimen was initially classified as *Anhanguera piscator*.

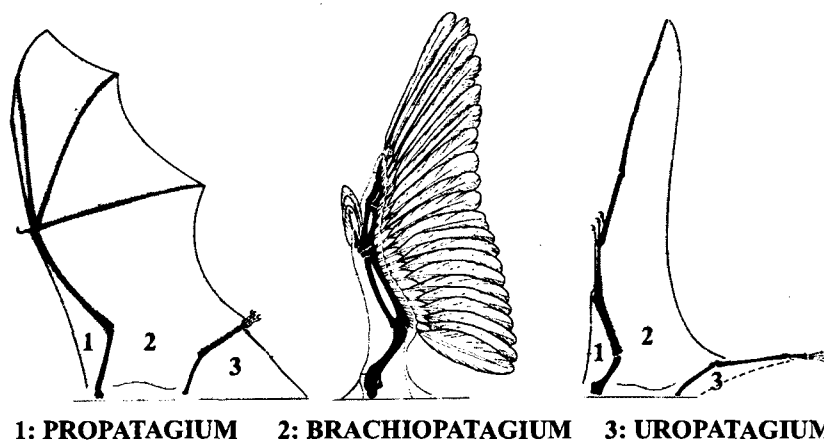
fossil remains are one of the most complete to date. Additionally, it is one of the few specimens where the three-dimensionality of the joints have been preserved, and was studied by Chatterjee and Templin[9], and Wilkinson[4] to infer the ranges of motion. Wilkinson[4] studied this specimen among other ornithocheirids to infer a complete wing configuration of an ornithocheirid. The wealth of paleontological data available compels us to study the flapping flight of ornithocheirids, and of NSM-PV 19892 in particular.

We note that Kellner and Tomida[2] first described NSM-PV 19892 as *Anhanguera piscator*. Unwin[28] reassigned it however as *Coloborhynchus robustus*. The classification of this specimen is still a source of discussion. In this study, we refer to this specimen as *Coloborhynchus robustus* using the most recent classification.

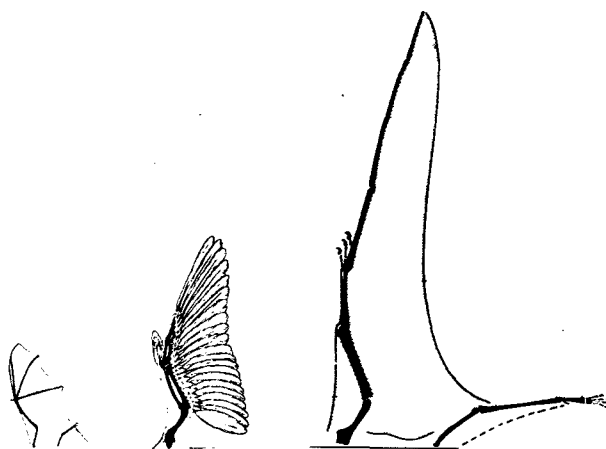
In this section, we first describe the general characteristics of the pterosaur wing. In particular, we compare its wing structure to those of birds and bats, then discuss the assumptions made for the wing membrane and the wing bones. As some bone dimensions were missing or not measured from the fossil remains of NSM-PV 19892, we estimate the missing lengths and cortical thicknesses of the wing bones. We then define the nomenclature that we use to define the joint motions in the axis system defined in figure 1 in the nomenclature. Using results from previous studies on joint motions, we then define, using our nomenclature, the range of active joint motions and the joint angles in glide.

2.2.1 Comparison of the wing structure of pterosaurs, birds and bats

The wing structure of pterosaurs is unique among vertebrates, and is described in detail by Wellnhofer[8]. As shown in figure 2.2, in birds, feathers are attached to the



(a) Comparison of bat, bird and pterosaur wing structures. In bird wings (middle), the wing is made of feathers attached to the wing bones. In bat wings (left), the wing is made of skin membrane attached to the wing bones. It is believed that pterosaur wings (right) were also made of skin membrane. The membranes stretching between the neck and the wrist (1), between the four wing fingers and the body (2), between the legs are called propatagium, brachiopatagium, and uropatagium respectively. In pterosaurs, the brachiopatagium (2) stretches between the body and the elongated fourth digit.



(b) Comparison of the size of bat, bird and pterosaur wings. Pterosaurs' unique wing structure enabled them to evolve to wingspan greater than ten meters. We display, from left to right, wings of a bat, a bird and a pterosaur with wingspans of one and a half, three and five meters respectively.

Figure 2.2: Comparison of the structures and sizes in bat, bird and pterosaur wings. Pictures adapted with permission from Wellnhofer[8].

wing bones. Pterosaur wings would have been made of skin membrane attached to the wing bones. The wing membrane of bats and pterosaurs is divided into three main sections, referred to as patagia, the propatagium, the brachioapatagium and the uropatagium. Due to lack of fossil evidence, the properties and attachment points of these membranes are still a source of debate for pterosaurs.

The propatagium stretches between the neck and the pteroid bone, located at the wrist in front of the wing bones. The uropatagium stretches between the legs. The brachioapatagium, also called cheiropatagium, stretches between the body, the wing bones and the legs. In bats, it stretches also between four wing fingers. In the case of pterosaurs, however, it stretches between the body and the elongated fourth finger, and is divided into the tenopatagium, also called plagiopatagium, and actinopatagium, also called dactylopatagium. The actinopatagium, stretching from the wrist to the tip, is reinforced by slender structures called actinofibrils. Figure 2.3 illustrates patterns seen in the wings of well-preserved specimens, as first observed in the specimen described by Zittel[14]. These patterns are associated with the presence of actinofibrils. The tenopatagium, like the propatagium and the uropatagium, do not display these structures. In this study, we refer to the actinopatagium also as the outboard section of the wing, and the area covering the propatagium and tenopatagium as the inboard section of the wing.

Fossil remains of the pteroid bone are usually incomplete with some part of the bone broken off. Its position and function in flight are also source of numerous discussions. Paleontologists are divided on whether the pteroid bone would have pointed towards the body or forward in flight. Most fossils show the pteroid pointing towards the body. However, as discussed by Wilkinson[4] and Unwin[28], this position is not related to the flight position, because the wing would return to a relaxed state

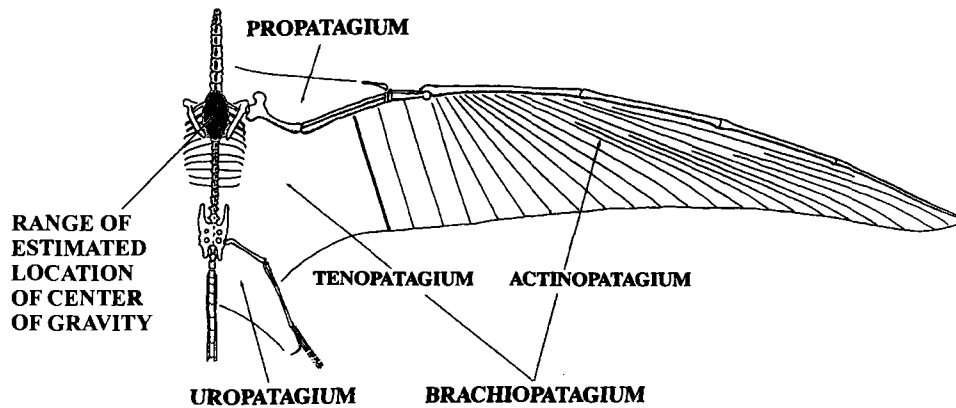


Figure 2.3: Diagram of a right pterosaur wing based on the fossils of the pterosaur *Rhamphorhynchus* described by Zittel[14]. The brachiopatagium is divided into two parts - the tenopatagium and the actinopatagium. The actinopatagium, stretching from the wrist to the tip, is reinforced by actinofibrils illustrated by the pattern of lines. The lines shown represent the orientations of the actinofibrils and not their actual spacing. The tenopatagium, like the propatagium and the uropatagium, do not display these structures. We also show the range of possible locations for the center of gravity, as estimated by Bennett[15]. Figure adapted from Bennett[16].

after the death of the animal. Wilkinson[29] explored the aerodynamic effect of a wing with the pteroid bone pointing forward. Provided it would have withstood the aerodynamic loads, that position increased the area of the propatagium, creating a leading-edge flap which could have been used in slow flight maneuvers, such as landing and take-off. In this study on flapping flight, the creation of thrust is mostly created by the outboard sections of the wing, so the position of the pteroid does not have a significant impact on propulsive efficiency during level flapping flight. For this reason, we do not study the motion of the pteroid, and we assume that the pteroid bone points toward the body.

2.2.2 Membrane attachment on the body

As reported by Unwin[28], several fossils of smaller pterosaurs with membrane imprints show that the membrane would have been attached to the leg, and maybe at the ankle, similarly to bats. Unfortunately, only partial membrane imprints have been found for larger pterosaurs, and it is not clear where the membrane would have been attached. The attachment of the membrane is related to the role of the hindlimbs during flight and walking. If the wing membrane was attached to the ankle, the motion of the hind limbs could have played an important role in controlling the shape of the wing, as discussed by Wilkinson[4]. However, it is unclear whether the legs could have supported the membrane tension loads, and what would have been their position during flight.

For larger pterosaurs, the weight of the animal imposes speeds at take-off and landing that might require some form of running or a few steps to accelerate, as discussed by Chatterjee and Templin[9]. For these scenarios, a membrane attachment at the ankle might interfere greatly with the motion. The membrane attachment is source of debate for all the stages of pterosaur flight. In this study, we investigate two attachment scenarios, with the wing membrane attached either at the hip or at the ankle.

2.2.3 Approximations for the properties of the wing membrane

The membrane wings of pterosaurs are the subject of numerous studies and discussions. The wing described by Zittel[14] exhibits one of the best imprints of the membrane actinofibrils, and especially for the orientation and distribution of fibers. As

discussed by Bennett[16], actinofibrils were believed to be keratinous or collagenous structures running along the underside of the membrane. If the reinforcing fibers were embedded within the skin membrane, the fibers would have most likely been made of collagen. If the fibers were located outside of the skin membrane, they would have most likely been made of keratin. These structures would have played an important role as a structural reinforcement and for controlling the flying shape of the wing.

Martill and Frey[30] and Frey et al.[31] described the partial remains of wing membrane found for the pterosaur *Rhamphorhynchus*. Using different light spectra, these specimens have shown various patterns attributed to actinofibrils, blood vessels and muscle fibres. They found that the fibers were embedded in the skin thickness among layers of muscles and connective tissue, and that the reinforcing fibers were present throughout the wing membrane. However, these fibers were aligned in high density only in the actinopatagium. The material properties of these remains to be inferred, but these results would indicate that the fibers were made of collagen. Although pterosaur of the *Rhamphorhynchus* species were smaller and evolved earlier than ornithocheirids, these findings are used to define approximations of the membrane properties.

On the wing of the pterosaur *Rhamphorhynchus* described by Zittel[14], Wellnhofer[8] estimated that the actinofibrils had a diameter of about 0.05 mm with a spacing of 0.08-0.25 mm. Martill and Frey[30] and Frey et al.[31] measured the layer of the actinofibrils to be about 0.18-0.20 mm thick. Bramwell and Whitfield[5] estimated the membrane thickness to be 0.3 mm in the pterosaur *Pteranodon ingens*, considering it should be about twice the thickness of the wing membrane measured on the bat *Pteropus giganteus*. However, as discussed by Frey et al.[31], bats are mainly nocturnal flyers because their wing membranes can not withstand significant sun exposure. We

do not know how much soft tissue is missing in the remains found, but Frey et al.[31] estimated the membrane would be about 1 mm thick, suggesting that pterosaurs could also have flown during the day.

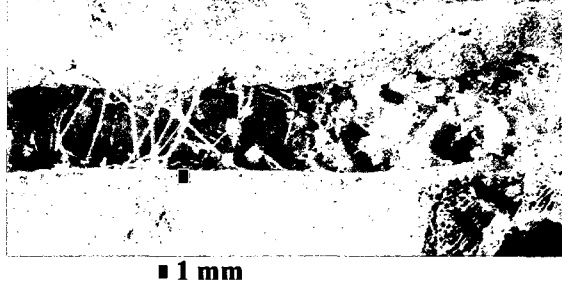
In this study, we assume that the membrane has a uniform thickness of 1.0 mm on the wing. As illustrated in figure 2.3, we assume that the fiber reinforcements affect mostly the actinopatagium. In the aerodynamic model detailed in chapter 3, we therefore assume that the actinopatagium was much stiffer than the other wing membranes, such that the membrane wing shape outboard of the wrist could be defined by the leading-edge bone structure. This assumption is used in the approximations for the wing geometry that we define in section 3.5.1. In the aeroelastic model detailed in chapter 4.1, we assume, for simplicity of the model, that the mechanical properties are the same in all the patagia. The variations of the load on the inboard sections of the wing are small compared to the those on the outboard section, so this simplification should not significantly impact the flapping motion. As the properties of the membrane are quite uncertain, we also conduct a sensitivity analysis of the mechanical properties of the membrane.

2.2.4 Wing bones of pterosaurs

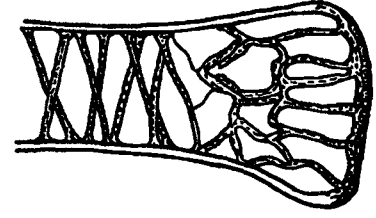
Although almost complete, the fossil remains of NSM-PV 19892 have several missing or fragmented bones. The lengths of the incomplete bones are estimated in section 2.2.5. As shown in figure 2.4, pterosaur wing bones are hollow with a thin wall as detailed by de Ricqlès et al.[32], and share many characteristics with bones of large birds. Notably, most bones have an elliptic cross-section at mid-length, and have a uniform cortical thickness, except near the joints. As discussed by Currey[33], the cortical bone tissue in fossil remains is highly mineralized, possibly more than large

Table 2.1: List of published material properties of bone

Bone type	Cortical bone	Flamingos
Source		Currey[33]
Young's Modulus E (GPa)	20-30	28.2



(a) Internal structure of the humerus of a specimen of the pterosaur *Santanadactylus* from Brazil. The wall of this bone is 0.5 mm thick. Picture reproduced with permission from Wellnhofer[8].



(b) Diagram of the internal structure of a pterosaur wing bone. Diagram adapted from de Ricqlès et al. [32].

Figure 2.4: Illustration of the internal structure of pterosaur wing bones. These were hollow with a very thin wall and were reinforced by internal struts, making them light yet strong. The cortical thickness is relatively homogeneous along the length of the bone, except near the joints where it is thicker.

birds. We list in table 2.1 available data on bone material properties. For this study, we use a Young's modulus of 30 GPa, corresponding to the upper bound of moduli measured in vertebrates, and assume a Poisson ratio ν of 0.3.

Fossil remains exhibit pneumatic foramen which allow the bones to be pressurized. In addition, internal struts act as reinforcements resulting in a strong yet lightweight structure. It is believed that the fourth metacarpal and the ulna would fail under buckling, as discussed by Bramwell and Whitfield[5].

2.2.5 Estimates for the lengths and cortical thicknesses of the bones in the wing

Although almost complete, the fossil remains of NSM-PV 19892 had several incomplete wing bones, and in particular the phalanges of the fourth digit. During the SUNG Replica Project[26], the missing bone lengths were estimated by Jim Cunningham from allometric relationships available for specimens of comparable sizes, for another species of pterosaurs, *Quetzalcoatlus species*. Although *Quetzalcoatlus species* and *Coloborhynchus robustus* have evolved at different periods, these estimates were deemed reasonable in light of the available data at the time. Wilkinson[4] recently proposed allometric relationships for ornithocheirids, based on ten different fossil remains.

Table 2.2 shows the length of the main wing bones as reported by Kellner and Tomida[2], as inferred by Jim Cunningham from available allometric data from the pterosaur *Quetzalcoatlus species*, and as inferred from the statistical regressions derived for ornithocheirids by Wilkinson[4]. The lengths estimated from the statistical regressions were computed using the length of the ulna. The wrist bones (proximal carpus and distal carpus) and digits I, II, and III were omitted because of their relative small size. We notice differences in estimate for the last three phalanges of the fourth digit. However, these differences amount to only a 6% in maximum difference in total span, and we therefore use only the estimates by Cunningham[3] for our model.

To infer the structural and inertial properties of the wing bones, we need the thickness of the wing bones. Such measurements are available for several specimens, but not for NSM-PV 19892, and must be estimated from other specimens. Table 2.3 shows the available wing bone cortical thickness provided by Bramwell and Whitfield[5], and estimated from measured data provided by Habib[6], and reported data by Bramwell

Table 2.2: Lengths of the main wing bones of *Coloborhynchus robustus*. The lengths listed have been reported by Kellner and Tomida[2], or estimated by Cunningham[3], or using the regression laws derived for ornithocheirids by Wilkinson[4]. We also include, for reference, the lengths in mm of the bones of *Pteranodon ingens* reported by Bramwell and Whitfield[5].

Source Lengths	Kellner and Tomida (reported)	Cunningham (estimated)	Wilkinson (estimated)	Bramwell and Whitfield (reported)
Humerus	254	255	284	290
Radius/Ulna	390	390	390	347
Metacarpal IV	255	256	267	671
Phalange I	-	561	560	779
Phalange II	-	490	534	614
Phalange III	-	388	435	400
Phalange IV	-	238	343	246

and Whitfield[5]. The thicknesses provided by Bramwell and Whitfield[5] are estimated for a 7m wingspan specimen of the pterosaur *Pteranodon ingens*. Although slightly larger than the specimen we study, these provide a good reference for comparison. The thicknesses for *Coloborhynchus robustus* were estimated by scaling the measured thickness to the anterior-posterior length or dorso-ventral widths taken at mid-length of the bone. The values listed in the table are the average of these estimates made from up to fifteen specimens. For our mass estimates and for the aeroelastic model, we choose the highest value of the estimated thicknesses in order to have a conservative estimate of the dimensions. In the case of the third and fourth phalanges of the wing digit, there are not enough specimens to make such an estimate, and we choose the thicknesses reported for bones with the closest dimensions.

Table 2.3: Cortical thicknesses of the main wing bones of *Coloborhynchus robustus*. The bone cortical thicknesses listed have been reported by Bramwell and Whitfield[5] for *Pteranodon ingens*, or estimated from the anterior-posterior or dorso-ventral widths at the bone mid-length from the data provided by Habib[6] and Bramwell and Whitfield[5]. The chosen thicknesses are also listed. All dimensions are given in mm. Abbreviations: AP, anterior-posterior ; DV: dorso-ventral.

Bone name	Estimated from AP length	Estimated from DV length	Chosen	Reported
Humerus	1.8	1.2	1.8	1.6
Radius	0.9	0.8	0.9	1.3
Metacarpal IV	0.9	0.7	0.9	1.5
Phalange I	1.0	1.3	1.3	1.5
Phalange II	0.8	0.6	0.8	0.6
Phalange III	-	-	0.6	0.5
Phalange IV	-	-	0.5	0.5

2.2.6 Nomenclature for the wing geometry

The range of motions of joints is often described in anatomical terms relative to the proximal bone. In this study, we define the joint angles using the same axis orientation defined for the body, as shown in figure 2.5. The wing geometry is therefore defined by the location of each joint in the frame attached to the body. The frame attached to the body is noted with the 0 subscript, its origin is at the center of gravity of the animal, the axes are defined as in figure 1. As shown in figure 2.3, Bennett[16] estimated the center of gravity to be close to the shoulder. There is not enough fossil evidence to support a more accurate estimate on the mass and volume distribution of soft tissue, and therefore also a more accurate estimate of the position of the center of gravity. In this study, we therefore assume that the center of gravity is located at the shoulder joint.

We define a frame for each bone with the origin at the proximal joint. We identify each joint and frame with subscripts increasing distally from the shoulder (subscript

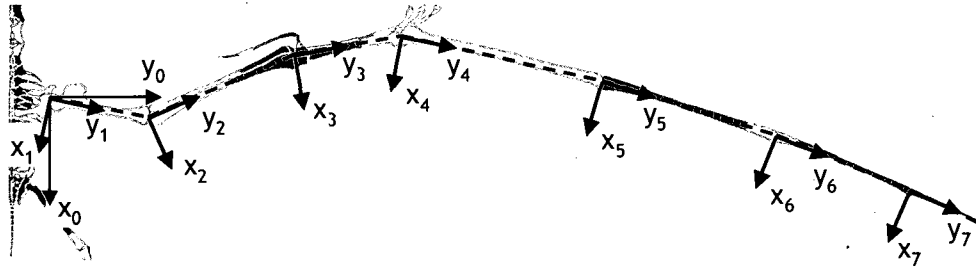


Figure 2.5: Top view of the orientation of the frames attached to the bones, superimposed on the skeleton from Tomida and Kellner[2]. The wing geometry is defined by the rotation of each bone relative to the joint at its proximal end. A frame, noted by its corresponding subscript, is attached to each bone with the origin at the proximal joint. The y -axis of each bone frame is defined by the length of the bone. The joint angles ϕ , θ , and ψ correspond to rotations about the x , y , and z -axes respectively as defined in figure 1. The orientation of the x_0 and y_0 axes is such that the view matches the outline in figure 2.1.

1) to the joint between the third and fourth phalange of the fourth digit (subscript 7). We align the y -axis of the frame with the length of the bone. The rotation of each joint is relative to the orientation of the proximal frame. Figure 2.5 illustrates the position and orientation of the frames attached to the bones.

2.2.7 Range of motions of the movable joints in the wing

The interpretation and inferred estimates of the range of joint motion depend on the three-dimensional quality of the joint remains. Using the nomenclature of the wing geometry defined above, we define the range of motion of each joint of the wing from the available published results for several very well preserved specimens of different pterosaur species. Bramwell and Whitfield[5] described the joint motions for the wing of a specimen of *Pteranodon ingens* with a 7m wingspan. Wellnhofer[8] described the joint motions for *Anhanguera* and other pterosaurs. Bennett[7] studied another

specimen of *Pteranodon*. Chatterjee and Templin[9] inferred the joint motions for *Anhanguera*. Wilkinson[4] studied ten fossil remains of ornithocheirids to infer the joints motions. These different studies of varied species and specimens indicate that the joints of the fourth digit were locked in position, and that the active motions during flight occurred at the shoulder, elbow, wrist, and knuckle. In all, the flapping gait can be described by seven degrees of freedom.

In this study, we do not account for the motion of the pteroid bone, since it is believed to have been used mostly during low-speed maneuvers, as discussed by Unwin et al.[29] and Wilkinson[4]. Additionally, the motion of the pteroid bone would have mainly modified the shape of the membrane proximal to the wrist. Since most of the thrust is created by wing distal to the wrist, the motion of the pteroid bone would probably have only a small role in cruise level flapping flight.

Although the reported ranges of joint motions have been inferred for different species, we assume that the specimens studied so far share enough commonalities to infer general estimates for derived pterosaurs, and for the NSM-PV 19892 specimen in particular. We compare in table 2.4 the different published ranges of motions described in our nomenclature. We note that Wilkinson[4] reported the ranges of motion for each joint along with the inferred orientation of the motion axes. Additionally, he provided the wrist joint motions for each carpal bone in the wrist, and the estimates we report combine roughly the range of motions of the carpals of interest. We include in table 2.4 the values from Wilkinson[4]. Bennett[7] and Wilkinson[4] have also described interrelated motions, especially at the elbow and wrist joints. However, implementing these motions and orientations of the axes adds a level of complexity, that does not seem adapted to the simplified model used in this study. We therefore assume that the joints move independently from each other, such that

a motion about one axis at a joint does not affect motions about other axes or at different joints.

We model the flapping motion such that it induces an oscillation about the chosen glide position. Wilkinson[4] proposed that the joints during glide would be set in close-packed positions, which corresponds to the most extended position of the joints. However, this position does not seem practical for flapping motions, as the animal would have not been able to oscillate the joints about these positions. We therefore assume that the glide angle for each joint is roughly the mid-angle of the range of motion, except at the knuckle. The range of motion inferred for the knuckle includes the motion to fold the wing when pterosaurs were on the ground, and the published range of motion certainly do not correspond to flight motions. For the knuckle glide position, we use the angle estimated by Chatterjee and Templin[9]. In the most extended position of the knuckle inferred by Wilkinson[4], the first phalange of the wing digit is aligned with the fourth metacarpal, which corresponds to five degrees about the chosen glide position. We therefore assume a five degrees amplitude for the motion of the knuckle during flapping flight. Table 3.4 details the chosen joint angles in glide position. The maximum oscillation amplitudes in table 2.5 are chosen so that, during the flapping motion, the joint angles stay within the allowed range.

2.2.8 Atmosphere in the Mesozoic and Lower Cretaceous

The size of the fossils of large pterosaurs has raised the question of why birds have not evolved to similar sizes once pterosaurs became extinct. The fossils of the biggest bird found, for *Argentavis magnificens*, were estimated to have a wingspan of 7 meters[34], whereas pterosaurs, like *Quetzalcoatlus northropi*, are believed to have reached wingspans up to 12 meters[35]. One typical argument is that gravity forces

Table 2.4: Angular range (in degrees) of movable joint motions for *Pteranodon*, *Anhanguera*, and ornithocheirids, as inferred by Bramwell and Whitfield[5], Bennett[7], Wellnhofer[8], Chatterjee and Templin[9], Wilkinson[4]. The values of allowed range of motion have been formulated in the nomenclature defined in section 2.2.6.

Joint motion		Bramwell & Whitfield	Bennett	Wellnhofer	Chatterjee & Templin	Wilkinson
Shoulder						
dihedral	ϕ_1	[-25 ; 70]	[-25 ; 70]	[-40 ; 40]	[-65 ; 60]	[-25 ; 70]
pitch	θ_1		[-35 ; 35]		[-42.5 ; 42.5]	[-50 ; 30]
sweep	ψ_1	[-65 ; 0]	[-65 ; 0]	[-25 ; 0]	[-70 ; -15]	[-30 ; 50]
Elbow						
sweep	ψ_2	[30 ; 60]	[30 ; 150]	[30 ; 70]	[35 ; 90]	[20 ; 110]
Wrist						
pitch	θ_3	[-10 ; 10]	[-10 ; 10]			[0 ; 40]
sweep	ψ_3	[-45 ; 17]	[-50 ; 0]	[-45 ; -15]	[-45 ; -15]	[-80 ; -5]
Knuckle						
pitch	θ_4					[-20 ; 0]
sweep	ψ_4	[-150 ; -15]	[-175 ; -5]	[-15 ; -15]	[-145 ; -15]	[-160 ; 0]

Table 2.5: Maximum amplitudes of joint motion about glide position (in degrees) for *Coloborhynchus robustus*

Joint name	Shoulder	Elbow	Wrist	Knuckle
Joint index i	1	2	3	4
ϕ_i	45	locked	locked	locked
θ_i	10	locked	10	locked
ψ_i	25	20	15	5

have changed as the crust of the Earth cools down. John McMasters[36] estimated that, if the Earth crust radius shrank by 20% over the last 100 million years, the gravity forces at that time would have been 31% smaller than nowadays. In flapping flight, gravity forces are correlated to the required lift forces to fly at fixed altitude. A sensitivity study of the magnitude of gravity is therefore equivalent to a sensitivity study of the mass estimates.

According to Budyko[37], Levenspiel[38] and Dudley[39], the Earth atmosphere at the time of pterosaurs could have been several times more dense than the current atmosphere, and the oxygen concentration could have been higher than today. Additionally, it is believed that the average atmospheric temperature was about several degrees warmer than today, and it is likely that atmospheric convection, thermals and winds would have been much stronger than today. The atmospheric conditions during that period are largely unknown, so we base our study on the flight of pterosaurs using values for today's atmosphere, and conduct a sensitivity study of the atmospheric density.

2.3 Estimates for the total mass and mass distribution

Total mass and mass distribution are key characteristics of a flying animal. We estimate reasonable flight speeds from the weight and the wing area. Additionally, if the mass of the wing is significant compared to the total mass of the animal, the motion of the wing will induce motions of the body, that conserve the position of center of gravity for the whole animal. Furthermore, the variations of forces during the wing motion induce a movement of the animal's center of gravity. Finally, on a

structural point of view, the mass distribution in the animal, and especially in the wing, affects the inertial properties of the wing structure, hence the dynamic response of the wing in motion.

Unfortunately, the fossil remains provide very little information on soft tissue, so that the total mass and mass distribution of pterosaurs can only be roughly estimated. This is a source of uncertainty and debate, and published mass estimates for pterosaurs greatly vary. Bramwell and Whitfield[5] estimated the body volume from the fossils and assumed an average density to estimate the mass distribution of *Pteranodon ingens*. The average density accounted for the density of bones, soft tissues and air cavities (trachea, lungs, air sacks). They estimated that a 7m wingspan specimen of *Pteranodon ingens* would have a mass of about 16.6 kg. Chatterjee and Templin[9] also proposed a mass model, and estimated a mass of 7.6 kg for *Coloborhynchus robustus* with a 4.7 m wingspan. As detailed in this section, we estimate a mass of 17.0 kg for *Coloborhynchus robustus*. Because of the large uncertainties in estimating the mass of pterosaurs, we use this estimate as a reference, and we conduct sensitivity studies.

During the SUNG pterosaur replica project, John Conway[40] collaborated with Chris Bennett to create a muscle cast of the wing of *Coloborhynchus robustus*, assuming that pterosaurs could have derived from archosaurs, as discussed by Unwin[28]. The muscle cast was used to estimate the required volume of the wing. However, estimating the mass distribution from this cast was a source of debate, as the muscle volume of the cast could not be based on power requirements. Future studies could aim at estimating the muscle volume required to achieve the flapping gait inferred from this study.

In this section, we estimate the distribution of mass, the position of center of

gravity, and the moments of inertia of *Coloborhynchus robustus*. We estimate the weight distribution in the wing, using trends of the inertial properties of the wings observed in birds and bats. We detail below the methods used to estimate the weight of the bones, the membrane, and of the soft tissue in the wing. We estimate the weight of the different components of *Coloborhynchus robustus* using the methods used by Bramwell and Whitfield[5] for *Pteranodon ingens* as comparison. Comparing our estimates with the published results for pterosaurs of similar wingspan, we finally propose a range of estimated weight for *Coloborhynchus robustus*. We note that the inertial properties shown in this section are used in the aerodynamic model, and in the aeroelastic model.

2.3.1 Inertial properties of the wings of birds and bats

Most aerodynamic studies on flapping flight focus on the forces created by the motion of the wing while considering that the body translates forward at constant velocity and altitude. However, observations of bats and birds have shown that the variation of the aerodynamic forces induces a vertical motion and change in orientation on top of the forward motion. Van den Berg and Rayner[17], Thollessen and Norberg[41] have studied the impact of inertial loads on the flapping motion of birds and bats respectively.

In figure 2.6, Van der Berg and Rayner[17] divided the wings of a bird, *Turdus merula*, and of a bat, *Pipistrellus pipistrellus*, into spanwise strips, measured the mass of each strip, and estimated the moment of inertia of each strip. We note that the wing mass in birds is largely concentrated near the shoulder, and the distribution of moment of inertia of each strip follows a bell-shaped curve. In bats, the distribution of moment of inertia is different due to the wingfingers spanning the brachioptagium.

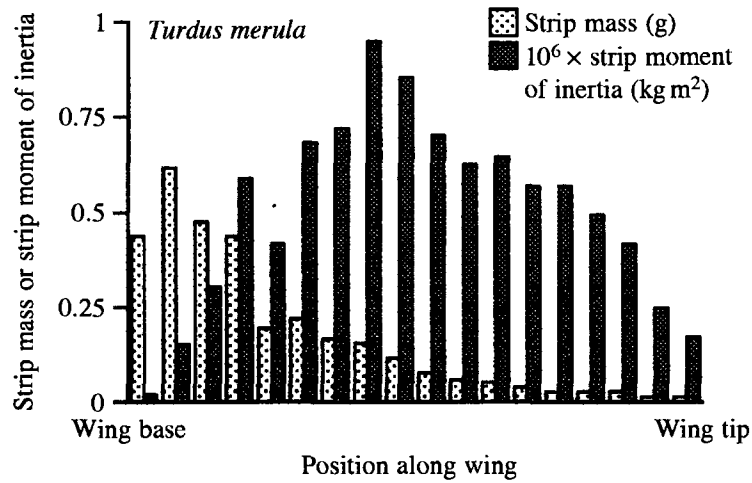
Van der Berg and Rayner[17] estimated, over 29 bird species and three bat species, that the power to overcome the inertia of the wing accounts for about 11-15% of the minimum required power for forward flapping flight.

For flapping flight, reducing the mass hence the moment of inertia near the tip reduces the inertial power. It is likely that the observed distribution in the wings of birds is the result of an evolutionary compromise between minimizing flapping power and maintaining structural integrity. Unlike bats, the wing of pterosaurs sustain the loads with only one wingfinger, so we assume that pterosaur wings would share similar trends to birds in the distribution of mass and moment of inertia. We estimate the soft tissue mass on each bone to follow such trends.

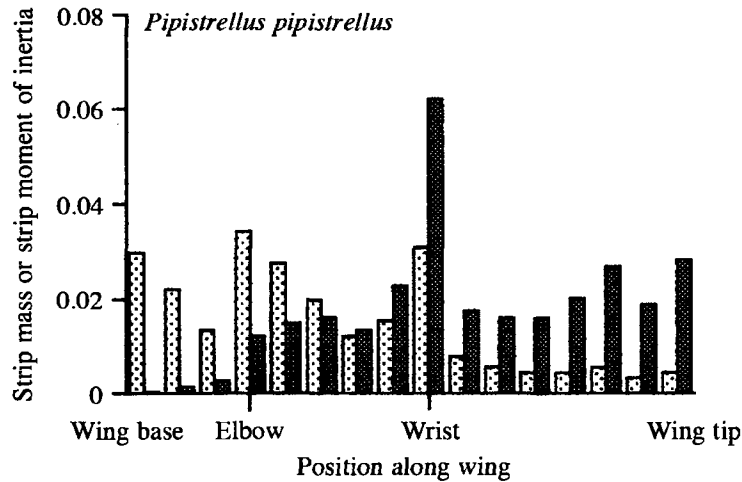
2.3.2 Mass of the wing bones

As described in section 2.2.4, the wing bones of pterosaurs were hollow and the cortical bone thickness was almost uniform. To estimate the mass of each bone, we therefore consider them as hollow tubes of uniform elliptic cross-section and wall thickness. However, the cross-sections of the bones at the joints are usually much larger than at mid-length. We therefore estimate the mass at the ends of a bone, by assuming the bone ends as elliptic discs of constant thickness. Distal to the wrist, this approximation seems reasonable. Although the cross-sections of the humerus, radius and ulna vary significantly, we expect that the soft tissue mass on these bones dominate the inertial properties.

We calculate the mass in the tubular section using the radius and thickness of the wing bones at mid-length. We note that the bone dimensions were measured from the pictures provided in Kellner and Tomida[2], and that we use the estimated cortical thickness from table 2.3. We calculate the bone mass from the estimated volume



(a) Distribution of mass and moment of inertia, for the bird *Turdus merula*



(b) Distribution of mass and moment of inertia, estimated for the bat *Pipistrellus pipistrellus*.

Figure 2.6: Distribution of mass and moment of inertia from root to tip for the wings of a bird, *Turdus merula*, and of a bat, *Pipistrellus pipistrellus*. In birds, the mass is concentrated towards the root of the wing, and the moment of inertia varies in a bell-shaped curve along the span. Figures adapted with permission from van der Berg and Rayner[17].

Table 2.6: Mass estimates of the main wing bones of *Coloborhynchus robustus*. The bones are assumed to be elliptic tubes of uniform cross-section and cortical thickness. We also list the mass estimates for the wing bones of *Pteranodon ingens*, derived from Bramwell and Whitfield[5] assuming an average tissue density of 1000 kg.m^{-3} . All dimensions are given in mm, the mass in g. Abbreviations: AP, anterior-posterior ; DV: dorso-ventral.

Bone name	Length	AP length	DV length	Cortical thickness	Mass	Mass <i>Pteranodon</i>
Humerus	255	38	42	1.8	208	123
Radius	385	24	30	0.9	106	61
Ulna	390	10	15	0.9	51	80
Metacarpal IV	256	20	25	0.9	59	205
Phalange I	561	22	35	1.3	241	202
Phalange II	490	15	17	0.8	71	50
Phalange III	288	18	18	0.6	47	16
Phalange IV	238	10	10	0.5	13	6

using a bone density of 1800 kg.m^{-3} , as used by Pennycuik[42, 43]. We note that we do not account for the weight of the wrist carpi, the pteroid bone or the smaller wing digits.

Table 2.6 summarizes the mass estimates of each bone and compares these to the estimates by Bramwell and Whitfield[5] for *Pteranodon ingens*. We estimate the total mass of the wing bones, for one wing, at about 0.80 kg, compared to 0.81 kg estimated for *Pteranodon ingens*.

2.3.3 Mass distribution of the wing membrane

Bramwell and Whitfield[5] estimated an average thickness of 0.03 mm for the wing membrane of *Pteranodon ingens*. However, Frey et al.[31] estimated from partial remains that the membrane was about 1 mm thick. In this study, we assume that the wing membrane has an uniform thickness of 1.0 mm and has a density of skin of 1100 kg.m^{-3} , measured for bat wings by Swartz et al.[44].

Table 2.7: Mass estimates between the joints of the main wing bones of *Coloborhynchus robustus*. The area between the joints is estimated from the chord distribution of the wing in glide position.

Joint name	Spanwise position (mm)	Chord (mm)	Membrane mass (g)
Shoulder	000	356	93
Elbow	240	351	137
Wrist	599	343	93
Knuckle	852	328	192
Phalange I - II	1413	295	137
Phalange II - III	1899	216	70
Phalange III -IV	2277	120	21
Wing tip	2485	0	

We calculate the membrane mass distribution in the wing from the glide geometry, and we assume that the variation of distribution of membrane mass is small during the flapping motion. This seems reasonable for small variations of sweep angles at the joints. We assume that the wing membrane wraps around the bones and other soft tissue, resulting in the wing membrane spanning from the leading edge to the trailing edge of the wing. With the chosen assumptions, the membrane mass distribution along the span is therefore directly related to the chord distribution along the span. Table 2.7 shows the distribution of membrane mass estimates between each joint. The mass of the membrane of one wing is estimated at about 743 g, compared to the estimated mass of 650 g for *Pteranodon* with a thinner membrane.

2.3.4 Overall mass distribution in the wing

The pterosaur fossil remains found so far have not yielded sufficient information to infer the mass distribution of soft tissue on the wing. We use the trends of distribution of mass and moment of inertia observed in birds, to estimate the overall weight distribution and moment of inertia I_{xx} about the root axis x , for *Coloborhynchus robustus*. We then infer the mass distribution of soft tissue, by subtracting the sum of the bone and membrane mass distribution from the overall mass distribution.

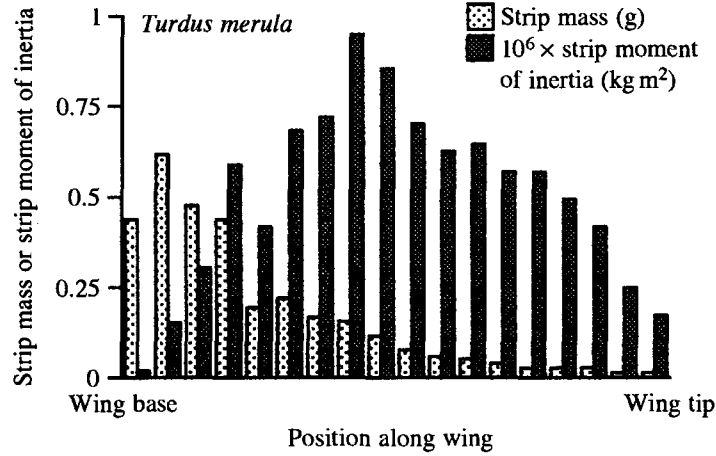
As detailed by Unwin[28] and Bennett[15], there are no clear marks of muscle attachment on the fourth digit, so it is believed that the most significant muscles on the wing were present between the shoulder and the knuckle. We therefore assume that the soft tissue mass is very small distal to the knuckle. We observe in table 2.9 that the maximum for the moment of inertia, combining the bone and membrane mass, occurs around the middle of the wing, on the first phalange of the fourth wing digit. We then adjust the mass of other soft tissue, such that the distribution of moment of inertia follows roughly a bell-shaped curve, and such that the distribution of total mass increases roughly linearly towards the wing root, as shown in figure 2.7(b). The estimated mass components and moment of inertia are detailed in table 2.8 and 2.9 respectively. We estimate the total mass for the wing to be 3.7 kg, compared to 3.2 kg estimated by Bramwell and Whitfield[5] for *Pteranodon ingens*. We find that the moment of inertia for a uniform membrane is significant on the distal part of the wing, such that it exceeds the moment of inertia of the bones. It seems likely that the distribution of membrane thickness on the wings of pterosaurs would have been tailored to reduce these moments of inertia towards the tip.

Table 2.8: Estimates of distribution of mass, expressed in g, for the wing of *Coloborhynchus robustus*.

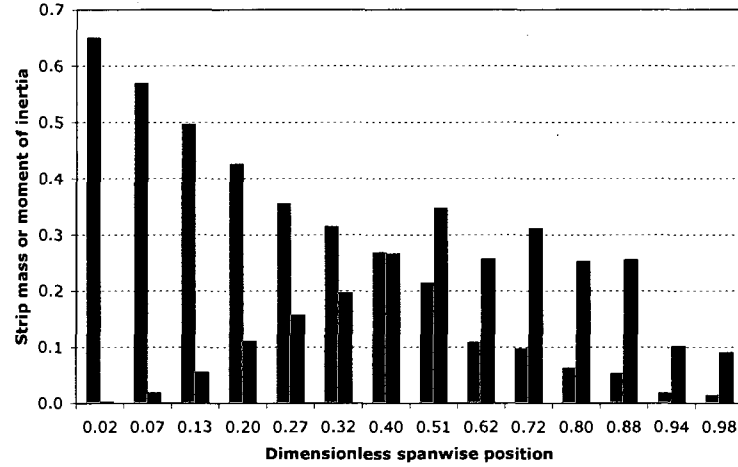
Bone segment	Bone	Membrane	Soft tissue	Overall mass
Humerus	208	93	920	1221
Radius/Ulna	157	137	630	924
Metacarpal IV	59	93	520	672
Phalange I	241	192	50	483
Phalange II	71	137	0	208
Phalange III	47	70	0	117
Phalange IV	14	21	0	35
			Total	3660

Table 2.9: Estimates of distribution of moment of inertia I_{xx} about wing root axis x , expressed in g.m^2 , for the wing of *Coloborhynchus robustus*.

Bone segment	Bone	Membrane	Soft tissue	Total moment of inertia I_{xx}
Humerus	4	2	16	22
Radius/Ulna	29	26	112	168
Metacarpal IV	32	49	273	354
Phalange I	316	250	50	616
Phalange II	196	373	0	569
Phalange III	207	302	0	509
Phalange IV	76	117	0	193
			Total	2429



(a) Distribution of mass and moment of inertia, for the bird *Turdus merula*. Figure reproduced with permission from van der Berg and Rayner[17].



(b) Strip mass and moment of inertia, estimated for the pterosaur *Coloborhynchus robustus*, plotted as a function of the dimensionless spanwise position $\frac{y}{b_{\text{ref}}}$. The strip mass and moment of inertia I_{xx} are plotted with grey and black bars respectively, and are expressed in kg and $\text{kg}\cdot\text{m}^2$ respectively.

Figure 2.7: Distribution of wing mass and moment of inertia from root to tip. For *Turdus merula* (figure 2.7(a)), the mass is concentrated towards the root of the wing and the moment of inertia varies in a bell-shaped curve along the span. For *Coloborhynchus robustus* (figure 2.7(b)), we estimated the soft tissue mass such that the total mass and inertia match these trends.

Table 2.10: Estimates of the dimensions for the soft tissue volume for the wing of *Coloborhynchus robustus*. All dimensions are expressed in mm.

Bone segment	Bone length	Inner radius	Outer radius	Muscle thickness
Humerus	255	20.0	38.5	18.5
Radius/Ulna	385	13.5	26.0	12.5
Metacarpal IV	256	11.3	27.1	15.9
Phalange I	561	14.3	15.2	0.9
Phalange II	490	8.0	8.0	0.0
Phalange III	388	9.0	9.0	0.0
Phalange IV	238	5.0	5.0	0.0

2.3.5 Distribution of soft tissue mass and volume on the wing

Based on inertial considerations, we have inferred the mass of soft tissue on each bone in the wing. We assume that muscle tissue accounts for most of the soft tissue mass, so we estimate the volume of soft tissue using a muscle density of 1060 kg.m^{-3} , as given by Pennycuick[43]. We model the soft tissue volume as a hollow tube, such that the inner radius matches the outer radius of the corresponding bone. Using the estimated soft tissue mass for each bone of table 2.9, we estimate the corresponding thickness distribution of the soft tissue tubes, listed in table 2.10. We assume that the soft tissue does not carry any load.

2.3.6 Overall mass distribution of *Coloborhynchus robustus*

We now estimate the overall mass distribution of *Coloborhynchus robustus*, accounting for all body parts, in order to estimate the total mass of the animal, the location of center of gravity x_{CG} and moments of inertia I_{yy} , relative to the origin of the body axes located at the shoulder joint. Except for the wings, the body components are very close to the root axis x , and therefore we assume that the moments of inertia I_{xx} of the body components are very small compared to the wings.

In the study of the *Pteranodon ingens*, Bramwell and Whitfield[5] estimated the volume of the different body parts, such as the head, neck, torso, wing and legs, and then proposed a range of mass estimates using a range of average tissue density. We use the same method to estimate the mass of the head, neck and torso and legs of *Coloborhynchus robustus*. In this study, we have not estimated the volume of the head, the femur, tibia and feet. However, the sizes of these body parts of *Pteranodon ingens* are close to those of the specimen of *Coloborhynchus robustus* that we study. We therefore assume that the mass estimates for the head and legs of *Pteranodon ingens* can also be used for *Coloborhynchus robustus*. We use the estimates for the wing detailed in section 2.3.4. We estimate the volume of the neck and torso from the dimensions given by Kellner and Tomida[2].

For the neck, we assume a cylinder of constant elliptical cross-section. The length of the neck is estimated from the reported lengths of cervical vertebrae, and an approximated length of 50mm for the 7th cervical vertebrae. The dimensions of the cross-sections are estimated from the average width and height of the cervicals. Bramwell and Whitfield[5] discussed the volume distribution in the neck, with a significant volume taken by the hollow bones, trachea, and oesophagus, such that only 30% of the neck volume would be solid. From their drawing, we approximate the neck height as 150% of the height of the vertebrae. The height and width of the neck vertebrae do not vary greatly between the head and the shoulder, so we assume that mass is distributed uniformly in the neck, so that the center of gravity of the neck is located at mid-length.

For the torso, we assume a cylinder of elliptical cross-sections that varies linearly from the neck to the pelvis. We estimate the dimensions of the shoulder and pelvic girdles from the drawings and pictures by Kellner and Tomida[2]. Similarly to the

neck, Bramwell and Whitfield[5] discussed that a significant volume of the torso was taken up by cavities such as lungs and air sacks, and estimated that only 30% of the torso volume would be solid. We do not know a priori how the mass would be distributed along the length of the torso. However, the torso is located quite close to the center of gravity, so the mass distribution in the torso does not greatly affect the position of the animal's center of gravity. We therefore assume that the center of gravity of the torso is also located at mid-length. Bramwell and Whitfield[5] proposed a range of mass estimates for the torso of *Pteranodon ingens*, and we compare their mid-range estimate with our results. There is a large uncertainty on the mass of the torso, so, for the rest of this study, we choose the average of these two estimates, as the reference mass estimate of the torso for *Coloborhynchus robustus*.

The mass, center of gravity x_{CG} and moments of inertia I_{yy} of each component of the animal are summarized in table 2.11. In all, we estimate that this specimen of *Coloborhynchus robustus* had a mass of about 17.0 kg, and we approximate the reference weight of the animal at 160 N. The resulting center of gravity for the entire animal would be located about 37 mm behind the shoulder joint. We also note that the mass of both wings would account for about 43% of the total mass of the animal, and that the center of gravity of one wing is about 0.61 m away from the shoulder, which is about 24% of the span of one wing.

The soft tissue preserved in fossil remains is too limited to infer organ and muscle volume, and there is a great uncertainty on the total mass and mass distribution estimates. We are not aware of another method to infer the mass distribution on the wing. We therefore study the sensitivities of the flapping motion and performance, to the total mass of the animal in chapter 5.

Table 2.11: Estimates for the distribution of mass, center of gravity x_{CG} and moments of inertia I_{yy} of each component of *Coloborhynchus robustus*. The estimates include the position of one wing's center of gravity y_{CG} , and moment of inertia I_{xx} about the root axis x . The masses are expressed in kg, distances in m, and moments of inertia ($\text{kg}\cdot\text{m}^2$).

Body part	Mass	x_{CG}	I_{yy}	y_{CG}	I_{xx}
Head	0.87	-0.477	0.198		
Neck	1.11	-0.161	0.039		
Wings	7.32	0.017	0.038	0.605	2.429
Legs	0.84	0.291	0.075		
Torso (this study)	5.05	0.0128	0.120		
Total	15.20	0.027	0.469		
Torso (<i>Pteranodon</i>)	8.66	0.128	0.206		
Total	18.80	0.047	0.555		
Averaged total	17.00	0.037	0.512		

2.4 Estimates of propulsive efficiency of migratory birds

One hundred years after the Wright brother's first flight, natural flyers are still a source of inspiration. Many researchers in the biology and aeronautics fields have investigated the flight of birds, bats and insects. Although many have successfully built ornithopters, man-made machines still do not compare with the endurance of migratory birds, as will be discussed in section 4.4. As discussed by Mueller[45], it is key to investigate the source of this performance gap. Although ornithopters have been reported to fly for minutes, Bar-tailed Godwits display extreme migration endurance, and have been reported by the United States Geological Survey (USGS) to fly non-stop from Alaska to New Zealand[46]. It is reasonable to assume that migratory birds have evolved to become very efficient flyers, and therefore are relevant examples of high propulsive efficiency in nature.

Findings of huge pterosaurs, like *Quetzalcoatlus northropi*[35] and other azdarchids,

with wingspans estimated at up to 12 meters, raise the question on the advantage of evolving to these sizes. Such giants are believed to be mainly gliders, as the largest birds alive today are also mainly soarers. However, pterosaurs, like *Coloborhynchus robustus*, might have been continuous flappers or motor-gliders, and if they were, they would have been near the limit of continuous flapping flight, hence very efficient. In this study, we aim at comparing the role of each joint motion on the performance during flapping flight, and we choose the propulsive efficiency as our performance metric.

In this section, we first relate metabolic power and mechanical power. We then define propulsive efficiency, and motivate our choice for the definition we use. We then list several methods of measuring the metabolic power. We then detail our method to estimate the average thrust created during the motion, by using relevant results from classical aerodynamic theory. Finally, we estimate the propulsive efficiency of several species of migratory birds, and we use these results to compare the performance of birds and pterosaurs.

2.4.1 Definition of propulsive efficiency

The general definition of the Froude efficiency is the ratio of useful work over total work done or input in the system. Efficiency can be defined in many ways, and the relevance of an efficiency definition relies on the definition of useful work and power input. In this section, we first show a method to estimate mechanical power deduced from measurements of metabolic power. We then detail different definitions of propulsive efficiency and motivate our choice of definition.

Mechanical power estimated from metabolic power

From a biological standpoint, understanding migration relates to the metabolic efficiency of an animal. The speed of migration is indeed related to the metabolic energy spent in migration, feeding stops, reproduction and other mechanisms, and the available energy from food consumption. About twenty percent of the energy spent by muscles is transformed into useful mechanical work, the rest is released as heat. The muscle efficiency, noted η_{muscle} , is defined by the ratio of mechanical work over muscle work. The basal metabolic rate, noted P_{BMR} , is the energy used by an animal at rest. As reported by Tucker[47], energy is also spent for circulation and respiration, which represent an increment of about 10 % of the metabolic cost. Tucker[47], Pennycuick[48], Norberg[49] and Ward et al.[11] relate metabolic power $P_{\text{metabolic}}$ and mechanical power $P_{\text{mechanical}}$ by:

$$P_{\text{metabolic}} = 1.1 \left[\frac{P_{\text{mechanical}}}{\eta_{\text{muscle}}} + P_{\text{BMR}} \right] \quad (2.1)$$

As a result, we can estimate the mechanical power from the metabolic power, basal metabolic rate and muscle efficiency, by:

$$P_{\text{mechanical}} = \eta_{\text{muscle}} \left[\frac{P_{\text{metabolic}}}{1.1} - P_{\text{BMR}} \right] \quad (2.2)$$

The basal metabolic rate has been measured for birds, and can be inferred from allometry as reported by Aschoff and Pohl[50]. Metabolic power has been measured using different methods for different species of birds. When comparisons are possible, each of these methods are shown to result in only slight variations of metabolic power.

It is important to note that Pennycuick[48], Rayner[51], Tucker[47] estimate the metabolic power experimentally, and estimate the mechanical power from analytic

aerodynamic models. However, the value of muscle efficiency η_{muscle} is still subject to uncertainty. Pennycuik[43] assumed it is constant across species and evaluated it at 0.23. Ward et al.[11] compared the metabolic rate of an European starling using respirometric measures and compared it to two aerodynamic models. Both models produced similar values of mechanical power. In order for the aerodynamic models to fit with the respirometric data, the muscle efficiency η_{muscle} would have to vary between 0.15 to 0.20 with flight speed ranging from 6 to 12 m.s⁻¹ with an average of 0.18. To this day, there is no known data on the variation of muscle efficiency with strain rate or muscle activation. For our purposes, we estimate mechanical power with a muscle efficiency ranging between 0.18 and 0.23.

Propulsive efficiency

From an aerodynamic perspective, the flapping motion of a wing relates to the propulsive efficiency, which compares the work on the fluid producing thrust compared to the cost of moving the wing in the fluid. Figure 2.8 illustrates a wing in flight and the main forces it is subject to. There are two opposite horizontal forces, thrust and drag, and two opposite vertical forces, lift and weight. For a vehicle in steady cruise flight, the opposite forces must be balanced. For a vehicle in unsteady motion, we define cruise level flight in a time-averaged sense.

The mechanisms that produce the lift, thrust and drag forces are closely coupled. A wing producing lift leaves a trailing vortex wake, which interacts with the flow on the wing and produces downwash. This is the basic mechanism of lift-induced drag. For a wing in unsteady motion, the wake structure is modified and can have a more pronounced effect on the wing. As a result, an arbitrary motion of wing does not necessarily create thrust. Betz[52] and Knoller[53] gave the first theoretical explanation

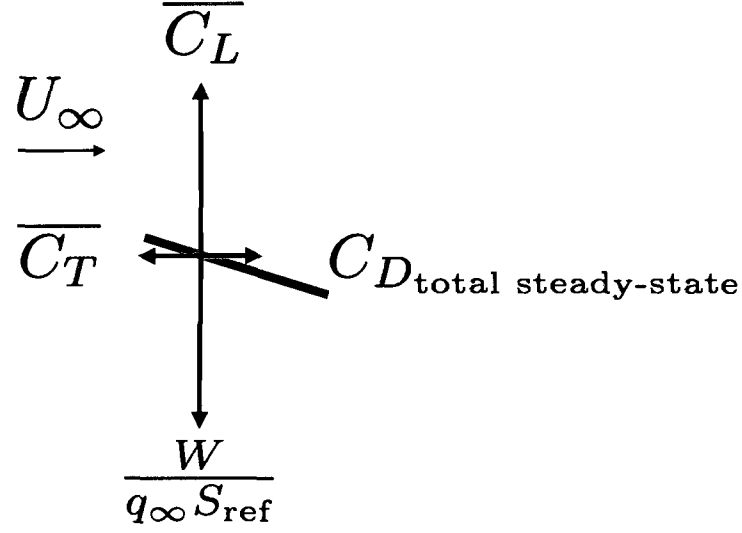


Figure 2.8: Diagram of an airfoil section of a wing (grey line) subject to horizontal and vertical forces (black arrows). The wing is moving at speed U_∞ from right to left. In cruise flight, the horizontal force (coefficients of thrust $\overline{C_T}$ and drag $C_{D_{total steady-state}}$) and vertical forces (coefficients of lift $\overline{C_L}$ and weight $W/(q_\infty S_{ref})$) are balanced on average during a period of the wing motion.

for a two-dimensional airfoil in unsteady motion. Their results were verified experimentally by Katzmayr[54]. Garrick[55] expanded the model and derived analytical formulations for thrust from inviscid aerodynamic theory. They show that, for a flat plate airfoil, thrust is created by leading-edge suction and is tightly correlated to the pressure distribution on the wing.

The propulsive efficiency is usually defined as the ratio of average work done by thrust forces over the average power input to move the wing. For a wing in a steady freestream with velocity U_∞ , the propulsive efficiency noted $\overline{\eta}$ is related to the average thrust \overline{T} and the average mechanical power $\overline{P}_{mechanical}$, by:

$$\overline{\eta} = \frac{\overline{T}U_\infty}{\overline{P}_{mechanical}} \quad (2.3)$$

We define the dimensionless coefficients $\overline{C_T}$, the average thrust coefficient, and $\overline{C_P}$, the average mechanical power coefficient, by:

$$\overline{C_T} = \frac{\overline{T}}{\frac{1}{2}\rho U_\infty^2 S_{ref}} \quad (2.4)$$

$$\overline{C_P} = \frac{\overline{P}_{\text{mechanical}}}{\frac{1}{2}\rho U_\infty^3 S_{ref}} \quad (2.5)$$

and the propulsive efficiency can be written:

$$\overline{\eta} = \frac{\overline{C_T}}{\overline{C_P}} \quad (2.6)$$

This is the usual notation of the Froude efficiency of a two-dimensional airfoil subject to unsteady motion. The definition of thrust and power changes in the literature depending on the method used to calculate the thrust and mechanical forces. For example, on the one hand, Hall and Hall[56] proposed a method to find the optimal motion for flapping flight by minimizing the power shed into the wake, and computed thrust and power from control volume integrals. They defined the net thrust as the resulting horizontal forces. They defined the mechanical power as the difference between the power losses due to viscous forces, and the power loss due to gliding flight at the same average lift coefficient $\overline{C_L}$. On the other hand, Neef[18] studied the flapping motion of rectangular wings using both Euler and Navier-Stokes formulations, and computed the thrust and power from the integration of pressures on the wing. In the Euler calculations, the resulting net thrust corresponds to the net inviscid thrust. In the Navier-Stokes calculations, the resulting net thrust also incorporates the viscous drag forces on the wing. Neef[18] proposed also a corrected definition of propulsive efficiencies adding the lift-induced drag to the net thrust. Discussed also by Mueller

and de Laurier[45], such a corrected propulsive efficiency is meant to be closer to the propulsive efficiency defined for propellers.

The thrust required for a propeller is equal to the drag created by the aircraft, in which case the wing is in a fixed position. In order to compare the propulsive efficiency of flapping flight and of propellers on a fixed wing, we define in this study the total average thrust \bar{T} as equal to the total drag $D_{\text{total steady-state}}$ computed for the wing in steady glide position at a given lift coefficient. The propulsive efficiency $\bar{\eta}$ is therefore written

$$\bar{\eta} = \frac{C_{D_{\text{total steady-state}}}}{\bar{C}_P} \quad (2.7)$$

We only have the description of wing and joints for the pterosaur *Coloborhynchus robustus*, so, in this section, we estimate the propulsive efficiency of migratory birds using available measurements for mechanical power and estimates of total thrust based on analytical results.

2.4.2 Methods to measure metabolic power

The main sources of energy of vertebrates are lipids, carbohydrates and proteins. The oxidation of these fuels produce carbon dioxide and water which are mainly released by the lungs. In principle, flight costs can be deduced directly from the amount of fuel oxidized. Five main procedures to measure the energy expenditure of vertebrate flyers are described in the literature:

- Mass loss: by measuring the mass lost between flights or in a wind tunnel, one can deduce the amount of energy spent. This approach assumes that all mass loss is due to energy consumption and water is released only during respiration. The inference on energy consumption requires assumptions on the energy source.

For free flying birds, the distance flown and winds encountered is source of uncertainty. This technique is more accurate for long flights.

- Doubly labeled water technique (DLW): stable isotopes of hydrogen and oxygen are injected into the blood in the form of $^2\text{H}_2^{18}\text{O}$ or $^3\text{H}_2^{18}\text{O}$, the difference in concentration before and after the flight measures the amount of gases expired. This approach assumes that the water content and body composition of the animal is constant, all the body water is uniformly labelled and the isotopes behaves the same way.
- Respiratory gas exchange: the animals are fitted with a gas mask that measures the gases inhaled and exhaled by the bird. The mask which covers the face is linked by a tube to the measuring device. Because of the set-up, the animals are restrained by the tube and can not fly more than twenty minutes in a wind-tunnel. Another method measures the composition of the exhaled air downstream of the bird flying in a wind-tunnel. These methods require training of the animals. The respiratory quotient (RQ : ratio of CO_2 produced over the O_2 intake) depends on the source of energy, hence food source and species.
- Heart rate: heart rates can reflect oxygen consumption. Energy measurement from heart rate measurements can be calibrated by energy measurements from respiratory measurements. This provides an indirect and less intrusive method of measuring respiratory gas exchange. ECG's have been planted on migrating birds but measurements did not correlate well with other methods.
- Strain and tension of pectoralis muscle: the pectoralis major is the main flight muscle and is used on the downstroke. The deltopectoral crest can be used to place a strain gauge. After calibration, the strain and tension of pectoralis can

be measured to evaluate the work done by that muscle. Depending on the flight speed hence the flight stroke, other muscles produce significant work. During forward flight at reasonable speeds, pectoralis produces 90 % of the total work.

Ward and Rayner[11] and Dial[57] have shown experimentally that measurements of energy expenditures for the bird European Starling *Turdus vulgaris* yielded similar results by measuring the respiratory gas exchanges, the pectoralis strain and tension or using the doubly labeled water techniques. Therefore, the data from any of these techniques is appropriate to estimate the metabolic power.

2.4.3 Method to estimate drag

The available data on birds and bats does not enable a direct calculation of propulsive efficiency. Ideally, we would measure the thrust and mechanical power directly from the animal of interest in controlled conditions. Although flight measurements of metabolic power have been performed for several species of birds, mechanical power can only be inferred using equation 2.2. We note that the proposed values of muscle efficiency η_{muscle} range between 0.18 and 0.23. Mechanical power is therefore estimated using this range.

Willis et al.[58, 59] have recorded the detailed wing kinematics of a bat in flapping flight, and used the data to infer the aerodynamic forces using advanced computational aerodynamic tools. Applied to the flapping flight of birds, such a combined analysis would provide interesting insights on thrust production and would reduce the uncertainties in estimating the mechanical power from metabolic power.

Drag can be regarded as the combination of zero-lift drag, lift-dependent drag and compressibility drag. Although these different drag components usually influence each

other and can not be separated in the study of a full vehicle configuration, this breakdown is appropriate for preliminary estimates. Zero-lift drag, also called parasite drag, combines the effects of non-lifting skin-friction, roughness and pressure forces. We define the total parasite drag D_{par} as the sum of the parasite drag of the body, tail and wing noted D_{body} , D_{tail} and D_{wing} respectively. Lift-dependent drag is divided into vortex drag which is the inviscid contribution, noted $D_{i_{\text{inv}}}$, and lift-dependent viscous drag, noted $D_{i_{\text{visc}}}$. Compressibility drag is produced by the presence of shock waves at transonic and supersonic speeds. Natural flyers fly at very low Mach number so we will neglect the latter. In all, we can define the total drag D_{total} by:

$$D_{\text{total}} = D_{\text{body}} + D_{\text{tail}} + D_{\text{wing}} + D_{i_{\text{visc}}} + D_{i_{\text{inv}}}. \quad (2.8)$$

Pennycuik[43], Tucker[47], Greenewalt[60], Rayner[61] used similar descriptions of drag with slight variations. As there is usually no direct measurement of aerodynamic forces available for a bird in flight, drag is estimated using different techniques. Typically, the different drag components are estimated for the animal in glide and do not include the drag increments due to the motion of the wing. Additionally, the drag due to the body is not usually measured and is inferred from statistical models or simplified aerodynamic models. The aerodynamic models described by Pennycuik[43], Tucker[47] and Rayner[61] are generally used to estimate the mechanical and metabolic power in order to compare it with measurements. However, such estimates of mechanical power do not generally include the unsteady effects of the wing motion and therefore correspond to a propulsive efficiency of 100%.

2.4.4 Estimate of propulsive efficiency for migratory birds

There is a large collection of data from the observations of birds, relating to feeding and migration patterns, as detailed by Lindstrom and Alerstam[62], Alerstam and Hedenström[63] and Rayner[51]. However, we are interested in only several examples of migratory birds, that are the most likely to be very efficient. The chosen bird species are the Great knot *Calidris tenuirostris*, the Bar-tailed godwit *Limosa lapponica*, the European starling *Sturnus vulgaris*, and the Whooper swan *Cygnus cygnus*. Measurements on specimens of Great knot have been made before and after their migration flight, as reported by Pennycuick and Battley[64]. For the Bar-tailed godwit, the specimens could not be located and measured at the end of the migration flight, however Pennycuick[64] has estimated the energy expenditure and variation of mass in the migration flight with a time-marching simulation, using the measurements reported by Piersma and Gill[65] on specimens in Alaska before their migration flight.

Unfortunately, among the chosen species of migratory birds, measurements of metabolic power and inferred estimates for mechanical power are only available for the European starling, given by Ward and Rayner[11]. We therefore estimate the propulsive efficiency for only this species as the ratio of the total steady-state drag coefficient to the estimated mechanical power coefficient. Nevertheless, we compare in table 2.12, the dimensions, flight conditions and total drag estimates for the species considered. The dimensions of the birds are provided by Flight 1.20[10]. The flight conditions are estimated by Flight 1.20[10] at the flight speed for minimum total drag calculated at sea-level.

We observe in table 2.12 that, at the speed of minimum power, the average lift coefficients range between 0.53 and 0.76, the reduced frequencies range between

0.14 and 0.20, and the lift-to-drag ratio ranges between 8.9 and 13.9. Using the mechanical power estimates from Ward and Rayner[11], the estimates of propulsive efficiency for the European starling range between 47% and 56%. Such estimates are rather low compared to efficiencies of the order of 80% estimated by Hall and Hall[56] from aerodynamic considerations. We note that the average lift-to-drag ratio estimated for the European Starling is the lowest among the species considered. We therefore expect the propulsive efficiency for the other species to be higher. Refined estimates of body drag, of mechanical power, and especially of muscle efficiency could be used to improve these estimates. We will compare these estimates of propulsive efficiency with the values for *Coloborhynchus robustus* in chapter 5.

2.5 Summary

In this chapter, we have first described the anatomy and allowable wing motions of the wing of pterosaurs, and in particular of the specimen NSM-PV 19892 classified as *Coloborhynchus robustus*. We have also detailed estimates of total mass, mass distribution, and inertial properties for this specimen. If pterosaurs were continuous flappers, they would have been close to the limit of possible flapping flight, and therefore would have been very efficient. To understand the importance of each wing joint motion, we focus, in this study, on finding which joint motions contribute most to propulsive efficiency. Finally, we have discussed and detailed the definition of propulsive efficiency used in this study. Migratory birds are also very efficient flappers by necessity, and therefore constitute good points of comparison. We have estimated that the European Starling has a propulsive efficiency between 47% and 56% at its speed for minimum total drag, and we will compare these results with the estimates

Table 2.12: Key flight characteristics for four species of migratory birds. The dimensions are provided by Flight 1.20[10]. The flight conditions are computed by Flight 1.20[10] at the flight speed for minimum total drag calculated at sea-level. The propulsive efficiency is estimated for the European Starling with values of mechanical power given by Ward and Rayner[11].

Bird species	Whooper swan <i>Cygnus cygnus</i>	Bar-tailed Godwit <i>Limosa lapponica</i>	Great Knot <i>Calidris tenuirostris</i>	European Starling <i>Sturnus vulgaris</i>
Flight 1.20 inputs				
Total mass (kg)	12.50	0.367	0.233	0.082
Total weight (N)	122.6	3.600	2.286	0.803
Wing span b_{ref} (m)	2.560	0.748	0.587	0.384
Wing area S_{ref} (m ²)	0.756	0.0568	0.0396	0.0253
Average chord \bar{c} (m)	0.295	0.0759	0.0675	0.0659
Aspect ratio	8.67	9.85	8.70	5.83
Flight 1.20 estimates				
Flight speed V_{mp} (m.s ⁻¹)	20.5	11.7	11.4	9.9
Flapping frequency (Hz)	3.34	6.85	8.22	9.68
Reduced frequency k	0.15	0.14	0.15	0.20
Average lift coefficient $\overline{C_L}$	0.63	0.76	0.73	0.53
Wing Reynolds number	417500	61300	53000	44980
Total drag $D_{\text{total steady-state}}$ (N)	8.92	0.302	0.222	0.0060
Drag coefficient $C_{D_{\text{total steady-state}}}$	0.0458	0.0547	0.0607	0.0596
Lift-to-drag ratio $\frac{\overline{C_L}}{C_{D_{\text{total steady-state}}}}$	13.76	13.89	12.03	8.89
Measurements and estimates from Ward et al.[11] for the European starling				
Range of measured metabolic power $\overline{P_{\text{metabolic}}}$ (W)				11.5 - 12
Range of estimated mechanical power $\overline{P_{\text{mechanical}}}$ (W)				1.6 - 1.9
Range of coefficient of mechanical power $\overline{C_P}$				0.106 - 0.126
Range of propulsive efficiency $\overline{\eta} = \frac{C_{D_{\text{total steady-state}}}}{\overline{C_P}}$				0.473 - 0.562

computed for *Coloborhynchus robustus*.

Chapter 3

Aerodynamic Model

3.1 Introduction

With the recent progress of computational power, several computational fluid dynamics (CFD) methods have been developed to study unsteady flows, and have been shown to qualitatively reproduce wind-tunnel experiments, as reported by Tuncer and Platzer[66], Jones et al.[19], Platzer et al.[67]. Although advanced methods can be quite accurate, these rely on the quality of the description of the wing geometry. However, as discussed in the previous chapter, there are still many missing elements in the fossil remains, in order to infer a detailed wing geometry for pterosaurs. We therefore aim at choosing a method that yield a good compromise between the precision of the results with the appropriate resolution required for the geometry, considering the available information.

In this chapter, we detail the unsteady aerodynamic code - named UVLM - that we have developed to study the flapping flight of pterosaurs. We first estimate several

key flow parameters in the flight of large pterosaurs, and of *Coloborhynchus robustus* in particular, and discuss the flow assumptions we make. We then summarize the computational method developed to compute the aerodynamic forces during the motion, and compare the results from UVLM with available results for the motion of rectangular wings. We finally detail the model used to approximate the pterosaur wing geometry in the aerodynamic study, how we estimate the viscous drag forces, and how we incorporate the inertial effects due to the wing and body motions.

3.2 Flow assumptions for *Coloborhynchus robustus*

As discussed in section 2.3, estimates for the weight of an adult specimens of *Coloborhynchus robustus* vary over a wide range. In section 2.3, we estimated the mass of the current specimen to be 17 kg, and we approximate the reference weight to be 160 N. In section 2.2.7, we estimated the joint angles of the wing for the glide position, and use this wing configuration to estimate the reference wing dimensions, such as the average chord \bar{c} , reference span b_{ref} and reference wing area S_{ref} . James Cunningham[3] and Paul MacCready[68] estimated that pterosaurs would have flown at an average $\overline{C_L}$ between 0.5 and 0.9. Using the scaling law derived by Nudds et al.[69], we can estimate the flapping angular amplitude from the span. Table 3.1 shows estimated key flow characteristics for a specimen flying at an average $\overline{C_L}$ of 0.7. The dimensionless quantities estimated in this section are evaluated for an animal flying at sea-level in present day atmosphere.

The Mach number is the ratio of speed to acoustic speed and is a measure of the compressibility effects. Consider a the speed of sound and the freestream velocity

U_∞ ,

$$M = \frac{U_\infty}{a} \quad (3.1)$$

with the speed of sound a defined for perfect gases by

$$a = \sqrt{\gamma \frac{P}{\rho}} \quad (3.2)$$

with $\gamma \approx 1.4$ for air, p the fluid pressure and ρ the fluid pressure density. For air, compressibility effects typically arise for a Mach number around $M = 0.5 - 0.6$. The estimated Mach number M is very small ($M = 0.05 \ll 1$), so we can assume the flow to be incompressible.

The Reynolds number Re compares the inertial and viscous forces in the fluid. Consider c the wing chord as length characteristic and μ the fluid dynamic viscosity, Re is defined by

$$Re = \frac{\rho U_\infty c}{\mu} \quad (3.3)$$

In our case, the estimated Reynolds number Re based on the average wing chord is 3.0×10^5 . For high Reynolds number flows ($Re > 1.0 \times 10^6$), the viscous effects are confined to the boundary layer and the wake regions of the wing. For low Reynolds flows ($Re < 3.0 \times 10^5$), the extent over which viscous effects are felt is larger. For very low Reynolds number flows ($Re < 1.0 \times 10^3$), the flow is typically laminar. In most Reynolds number cases, the flow can transition from laminar to turbulent. However, these flow transitions are hard to predict. Computing the unsteady flow over the wing considered here would require the use of the unsteady Navier-Stokes solvers. Unfortunately, the computational cost of current Navier-Stokes CFD codes is high with typical CPU times for one run on the order of one day. As we aim at optimizing the joint motion of the flapping wing, which can require several hundreds

or thousands of runs, such codes are impractical. We therefore assume the flow to be inviscid and we estimate the viscous drag, due to the friction in the boundary layer, using steady-state analytical results.

The Froude number Fr compares inertial forces and gravitational forces. Gravitational forces are usually neglected in flapping flight so this quantity will not be used. The Strouhal number St and the reduced frequency are measures of the motion unsteadiness. Consider A and ω the amplitude and circular frequency of the periodic motion, the Strouhal number St is given by

$$St = \frac{A\omega}{U_\infty}, \quad (3.4)$$

and the reduced frequency k by

$$k = \frac{\omega c}{2U_\infty} \quad (3.5)$$

As discussed by Ames et al.[70], for reduced frequencies k below 0.03, the wake effects are not very important and the flow is generally considered quasi-steady. For $0.03 < k < 0.1$, the wake effects are significant but the apparent-mass accelerations are negligible. Beyond that, the flow is considered fully unsteady and for $k > 1$ the acceleration effects begin to dominate. Here, the reduced frequency k was estimated at $k = 0.13$, so we have to account for unsteady effects.

Stall occurs when the flow detaches from the surface. This separation creates a loss in lift forces and a significant increase in drag forces. The onset of stall is usually determined by the angle of incidence α of the airfoil and the Reynolds number Re . Tuncer et al.[71] studied the dynamic stall of a NACA 0012 airfoil using a Navier-Stokes CFD method at a Reynolds number of 1.0×10^6 , and estimated that dynamic stall occurred beyond an instantaneous angle of incidence of $\alpha_{DS} = 14.8$ degrees for

Table 3.1: Estimates of key flow parameters for a specimen of *Coloborhynchus robustus*, weighing 160 N, flying at an average $\overline{C_L}$ of 0.7. The reference length are taken from the glide position as specified in table 3.4. ($\rho = 1.23 \text{ kg.m}^{-3}$ and $\mu = 1.82 \times 10^{-5} \text{ kg.m}^{-1}.\text{s}^{-1}$)

Span b_{ref} (m)	4.8	Mach number M_∞	0.05
Mean chord \bar{c} (m)	0.28	Reynolds number Re ($\times 10^6$)	0.32
Wing Area S_{ref} (m^2)	1.3	Strouhal number S_t	0.28
Aspect Ratio AR	17	Reduced frequency k	0.13
Weight W (N)	160	Flapping frequency f (Hz)	2.6
Flight Speed U_∞ (m.s^{-1})	17	Flapping full-amplitude ϕ (degrees)	46

$k = 0.1$, and $\alpha_{DS} = 17.1$ degrees for $k = 0.2$. Isogai[72] conducted a similar study for a NACA 0012 airfoil using at a Reynolds number of 1.0×10^5 , and showed that dynamic stall occurred beyond an instantaneous angle of incidence of $\alpha_{DS} \sim 15 - 20$ degrees for $k = 0.15 - 0.30$. For a flat plate airfoil, an angle of incidence of 15 corresponds to a lift coefficient of $C_l = 1.64$. We assume that, in typical cruise flight conditions, an efficient pterosaur would have ensured that the wings would not stall at any point of the flapping motion. Provided that the local angle of incidence or section lift coefficient remains under these limits everywhere on the wing, we can assume that the flow remains attached during the oscillations, so that vorticity is shed only at the trailing edge of the wing.

In all, we assume that we can model flapping flight of pterosaurs as an incompressible, irrotational and inviscid flow. Based on these assumptions, we have developed an unsteady aerodynamic computational code, that we refer to as UVLM, from existing unsteady potential flow methods. In the next section, we give a general description of UVLM.

3.3 Unsteady three-dimensional vortex-lattice code (UVLM)

As they move forward, wings leave a trailing wake, which interacts with the flow field on the wing. In the case of unsteady motions, the variations of forces and position of the wing create variations of strengths and position of the wake. To correctly estimate flapping flight efficiency, we must therefore correctly model the unsteady aerodynamic effects of a wing in motion. As we aim at finding the best joint motions during flapping flight, we need to choose a method that yields a suitable compromise between accuracy in the results and speed for the optimization procedure.

In this section, we first present several published methods relevant to study the aerodynamics of flapping flight and motivate the choice to implement an unsteady vortex-lattice method. We then describe the main features and adaptations implemented in UVLM. We also define the forces, power and propulsive efficiency from the quantities computed by UVLM. Finally, we discuss the parameter settings to ensure the convergence of the code.

3.3.1 Choice of aerodynamic method

Analytical methods

Otto Lilienthal[73] was one of the first authors to document observations of wing motions of birds in flight. Only forty years later, did Theodorsen[74], Garrick[55], and Küssner[75] derive analytical solutions for the general theory of oscillating airfoils. These solutions accounted for the unsteady wake effects to derive lift and thrust equations for heaving and pitching airfoils in inviscid two-dimensional flow. However, these solutions are valid only for low reduced frequencies and for small heaving and

pitching motions.

Betteridge and Archer[76] studied the flapping motion of a wing by approximating the time-varying spanwise lift distribution with several chosen coefficients of a Fourier series. Archer et al.[77] extended the study by including pitching motions and by comparing the results with wind-tunnel experiments. In both studies, the interaction with the wake was simplified using a quasi-steady approximation. Lan[78] used an unsteady quasi-vortex lattice method (QVLM) to study the propulsion and efficiency of fish tails and dragonflies. However, the unsteady QVLM simplified the trailing wake by a series of lines extending from the wing panels to the far wake behind the wing. Phlips et al.[79] studied the unsteady effects of flapping flight of birds by combining a lifting line method and a simplified description of the unsteady wake behind the wing. Using a quasi-steady approximation, Jones[80] minimized the energy spent for a wing subject to root flapping motion, by minimizing the lift-induced drag for a prescribed variation of wing root bending moment. Although these methods studied the motions of three-dimensional wings with large amplitudes, the unsteady aerodynamic effects, especially the interaction with the wake, were simplified.

During the development of large ornithopters, de Laurier[23] divided a three-dimensional wing into a series of two-dimensional airfoil sections, and computed the aerodynamic forces by applying the analytical results from Garrick[55] at each section. His method was subject to the same limitations in terms of motion amplitude and frequencies as the analytical solutions by Garrick[55]. This study was expanded to include structural deformations, as detailed in de Laurier[23] and Larijani[81]. Although the computed results matched reasonably well with experiments, the wing structure was modeled as a torsional beam, and is therefore not suitable for the membrane wings that we study.

Potential methods

In the 1990's, increases in computational power permitted the use of more complex numerical methods and the modeling of the aerodynamics of a wing of arbitrary shape and its wake. The methods developed then were mainly based on potential flow assumptions. Vest and Katz[82] developed an inviscid three-dimensional code to study the motion of pigeon wings using an unsteady vortex-lattice method. They also compared the computed aerodynamic forces with experiments performed for a rigid model of the pigeon wing. The computed lift and thrust forces matched reasonably well with the experiments, except for some portion of the motion when the flow would have probably separated during the experiment.

Smith[83] developed an unsteady three-dimensional panel code coupled with a structural code, based on the finite-element method, to study the flight of moths. The results from the computational model were compared to wind tunnel experiments for a flexible model of a moth wing. The observed discrepancies were attributed to separation and leading-edge effects that were not modeled in the panel code. Jones and Platzer[20] and Jones et al.[84] used an unsteady two-dimensional panel code, called UPOT, to calculate the forces of two-dimensional airfoils in heaving and pitching motions, and showed that the computed wake shapes matched to wind-tunnel experiments.

In order to minimize the flapping power of wing, Hall and Hall[56, 85] developed a code, referred to as HallOpt, based on a three-dimensional vortex-lattice model of the wake behind the wing. Willis et al.[86] developed an unsteady panel method, called FastAero, for computations of unsteady motions. Willis et al.[87] explored the effect on mechanical power of different wing motions observed in birds, using both FastAero and HallOpt.

Computational Fluid Dynamics

More recently, the available computational power has enabled the development of unsteady Computational Fluid Dynamics (CFD) codes based on the Euler and Navier-Stokes equations, which can model complex aerodynamic phenomena such as compressibility and viscous effects. Most of the published results have been computed either for two-dimensional airfoils or for rigid rectangular wings in heaving, pitching, flapping and twisting motions as shown in figure 3.3.1.

Tuncer and Platzler[66] used a two-dimensional unsteady Navier-Stokes code to study the heaving and pitching motions of an airfoil. They observed that the wake deformations predicted by the numerical results were in good agreement with the wind-tunnel experiments. Jones et al.[19] compared the results for a rectangular wing in heaving and pitching motion, between CMARC[88], an unsteady panel code, FLOWer, an unsteady Euler and Navier-Stokes code, and wind-tunnel experiments. They showed that, for high Reynolds number flow ($Re = 1.0 \times 10^6$), the results from the panel and Euler codes agreed well. The comparison between the Navier-Stokes and the wind-tunnel experiments were harder because of measurements difficulties. Neef[18] extended the study to flapping and linear twisting oscillations of a rigid rectangular wing using FLOWer. The numerical results of these last two studies are used for comparison with UVLM, the code developed for this study.

Willis et al.[59] have recently expanded their previous work by also using an unsteady Navier-Stokes code, called 3DG, and by accounting for the fluid-structure interaction. These tools were also used to study the aerodynamic forces for the flapping flight of bats, as discussed by Willis et al.[58].

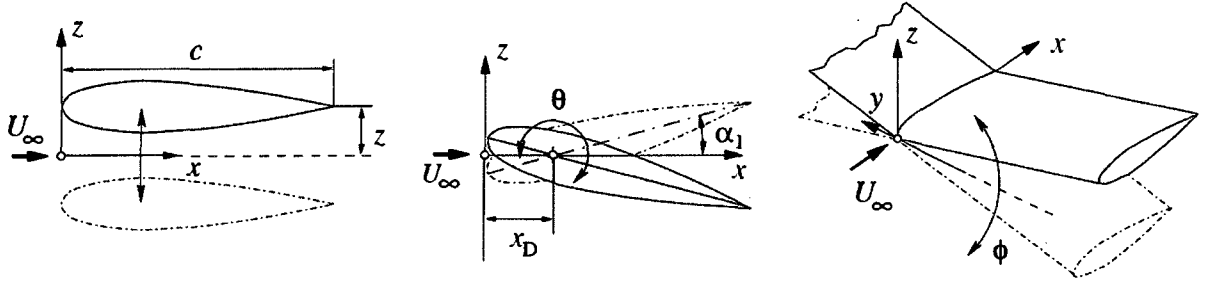


Figure 3.1: Description of main wing motions studied : heaving (left), pitching (middle), flapping (right). Picture reproduced with permission from Neef[18]. Heaving corresponds to a vertical translation of the wing along the z -axis. When pitched, the wing is rotated by the angle θ about an axis parallel to the y -axis at the center of rotation located at x_D . In this study, the rectangular wing is pitched about the leading edge of the wing. Neef also studied twisting the wing linearly by α_1 but these results are not included here. Flapping corresponds to rotating the wing about the x -axis by the angle ϕ .

Motivation for the unsteady vortex-lattice method

CFD models offer great detail and accuracy in understanding the aerodynamics of flapping rectangular wings. Unfortunately, the computational cost of current Navier-Stokes CFD codes is still prohibitive with typical CPU times for one run on the order of one day. In this study, we aim at optimizing the joint motion of the flapping wing, which can require several hundreds or thousands of runs, so such codes are impractical for our purposes.

Tools based on panel methods, such as CMARC[88] or the one described by Smith[83], could prove useful for our study. However, these require numerous panels near the leading-edge, in order to calculate thrust forces with reasonable accuracy. As discussed in section 2.2, there are still many missing elements to infer a detailed wing geometry from the fossil remains. Panel methods therefore do not seem adequate for our study.

Pterosaur wings were likely to be thin except near the bones and proximal of

the wrist where the bones, muscle and air sacks would have created a significantly thick section. However, thrust production of a flapping wing is mainly created by the outboard sections of the wing. Therefore modeling the inner wing as a thin wing should not affect the contribution of each joint motion to propulsive efficiency. Vortex-lattice methods model wings as thin surfaces, and can efficiently calculate leading-edge suction forces. We therefore choose an unsteady vortex-lattice method to calculate the forces on the pterosaur wing.

Neef[18] compared the average thrust computed using different methods for a rectangular heaving motion for reduced frequencies between $0.05 < k < 0.20$. He compared the results from the unsteady panel code CMARC[88], FLOWer using Euler equations, and FLOWer using Navier-Stokes equations. He showed that the results from the panel codes were 5%-6% higher than from the Euler results, and that the Euler results were 4%-8% higher than those from the Navier-Stokes results. In the two-dimensional case, he showed that the flat plate analytical solution was within 5%-10% of the Navier-Stokes solutions. We therefore estimate that using an unsteady vortex-lattice method will yield results within 5-15% of Navier-Stokes results for a fraction of the computational cost.

Provided that our flow assumptions remain valid, this choice of method is therefore a reasonable compromise in light of the computational efficiency required for the optimization and of the large uncertainties in the estimates made in chapter 2. Future studies could refine our results by combining the current method and an advanced unsteady CFD code in a multi-fidelity optimization method.

3.3.2 General description of UVLM

We developed a code, referred to as UVLM in this study, based on the unsteady three-dimensional vortex-lattice method detailed in Katz and Plotkin[1]. We summarize in this section the main results used in the code. The sequence of the different steps of the code are illustrated in figure 3.2.

Key results used

The wing geometry and the wake are discretized into quadrilateral panels, modeled as vortex rings of uniform strength. Using results from the Biot-Savart Law, the velocity induced by the vortices can be calculated at the collocation points, positioned such that the steady Kutta condition is valid on any panel. The vorticity shed at the trailing edge is calculated using Kelvin's theorem, and we assume that the vorticity in the wake does not decay with time. If the wake is modeled as a rigid surface, the wake panels are stationary once deposited by the wing motion. It is also possible to let the wake elements move freely. In this case, the motion of the wake elements is caused by the velocities induced by the other wake elements. Letting the wake move freely leads to a significant increase in computation time. In this study, the results obtained with the free and rigid wake are identical, so the UVLM results shown in this study use a rigid wake model.

Solving the vortex strength distribution

The strengths of the vortices on the wing are solved using the boundary conditions on the wing, which impose that the total velocity is zero across the wing surface. The contributing velocities are calculated at the collocation point of each wing panel, and include the velocities due to the kinematic motion, the velocities induced by the

other wing panels and by the wake. The velocities induced by the vorticity from the other wing panels are still unknown at this point. We therefore compute the velocities induced by the wing panels for vortices of unit strength, and assemble them into an influence matrix. Solving for the vortex strength problem becomes a linear problem of the form $[\mathbf{A}]\{\mathbf{x}\} = \{\mathbf{b}\}$, with $[\mathbf{A}]$ the influence matrix, $\{\mathbf{x}\}$ the vortex strength distribution, and $\{\mathbf{b}\}$ the sum of the kinematic and wake-induced velocities.

Computing pressure, forces and moments

The pressure distribution is calculated from the distribution of vortex strengths by using the unsteady Bernoulli equation, which is used to compute the forces, moments and mechanical power. The method developed by Katz and Plotkin[1] has been shown to estimate the lift forces reasonably well, but does not compute the leading-edge suction force explicitly. As a result, a lot of uniform chordwise panels are required to adequately compute the leading-edge suction force. We therefore use the interpolation method derived by Lan[78] in his description of a quasi-vortex lattice method. With a cosine distribution of the panel sizes in the chordwise distribution, he showed that the leading-edge suction force, hence the thrust force, can be computed at each chordwise section from the chordwise vortex strength distribution with a reasonably small number of panels.

3.3.3 Adaptations to the method for pterosaur flapping flight

The methods developed by Katz and Plotkin[1] and Lan[78] were first developed for the study of planar wings. UVLM incorporates several modifications to adapt these methods to the geometry and the motion of a pterosaur wing.

We study the flapping flight of pterosaurs accounting first for the aerodynamic

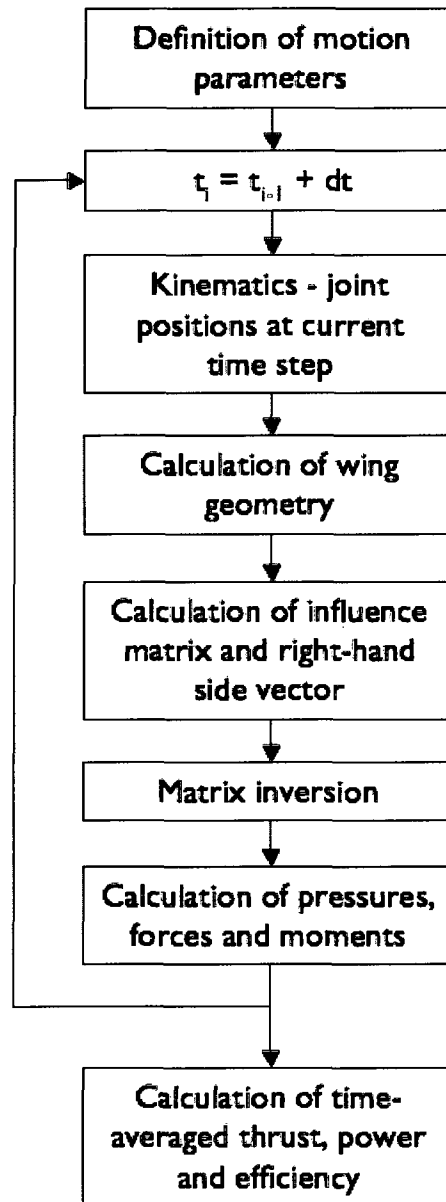


Figure 3.2: Flow chart of the UVLM code. The position of the joints is recalculated at each time step and defines the wing geometry. The wing-induced and wake-induced velocities are then calculated at every panel which are used in the influence matrix. The velocities induced by the wing kinematics are calculated to create the right-hand side vector. The vorticity distribution is the solution of this linear system. Using the unsteady Bernoulli equation, the code calculates the pressure jump across the wing which lead to force and moment calculations.

effects, and then for the aeroelastic effects. In the aerodynamic study, the wing geometry is defined by the motion of the bones at the movable joints. Because of the missing information in the fossil remains, we make several simplifying assumptions to define the wing geometry detailed in section 3.5.1. In the aeroelastic model detailed in chapter 4, the wing geometry also accounts for the deflections of the bones and of the membrane, due to inertial and structural loads. We note that, in both aerodynamic and aeroelastic studies, we are interested in flapping flight at cruise, so we assume the motions are symmetric about the body x - z plane, and we therefore need to model only one wing.

The joint motions can induce large changes in the wing geometry. At the start of every time step, we therefore recompute the position of the panels. We then compute the aerodynamic influence matrix and the velocities on each panel induced by the wing motion. As shown in the flow chart in figure 3.2, we then calculate the instantaneous forces after solving for the vortex distribution. The calculations are carried out for several periods, such that the forces and power become periodic. Finally, we calculate the time-averaged forces, moments, power and propulsive efficiency over the last period of the motion.

3.3.4 Definition of forces

Definition of forces computed by UVLM

The wing geometry is defined in the frame attached to the center of gravity of the animal. However, the animal changes position and orientation during the motion, and the definitions of forces on the animal need to be defined in a fixed inertial frame of reference. The horizontal force F_X , side force F_Y and vertical force F_Z computed by UVLM are defined respectively along the X , Y and Z -axes in the inertial frame

of reference. In contrast, the moments M_x , M_y , M_z are defined about the x , y and z -axes in the frame attached to the center of gravity of the animal.

In this study, we define the lift force L equal to the vertical force F_Z . Because UVLM is an inviscid method, the computed horizontal force F_X therefore corresponds to the inviscid net horizontal force, which we note $F_{X_{\text{inv}}}$ for additional clarity. In the inertial frame of reference, if a wing creating lift on average ($\bar{L} > 0$) is not actuated, $\overline{F_{X_{\text{inv}}}}$ is positive because of the lift-induced drag. If the wing motion creates thrust, $\overline{F_{X_{\text{inv}}}}$ becomes negative. The methods and published results, that we compare UVLM with, do not include viscous calculations, so we only compare the computed coefficients of inviscid lift C_L and net horizontal forces $C_{F_{X_{\text{inv}}}}$.

Definition of drag components

A flapping gait is desirable for cruise flight when thrust equates drag. We therefore need to estimate the drag components that are not computed by the vortex-lattice method. Recalling the notations of section 2.4.3, the total drag D_{total} is defined by

$$D_{\text{total}} = D_{\text{body}} + D_{\text{tail}} + D_{\text{wing}} + D_{i_{\text{visc}}} + D_{i_{\text{inv}}}. \quad (3.6)$$

In steady-state conditions, the vortex drag $D_{i_{\text{inv}}}$ is equal to the inviscid net horizontal force $F_{X_{\text{inv}}}$ computed by UVLM. In the case of the pterosaur, the body drag D_{body} includes the parasite drag of the head, neck and torso. We assume that the head, neck, body and legs do not move significantly during the wing motion and therefore assume that steady-state estimates are appropriate. The results are detailed in section 3.5.2. In contrast to the inviscid forces computed by UVLM, we define the total viscous drag D_{viscous} as the sum of the zero-lift drag and of the lift-induced viscous drag given

by

$$D_{\text{viscous}} = D_{\text{body}} + D_{\text{tail}} + D_{\text{wing}} + D_{i_{\text{visc}}}. \quad (3.7)$$

For the wing parasite drag, we compute the local section parasite drag coefficient $C_{d_{\text{wing}}}(j, t)$ at each spanwise station j at every time step t . We then calculate the wing drag coefficient $C_{D_{\text{wing}}}(t)$ by

$$C_{D_{\text{wing}}}(t) = \sum_j C_{d_{\text{wing}}}(j, t) \frac{q_{\text{local}}(j, t)}{q_{\infty}} \frac{c(j) \Delta y(j)}{S_{\text{ref}}} \quad (3.8)$$

with $q_{\text{local}}(j, t)$ the local dynamic pressure based on the section total velocity, q_{∞} the reference dynamic pressure, $c(j)$ the section chord at spanwise station j , $\Delta y(j)$ the spanwise width of the chordwise section, and S_{ref} the reference wing area, defined from the glide geometry. Values of section parasite drag coefficient can be obtained from wind tunnel data or from estimates using softwares like XFOIL[89]. As we assume that the wings of pterosaurs were thin, we estimate the section parasite drag by assuming a turbulent flat plate airfoil.

We then compute the lift-induced viscous drag coefficient $C_{D_{i_{\text{visc}}}}$ at every time step, given by

$$C_{D_{i_{\text{visc}}}}(t) = K C_{D_{\text{wing}}}(t) C_L^2(t), \quad (3.9)$$

with C_L the lift coefficient, $C_{D_{\text{wing}}}$ the wing parasite drag coefficient computed at time t , and K a constant. The value of K is estimated at 0.60, from fitting drag polars of NACA 0012 and NACA 0009 airfoils calculated at a Reynolds number of 300,000 using XFOIL[89]. For comparison purposes, K has been determined to be about 0.38 from flight test data of DC-8 and DC-9 commercial aircrafts, as discussed by Kroo[90].

Definition of maximum section lift coefficient

As discussed in section 3.2, we assume that the flow is attached during the motion. In order to verify the validity of this assumption, we estimate the maximum absolute value of section lift coefficient on the wing, reached during the last period of the motion. We define $C_{l_{\max}}$ by

$$C_{l_{\max}} = \max_{j,t} [|C_l(j, t)|] \quad (3.10)$$

with C_l the local section lift coefficient based on the the local dynamic pressure and chord.

3.3.5 Definition of power and propulsive efficiency

To compute propulsive efficiency, we need to compute the mechanical power P due to the actuated wing motion. We define the mechanical power P corresponding to the flapping motion, such that it is zero if the wing is held at a steady position even in a lifting case ($\overline{C_L} \neq 0$). As the joint motions induce complex kinematic relationships for the wing geometry, we compute the power P at time t as the sum of the product of forces and kinematic velocities, computed over all wing panels. The kinematic velocities, due to the actuated motion, are computed from the motion of the wing panels in the frame attached to the center of gravity of the animal, so we compute power using the forces computed in the same frame. In all, the mechanical power P at time t is given by

$$P(t) = \sum_i \sum_j [F_x(i, j) (u(i, j) - U_\infty) + F_y(i, j)v(i, j) + F_z(i, j)w(i, j)], \quad (3.11)$$

with i, j the chordwise and spanwise index of each panel respectively, F_x, F_y, F_z the forces along the x, y , and z axes respectively, and u, v, w the kinematic velocities along the x, y and z axes respectively. The x, y and z axes are defined in the frame attached to the center of gravity of the animal.

Using equation 2.7 defined in section 2.4.1, the average propulsive efficiency $\bar{\eta}$ is given by

$$\bar{\eta} = \frac{C_{D_{\text{total steady-state}}}}{\overline{C_P}}, \quad (3.12)$$

with $\overline{C_P}$ the average mechanical power coefficient due to the flapping motion and $C_{D_{\text{total steady-state}}}$ the total steady-state drag computed using equation 3.6 at the same lift coefficient as in flapping flight.

3.3.6 Code convergence

In this section, we discuss the choice for an appropriate size for the panels and time steps. As the size of the panels and time steps is reduced, the accuracy tends to increase. A code is deemed converged when the accuracy does not increase beyond a set threshold, as the spatial (panel size) or temporal (time step size) resolution is increased. However, as the resolution is increased, so does computation time. The most time-consuming computations in the code lie in the creation of the influence matrix and solving for the linear system. The time for these calculations is roughly proportional to the square of the number of panels, and roughly linearly proportional to the number of time steps. In this study, we seek a suitable compromise between accuracy and computation time for the optimization procedure, and the threshold for convergence is set to 1% for all values of interest.

Size of the wing panels

For an uniform panel distribution in the chordwise direction, the accuracy is roughly linearly dependent on the number of panels. The interpolation method derived by Lan[78] uses a cosine chordwise distribution and the number of chordwise panels required to reach the same level of accuracy is greatly reduced. The accuracy of the lift distribution in the chordwise direction is key for the appropriate estimate of the leading-edge suction, hence thrust forces. For a rectangular wing, using the cosine chordwise distribution, we find that there is no real accuracy gain beyond twenty panels in the chordwise direction.

Lan[78] also derived a cosine distribution in the spanwise direction. However, for a complex wing geometry, with changes in sweep or dihedral in particular, each wing section would need its own cosine distribution. In the case of the pterosaur wing, we divide the wing geometry in the spanwise direction, such that each wing section corresponds to a wing bone. Figure 3.3 compare the lift and thrust coefficients for a rectangular wing in heaving motion for different number of panels. For the rectangular wing, we find that the convergence threshold is met for 20 panels in the spanwise direction. In all, the converged grid for the rectangular wing has 20 panels in the chordwise direction, and 20 panels in the spanwise direction.

Size of the time steps

The size of the time step influences the size of the panels in the wake. It is generally recommended to keep the length of the panel in the wake roughly equal to the length of the wing panels in the chordwise direction. We define the time step size differently in the case of a periodic motion, and in the case of an accelerated wing. In the first case, the length of the time step is specified by the desired number of time steps per

period. In the latter case, the length of the time step is based on the average length \overline{dx} of the wing panels in the chordwise direction, and freestream velocity U_∞ , and is given by

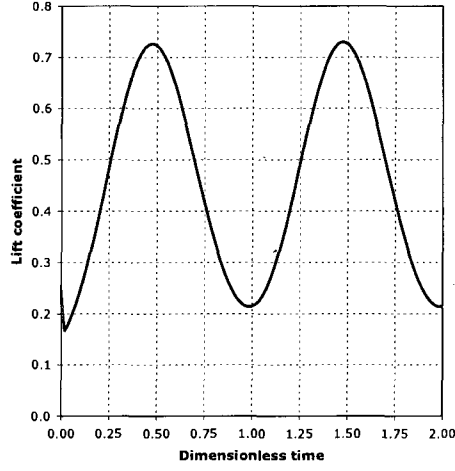
$$dt_{\text{accelerated wing}} \propto \frac{\overline{dx}}{U_\infty} \quad (3.13)$$

In the case of periodic motions, 50 or 100 time steps per period seems adequate as shown in figure 3.4. In the case of an accelerated wing, we estimate the adequate length of the time step by comparing the computed results with the analytic solution derived by Wagner[91], as described in section 3.4.2. We compared the analytic solution to the lift of an accelerated flat rectangular wing of very high aspect ratio ($AR = 100$), for different length of the time step. We find that an appropriate panel size for this case is $dt = \frac{\overline{dx}}{4U_\infty}$.

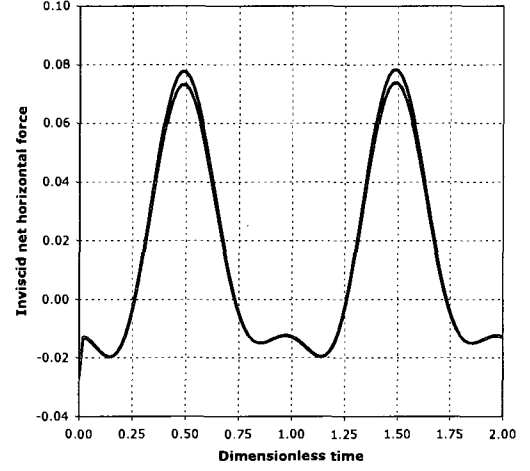
3.4 Comparison with published results

Before using the codes to optimize the flapping gait of pterosaurs, we assess the validity of the results computed by UVLM. As we cannot directly compare results for a pterosaur wing in motion, we compare the results separately for a wing of arbitrary geometry in the steady case, and for a rectangular wing in unsteady motion in the two-dimensional and three-dimensional case. For this purpose, the comparison is done with analytical and numerical results available in the literature, and the existing commercial codes TORNADO[92] and LINAIR[93] also based on potential flow theory.

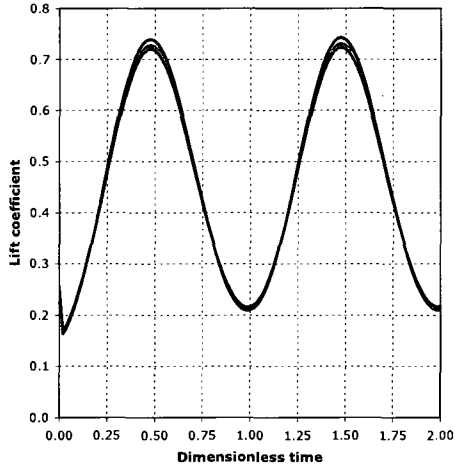
First we compare the spanwise lift distribution of wing with various geometries



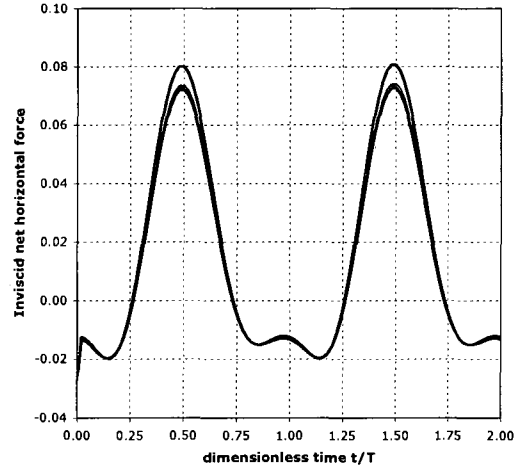
(a) Lift coefficient C_L as a function of the dimensionless time $\frac{t}{T_{\text{period}}}$ during the first two period of the motion



(b) Inviscid net horizontal force coefficient $-C_{F_{X_{\text{inv}}}}$ as a function of the dimensionless time $\frac{t}{T_{\text{period}}}$ during the first two periods of the motion

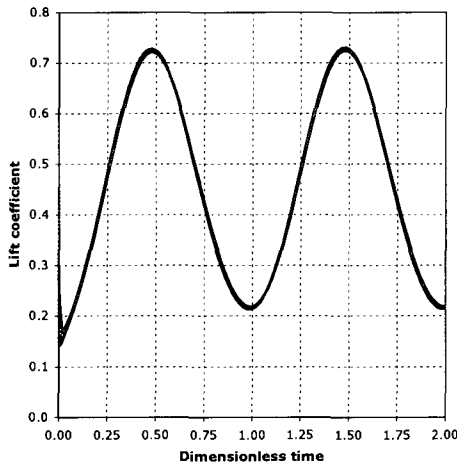


(c) Lift coefficient C_L as a function of the dimensionless time $\frac{t}{T_{\text{period}}}$ during the first two periods of the motion

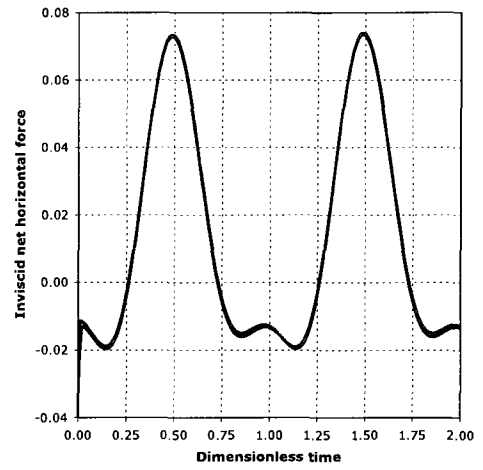


(d) Inviscid net horizontal force coefficient $-C_{F_{X_{\text{inv}}}}$ as a function of the dimensionless time $\frac{t}{T_{\text{period}}}$ during the first two periods of the motion

Figure 3.3: Comparison of the lift and inviscid net horizontal forces for several wing panel sizes. We consider here the case of a rectangular wing of $AR=8$ under combined heaving and pitching motion ($\frac{z_0}{c} = 0.52$, $\theta_0 = 2$ degrees, $\varphi_{\theta_0} = 90$ degrees, $k = 0.1$). In figures 3.3(a) and 3.3(b), the blue, green, red and black lines correspond to 10, 20 and 30 chordwise panels respectively. In figures 3.3(c) and 3.3(d), the blue, green, red and black lines correspond to 7, 14, 21 and 28 spanwise panels respectively.



(a) Lift coefficient C_L as a function of the dimensionless time $\frac{t}{T_{\text{period}}}$ during the first two periods of the motion



(b) Inviscid net horizontal force coefficient $-C_{F_{X_{\text{inv}}}}$ as a function of the dimensionless time $\frac{t}{T_{\text{period}}}$ during the first two periods of the motion

Figure 3.4: Comparison of the lift and inviscid net horizontal forces for 50, 100 and 150 of time steps per period, in blue, green and red lines respectively. We consider here the case of a rectangular wing of $AR=8$ under combined heaving and pitching motion ($\frac{z_0}{c} = 0.52$, $\theta_0 = 2$ degrees, $\varphi_{\theta_0} = 90$ degrees, $k = 0.1$).

in steady motions with a lifting-line code and a steady vortex-lattice code. Then we compare the unsteady lift force of a two-dimensional flat plate airfoil suddenly accelerated with analytical results. Then we compare the unsteady forces of a two-dimensional flat plate airfoil in heaving and pitching motion with analytic results and numerical results from an unsteady two-dimensional potential code. Finally, we compare the unsteady forces of a rectangular wing of finite span in heaving, pitching, flapping and twisting motions with numerical results.

3.4.1 Comparison with steady results

In the steady case, we compare results from UVLM with results computed with LINAIR[93] and TORNADO[92]. LINAIR is a steady lifting-line code developed by Desktop Aeronautics, and provides a fast analysis of the three-dimensional aerodynamic effects for arbitrary wingshapes. TORNADO is a steady vortex-lattice code developed by KTH and University of Bristol. As both codes are based on the potential flow theory, these are appropriate to check the results from UVLM.

We compare results for several modified rectangular wings changing the taper ratio, sweep, and dihedral angles of the outboard section. We also compare results for the pterosaur wing in glide position for the planar and curved wing planform as detailed in section 3.5.1. The three codes are in good agreement for the pterosaur wing geometry as shown in figure 3.5

3.4.2 Sudden acceleration of flat plate airfoil

Wagner[91] studied the transient lift force of a flat plate airfoil suddenly accelerated to steady velocity U_∞ . At time $t < 0$, the airfoil at an angle of attack θ is at rest. At time $t = 0$, the airfoil is instantly accelerated to U_∞ . Because the airfoil creates lift,

Kelvin's theorem states that circulation is deposited into the wake, creating a starting vortex of finite strength. Because of the instantaneous acceleration, the circulation and therefore the lift at $t = 0$ is infinite. At time $t > 0$, the airfoil remains at U_∞ and the starting vortex influences the flow on the airfoil. A key result from this study is that the lift at $t \rightarrow 0+$ is half of the steady-state value ($t \rightarrow \infty$). As the distance of the starting vortex to the airfoil increases, its influence decreases and the lift force on the airfoil approaches steady-state. Wagner derived the section lift C_l as function of time and angle of attack θ , and defined the lift alleviating function ϕ as a function of s , a dimensionless time variable. Because this function is hard to evaluate, approximations listed by Azuma[] are written

$$C_l(s) = 2\pi\theta\phi(s) \quad (3.14)$$

$$\phi(s) \approx 1 - 0.65e^{-0.0455s} - 0.335e^{-0.3s} \quad (3.15)$$

$$\phi(s) \approx \frac{s+2}{s+4} \quad (3.16)$$

$$\text{with } s = \frac{2U_\infty t}{c} \quad (3.17)$$

with U_∞ the freestream velocity, and c the airfoil chord length.

Wagner's function is typically used to test the validity of unsteady aerodynamic codes, and to estimate an appropriate time step size dt . The two dimensional case is equivalent to the three-dimensional case for a wing of infinite aspect ratio. To compare our three-dimensional code with this two-dimensional solution, the lift coefficient is therefore computed in UVLM for a rectangular wing of very high aspect ratio ($AR=100$). We compared results from UVLM with Wagner's function, for a flat plate airfoil set at a constant angle of attack $\bar{\theta}$ of 5 degrees. We found that, with an

appropriate choice of time step size dt , the results match closely.

3.4.3 Heaving and pitching motion of a flat plate airfoil

Garrick[55] and Küssner[75] derived the analytic solution for the forces, power and propulsive efficiency of a flat plate airfoil in heaving and pitching motions. Due to the assumptions made, these analytic results are valid only for low frequencies and amplitudes, so we also use numerical results from Jones et al.[19] for our comparisons. Jones and Platzzer[20] developed a two-dimensional unsteady potential code, called UPOT, and also used an unsteady three-dimensional panel code, called CMARC[88] distributed by AeroLogic Inc. We ran additional cases using CMARC to complement the results provided by Jones et al[19].

The two dimensional case is equivalent to the three-dimensional case for a wing of infinite aspect ratio, so the computations using UVLM and CMARC were performed for a rectangular wing of very high aspect ratio ($AR=100$). The grid used in UVLM had 20 chordwise and 20 spanwise panels, with 120 time steps per period. A NACA 0014 airfoil section was used in UPOT and CMARC, and a flat plate airfoil was used in UVLM. Jones et al.[19] ran UPOT cases with 200 chordwise panels and 120 time steps per period, and CMARC cases with 20 chordwise panels, 20 spanwise panels and 100 time steps per period. The additional cases we ran with CMARC used a grid with 120 chordwise and 20 spanwise panels, with 100 time steps per period. In all the cases run, the solution had converged with the chosen grid resolution.

We compare results for a set of heaving amplitudes and reduced frequencies as shown in table 3.2. We note that the analytic results by Garrick[55] do not account for the transient effect due to starting vortex. The unsteady codes UPOT, CMARC

Table 3.2: Amplitudes and reduced frequencies considered for the comparison of the lift and thrust forces for a two-dimensional airfoil subject to heaving motion.

k	0.1	0.2	0.5	1.0
$\frac{z_0}{c}$	0.4	0.4	0.4	0.4

and UVLM, however, are run, such that, at the first time step, the airfoil is simultaneously accelerated to the freestream forward velocity, and in the pitching and heaving motion. Except for the case with high frequencies, we observe that it takes about one period for the influence of the starting vortex to become small enough, such that the forces become periodic. In all cases, the airfoil motion is simulated for at least two periods, and the time-averaged force and power coefficients were calculated during the last period of the simulation.

The UVLM results are within 3 % of the analytical results and of the CMARC results published by Jones et al.[19] for reduced frequencies $k \leq 0.2$. However, we find that peak forces differed by 9% and 35% for $k = 0.5$ and $k = 1.0$ respectively. In these last two cases, all the methods used predict very high values of lift coefficient C_L . As we have not modeled any stalling effect in UVLM, these cases are not appropriate for comparison. Validation of high frequency cases thus requires the motion amplitude to be proportionally reduced in order to keep the maximum values of C_L within reasonable values. This is done by maintaining constant the product $k \times \frac{z_0}{c}$ of the dimensionless vertical amplitude with the reduced frequency. In the cases specified in table 3.3, we find that the analytical and the UVLM results match for reduced frequencies $k \leq 1.0$.

Table 3.3: Amplitudes and reduced frequencies with the product $k \times \frac{z_0}{c}$ held constant, for the case of a two-dimensional airfoil subject to heaving motion.

k	0.1	0.2	0.5	1.0
$\frac{z_0}{c}$	1.0	0.5	0.2	0.1

3.4.4 Heaving, pitching, flapping and twisting motions of a rectangular wing

Having compared unsteady results for a two-dimensional airfoil, we now compare results for several motions of a three-dimensional wing. We compare results with numerical results published by Jones et al.[19], by Neef[18], and computations using CMARC[88]. Jones et al.[19] studied heaving and pitching motions of the wing. Neef[18] also studied flapping and twisting motions. Neef[18] developed a three-dimensional unsteady Euler code, called FLOWer. Jones et al.[19] used both CMARC and FLOWer for their calculations. The simulations included the same motions as described in section 3.4.3, but for a rectangular wing of aspect ratio $AR = 8$, with NACA 0014 airfoil sections. The grid for the Euler code consisted of $160 \times 32 \times 40 = 204,800$ grid points in O-O topology, with 80 steps per period. Jones et al.[19] used CMARC with a grid of 20 chordwise panels and 20 spanwise panels with 100 time steps per period. We ran additional cases with CMARC using 120 chordwise and 20 spanwise panels with 100 time steps per cycle. The UVLM simulations were carried out for a wing with flat plate airfoil sections. The results converged for a grid with 20 panels chordwise and 20 panels spanwise with 120 time steps per period. As discussed in the previous section, all simulations were run for at least two periods and the time-averaged force and power coefficients were calculated during the last period of the simulation.

We first compare results for the heaving motion between UVLM and CMARC. Figures 3.6 and 3.7 compare the lift and thrust forces during the second period of heaving motion, for a rectangular wing of aspect ratio $AR = 8$. As observed in the two-dimensional case, the results match for low reduced frequencies, and the results differ by up to 33% for higher frequencies. As discussed in the two-dimensional case, we also compare motions with increased reduced frequencies k , while the heaving amplitude $\frac{z_0}{c}$ is reduced, such that the product $k \times \frac{z_0}{c}$ constant. As shown in figures 3.8 and 3.9, the results agree within 3% for $k \leq 0.2$. For $k = 1.0$, the differences at the peaks are still amount to 17%. The source of these differences is discussed in section 3.4.5.

We then compare results from UVLM and FLOWer for the combined heaving and pitching, flapping and twisting motions, as shown in figures 3.10, 3.11 and 3.12. The results agree within 6%. However we notice some differences of up to 13% in peak lift and thrust for $\bar{\theta}_0 = 4$ degrees. For these motions, UVLM results yield smaller peak lift and higher peak thrust values. The source of the differences in lift force lies in the lift curve slopes of flat plate and NACA 0014 airfoils. A flat plate airfoil produces slightly less lift at higher angles of attack. The difference in thrust force could also come from the curvature of the leading-edge for the NACA 0014 airfoil, which results in losses for the leading-edge suction forces, compared to a flat plate airfoil. De Laurier[23] indeed argued that leading-edge suction forces for typical airfoils are lower than for flat plate airfoils. Additionally, the Euler grid could have been too coarse to resolve the stronger leading-edge suction peak.

3.4.5 Discussion of results

We now discuss the possible sources of disagreement between the results from UVLM, UPOT, CMARC and published results. We have identified three main differences between the methods used, including the choice of wake model and Kutta condition, the validity of potential methods for high angles of incidence, and the limitations of thin airfoil approximations.

Wake model and Kutta condition

In the analytic results derived by Garrick[55] and Küssner[75], the wake is shed behind the airfoil at $z = 0$, regardless of the motion of the airfoil flat. Once deposited, the position of the wake remains fixed - rigid wake model - and the vorticity remains constant with time. In UVLM, UPOT and CMARC, the wake is deposited behind the wing as it moves. In the case of a sinusoidal heaving motion, the wake adopts a sinusoidal shape. In these three codes, the user can also specify whether the wake is rigid, or can move freely after being deposited. However, we do not observe a big difference in results between the rigid wake and free wake model, as the roll-up of the wake happens sufficiently far from the wing to have an effect on the wing lift distribution.

Jones et al.[19] showed that the results from UPOT and CMARC agree well with the analytical results theory for motions with low amplitudes $\frac{z_0}{c}$ and low reduced frequencies k . For motions with high amplitudes and high reduced frequencies, the differences lie mainly in the wake model, as discussed by Jones and Platzer[20].

In UVLM, we use the steady Kutta condition, and the wake panel behind the wing is tangential to the trailing-edge panels of the wing. Hansu and Hancock[] discussed the appropriate assumptions for the Kutta condition in unsteady motions,

and proposed a method to infer the appropriate angle of the wake panel with respect to the airfoil. This model was used by Jones and Platzer[20] in UPOT.

High angles of incidence

The method used in UVLM does not model any viscous effects encountered at high angles of attack, especially dynamic stall. We observe significant differences for motions with high frequency and amplitude, where values of lift force beyond $C_L > 1.50$ are predicted by our method. We note that CMARC includes options to model boundary layer considerations, and the results by Jones et al.[19] could include such effects. The maximum angle of incidence reached during the motion is related to the vertical motion amplitude and frequency. As discussed in section 3.4.4, this issue can be solved by fixing the product of amplitude and frequency at values, such that the value of angle of incidence remains below the dynamic stall angle α_{DS} of the airfoil.

In this study, we assume that an efficient pterosaur would have ensured that the wing would not be stalled at any moment of the flapping motion. We therefore monitor the maximum section lift coefficient $C_{l_{\max}}$ reached during the second period of the motion, and impose a constraint on the maximum attainable value. As discussed in section 3.2, Tuncer and Kaya[66], Isogai et al.[72] estimated, for the symmetric airfoil NACA 0012, the dynamic stall angle of incidence at $\alpha_{DS} \sim 15$ degrees. The corresponding lift coefficient for a flat plate airfoil is $C_{l_{DS}} = 1.64$. To ensure that the wing is not stalled during the motion, we enforce a stricter constraint, so, in this study, we limit the value of the section lift coefficient at $C_{l_{\max}} = 1.50$.

Thin airfoil approximation

UPOT and CMARC are based on the unsteady panel method, which models the volume of the wing. UVLM, however, is based on the unsteady vortex-lattice method, which models the wing as a thin surface. Results of lift coefficient for symmetric airfoils are rather similar to a flat plate airfoil. However, differences appear for higher angles of attack because of the thickness distribution. Therefore the values of lift coefficient during a motion will differ mostly near the peaks. Although we notice some differences, we deem that the results are close enough to justify the relative advantage of the vortex-lattice method over the panel method.

Conclusion

In all, the developed code UVLM matches within 13% with the Euler results and within 3% with CMARC in the range of amplitude and reduced frequencies, that are appropriate for the assumptions of potential flow methods. We do not feel confident using UVLM for more extreme cases, which would require additional modifications and comparisons with higher-order methods and experiments. We find that the range of aerodynamic parameters for pterosaurs, estimated in section 3.2, are well within these reasonable bounds, so using UVLM is adequate for computing the unsteady forces of the pterosaur wing.

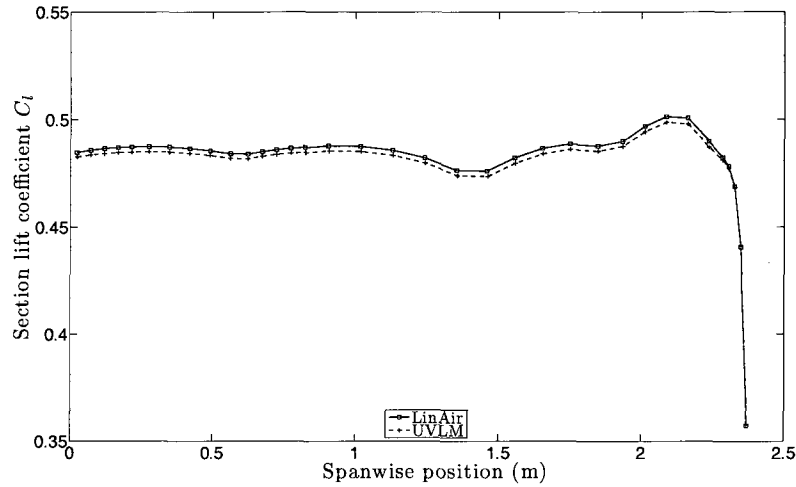
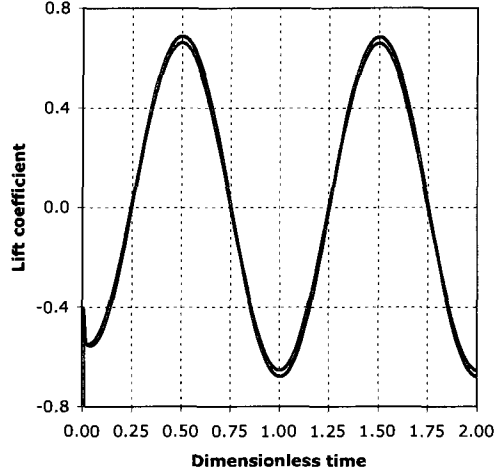


Figure 3.5: Comparison of the unsteady vortex-lattice code UVLM with lifting-line code LinAir for the distribution of section lift coefficient C_l for the planar pterosaur wing geometry, with five spanwise panels per bone. The plot shows the right wing at a steady angle attack $\bar{\theta}_0$ of five degrees.

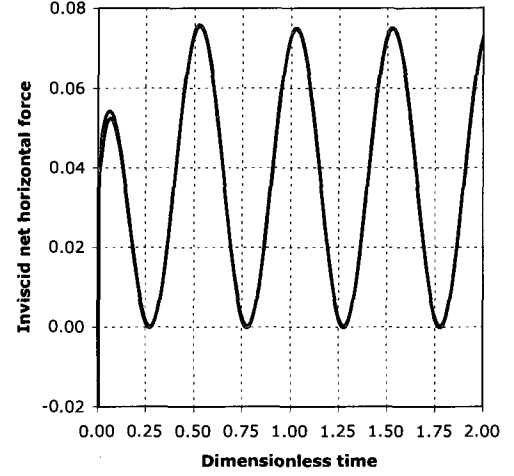
3.5 Aerodynamic model for *Coloborhynchus robustus*

3.5.1 Wing model of *Coloborhynchus robustus* used in the aerodynamic study

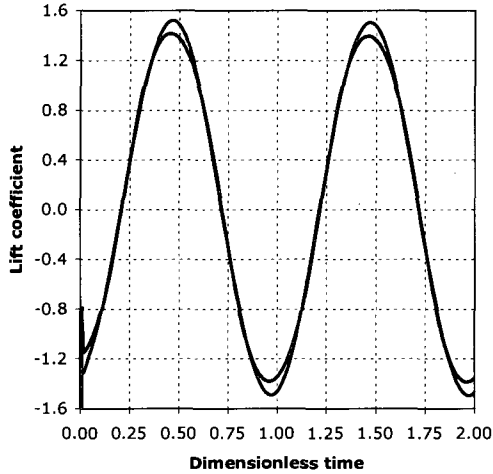
In this section, we detail the assumptions used to define the wing geometry for the aerodynamic study. As discussed in section 2.2.2, due to lack of fossil evidence for derived pterosaurs, there is no consensus among paleontologists whether the membrane wing is attached to the body at the hip, or to the leg at the knee or at the ankle. Similarly the shape of the propatagium is not known. A precise airfoil shape is important for estimating gliding performance and lift to drag ratios, but will not greatly affect estimates of thrust and power. In the aerodynamic study, we therefore



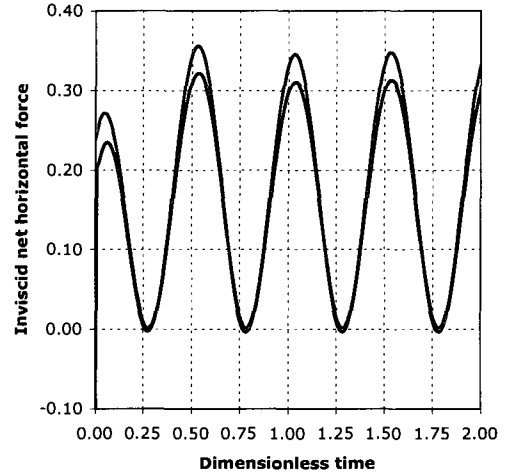
(a) Lift coefficient C_L as a function of the dimensionless time $\frac{t}{T_{\text{period}}}$ during the first two periods of the motion



(b) Inviscid net horizontal force coefficient $-C_{F_{X_{\text{inv}}}}$ as a function of the dimensionless time $\frac{t}{T_{\text{period}}}$ during the first two periods of the motion

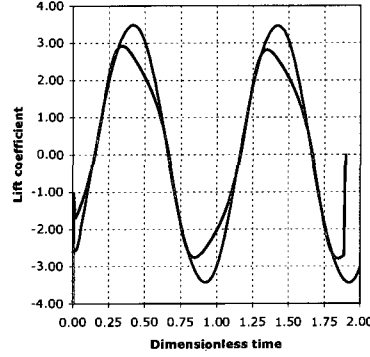


(c) Lift coefficient C_L as a function of the dimensionless time $\frac{t}{T_{\text{period}}}$ during the first two periods of the motion

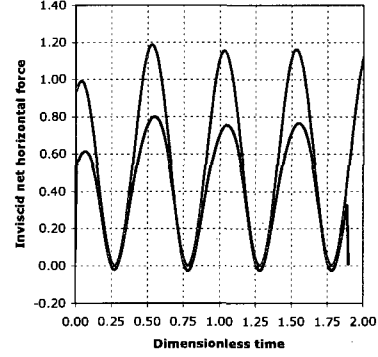


(d) Inviscid net horizontal force coefficient $-C_{F_{X_{\text{inv}}}}$ as a function of the dimensionless time $\frac{t}{T_{\text{period}}}$ during the first two periods of the motion

Figure 3.6: Comparison of the unsteady vortex-lattice method code UVLM with the unsteady panel code CMARC for the case of a rectangular wing of $AR=8$ in heaving motion. Figures 3.6(a) and 3.6(b) correspond to the heaving motion defined by $\frac{z_0}{c} = 0.4, k = 0.2$. Figures 3.6(c) and 3.6(d) correspond to the heaving motion defined by $\frac{z_0}{c} = 0.4, k = 0.5$. The blue and green lines correspond to the results from CMARC, as computed by Jones[19], and UVLM respectively.

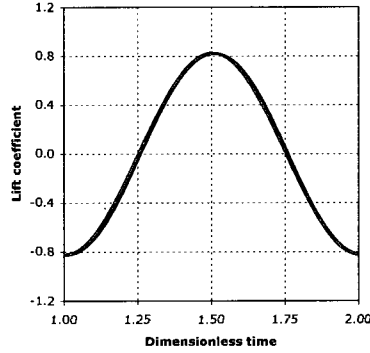


(a) Lift coefficient C_L as a function of the dimensionless time $\frac{t}{T_{\text{period}}}$ during the first two periods of the motion

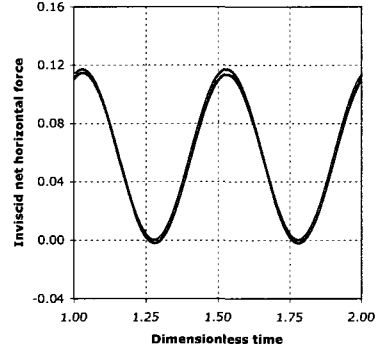


(b) Inviscid net horizontal force coefficient $-C_{F_{X_{\text{inv}}}}$ as a function of the dimensionless time $\frac{t}{T_{\text{period}}}$ during the first two periods of the motion

Figure 3.7: Comparison of the unsteady vortex-lattice method code UVLM with the unsteady panel code CMARC for the case of a rectangular wing of $AR=8$ in heaving motion ($\frac{z_0}{c} = 0.4, k = 1.0$). The blue and green lines correspond to the results from CMARC, as computed by Jones[19], and UVLM respectively. This choice of reduced frequency and amplitude is not appropriate for a meaningful comparison.

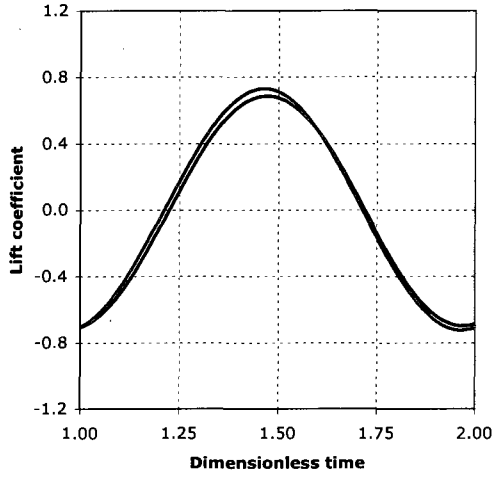


(a) Lift coefficient C_L as a function of the dimensionless time $\frac{t}{T_{\text{period}}}$ during the second period of the motion

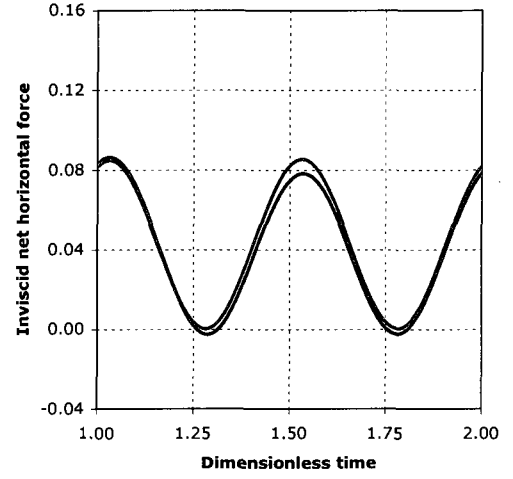


(b) Inviscid net horizontal force coefficient $-C_{F_{X_{\text{inv}}}}$ as a function of the dimensionless time $\frac{t}{T_{\text{period}}}$ during the second period of the motion

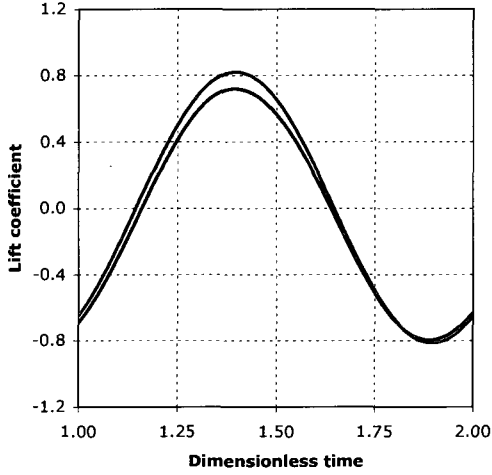
Figure 3.8: Comparison of the unsteady vortex-lattice method code UVLM with the unsteady panel code CMARC for the case of a rectangular wing of $AR=8$ in heaving motion ($\frac{z_0}{c} = 0.5, k = 0.2, \frac{z_0}{c} \times k = 0.1$). The blue and green lines correspond to the results from CMARC and UVLM respectively.



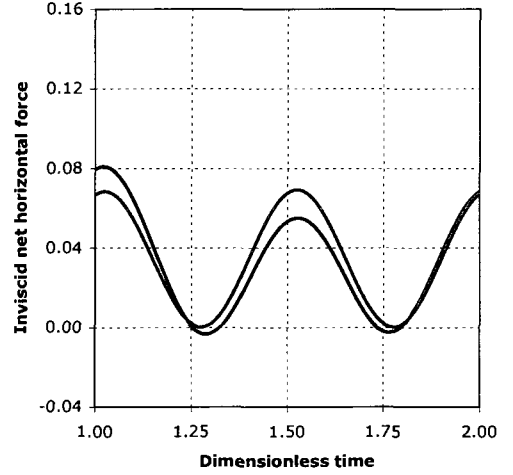
(a) Lift coefficient C_L as a function of the dimensionless time $\frac{t}{T_{\text{period}}}$ during the second period of the motion



(b) Inviscid net horizontal force coefficient $-C_{F_{x_{\text{inv}}}}$ as a function of the dimensionless time $\frac{t}{T_{\text{period}}}$ during the second period of the motion

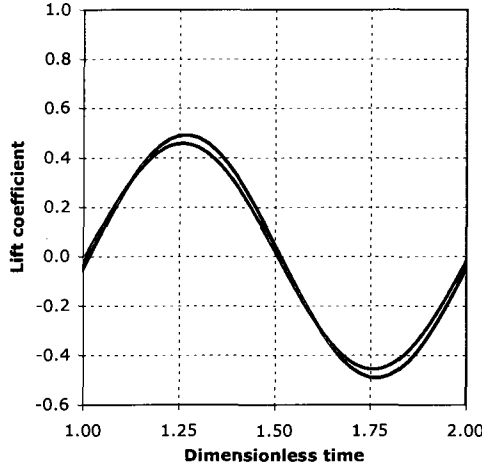


(c) Lift coefficient C_L as a function of the dimensionless time $\frac{t}{T_{\text{period}}}$ during the second period of the motion

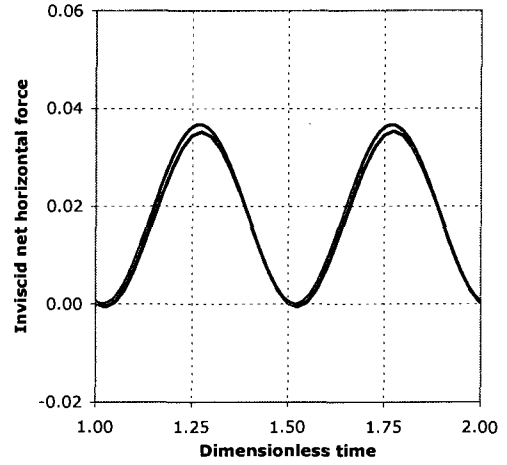


(d) Inviscid net horizontal force coefficient $-C_{F_{x_{\text{inv}}}}$ as a function of the dimensionless time $\frac{t}{T_{\text{period}}}$ during the second period of the motion

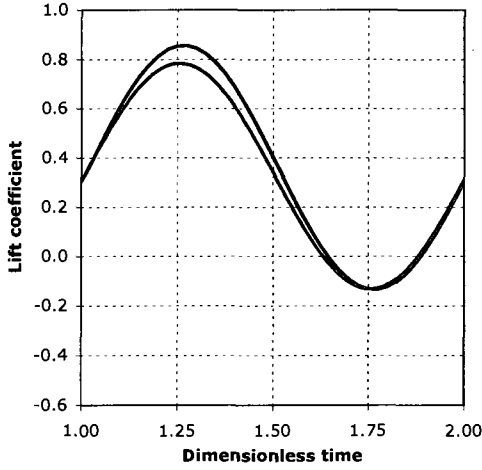
Figure 3.9: Comparison of the unsteady vortex-lattice method code UVLM with the unsteady panel code CMARC for the case of a rectangular wing of $AR=8$ in heaving motion. Figures 3.9(a) and 3.9(b) correspond to the heaving motion defined by $\frac{z_0}{c} = 0.2, k = 0.5, \frac{z_0}{c} \times k = 0.1$. Figures 3.9(c) and 3.9(d) correspond to the heaving motion defined by $\frac{z_0}{c} = 0.1, k = 1.0, \frac{z_0}{c} \times k = 0.1$. The blue and green lines correspond to the results from CMARC and UVLM respectively.



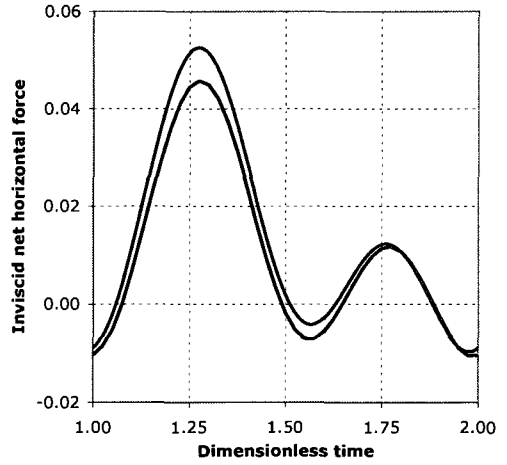
(a) Lift coefficient C_L as a function of the dimensionless time $\frac{t}{T_{\text{period}}}$ during the second period of the heaving motion, for $\bar{\theta}_0 = 0$ degrees



(b) Inviscid net horizontal force coefficient $-C_{F_{X_{\text{inv}}}}$ as a function of the dimensionless time $\frac{t}{T_{\text{period}}}$ during the second period of the heaving motion, for $\bar{\theta}_0 = 0$ degrees

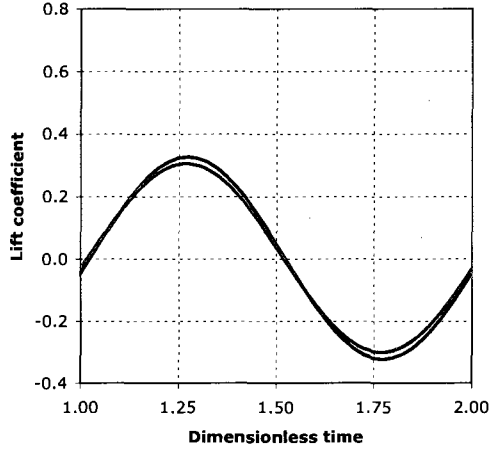


(c) Lift coefficient C_L as a function of the dimensionless time $\frac{t}{T_{\text{period}}}$ during the second period of the heaving motion, for $\bar{\theta}_0 = 4$ degrees

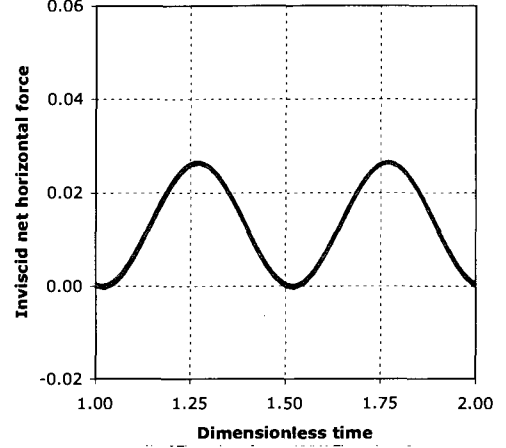


(d) Inviscid net horizontal force coefficient $-C_{F_{X_{\text{inv}}}}$ as a function of the dimensionless time $\frac{t}{T_{\text{period}}}$ during the second period of the heaving motion, for $\bar{\theta}_0 = 4$ degrees

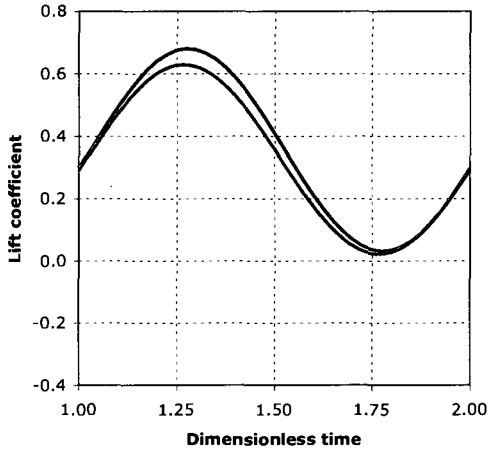
Figure 3.10: Comparison of the unsteady vortex-lattice code UVLM with the Euler code developed by Neef[18] for the case of a rectangular wing of $AR=8$ under heaving motion ($\frac{z_0}{c} = 0.52$, $k = 0.1$), for a steady angle-of-attack $\bar{\theta}_0 = 0$ degrees. The blue and green lines correspond to results from Neef and UVLM respectively.



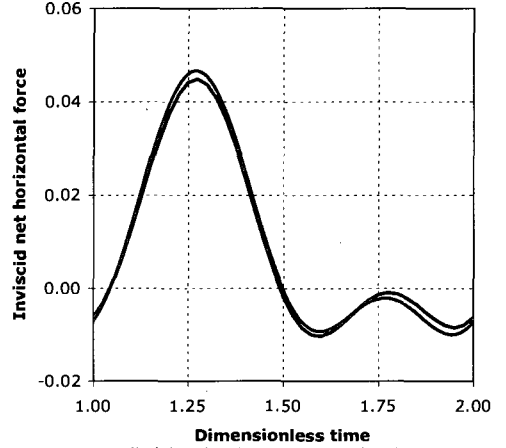
(a) Lift coefficient C_L as a function of the dimensionless time $\frac{t}{T_{\text{period}}}$ during the second period of the combined heaving and pitching motion, for $\bar{\theta}_0 = 0$ degrees.



(b) Inviscid net horizontal force coefficient $-C_{F_{x_{\text{inv}}}}$ as a function of the dimensionless time $\frac{t}{T_{\text{period}}}$ during the second period of the combined heaving and pitching motion, for $\bar{\theta}_0 = 0$ degrees.

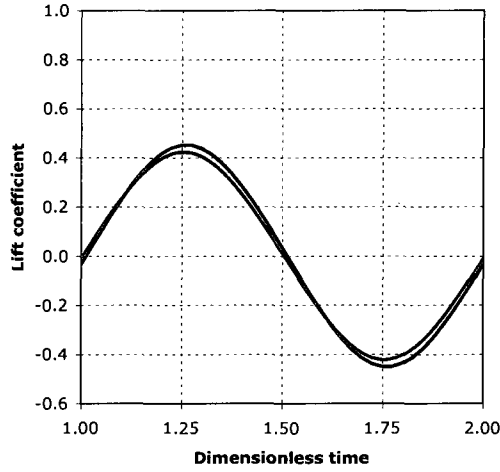


(c) Lift coefficient C_L as a function of the dimensionless time $\frac{t}{T_{\text{period}}}$ during the second period of the combined heaving and pitching motion, for $\bar{\theta}_0 = 4$ degrees.

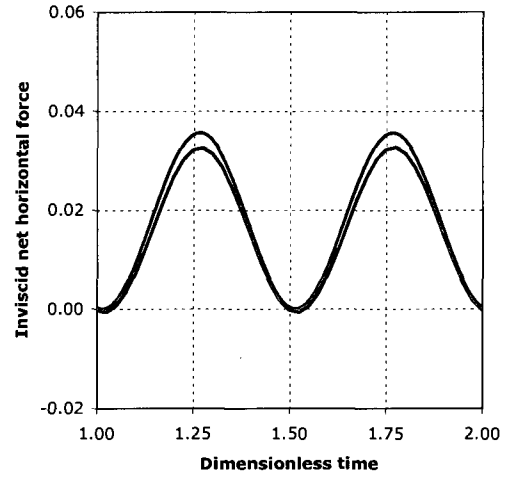


(d) Inviscid net horizontal force coefficient $-C_{F_{x_{\text{inv}}}}$ as a function of the dimensionless time $\frac{t}{T_{\text{period}}}$ during the second period of the combined heaving and pitching motion, for $\bar{\theta}_0 = 4$ degrees.

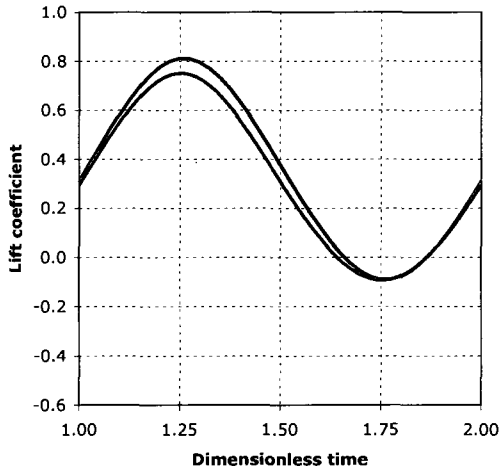
Figure 3.11: Comparison of the unsteady vortex-lattice code UVLM with the Euler code developed by Neef[18] for the case of a rectangular wing of $AR=8$ under combined heaving and pitching motion ($\frac{z_0}{c} = 0.52$, $\theta_0 = 2$ degrees, $\varphi_{\theta_0} = 90$ degrees, $k = 0.1$), for a steady angle-of-attack $\bar{\theta}_0 = 0$ degrees. The blue and green lines correspond to results from Neef and UVLM respectively.



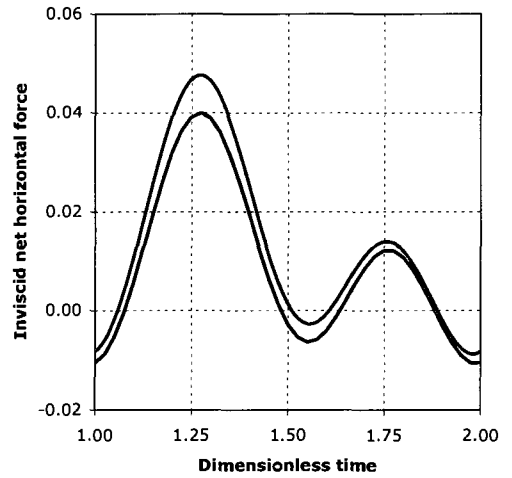
(a) Lift coefficient C_L as a function of the dimensionless time $\frac{t}{T_{\text{period}}}$ during the second period of the flapping motion, for $\bar{\theta}_0 = 0$ degrees



(b) Inviscid net horizontal force coefficient $-C_{F_{X_{\text{inv}}}}$ as a function of the dimensionless time $\frac{t}{T_{\text{period}}}$ during the second period of the flapping motion, for $\bar{\theta}_0 = 0$ degrees



(c) Lift coefficient C_L as a function of the dimensionless time $\frac{t}{T_{\text{period}}}$ during the second period of the flapping motion, for $\bar{\theta}_0 = 4$ degrees



(d) Inviscid net horizontal force coefficient $-C_{F_{X_{\text{inv}}}}$ as a function of the dimensionless time $\frac{t}{T_{\text{period}}}$ during the second period of the flapping motion, for $\bar{\theta}_0 = 4$ degrees

Figure 3.12: Comparison of the unsteady vortex-lattice code UVLM with the Euler code developed by Neef[18] for the case of a rectangular wing of $AR=8$ under flapping motion ($\phi_0 = 15$ degrees, $k = 0.1$), for a steady angle-of-attack $\bar{\theta}_0 = 0$ degrees (figures 3.12(a) and 3.12(b)) and $\bar{\theta}_0 = 4$ degrees. The blue and green lines correspond to results from Neef and UVLM respectively.

use flat plate airfoils.

Pterosaur wing volume

Unwin[28] discussed how the wing bones would have been pneumatized and would have been linked to a network of airsacks. Similarly to birds, the airsacks inflate during flight and define the airfoil shape in the wing. However, the extent of the airsacks in pterosaur wings is still subject of discussion, especially in the propatagium. If the propatagium membrane was thin like in the actinopatagium, the inner wing volume would have created an airfoil shape that is aerodynamically inefficient. However, if the propatagium was inflated, it might have created a streamlined airfoil, with a volume that could accomodate for the bone and muscle volume without an excessive drag penalty.

It is reasonable to believe that evolution would have penalized very inefficient wings in the aerodynamic sense, and that pterosaur wings would have had reasonable airfoil shapes. Further studies on the required muscle volume in the wing could help infer constraints on the wing airfoil shapes. In this study, however, we will not take these aspects into consideration, and make simplifying assumptions on the wing shape.

Extent of the membrane

Thrust during the flapping motion is mostly driven by the wing distal to the wrist. The shape of the wing proximal to the wrist, referred to as the inner wing, is therefore not as important to estimate performance for flapping flight, as it is for gliding flight. Therefore, at this stage, we assume that the trailing edge of the membrane wing is attached to the hip, and that the leading edge of the propatagium is attached to the

base of the neck. The attachment of the trailing edge of the membrane is the subject of a sensitivity study in chapter 5.

As described in section 2.2.3, the actinofibrils reinforce the actinopatagium thus making it stiffer than the tenopatagium and the propatagium. We assume that the actinopatagium extends spanwise from the wrist to the tip. In UVLM, the chordwise sections of the wing are defined as parallel to the x -axis, such that the proximal trailing-edge of the actinopatagium is located aft of the wrist with the same spanwise position y , as shown in figure 3.14.

Due to its increased stiffness, we assume that the shape of the actinopatagium is defined by the position and orientation of the leading-edge bones distal to the wrist. To model the flexibility of the propatagium and tenopatagium, we assume that the leading-edge of the propatagium is defined by a straight line between the neck attachment point and the pteroid. We also assume that the trailing-edge of the tenopatagium is defined by a straight line between the hip attachment point and the proximal trailing-edge of the actinopatagium, aft of the wrist.

Geometry defined by the angles at the joints

The wing model used in the aerodynamic study does not include aeroelastic effects, hence assuming the bones and joints are infinitely stiff. The wing geometry is therefore defined directly by the joint angles, and is changed from the glide positions by the motion of the active joints.

As we assume infinitely stiff bones and joints, the relative angle θ_i of a bone i combines the angle θ_{i-1} of the proximal bone and the rotation of the current bone i .

Table 2.5 shows that only the shoulder and the wrist have an active rotation θ , so

$$\theta_i = \theta_1 + \theta_3, \text{ for } i > 3. \quad (3.18)$$

As the wing distal to the wrist is defined by the leading-edge bones, we assume that each airfoil section is rotated by θ_i distal to the wrist. With this wing model, we note that a rotation θ_1 has the same effect as a rotation θ_3 of the same amplitude. We therefore simplify the wing motion by considering the wrist pitch rotation θ_3 with the combined range of motion of θ_1 and θ_3 .

Planar and curved wing geometries

The joints of the fourth wing digit are believed to be locked in position and result in a curved geometry, as shown in figure 3.13. The internal reinforcements against buckling (de Ricqlès et al.[32]) suggest that the structure of the wing bones is designed to mainly withstand compressive stresses, which would be consistent with a curved geometry. To understand if this geometry could have an aerodynamic advantage in flapping flight, we also consider a planar wing geometry. In the planar wing geometry, we adjust the joint angles such that the projected curved and planar geometries are quite close, as shown in figure 3.13 and 3.14. The joint angles for both geometries are detailed in table 3.5.

Summary

In all, we model the wing, in the frame attached to the center of gravity of the animal, using the following assumptions :

- the propatagium leading-edge is a straight line between the body and the wrist,

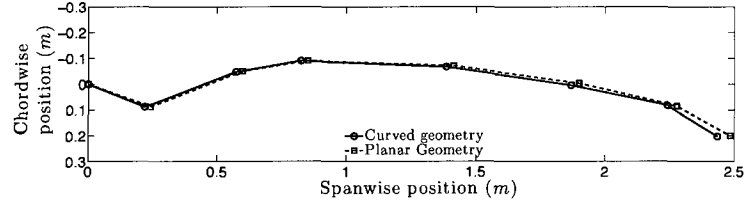
Table 3.4: Joint angles (in degrees) of right wing in glide position for the curved geometry. The abbreviations Sh., Elb., Wri., Knu., and Ph. refer to the shoulder, elbow, wrist, knuckle and interphalangeal joint.

Joint name	Shoulder	Elbow	Wrist	Knuckle	Ph.I-II	Ph.II-III	Ph.III-IV
Joint index i	1	2	3	4	5	6	7
ϕ_i	23	-9	-6	-10	-5	-6	-8
θ_i	0	0	0	0	0	0	0
ψ_i	-22	43	-10	-10	-5	-2	-18

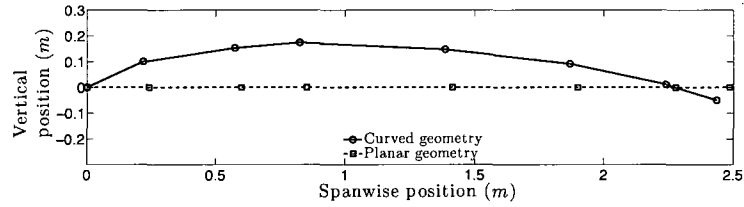
Table 3.5: Joint angles (in degrees) of right wing in glide position assuming a planar geometry. The abbreviation Ph. refers to an interphalangeal joint.

Joint name	Shoulder	Elbow	Wrist	Knuckle	Ph.I-II	Ph.II-III	Ph.III-IV
Joint index i	1	2	3	4	5	6	7
ϕ_i	0	0	0	0	0	0	0
θ_i	0	0	0	0	0	0	0
ψ_i	-20	41	-12	-11	-6	-5	-16

- the projection on the x - y plane of the straight line between the hip and the tip defines the trailing-edge x and y coordinates,
- in glide position, the wing section trailing-edge z -coordinates are the same as the corresponding wing section's leading-edge,
- the rotation angles θ_1 and θ_3 rotate the wing bones distal of the wrist,
- the tenopatagium trailing-edge is a straight line between the hip and the trailing-edge aft of the wrist,
- the wing chordwise sections are defined as flat plate airfoils between the leading-edge and the trailing-edge.



(a) Top view of the joint positions in glide position. The orientation of the x axis is such that the view matches the outline in figure 3.14(a).



(b) Front view of the joint positions in glide position.

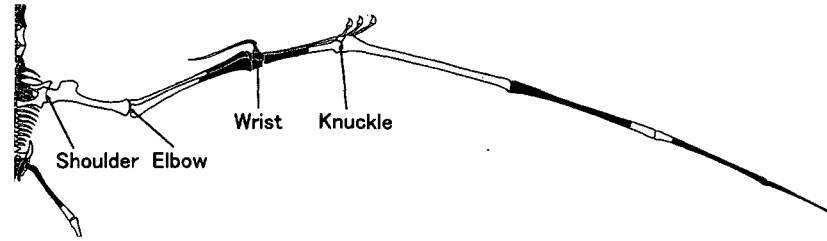
Figure 3.13: Top view and front view of the joint positions for the planar and curved glide geometries of *Coloborhynchus robustus*. The markers represent the joints, the lines represent the bones.

3.5.2 Estimates of the drag components

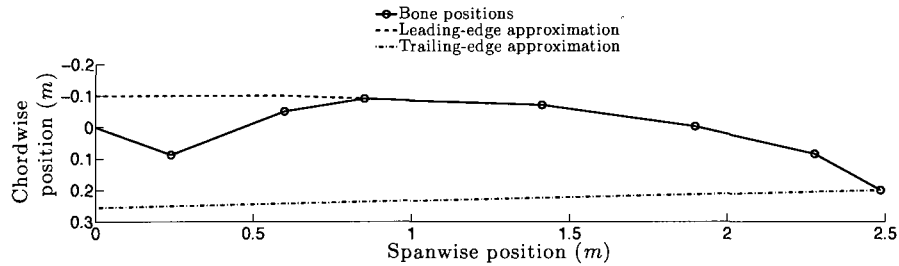
In this section, we detail the estimates of the steady-state drag for *Coloborhynchus robustus*. We estimate the body parasite drag by considering the different components of the body, such as the head, neck, torso, and the legs.

Parasite drag

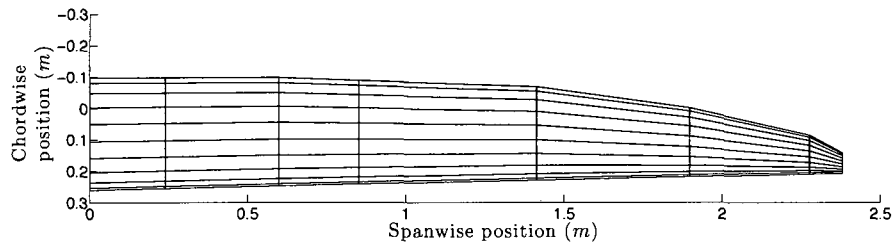
We assume that the motions of the head, neck, torso and legs are small enough to neglect variations in parasite drag, and therefore to use the steady-state estimates. We are mainly interested in the forces produced by the wing motion, so, for this study on flapping flight, we do not account for the lift and thrust forces created by the membrane between the legs, called uropatagium. We therefore assume that the uropatagium is only slightly loaded, and neglect its contribution to the lift-induced



(a) Layout of the wing bones of *Coloborhynchus robustus*. Picture adapted from Kellner and Tomida[2].



(b) Position of the wing bones with our approximations for the wing leading-edge and trailing-edge.



(c) Example of the wing geometry used in the vortex-lattice code UVLM. A geometry with ten chordwise panels and one spanwise panel per bone is shown.

Figure 3.14: Illustration of the approximations in the wing geometry of *Coloborhynchus robustus*. We show here the example of the glide geometry. From the position of the joints (figure 3.14(a)), we define the leading-edge and trailing-edge of the wing (figure 3.14(b)), using the geometric assumptions in section 3.5.1. We then define the wing panels (figure 3.14(c)), used in the vortex-lattice code UVLM, by choosing the number of chordwise panels and the number of spanwise panels per bone. For numerical stability reasons, the paneling needs a finite chord at the tip, so the geometry is truncated near the tip.

viscous drag. We estimate the parasite drag coefficient $C_{D_{\text{par}}}$ defined by

$$C_{D_{\text{par}}} = k_{\text{form factor}} C_f \frac{S_{\text{wetted}}}{S_{\text{ref}}}. \quad (3.19)$$

with $k_{\text{form factor}}$ the form factor coefficient, C_f the skin-friction coefficient, S_{ref} the reference wing area, and S_{wetted} the wetted area. The wetted area S_{wetted} is defined as the area in contact with the fluid, whereas the reference wing area S_{ref} is defined as the projected area of the wing. In our study, we consider that the wing stops at the shoulder line, not at the spine of the animal. The exposed wing area S_{exposed} is therefore equal to the reference wing area S_{ref} .

Form factor

The form factor coefficient $k_{\text{form factor}}$ takes into account the variation of velocity due to the shape of the surface, and is estimated using the methods described by Kroo[90]. We assume that the head, neck and torso form one body of revolution of fineness ratio 5, yielding a form factor of 1.3, considering the Mach number at $M = 0.05$. For the uropatagium, the form factor depends on the wing thickness ratio $\frac{\text{thickness}}{\text{chord}}$ and Reynolds number Re . The airfoil thickness ratio $\frac{\text{thickness}}{\text{chord}}$ is defined as the ratio of the maximum thickness over the chord. For a 5% thick uropatagium with $Re \simeq 3.0 \times 10^5$, $k_{\text{form factor}} = 1.1$. For a 10% thick uropatagium, $k_{\text{form factor}} = 1.2$. In this study, we assume that the muscle volume creates a 10% thick airfoil on the legs, and a 5% thick airfoil on average on the wing.

Wetted area

The wetted area S_{wetted} depends on the shape of the surface. We model the shape of the head, neck and torso as cylinders, and estimate the wetted area of the connected

Table 3.6: Estimates of the viscous drag for a 160 N specimen of *Coloborhynchus robustus* gliding at a steady lift coefficient $\overline{C_L} = 0.70$.

$S_{\text{body exposed}}$ (m ²)	0.78	$k_{\text{form factor body}}$	1.3	$C_{D_{\text{body}}}$	0.0032
S_{tail} (m ²)	0.13	$k_{\text{form factor tail}}$	1.2	$C_{D_{\text{tail}}}$	0.0013
S_{wing} (m ²)	1.33	$k_{\text{form factor wing}}$	1.1	$C_{D_{\text{wing}}}$	0.0123
				$C_{D_{i_{\text{visc}}}}$	0.0036
				$C_{D_{i_{\text{inv}}}}$	0.0096
				$C_{D_{\text{total steady-state}}}$	0.0303

cylinders. For the uropatagium, we calculate it with :

$$S_{\text{wetted}} = 2.0 \left(1 + 0.2 \frac{\text{thickness}}{\text{chord}} \right) S_{\text{exposed}}. \quad (3.20)$$

We assume that the uropatagium leading-edge is defined by the leg bones, and that the trailing-edge is defined by a straight line between the ankle and the end of the tail. We position of the legs such that the femur is perpendicular to the spine and the tibia is parallel to the spine. In this position, the exposed area of the uropatagium S_{uro} is given by

$$S_{\text{uro}} = 2 \frac{L_{\text{tail}} + L_{\text{tibia}}}{L_{\text{femur}}} \quad (3.21)$$

with L_{tail} the distance between the hip and the end of the tail, L_{tibia} the length of the tibia, and L_{femur} the length of the femur, as given by Kellner and Tomida[2].

Turbulent skin-friction coefficient

We consider the flow on the head, neck, torso, wing and uropatagium surfaces to be fully turbulent, and the skin-friction coefficient C_f is estimated using the von Karman fit of the turbulent flat plate model, as described by Kroo[90]. Table 3.6 summarizes the estimates of steady-state drag for a 160 N specimen of *Coloborhynchus robustus* gliding at a steady lift coefficient $\overline{C_L} = 0.70$.

3.5.3 Model for the body accelerations

In order to model the accelerations of the body due to the variations of the forces, we first need to estimate the inertial properties of the animal. In section 2.3.6, we estimated the inertial properties of a wing and of the whole animal in the glide position, as summarized in table 3.7.

Impact of the wing motion

We observe that the center of gravity of a wing is almost aligned with the shoulder on the x and z axes. Since most of the mass in the wing is close to the shoulder, a change in shoulder sweep or pitch angle, respectively ψ and θ , will have little effect on the position of the wing's center of gravity. However, a change in dihedral angle ϕ_1 at the shoulder will have more impact. We can derive the kinematic relationship between the motion of the wing and the animal center of gravity about the glide position as

$$z_0(t) = -\frac{m_{\text{wing}}}{m_{\text{animal}}}d \sin(\phi_1(t)), \quad (3.22)$$

with $\phi_1(t)$ the shoulder dihedral angle, m_{wing} the mass of one half-wing, m_{animal} the total mass of the animal, and d the distance between the center of gravity of a half-wing and the center of gravity of the whole animal.

Impact of the variation of aerodynamic forces

The aerodynamic forces on the wing calculated by the unsteady code depend on the velocities due to the wing kinematics and those induced by the wake. We aim to investigate the effects of the motion of the body due to the variation of the aerodynamic forces. At every time step, we apply the equations of motion for a rigid body, at the

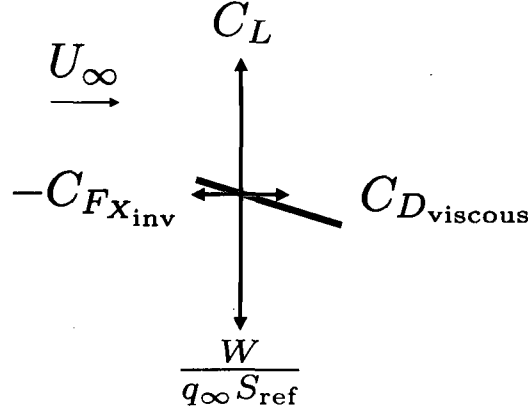


Figure 3.15: At every time step, we apply the equations of motion of a rigid body, at the center of gravity to evaluate the accelerations induced by the variation of aerodynamic forces and moments. The gray line represents a side view of the wing at an angle of attack. The lift force coefficient C_L and inviscid net horizontal force coefficient $C_{F_{X_{inv}}}$ are calculated by the unsteady vortex-lattice code UVLM. If the wing motion creates thrust, $C_{F_{X_{inv}}}$ is negative. The weight estimate $W/(q_\infty S_{ref})$ is chosen and the viscous drag coefficient $C_{D_{viscous}}$ is calculated as described in section 3.3.4.

center of gravity, accounting for all forces and moments, as shown in figure 3.15. As we consider only symmetric flapping motions about the x - z plane, the side force F_Y , and the moments about the x and z axes, C_{M_x} and C_{M_z} respectively, on each wing cancel out. The accelerations resulting from the force and moment coefficients are given by

$$\ddot{x}_0(t) = \frac{F_{X_{inv}}(t) + D_{viscous}(t)}{m_{\text{animal}}}, \quad (3.23)$$

$$\ddot{z}_0(t) = \frac{L(t) - W}{m_{\text{animal}}}, \quad (3.24)$$

$$\ddot{\theta}_0(t) = \frac{M_y(t)}{I_{yy}}, \quad (3.25)$$

with m_{animal} the total mass of the animal and I_{yy} the moment of inertia of the whole animal about the y axis. We note that, in the case where the body of the animal

follows a prescribed motion, the accelerations due to the motion are also included in the computation of the total acceleration of the body.

Numerical estimates of velocities and positions

As the aerodynamic forces are computed at the end of each time step, we resort to a time-stepping method. At the beginning of each time step i_t , we compute the accelerations due to the forces from the previous time step $i_t - 1$. We then estimate the velocity using the computed accelerations, and then we estimate the position using the updated velocity. In both cases, we use a numeric scheme derived from the second-order backward differencing scheme given by

$$\dot{f}(i_t) = \frac{1}{2dt} [3f(i_t) + 4f(i_t - 1) + f(i_t - 2)] \quad (3.26)$$

with f the function of interest defined at time step i_t , and dt the time step size

We first estimate the change in velocity due to the accelerations, then we estimate the position using the same scheme with the updated velocity, given by

$$\dot{X}(i_t) = \frac{1}{3} \left[-\dot{X}(i_t - 2) + 4\dot{X}(i_t - 1) - 2\ddot{X}(i_t - 1) \times dt \right], \quad (3.27)$$

$$X(i_t) = \frac{1}{3} \left[-X(i_t - 2) + 4X(i_t - 1) - 2\dot{X}(i_t - 1) \times dt \right] \quad (3.28)$$

with X the position or orientation function, i_t the time step number and dt the time interval between time steps. We note that, although the velocities and positions are estimated using a second-order scheme, the positions and orientations are estimated from the velocities, so are only first order accurate.

Table 3.7: Mass and moment of inertia I_{yy} of the right wing estimated for a 160 N specimen of *Coloborhynchus robustus*. We also list the corresponding position of the wing center of gravity relative to the body center of gravity.

Total mass of animal (kg)	17.0
Right wing mass (kg)	3.60
Moment of inertia I_{yy} (kg.m ²)	0.51
Position of the right wing C.G. relative to the body C.G.	
$x_{C.G Wing}$ (m)	0.015
$y_{C.G Wing}$ (m)	0.60

3.5.4 Grid convergence for the pterosaur wing

In section 3.3.6, we have discussed the parameters, that satisfy the convergence used in this study, for the panel and time step sizes of a rectangular wing. We now discuss the parameters for the converged grid for the pterosaur wing. Tables 3.10, 3.8, 3.9 compare the time-averaged forces, power and maximum section lift coefficient for different values of number of time steps per period, of number of chordwise panels, and of number of spanwise panels respectively. We find that, beyond 20 chordwise panels, 14 spanwise panels (2 panels per bone) and 50 time steps per period, the grid is converged. We therefore use the following parameters for all subsequent calculations:

- number of chordwise panels $N_{\text{chord}} = 20$
- number of spanwise panels $N_{\text{span}} = 14$
- number of periods $N_{\text{periods}} = 2$
- number of time steps per period $N_{\text{steps/period}} = 50$

Table 3.8: Variation of time-averaged quantities for different number of periods N_{periods} , and of time steps per period $N_{\text{steps/period}}$. The time-averaged quantities correspond to the curved wing geometry of *Coloborhynchus robustus*, modeled with 20 panels chordwise and 14 panels spanwise, with flapping motion parameters: $k = 0.10$, $\bar{\theta} = 5.0$, $\phi_1 = 10.0$, $\theta_3 = 4.0$, $\varphi_{\theta_3} = 90.0$.

	$N_{\text{periods}} / N_{\text{steps/period}}$				
	2 / 50	2 / 100	2 / 150	3 / 50	4 / 50
Average lift $\overline{C_L}$	0.4665	0.4620	0.4634	0.4625	0.4626
Average inviscid net force $\overline{C_{F_{X_{\text{inv}}}}}$	0.0127	0.0128	0.0126	0.0130	0.0130
Average mechanical power $\overline{C_P}$	0.0216	0.0214	0.0212	0.0218	0.0218
Average wing parasite drag $\overline{C_{D_{\text{wing}}}}$	0.0137	0.0134	0.0135	0.0134	0.0134
Maximum section lift $C_{l_{\text{max}}}$	1.253	1.244	1.242	1.254	1.254
Relative computation time	1.0	3.3	6.8	2.0	3.4

Table 3.9: Variation of time-averaged quantities for different number of panels N_{chord} in the chordwise direction. The time-averaged quantities correspond to the curved wing geometry of *Coloborhynchus robustus*, modeled for 2 periods with 50 time steps per period, with flapping motion parameters: $k = 0.10$, $\bar{\theta} = 5.0$, $\phi_1 = 10.0$, $\theta_3 = 4.0$, $\varphi_{\theta_3} = 90.0$.

	$N_{\text{chord}} \times N_{\text{span}}$		
	10×14	20×14	30×14
Average lift $\overline{C_L}$	0.4665	0.4665	0.4666
Average inviscid net force $\overline{C_{F_{X_{\text{inv}}}}}$	0.0142	0.0127	0.0127
Average mechanical power $\overline{C_P}$	0.0216	0.0216	0.0216
Average wing parasite drag $\overline{C_{D_{\text{wing}}}}$	0.0137	0.0137	0.0137
Maximum section lift $C_{l_{\text{max}}}$	1.261	1.253	1.254
Relative computation time	0.4	1.0	1.7

Table 3.10: Variation of time-averaged quantities for different number of panels N_{span} in the spanwise direction. The time-averaged quantities correspond to the curved wing geometry of *Coloborhynchus robustus*, modeled for 2 periods with 50 time steps per period, with flapping motion parameters: $k = 0.10$, $\bar{\theta} = 5.0$, $\phi_1 = 10.0$, $\theta_3 = 4.0$, $\varphi_{\theta_3} = 90.0$.

	$N_{\text{chord}} \times N_{\text{span}}$				
	20×7	20×14	20×21	20×28	20×35
Average lift $\overline{C_L}$	0.4698	0.4665	0.4653	0.4646	0.4643
Average inviscid net force $\overline{C_{F_{X_{\text{inv}}}}}$	0.0149	0.0127	0.0125	0.0124	0.0123
Average mechanical power $\overline{C_P}$	0.0222	0.0216	0.0214	0.0213	0.0212
Average wing parasite drag $\overline{C_{D_{\text{wing}}}}$	0.0137	0.0137	0.0136	0.0136	0.0136
Maximum section lift $C_{l_{\text{max}}}$	1.343	1.253	1.248	1.239	1.231
Relative computation time	0.2	1.0	2.2	4.0	6.1

3.6 Summary

In this chapter, we have first motivated the approximations, that we use to model the unsteady aerodynamics of pterosaur flight. We have then discussed the choice of the unsteady vortex-lattice method, and we have described the code that we have developed for this study, which we refer to as UVLM. We have also compared UVLM to other inviscid codes and published results for different wing geometries in the steady case, and for the unsteady motion of a rectangular wing. We have shown that the computed forces compare match analytical results and differ at most by 3% with unsteady panel codes and by 13% with Euler methods for cases that do not violate our model assumptions. Finally, we have detailed the model for the wing of *Coloborhynchus robustus* used in the optimization accounting only for the aerodynamic effects, as detailed in chapter 5.

Chapter 4

Aeroelastic Model

4.1 Introduction

In chapter 3, we detailed the aerodynamic model of the pterosaur wing. In addition to computing the aerodynamic forces, it is also key to account for the structural deformations of both the wing bones and membrane. As discussed in section 2.2.4, the wing bones of pterosaurs were believed to be thin and lightweight, and the thin wing membranes were believed to be reinforced by slender structures. Even in the case of an inextensible membrane, the wing membrane would undergo significant deformations due to the motion of the bones. In the aerodynamic model, we assumed that the shape of the wing is defined only by the position of the joints. In the aeroelastic model, however, the position of a joint is the combination of the flapping gait and the structural deformations.

Similarly to chapter 3, we describe in this chapter the aeroelastic model and compare computed results with published results, before we apply this method to the

optimization problem in chapter 5. We first detail the model used for the fluid-structure interactions. As our final purpose is to optimize the flapping motion for efficiency, the model chosen must have sufficient accuracy without a severe penalty in computational speed. Although the structural problem is non-linear, we motivate the choice of simplifying the structural model of the wing membrane and bone deformations, using a modal decomposition. We compare the deflections of a flapping wing using our method with measurements made on an ornithopter.

We then discuss the approximations used to build the structural model of the pterosaur wing. We compare computed results with analytical results for the structural deformations of a two-dimensional and a circular membrane. Finally we discuss the sensitivity of the wing shape in glide conditions and of the performance in flapping flight to the material properties chosen for the membrane.

4.2 Choice of unsteady aeroelastic model

4.2.1 Relevant studies in unsteady aeroelasticity

In aeroelastic problems, the fluid and structural loads are usually computed by separate methods, which need to be coupled to capture the fluid-structure interactions. Coupling methods are generally described as loose or strong coupling formulations. Strong coupling methods, such as described by Morand and Ohayon[94], solve for the structural displacements and the fluid forces simultaneously. The coupling terms are calculated at the surface of fluid-structure interaction. Loose coupling formulations usually solve for the structural displacements and aerodynamic loads iteratively by minimizing the residual forces. The residual forces are computed from the difference between the structural and the aerodynamic forces caused by updating the

displacements. The advantage of the strong coupling formulation is to solve the fluid-structure problem directly, but it requires the computation of the coupling terms. The coupling terms cannot be calculated if the formulation in the fluid and structural domain are not compatible. The advantage of the loose coupling formulation is the ease of implementation at the cost of iterative procedures to ensure convergence.

Several authors have previously investigated flapping flight with unsteady aeroelastic models based on loose coupling formulations. Smith[83] studied the flapping flight of moths. He combined an unsteady panel method to compute the aerodynamic loads and a finite-element method (FEM) for the structural deformations. He neglected the inertial and damping properties of the wing, and assumed small deformations at each time step. He compared the computational results with wind tunnel experiments using a moth model. The differences were attributed mainly to the dynamic stall effects, which were not accounted for in the aerodynamic model. Larijani[81] investigated the effects of dynamic stall for the flapping flight of the Human Ornithopter Project. He combined a non-linear unsteady aerodynamic model and a wing structural model. The aerodynamic model was based on the model described by de Laurier[23] which divided the wing into two-dimensional sections using the analytical results derived by Garrick[55]. Larijani[95, 81] added a dynamic stall model to the aerodynamic model, and included the damping properties measured experimentally on the wing structure. Lee[96, 97] investigated the control of flutter modes of a rectangular wing using Miniature Trailing Edge deflectors (MiTE). He modeled the aeroservoelastic problem by combining an unsteady vortex-panel method and a finite-element representation of the wing. Lian[98] investigated the flapping flight of Micro Aerial Vehicles (MAV) with membrane wings. He modeled the low

Reynolds number flow using an unsteady Navier-Stokes Computational Fluid Dynamics (CFD) model. He modeled the wing structure using an hyperelastic membrane model. He coupled the two solvers using the moving boundary technique and time synchronization. Farhat et al.[99] described a time-accurate algorithm for loosely-coupled fluid-structure interactions. They modeled the fluid using a three-dimensional Euler and Navier-Stokes solver called AERO-F and modeled the structure using a suite of finite-element analysis tools referred to as AERO-S. They showed that their algorithm was second-order accurate, and applied it to the transient non-linear response of a F-16 subject to a gravity excitation.

Although computational tools based on CFD and the finite-element method have been successfully used to model the fluid-structure interactions in the steady case, these studies of unsteady aeroelastic effects underline key challenges. To model the fluid-structure interaction, the fluid domain sends to the structural domain the aerodynamic loads computed for the current geometry, and the structural domain sends to the fluid domain the structural deformations computed for the current aerodynamic loads. The fluid and structural domain are usually computed using separate tools, hence meshed differently. The communication between the two domains therefore requires transformations of the sent information to be compatible with the domain of interest. In addition to that, the solutions in the two domains need to be matched such that the fluid and the structure are at equilibrium at every time step of the motion. In some cases, a mismatch between the length of the time step and the amplitude of the mismatch can lead to divergent solutions. These issues are usually solved by changing the time-integration scheme or by solving the problem iteratively at each time step. For example, Larijani[95] explored different choice of time integration schemes that would be stable with respect to the non-linear aerodynamic problem. He found that

only the time-integration scheme based on the Newmark scheme was stable enough. Similarly, Lian[98] used an implicit Wilson- θ method to ensure numerical stability. By modeling the wing structure using a finite-element method, the computations are sensitive to the high frequencies of the structure. These frequencies are not generally representative of the real structure, and damping schemes are generally required to limit their influence. Unless the damping ratios can be measured experimentally as in Larijani[95], damping scheme must be considered such as the proportional damping scheme used by Lee[97].

In this study, the aerodynamic loads are computed by UVLM based on the vortex-lattice method. At each time step, UVLM solves for the vorticity distribution on the wing and then computes the pressure and forces. Lee[97] used a loose coupling formulations and showed good agreement with experiments. This study focused on the unsteady motions of wings at low speed and low frequencies, as is the case for the motion of pterosaur wings. Similarly, Farhat et al.[99] showed that results using a second-order time-accurate loose coupling formulation were close to experimental measurements. A loose coupling formulation is therefore deemed an appropriate choice for this study. Because we are studying the unsteady motion of the wing in the time-domain, we also need to ensure the numerical stability of the time-integration scheme. We model the flapping motion over several periods and are interested in the quantities during the last period, and an inappropriate scheme would lead to large numerical errors. Because we are not specifically studying instability problems such as flutter, we aim at implementing a numerical scheme that provides sufficient stability. In this study, we combine the numerical time-integration scheme based on the Newmark method, as described by Larijani[95], and the conventional serial staggering scheme described by Farhat et al.[99].

4.2.2 Relevant membrane studies

As described by Calladine[100], thin surface structures are usually approximated as shell structures, which support tension and compression stresses, and support very small bending moments. In the limit of very thin structures, membranes can only resist tension stresses. A membrane is taut under biaxial tension, wrinkles if under uniaxial compression, and becomes slack under biaxial compression. This non-linear behaviour must be included in the material stress-strain relationship, and can become complex for anisotropic materials. The stresses in a membrane are related to the loads normal to the surface and the curvature of the surface.

A structure with bending stiffness requires strains in the material to deform, and, unless it is clamped, its only kinematic modes are its rigid body modes, which take place without a change in strain in the material. A membrane structure, however, has an infinite number of kinematic degrees of freedom, on top of the rigid body modes.

As summarized by Heppel[101], membrane deformations can be characterized by extensional deformations and inextensional deformations. Extensional deformations are linked to changes of stress, and are associated to the direct stiffness of the membrane. Inextensional deformations are linked to changes of curvature, and are associated to the geometric stiffness of the membrane. The direct stiffness depends on the state of stress and material properties, whereas the geometric stiffness depends on the shape and the state of stress. In the general case, deformations of the membrane are both inextensional and extensional. Solving for the membrane shape must account for the non-linear coupling between the direct and the geometric stiffness.

Membranes were first studied by Nielsen[102] and Thwaites[103] for the case of a two-dimensional membrane fixed at the leading-edge and the trailing-edge. The membrane was considered inextensible in a steady, two-dimensional potential flow.

This resulted in a compact integral solution to the problem given by

$$1 - \frac{C_{\text{Tension}}}{2} \int_0^1 \frac{\frac{d^2(y/\alpha)}{d\xi^2}}{2\pi(\xi - x)} d\xi = \frac{d(y/\alpha)}{dx} \quad (4.1)$$

where $y(x)$ defines the membrane camber along the chordwise coordinate x , α is the incidence angle, and C_{Tension} is the tension coefficient.

In the three-dimensional membrane problem, the membrane tension is not uniform and wrinkling has to be modeled. Due to this additional complexity, early works on three-dimensional membrane wings assumed an analytical shape derived from measurements, such as described by Rogallo[104] for conical wings. Kroo[105] estimated the wing shape of hang glider wings by minimizing the potential energy of the membrane structure using a Lagrangian description and a simplified stress-strain relationship. Further studies modeled the membrane using finite-element methods and considered only steady-state cases. Oden and Sato[106] studied the steady-state equilibrium of an inflated membrane using a finite-element model of the elastic membrane. Christie and Jackson[107] combined a three-dimensional vortex-lattice method with a finite-element method for the membrane. The shape of the membrane was solved iteratively, and was applied to compute the shape of a hang glider wing and a yacht sail in steady flow. Smith and Shyy[108] combined a vortex-lattice method and an incremental formulation of the elastic membrane problem to define a membrane wing element, which included a wrinkle model. Coupled to a time-stepping algorithm, they used this method to compute the shape of a wing with a free trailing edge and of a marine sail. Heppel[101] developed a dynamic relaxation analysis scheme, called Relax, to model the wrinkling of membranes. Paton et al.[109] later detailed the coupling required between CFX, a CFD code, and Relax for the design of sail. They

reported that good convergence is achieved with in the order of a few thousand nodes in the structure and in the order of several million cells in the fluid.

The problem of dynamic membranes was investigated more recently, and reviewed by Jenkins and Leonard[110] and by Jenkins[111]. Smalley and Tinker[112] performed linear modal analysis of inflated structures using NASTRAN[113], a commercial finite-element analysis code. They first computed the shape of the inflated structure, and then performed a modal decomposition. They showed that the modal decomposition of the inflated structure was much closer to experimental results, than in the non-inflated case. Using a similar approach, Scott et al.[114] coupled NASTRAN[113] with CFL3D, a CFD code developed at NASA. They first computed the deflected shape of a two-dimensional membrane in the steady case, then computed the modal decomposition, and finally investigated the flutter onset of the deflected membrane.

4.2.3 Methods chosen

In chapter 3, the choice of the unsteady vortex-lattice method was deemed appropriate in the range of motions considered and for the available information on the wing geometry. Similarly, there is currently too much uncertainty in the details of the pterosaur wing geometry and membrane properties to effectively use advanced membrane models. We therefore aim at choosing a structural model for the pterosaur wing that is appropriate for the chosen aerodynamic model and for the current knowledge on the wing.

The range of motion of the joints indicate that the pterosaur wing would have been subject to significant changes in shape and stress distribution due to the varying aerodynamic loads. We therefore need to recompute the deformations of the bones and membrane at every time step of the motion. Although iterative methods, like

the ones described by Heppel[101], can be used to accurately predict the shape of membranes, these methods are practical only for steady cases, because they could take up to ten iterations to converge at each time step. The recent methods used for sail design are usually coupled to advanced CFD methods with several thousand nodes for the structural domain, and in the order of a million cells for the fluid domain. This order of resolution is required to allow enough kinematic freedom for the membrane, and to adequately resolve the pressure distribution on the sail. Consequently, the required additional resolution and iterations would increase the current computational time by at least an order of magnitude. Using such methods seems appropriate only for future studies, when the membrane properties will be better characterized, and when a more detailed wing geometry can be inferred.

Frey et al.[31] attributed some observed patterns to muscle fibers in the pterosaur wing membrane. It is therefore likely that pterosaur would have actively controlled the shape of the membrane by both activating the muscles in the membrane and by changing the position of the joints. Although membranes are non-linear structures, the deformations can be considered linear for small deflections about a loaded equilibrium shape, as discussed by Smalley et al[112]. We therefore assume that pterosaurs would have controlled their membrane muscles and their wing joints during the wing motion, such that the changes in membrane stress distribution were small enough to maintain a linear structural behavior of the membrane. Assuming such behavior, we can model the linear structural displacements using a modal decomposition computed for the membrane tensioned under the steady glide loads.

As a result of these assumptions, we do not consider the variations of the mode shapes due to the time-varying aerodynamic loads and bone positions. Future studies could refine the membrane model by including the variation of the mode shapes

and frequencies as a function of time during the wing motion. If the variations of aerodynamic loads do not lead to severe structural non-linearities, the mode shapes could be computed for a reduced set of time steps. The modal decomposition could then be interpolated at intermediary time steps using matrix interpolation techniques as discussed by Amsallem et al.[115] and Amsallem and Farhat[116]. Because the reduced-order model is derived from the full-order structural model, if the structural non-linearities are deemed too important, the structural deformations would have to be computed directly from the full-order model at every time step.

4.3 Fluid-structure interaction model for pterosaur wings

In the aeroelastic model, the pterosaur wing is subject to deformations due to the joint motions and to the structural deformations. The deformations due to the joint motions are computed in the same manner as in the aerodynamic model. In this section, we detail the model used to compute the structural deformations and the coupling of the fluid and structure models. As discussed in previous sections, we reduce the non-linear membrane problem to the linear behavior about a loaded equilibrium shape. The linear structural problem is then reduced using a modal decomposition. The fluid and structure models are loosely coupled using a time-integration scheme based on the Newmark method.

4.3.1 General dynamic equations of motion

We define $\{\mathbf{y}(t)\}$ the vector of generalized nodal displacements due to the structural deformations at time t . The general dynamic equations of motion for an elastic

structure, neglecting external forces, is generally given in the matrix form by

$$[\mathbf{M}] \{\ddot{\mathbf{y}}(t)\} + [\mathbf{D}] \{\dot{\mathbf{y}}(t)\} + [\mathbf{K}] \{\mathbf{y}(t)\} = \{\mathbf{F}(t)\} \quad (4.2)$$

with $[\mathbf{M}]$ the generalized mass matrix, $[\mathbf{D}]$ the generalized damping matrix, $[\mathbf{K}]$ the generalized structural stiffness matrix and $\{\mathbf{F}\}$ the generalized nodal forces. $\{\mathbf{F}\}$ corresponds in practice to the aerodynamic loads transferred from the aerodynamic code to the structural code.

In this study, the aerodynamic pressure forces are computed in UVLM at the control points located at the center of the panel corners, whereas the structural nodal displacements act upon the corners of the aerodynamic panels. The nodal forces therefore need to be computed from the aerodynamic pressure forces. Using the equivalent work load method, the element nodal force vector $F_{N_{element}}$ is determined to exert the same amount of work on each element as the distributed pressure ΔP , and is written

$$F_{N_{element}} = \int \int_{element} \Delta P(x, y) a^T(x, y) dx dy \quad (4.3)$$

with a^T the shape function of the element. In UVLM, the pressure is assumed constant over each aerodynamic panel, and the shape functions used correspond to the structural element used in the Finite-Element Analysis code.

4.3.2 Modal decomposition of the wing structure

We model the linear structural displacements of the wing using a reduced-order model, based on the modal superposition method. This method is based on the Ritz-Galerkin method as described by Morand and Ohayon[94]. If we choose the n -first eigenmodes

\mathbf{y}_α of the wing structure clamped at the root, as basis vectors, we can then write

$$\{\mathbf{y}(t)\} = \sum_{\alpha=1}^n \mathbf{q}_\alpha(t) \mathbf{y}_\alpha = [\mathbf{H}] \{\mathbf{q}(t)\} \quad (4.4)$$

with $[\mathbf{H}] = [\mathbf{y}_1, \dots, \mathbf{y}_n]$ the basis of eigenvectors, and $\{\mathbf{q}(t)\}^T = [q_1, \dots, q_n]$ the coefficients of the projection. We compute the modal decomposition for the undamped structure, by solving the generalized eigenvalue problem, given by

$$[\mathbf{K}] \{\mathbf{y}(t)\} + [\mathbf{M}] \{\ddot{\mathbf{y}}(t)\} = \mathbf{0} \quad (4.5)$$

Assuming a sinusoidal response $\mathbf{y}(t) = \mathbf{y} \cos(\omega t)$, the problem is now written

$$[\mathbf{K}] \{\mathbf{y}\} - \lambda [\mathbf{M}] \{\mathbf{y}\} = \mathbf{0} \quad (4.6)$$

with $\lambda = \omega^2$. The solution to this problem yields the basis of eigenvectors \mathbf{H} and its corresponding frequencies ω_α . The stiffness and mass matrices can thus be written

$$[\mathbf{H}]^T [\mathbf{K}] [\mathbf{H}] = [\mathbf{\Lambda}] = \begin{bmatrix} \omega_1 & 0 & 0 \\ 0 & \ddots & 0 \\ 0 & 0 & \omega_n \end{bmatrix} \quad (4.7)$$

$$[\mathbf{H}]^T [\mathbf{M}] [\mathbf{H}] = [\mathbf{I}] = \begin{bmatrix} 1 & 0 & 0 \\ 0 & \ddots & 0 \\ 0 & 0 & 1 \end{bmatrix} \quad (4.8)$$

The reduced-order equation of motion for the undamped structure is therefore written

$$[\mathbf{I}] \{\ddot{\mathbf{q}}(t)\} - [\mathbf{\Lambda}] \{\mathbf{q}(t)\} = [\mathbf{H}]^T \{\mathbf{F}(t)\} \quad (4.9)$$

We then add the structural damping to the response, modeled by the damping matrix $[\mathbf{D}]$, which we note $[\mathbf{\Xi}]$ in the reduced-order formulation. In this study, we cannot measure the structural damping directly, so we use a proportional damping scheme as suggested by Lee[. The damping matrix is inferred from the stiffness matrix by

$$[\mathbf{D}] = 2 \frac{\zeta_{\max}}{\omega_{\max}} [\mathbf{K}] \quad (4.10)$$

with ζ_{\max} the critical damping ratio and ω_{\max} the maximum frequency of the structure. We choose a value of critical damping $\zeta_{\max} = 0.50$. ω_{\max} corresponds to the circular frequency of the highest mode considered. The reduced-order damping matrix $[\mathbf{\Xi}]$ is therefore given by

$$[\mathbf{\Xi}] = 2 \frac{\zeta_{\max}}{\omega_{\max}} [\mathbf{\Lambda}] \quad (4.11)$$

and the equation of motion for the damped structure becomes

$$[\mathbf{I}] \{\ddot{\mathbf{q}}(t)\} + [\mathbf{\Xi}] \{\dot{\mathbf{q}}(t)\} - [\mathbf{\Lambda}] \{\mathbf{q}(t)\} = [\mathbf{H}]^T \{\mathbf{F}(t)\} \quad (4.12)$$

At each time step of the wing motion, we solve this equation which yields the reduced-order displacements $\mathbf{q}(t)$. Expanding $\mathbf{q}(t)$ yields the structural displacements of the wing $\mathbf{y}(t)$, given by

$$\{\mathbf{y}(t)\} = [\mathbf{H}] \{\mathbf{q}(t)\} \quad (4.13)$$

This formulation enables an efficient computation of the structural deformations, and limits numerical instabilities due to the highest frequencies of the finite-element model. As discussed by Morand and Ohayon[94], the modal superposition method is well-suited for problems of low frequencies, corresponding to modes of low rank, which is the case for the flapping motions we consider. We note that UVLM models

the aerodynamic geometry with flat panels, so the nodal coordinates (x, y, z) are the only generalized displacements required in the reduced-order model.

4.3.3 Fluid-structure interaction coupling

We directly solve the generalized equation of motion 4.4 in the time domain, which is a second-order non-linear equation, using the Newmark integration scheme as described by Larijani[95]. The non-linear terms in time are linearized by using a Taylor series approximation. The Newmark method describes the nodal displacements $\{\mathbf{y}\}^{n+1}$ and velocities $\{\dot{\mathbf{y}}\}^{n+1}$ at time step $n + 1$ as a function of the previous time step n by

$$\{\dot{\mathbf{y}}\}^{n+1} = \{\dot{\mathbf{y}}\}^n + [(1 - \delta) \{\ddot{\mathbf{y}}\}^n + \delta \{\ddot{\mathbf{y}}\}^{n+1}] \Delta t \quad (4.14)$$

$$\{\mathbf{y}\}^{n+1} = \{\mathbf{y}\}^n + \{\dot{\mathbf{y}}\}^n \Delta t + [(0.5 - \beta) \{\ddot{\mathbf{y}}\}^n + \beta \{\ddot{\mathbf{y}}\}^{n+1}] \Delta t^2 \quad (4.15)$$

with δ and β parameters determined to obtain integration accuracy and stability. Newmark proposed an unconditionally stable scheme, known as constant acceleration method, with $\delta = \frac{1}{2}$ and $\beta = \frac{1}{4}$. Larijani[95] derived the generalized equations of motion using the Newmark method, such that the nodal displacements at time step $n + 1$ are a function of the aerodynamic forces at time step $n + 1$ and the nodal displacements, velocities and accelerations at time step n . Using equation 4.15, we first express the nodal acceleration $\{\ddot{\mathbf{y}}\}^{n+1}$ in terms of $\{\mathbf{y}\}^{n+1}$ and the quantities of the previous time step, given by

$$\begin{aligned} \{\ddot{\mathbf{y}}\}^{n+1} &= \frac{1}{\beta \Delta t^2} \left[\{\mathbf{y}\}^{n+1} - \{\mathbf{y}\}^n - \Delta t \{\dot{\mathbf{y}}\}^n - \left(\frac{1}{2} - \beta \right) \Delta t^2 \{\ddot{\mathbf{y}}\}^n \right] \\ &= \frac{1}{\beta \Delta t^2} \{\mathbf{y}\}^{n+1} - \frac{1}{\beta \Delta t^2} \{\mathbf{y}\}^n - \frac{1}{\beta \Delta t} \{\dot{\mathbf{y}}\}^n - \left(\frac{1}{2\beta} - 1 \right) \{\ddot{\mathbf{y}}\}^n \end{aligned} \quad (4.16)$$

Using this expression in equation 4.14, we can then express the nodal velocity $\{\dot{\mathbf{y}}\}^{n+1}$ in terms of $\{\mathbf{y}\}^{n+1}$ and the quantities of the previous time step, given by

$$\begin{aligned}\{\dot{\mathbf{y}}\}^{n+1} &= \{\dot{\mathbf{y}}\}^n + (1 - \delta) \Delta t \{\ddot{\mathbf{y}}\}^n \\ &\quad + \delta \Delta t \left[\frac{1}{\beta \Delta t^2} \{\mathbf{y}\}^{n+1} - \frac{1}{\beta \Delta t^2} \{\mathbf{y}\}^n - \frac{1}{\beta \Delta t} \{\dot{\mathbf{y}}\}^n - \left(\frac{1}{2\beta} - 1 \right) \{\ddot{\mathbf{y}}\}^n \right] \\ &= \frac{\delta}{\beta \Delta t} \{\mathbf{y}\}^{n+1} - \frac{\delta}{\beta \Delta t} \{\mathbf{y}\}^n - \left(\frac{\delta}{\beta} - 1 \right) \{\dot{\mathbf{y}}\}^n - \frac{\Delta t}{2} \left(\frac{\delta}{\beta} - 2 \right) \{\ddot{\mathbf{y}}\}^n\end{aligned}\quad (4.17)$$

By defining the following coefficients,

$$\begin{aligned}a_0 &= \frac{1}{\beta \Delta t^2} \\ a_1 &= \frac{\delta}{\beta \Delta t} \\ a_2 &= \frac{1}{\beta \Delta t} \\ a_3 &= \frac{1}{2\beta} - 1 \\ a_4 &= \frac{\delta}{\beta} - 1 \\ a_5 &= \frac{\Delta t}{2} \left(\frac{\delta}{\beta} - 2 \right) \\ \text{with } \beta &= \frac{1}{2} \\ \delta &= \frac{1}{4}\end{aligned}$$

equations 4.16 and 4.17 can be written

$$\{\ddot{\mathbf{y}}\}^{n+1} = a_0 \{\mathbf{y}\}^{n+1} - a_0 \{\mathbf{y}\}^n - a_2 \{\dot{\mathbf{y}}\}^n - a_3 \{\ddot{\mathbf{y}}\}^n \quad (4.18)$$

$$\{\dot{\mathbf{y}}\}^{n+1} = a_1 \{\mathbf{y}\}^{n+1} - a_1 \{\mathbf{y}\}^n - a_4 \{\dot{\mathbf{y}}\}^n - a_5 \{\ddot{\mathbf{y}}\}^n \quad (4.19)$$

By substituting the accelerations and velocities at time step $n + 1$ with these expressions into equation 4.2, we can express the nodal displacements $\{\mathbf{y}\}^{n+1}$ as a function of the displacements, velocities and accelerations computed at the previous time step. Equation 4.2 is then written

$$\begin{aligned}
 ([\mathbf{K}] + a_0 [\mathbf{M}] + a_1 [\mathbf{D}]) \{\mathbf{y}\}^{n+1} &= \{\mathbf{F}\}^{n+1} \\
 &+ [\mathbf{M}] (a_0 \{\mathbf{y}\}^n + a_2 \{\dot{\mathbf{y}}\}^n + a_3 \{\ddot{\mathbf{y}}\}^n) \\
 &+ [\mathbf{D}] (a_1 \{\mathbf{y}\}^n + a_4 \{\dot{\mathbf{y}}\}^n + a_5 \{\ddot{\mathbf{y}}\}^n) \quad (4.20)
 \end{aligned}$$

Using the reduced-order model formulation, equation 4.20 can be written

$$\begin{aligned}
 ([\mathbf{I}] + a_0 [\mathbf{\Lambda}] + a_1 [\mathbf{\Xi}]) \{\mathbf{q}\}^{n+1} &= [\mathbf{H}]^T \{\mathbf{F}\}^{n+1} \\
 &+ [\mathbf{I}] (a_0 \{\mathbf{q}\}^n + a_2 \{\dot{\mathbf{q}}\}^n + a_3 \{\ddot{\mathbf{q}}\}^n) \\
 &+ [\mathbf{\Xi}] (a_1 \{\mathbf{q}\}^n + a_4 \{\dot{\mathbf{q}}\}^n + a_5 \{\ddot{\mathbf{q}}\}^n) \quad (4.21)
 \end{aligned}$$

We note that the Newmark method is an implicit scheme. However, in UVLM, the computed forces $\{\mathbf{F}\}^{n+1}$ are in fact $\{\mathbf{F}\}^n$, because the aerodynamic forces are computed from the wing geometry defined at the beginning of the time step, and hence with the structural displacements $\{\mathbf{q}\}^n$. Without modification, this coupling corresponds to the conventional serial staggering scheme. This scheme has been shown to be prone to numerical instabilities as discussed by Farhat et al.[99]. As suggested by Larijani[95], this issue can be solved by subiterating the structural displacements and the aerodynamic forces to enforce convergence of the residual forces below a set tolerance. However, such an iterative approach is time consuming. We have found that stability is typically ensured with one subiteration for the motions considered.

Further studies could investigate the accuracy and computational performance of a stronger coupling scheme or of a second-order time-accurate scheme similar to the one described by Farhat et al.[99].

At the first time step, we initialize the nodal displacements, velocities and accelerations to zero. The nodal velocities and accelerations are computed from the nodal displacements using the same numerical schemes as for the velocities and accelerations of the aerodynamic panels. The initial spike in lift forces due to the starting vortex induces initial vibrations which are typically not visible after the first half period.

4.4 Comparison with measured wing motion of an ornithopter

Before applying the method described above to pterosaur wings, we compare computed results with measurements available for an ornithopter wing. We choose an ornithopter design, such that the wing structure and motion are simple to model and to compare with. The chosen ornithopter was designed and built by Steve Morris[12] independently from this study.

In this section, we first present the ornithopter, and then the computational representation of the wing. Finally we compare the motions computed and observed in free flight. We note that only the values for the motion of the tip are currently available which makes the comparison less conclusive.

4.4.1 Choice of ornithopter used for comparison

Several successful man-made ornithopters have been developed in the last decades, such as Sean Kinkade's ParkHawk[117], de Laurier's Quarter-Scale Ornithopter[118],

Hoerst Rabiger's EV7 and EV8[119], and Albert Kempf's True Fly[120]. The wing motions of these models involved flapping and twisting motions. The twisting motion was either controlled actively, such as in the EV7 and True Fly, or was the result of passive deformations. In the latter case, the wing structure was tailored to achieve the desired motion amplitude and phase. Controlling the twist motion is a key design challenge because of the difficulty in predicting the inertial and aerodynamic loads. However successful, these designs have a limited flight time because they suffer from poor efficiencies. Designs with membrane wings or with torsionally soft wings also have poor gliding performance, because the wing structure is tailored only for flapping flight. Models, such as the Quarter-Scale Ornithopter and EV7, have been designed from aerodynamic analyses, and usually have complex mechanisms to actuate the wings.

In addition to these efforts, Steve Morris[12] has recently been developing an ornithopter with the goals of improving the propulsive efficiency while maintaining the design simple, and limiting the glide performance losses. Because of the simple wing structure and the availability of measurements, this model is a good candidate to test the aeroelastic model. The ornithopter and flight measurements have been made available to us between test flights, and we use these for comparison.

4.4.2 Description of the ornithopter tested

The ornithopter developed by Steve Morris[12] was composed of two rectangular wings actuated only in the flapping motion. The twist motion was controlled passively by tailoring the torsional stiffness of the wings. These were driven at the root by a single motor. The amplitudes of the flapping was between 20 to 30 degrees about the set average dihedral. A locking mechanism also maintained the wings at moderate

dihedral angle during glide. The motion frequency was between 2-4 Hz. Flight times were usually in the 2 to 4 minutes range, with an estimated 30% efficiency in the best flights. The total wingspan was about 2.10 m with an aspect ratio of 7.45. The ornithopter weighed 1.50 kg in the last design iterations. Table 4.1 summarizes the main design characteristics.

The mechanical properties of the wing were modified between each design iterations. The wing modifications aimed at tailoring the torsional stiffness and inertial properties for propulsive efficiencies. One of the remaining main challenges is to correctly time the phase angle between the active flapping motion and the passive torsion of the wing. Ideally, the phase angle should be about 90 degrees, and measurements have shown that significant changes occur at the motion reversal, where the inertial loads are the most severe.

Several wing design iterations included replacing the outboard foam sections with membrane cloth, changing the position of the main structural spar, adding sweep angle along the span, and adding a passive joint at mid-span. The membrane cloth provided the most significant wing design improvement. The flapping mechanism was also altered several times, with an increase in the flapping amplitude and the addition of springs at the root to create a restoring force at the beginning of the downstroke. Tailoring the amplitude and frequency proved to be the most effective mean of increasing efficiency. The ornithopter wing that was made available for testing is referred to foam wing 3 by Steve Morris.

For the ornithopter wings that we study, the main spar was made of spruce with a layer of carbon fiber to add some bending stiffness. The inboard section of the wing was built with polystyrene foam and balsa wood sections to give the desired airfoil shape. The outer sections of the wing had a smaller foam volume near the spar, with

Table 4.1: Main characteristic of the ornithopter designed and built by Steve Morris[12].

Wingspan (m)	2.10	Flapping half-amplitude (degrees)	20-30
Wing area (m ²)	0.58	Average dihedral (degrees)	10-20
Chord (m)	0.28	Flapping frequency (Hz)	2-4
Aspect ratio	7.45	Mass (kg)	1.50

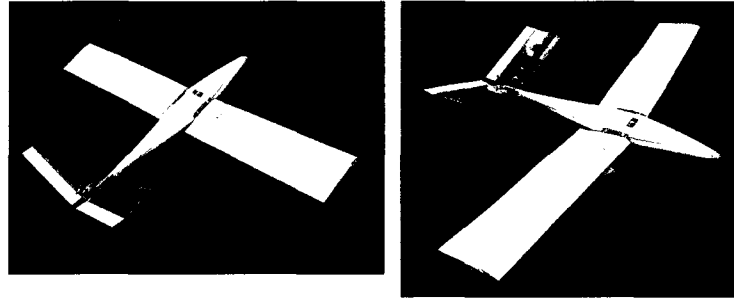


Figure 4.1: Picture of the general ornithopter design with foam wing 3. Picture taken by Steve Morris[12].

the rest of the airfoil defined by a thin layer of foam sheet. The upper surface of the foam was slit open at 45 degrees relative to the spar, in order to give the wing more torsional flexibility. Figures 4.1 illustrate the overall wing design.

4.4.3 Computational model of the ornithopter wing

In order for the computational model of the wing structure to work easily with the aerodynamic code, it is key to ensure the compatibility of the nodal definitions. Because UVLM uses a thin wing model, we therefore model the ornithopter wing as a flat plate structure. The mechanical properties of materials used by aircraft modelers are usually not given or have large uncertainties. As discussed by Green et al.[121], the mechanical properties of wood can vary greatly depending on the moisture content and alignment of the wood fibers. Because of the slits in the foam, the foam volume cannot be considered a closed volume. It is therefore easier to model the wing

as a single material with properties determined from static bending and torsion tests. Because the wing is quite flexible in torsion but quite stiff in bending, we model the wing with a single linear orthotropic material. Because we model the wing as a thin plate, the properties in the vertical direction do not have an impact on the deformations. In this study, we choose the same properties in the vertical direction as in the chordwise direction. In order to match the inertial properties, the thickness of the plate is increased near the spar where the foam volume is greater. The thin sections were modeled with a 14 mm thickness corresponding to the thickness of the foam covering. The thick sections were modeled with a 80 mm thickness corresponding to the area of the airfoil sections per unit length.

The static deflection tests used a 100 g weight applied at the wing tip near the leading edge for the bending test, and near the trailing edge for the torsion test. We found that the vertical deflections for the bending test was about 15 ± 1 mm at the leading edge. For the torsion test, the leading edge deflected vertically by 15 ± 1 mm and the trailing edge deflected vertically by 108 ± 1 mm. In the finite-element code, we first Taylor the Young's modulus in the spanwise direction to match the bending deflections, then the Young's modulus in the chordwise direction and the shear moduli to match the torsional deflections.

We compare in table 4.2 the mechanical properties chosen for two examples of composite materials, AS4/3501-6 Carbon-epoxy and S2-Glass-epoxy. The ratio of Young's moduli in the fiber and transverse directions for the carbon-epoxy and fiberglass-epoxy composites are 14 and 5 respectively. Similarly, the ratio of shear modulus with the transverse modulus are 1.4 and 2 respectively. For our estimates, we set the ratio of Young's modulus of the spanwise direction over the one in the chordwise direction at 6. Similarly, the ratio of transverse modulus shear modulus was set at 2. The

Table 4.2: Mechanical properties of two composite materials and the orthotropic material used for the ornithopter wing model. The two composite materials are AS4/3501-6 Carbon-epoxy and S2-Glass-epoxy, with values given by Sun[13]. Longitudinal refers to the direction of the fiber. In the model for the ornithopter wing, the longitudinal properties are in the y -direction, and transverse corresponds to the x and z -directions.

	Carbon Epoxy	Glass Epoxy	Ornithopter Wing
Longitudinal Young's modulus E_1 (MPa)	140.0	43.0	6.0
Transverse Young's modulus E_2 (MPa)	10.0	9.0	1.0
Shear Modulus G_{12} (MPa)	7.0	4.5	0.5
Poisson's ratio ν_{12}	0.30	0.27	0.25

carbon-epoxy and fiberlass-epoxy composites have Poisson's ratio of 0.3 and 0.27 respectively, and we choose a value of 0.25 for consistency. With this choice of material properties, the vertical deflections at the tip computed with the finite-element analysis were estimated at 14 mm for the bending case. For the torsional deflection, the vertical deflections were 14 mm and 105 mm at the leading-edge and the trailling-edge respectively.

The ornithopter wings are light relative to the weight of the ornithopter, with one wing weighing 169 g which represents about 12% of the total mass of the ornithopter. We also measure the position of the center of gravity and compare it to the finite-element model in table 4.3. We find that the finite-element model overestimates the mass with a center of gravity further aft and outboard than measured on the wing. We note that the wing used for the measurements had been significantly modified after the recorded flight. We are therefore unable at this stage to refine the finite-element model. Further experiments could use a new wing with more characterized properties.

Table 4.3: Comparison of the wing mass and position of the center of gravity measured on the ornithopter wing and the finite-element model.

	Measured	FEA model
Mass (g)	169	233
Position of center of gravity		
$x_{C.G.}$ (m)	0.054	0.093
$y_{C.G.}$ (m)	0.296	0.434

4.4.4 Comparison of computed and observed wing motions

For the aeroelastic computations, we compute the first ten modes and structural mode shapes for the wing, which define the modal basis to project the aerodynamic forces on. In the gliding case, the bending deflections are on the order of 47 mm at the leading-edge of the tip, and the wing tip was twisted by -0.4 degrees. Out of the ten modes, only the first seven modes have an influence on the deformations in gliding flight. However, for the flapping motion, the roles of the other modes may also become significant. We therefore compare the effects of the number of modes included in the structural model for given motion parameters. The wing is moving at a reduced frequency $k = 0.2$ with a flapping amplitude set at 20 degrees with a zero average offset. The ornithopter is flying at an average speed of $U_\infty = 10\text{m.s}^{-1}$ and a constant angle of attack $\bar{\theta} = 5$ degrees. Figure 4.2 compares the predicted tip deflections for the cases considering the first three, five, seven and ten modes. We find that the lift and thrust forces are identical for three to seven modes. When ten modes are considered, the forces are slightly shifted in time and with higher peak forces. These differences are due to the proportional damping scheme we have chosen. By changing the number of modes considered, we increase the highest frequency of the structure, and in turn we also modify the damping of the other modes. By forcing the structural damping ratio to be defined by one chosen frequency, the responses become identical

beyond five modes. In this study, we therefore choose to model the structural deformations of the wing with the first five modes of the modal decomposition.

The only available measurements are from the videos of the flights, which limits the available data to the tip vertical deflections. For this reason, we do not account for the body accelerations in the computations. Further experiments could include measurements of the vehicle's acceleration, orientation, speed and altitude.

The deflections of the tip were inferred from the images captured during the flight tests. Figure 4.3 shows a sequence of pictures during one period of motion with lines representing the tip twist angle and the ornithopter angle of attack. From the angle measured on these pictures, phase diagrams were drawn for the tip twist angle as a function of the wing dihedral. The bending loads also modified the vertical deflections from the commanded motion, so we plot the tip twist angle as a function of the dihedral of the deformed wing.

As discussed in section 3.4.4, the results for UVLM compare well with results at reduced frequencies of $k = 0.2$, but to a lesser extent with reduced frequencies of $k = 0.5$. Additionally, for motions with high frequencies, the inertial loads can dominate the aerodynamic effects. The inertial properties of the computational model could not be compared with the real wing, so we expect large discrepancies for the higher frequency cases. We therefore expect better agreement with lower reduced frequencies. The parameters of the motion of the chosen flight test are given in table 4.4. We note that we do not model the restoring forces of the spring connected to the ornithopter wing. In the flight test considered, the springs did not have a visible effect on the motion.

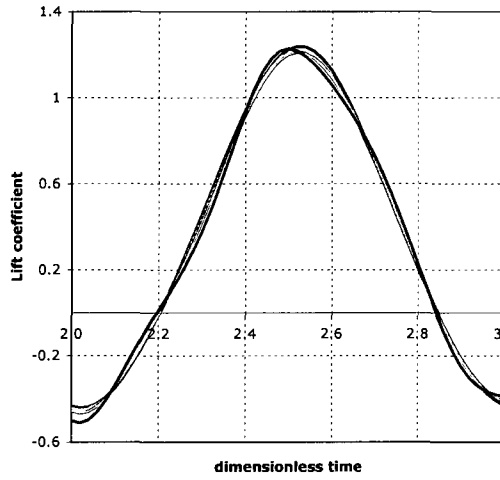
Two key parameters for the computational simulations are the forward velocity

Table 4.4: Parameters of the chosen flight test for comparison.

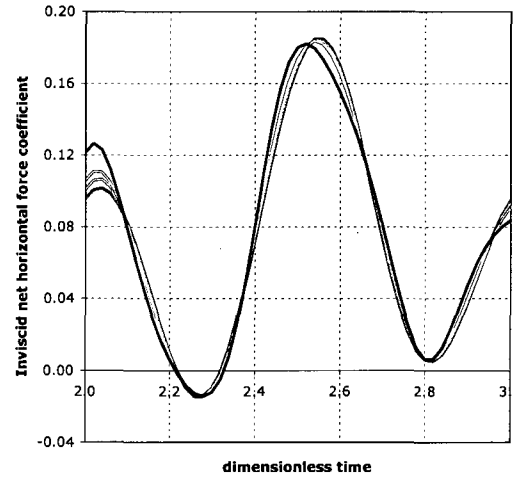
Flapping half-amplitude (degrees)	20	Average lift coefficient	0.5-1.0
Average dihedral (degrees)	10	Flight speed (m.s ⁻¹)	6.5-9.0
Flapping frequency (Hz)	2-3	Reduced frequency	0.20-0.54

and reduced frequency, which could not be directly measured from the flight tests. Although the pitch angle of the vehicle can be measured, its angle of attack relative to the wind is hard to infer because it is usually climbing. We therefore adapt these two parameters so that the results compare well with the measured values. We assume that the average lift coefficient during flight is between 0.3 and 1.0, which corresponds to flight speeds ranging between 6.5 and 12.0 m.s⁻¹. The motion frequency of the flight test considered is 2-4 Hz, which corresponds to a range of reduced frequency between 0.27 and 0.54 at 6.5 m.s⁻¹ and between 0.20 and 0.39 at 12.0 m.s⁻¹. This constitutes a big range of possible conditions. We therefore test only several cases of reduced frequencies and flight speed.

We show in figure 4.4 the data points of the measurements and the computed results for two cases, with the twist angle plotted against the dihedral angle. We note that the tested combinations of flight speed and reduced frequency within the range we specified yielded small amplitudes of twist angles. By choosing a reduced frequency of $k = 0.45$ and a flight speed of $U_\infty = 12.0$ m.s⁻¹, the computed results were within a few degrees in amplitude (maximum difference of 4 degrees) and almost in phase with the experiments. These parameters correspond to a flapping frequency of 5.6 Hz. These differences indicate that the inertial properties of the wing need to be refined. Future studies could include measurements of the unsteady wing deformations in a wind-tunnel with controlled parameters. Such measurements could be used to refine the comparisons and could yield paths to improve on the models for the wing structure and the fluid-structure interaction.



(a) Lift coefficient C_L as a function of the dimensionless time $\frac{t}{T_{\text{period}}}$ during the third period of the motion



(b) Inviscid net horizontal force coefficient $-C_{F_{x_{inv}}}$ as a function of the dimensionless time $\frac{t}{T_{\text{period}}}$ during the third period of the motion

Figure 4.2: Comparison of the lift and inviscid net horizontal forces for different number of modes included in the structural model of the ornithopter wing. The red, blue, green and black lines correspond to the cases with respectively three, five, seven and ten modes.

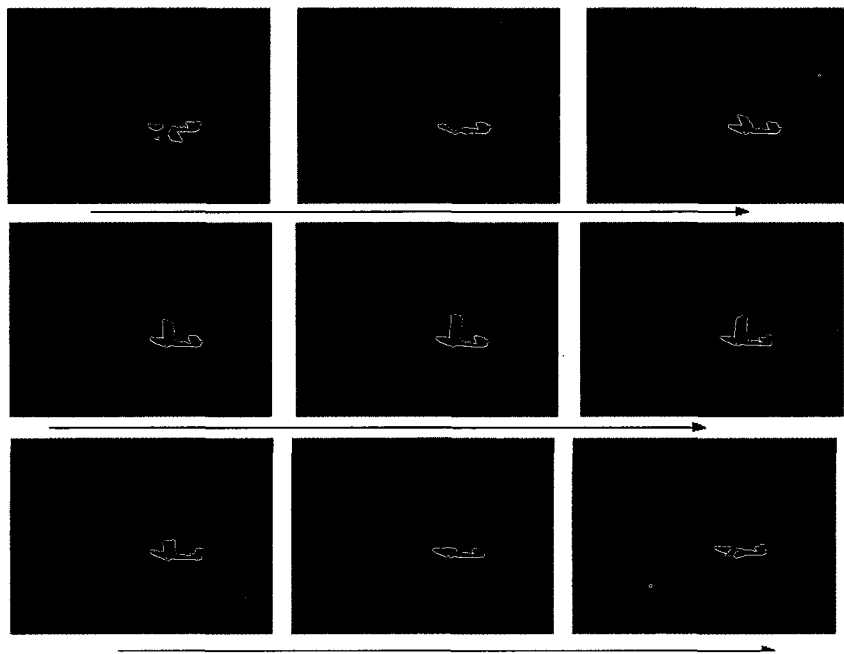


Figure 4.3: Pictures of the ornithopter wing motion during one period. Picture taken by Steve Morris[12]. Videos of the flights are available on YouTube.

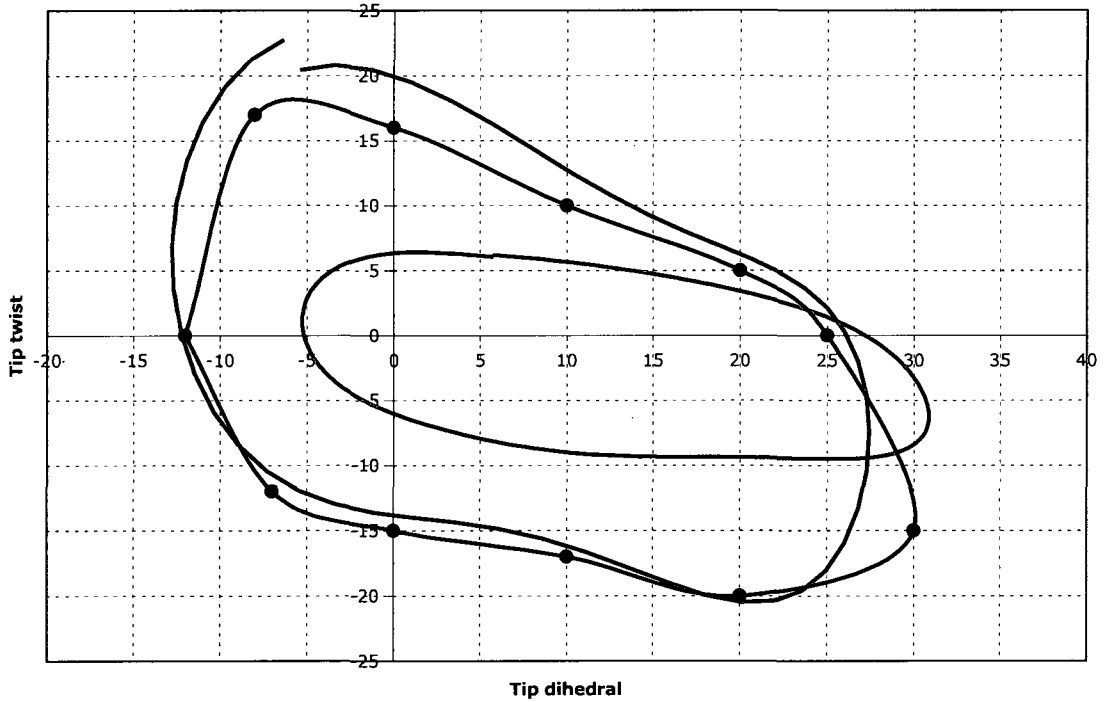


Figure 4.4: Comparison of the computed and observed tip motion for the ornithopter wing. The observed values are plotted in black. The green line corresponds the closest computed motion ($k = 0.29$, $U_\infty = 9.0 \text{ m.s}^{-1}$) within the estimated bounds of flight speed U_∞ and reduced frequency k . The blue line corresponds to the computed motion with $k = 0.45$ and $U_\infty = 12.0 \text{ m.s}^{-1}$, yielding a motion frequency of 5.6 Hz. The computed values are plotted for the third period of the motion. Angular values are given in degrees.

4.5 Aeroelastic model for *Coloborhynchus robustus*

We now detail the approximations used in the aeroelastic model of the pterosaur wing. At each time step, the structural models interacts with the aerodynamic model to update the deformations of the wing subject to the aerodynamic loads. We therefore define the structural model to be compatible with the aerodynamic model.

In this section, we use these estimates to create the inertial and structural model of the pterosaur wing used in the finite-element analysis. We first detail the model for the bones and the soft tissue attached to them. We then detail the model for the wing membrane.

4.5.1 Approximations for the wing bones

We do not have the actual bone geometry or the bone thickness distribution of the fossil bones. We therefore model the bone structural properties using geometric simplifications. As discussed in section 4.5.1, we approximated the bone geometry by considering tubes of constant cross-section and wall thickness, shown in table 4.5. We recall that the dimensions were measured and estimated at the mid-length of the bones. This approximation seems reasonable distal to the wrist. Although the cross-sections of the humerus, radius and ulna vary greatly, we expect that, during the flapping motion, the bone deformations proximal to the wrist are small compared to the deformations for the bones distal to the knuckle. Further studies could use the detailed three-dimensional geometry of the available bones to improve the accuracy of the model.

As discussed in section 4.5.1, the wing bones had elliptical cross-sections, especially

distal to the wrist. It is likely that the long axis of the cross-section was oriented to give the maximum stiffness in the direction of the maximum loads. Because a membrane has very little bending stiffness, the bones would be subject to the tension loads of the membrane. It is therefore likely that the bones were oriented with the long axis aligned with the membrane at its attachment point. We do not know a priori the membrane shape near the bones, and we therefore simplify the bone model by assuming circular cross-sections of the bones. The diameters are taken as the long axis of the elliptic cross-sections, as shown in table 4.5. This assumption adds some stiffness to the bones, but should not significantly change the computed deformations.

Additionally, the wing bones are linked at the joints, which are complex assemblies of connective tissues, such as bones, muscles, ligaments, cartilages, and tendons. Passive dynamic deformations also occur during a joint motion, as discussed by Dyrby and Andriacchi[122] on the motion of the human knee. However, joint dynamics are usually inferred from experimental measurements. Computational models of joints typically require precise solid geometry of the bones and soft tissue. In this study, we do not model the structural deformations of the joints, and assume that the connections between the wing bones at the joints are stiff. Our structural model therefore accounts only for the deformations of the wing bones and membrane. Future studies could develop a simplified model of the flexibility of the joints, and investigate the impact on the flapping gait.

We estimated in section 2.3.2 the weight of the bones and in section 2.3.5 the weight of the soft tissue attached to the bones. Bones provide a much stiffer structure than the muscle attached to it. In this study, we therefore assume that the soft tissue do not carry any loads. However, the mass distribution of soft tissue can have significant inertial effects. We therefore combine the mass of the soft tissue in the

Table 4.5: Dimensions of the bone used in the structural model of the pterosaur wing. To estimate the mass in section 2.3.2, the bones were assumed to be elliptic tubes of uniform cross-section and cortical thickness. In the aeroelastic model, the bone are assumed to be circular tube of uniform diameter and tickness. All dimensions are given in mm. Abbreviations: AP, anterior-posterior ; DV: dorso-ventral.

Bone name	AP length	DV length	Cortical thickness	Chosen diameter	Chosen thickness
Humerus	38	42	1.8	42	1.8
Radius	24	30	0.9	30	0.9
Ulna	10	15	0.9	15	0.9
Metacarpal IV	20	25	0.9	25	0.9
Phalange I	22	35	1.3	35	1.3
Phalange II	15	17	0.8	17	0.8
Phalange III	18	18	0.6	18	0.6
Phalange IV	10	10	0.5	10	0.5

bone elements by adjusting the mass density of the corresponding element.

In all, we model the wing bones and attached soft tissue as a series of three-dimensional beams, with uniform circular cross-sections. In the aerodynamic model, we found that the aerodynamic forces were well described with two spanwise panels per bone. In the aeroelastic model, each bone is therefore divided into two elements. As discussed in section 4.5.1, we model the bones as linear elastic isotropic structures, and the chosen Young's modulus and Poisson's ratio are $E = 30$ GPa and $\nu = 0.3$ respectively.

4.5.2 Approximations for the wing membrane

As detailed in section 2.2.1, the wing membrane is divided into three subregions - the propatagium, the brachiopatagium and the actinopatagium. The actinopatagium is believed to be reinforced by slender structures called actinofibrils. Currently, we lack information on the membrane properties to model the wing membrane structure

accurately. Some required membrane properties include thickness distribution and material properties of the actinofibrils. Bennett[16] inferred that the actinofibrils were likely made of hardened keratin if these were external, or made of collagen if these were internal. Findings by Frey et al.[31] suggests that actinofibrils were internal, and therefore made of collagen. As reported by Bennett[16], the Young's modulus of collagen was measured at $E_{\text{collagen}} = 1300 \text{ MPa}$.

For our structural considerations, we consider that the wing membrane has an uniform thickness. In this study, we consider the propatagium, brachiopatagium, and actinopatagium to have the same properties. In order to study the effect of the membrane properties, we model the membrane as an isotropic structure with a thickness of 1.0 mm, with the material properties defined in the direction of the actinofibrils. We also assume that the mass density is uniform, using the skin density of 1100 kg.m^{-3} reported by Swartz et al.[44]. Although an isotropic membrane model does not address the role of the actinofibrils, the uncertainties in the membrane structure remain too large at this point to investigate this topic.

Frey et al.[31] suggested that the dense layer of actinofibrils was about 0.1 to 0.2 mm. Kellner et al.[123] measured the actinofibrils to be 0.1 mm in diameter, with a density of 4 to 7 fibers per mm, which corresponds to a 40% to 70% fiber density. We assume that the rest of the membrane thickness does not contribute to its structural properties, such that the material properties of the skin is dominated by the properties of the actinofibrils. Considering a 0.1 mm thick layer of collagen fibers with a 40% to 70% fiber density, the composite Young's modulus in the direction of the fibers is between 52 to 91 MPa. Because of the uncertainty in the thickness of the membrane, we assume that the Young's modulus of the pterosaur membrane was 100 MPa.

Table 4.6: Chosen values of material properties for the three membrane models considered for the pterosaur wing.

Membrane model	Stiff model	Pterosaur model	Flexible model
Young's modulus E (MPa)	1000	100	37
Poisson's ratio ν	0.3	0.3	0.3

Because the membrane properties are largely unknown, we consider two other membrane models, referred to as the flexible and stiff membrane models. These models are used to investigate the impact of the membrane stiffness on the flapping gait and propulsive efficiency. In the stiff membrane model, we assume that the layer of actinofibrils accounts for most of the thickness, which results in a Young's modulus of about 1000 MPa. In the flexible membrane model, we consider the properties of bat skin. As reported by Watts et al.[124], bat skin is an anisotropic material. The Young's modulus in the chordwise direction was measured at 37 MPa, and 3 MPa in the spanwise direction. In this study, we choose the chordwise value, which is about three times lower than the pterosaur model and about 30 times lower than the stiff model. In all models, we choose a Poisson's ratio of $\nu = 0.3$, which is typical of isotropic materials.

Table 4.6 summarizes the values used for the wing membrane models. The orientation and density of the actinofibrils varied along the span. Further studies could investigate the impact of such variations on the wing properties and the flapping flight performance.

4.6 Verification of the membrane model in the finite-element analysis

The approximations defined above are used to build the structural model of the pterosaur wing in the finite-element analysis (FEA) code ANSYS[125]. As discussed in section 4.2.3, we assume that pterosaurs would have controlled their wings such that the structural behaviour remains linear during the wing motion. The structural deformations are computed from the modal decomposition, which is computed for the wing subject to gliding flight loads.

In this section, we first specify the details of the FEA model. We then compare the results using these numerical choices with analytical results for a two-dimensional membrane and a circular membrane ring subject to uniform pressure.

4.6.1 Details of the FEA model for the pterosaur wing

The pterosaur wing model is built in the FEA code ANSYS[125]. The bones are represent as linear beam elements (BEAM 4) and the membrane elements are represented using triangular shell elements (SHELL 181). The element SHELL 181 has the option to be represented as pure membrane elements or as shell elements with bending properties. As discussed by Heppel[101], it is key to allow a sufficient kinematic freedom in the membrane, and for this purpose, it is recommended to model the membrane using 6-node triangular membrane elements. The nodes in the FEA model were located at the corner panels of the aerodynamic code UVLM. As discussed in section 3.3.6, we find that the aerodynamic forces of the pterosaur wing are well described with 20 panels chordwise and 14 panels spanwise, for a total of 280 panels. Ideally, the wing would have to be described with in the order of several thousand

membrane elements. However, the aerodynamic panels in UVLM are flat between the corner points, so the additional number of nodes would not significantly change the solution.

Figure 4.5 illustrates the triangular mesh used. We observe that the mesh is quite coarse and that the element shapes are quite elongated near the leading-edge and trailing-edge. This mesh resolution leads to numerical difficulties with the membrane formulation, and we have to switch to the shell element formulation instead. By adding the bending stiffness to the element, we artificially increase the stiffness of the structure which helps with the convergence of the structure. We show in sections 4.6.2 and 4.6.3, that the results using this formulation compare very well with analytical results. Future studies using higher-fidelity methods would require an order of magnitude more elements compared to this study, both for the aerodynamic and structural meshes.

As discussed in section 4.5.1, the bone density was modified at each element to include the inertial properties of the muscles. The inertial properties computed by ANSYS compare well with our estimates shown in table 4.7. The element SHELL 181 also computes the stress distribution over the thickness, and the results did not converge for the chosen wing membrane thickness of 1 mm. This numerical issue was solved by increasing the thickness ten-fold to 10 mm, and reducing the Young's modulus and density proportionally. We show in sections 4.6.2 and 4.6.3 that the results computed for a thickness of 10 mm compare very well with analytical results for a thickness of 1mm.

We defined the planar wing geometry as reference, and place the initial nodal positions in the FEA model accordingly. As a result, the wing membrane is laid flat and is attached to the bones in the glide position. We do not know a priori what

the membrane shape was at rest, and whether the membrane was pre-stressed in this position. We assume that the wing membrane is not subject to stresses in the initial configuration. In section 4.7.1, we discuss the impact of moving the joints to tension the wing membrane. The wing is then subject to the gliding flight pressure loads. In order to apply the actual pressure distribution, the FEA code would need to be coupled to the aerodynamic code directly in order to solve for the pressure distribution and the wing shape. In this study, we instead apply a uniform pressure load corresponding to the wing loading, which is the animal weight divided by its wing area. For a 160 N specimen, the wing loading amounts to 120 Pa.

As discussed in section 4.2.2, solving for the membrane shape is a non-linear problem because of the combined geometric and direct stiffnesses. ANSYS provides several options to solve for the displacements. The solver used for large displacements accounts for the non-linear effects and is recommended for membrane models. By including the displacements and the stresses of the wing under the pressure loads, the modal decomposition accounts for the linear behavior of the tensioned wing membrane. By not accounting for these stresses, the modal decomposition yields modes of very small frequencies corresponding to the kinematic degrees of freedom of the slack membrane.

As mentioned previously, we modify several parameters to help with convergence of the finite-element analysis. We add shell bending stiffness to the membrane formulation, and increase the desired thickness from 1 mm to 10 mm. We compare the computed deflections of the membrane with analytical results for a two-dimensional membrane and for a circular membrane.

Table 4.7: Estimates for the total mass and position of the center of gravity about the root axis x for one wing. The masses are expressed in kg, distances in m.

	Mass	x_{CG}	y_{CG}
Our estimates	3.66	0.017	0.61
FEA model	3.84	0.021	0.80

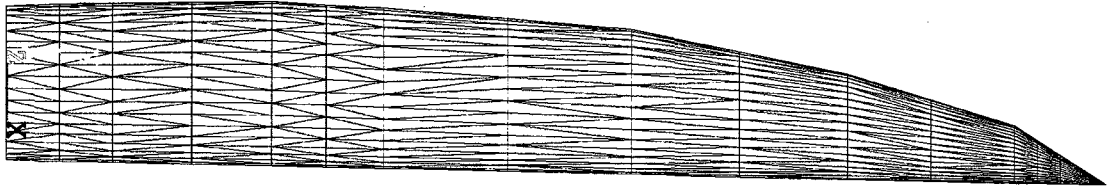


Figure 4.5: Structural mesh of the pterosaur wing based on the nodal positions specified by the aerodynamic code UVLM.

4.6.2 Deflections of two-dimensional membrane subject to uniform pressure

Analytical results have been described by Song et al.[126] for a two-dimensional membrane subject to uniform pressure loads. The membrane is constrained in displacements but is free to rotate at the leading and trailing edge, and is laid flat before the pressure is applied. In this case, the vertical deflections z are described by a parabola of the form

$$z = z_{\max} 4x(1 - x) \quad (4.22)$$

with c the membrane chord, z_{\max} the maximum deflection, and x the chordwise position such that $x \in [0.0; 1.0]$. In the static equilibrium, we assume a uniform

tension F_T in the membrane related to the applied pressure difference Δp given by

$$2F_T \sin(\beta_{\text{contact}}) = c\Delta p \quad (4.23)$$

with β_{contact} the contact angle at the leading-edge and trailing-edge. We note that the contact angles β_{contact} at the leading-edge and trailing-edge are equal because of the symmetry of the problem. Because the vertical deflections are described by a parabola, the contact angle β_{contact} is given by

$$\beta_{\text{contact}} = z'(0) = z'(1) = 4z_{\text{max}} \quad (4.24)$$

The membrane tension is also related to the elongation of the membrane Δc , which is the difference between the arc length of the parabola and the unit chord length. We consider the case of a linearly elastic membrane, so the tension F_T is given by

$$F_T = F_{T0} + Eh \frac{\Delta c}{c} \quad (4.25)$$

with F_{T0} the initial pretension applied to the membrane, E the Young's modulus, h the membrane thickness. The Weber number We is the dimensionless aerodynamic loading parameter defined by

$$We = \frac{c\Delta p}{Eh}. \quad (4.26)$$

By combining equations 4.23, 4.25 and 4.26, we can express the Weber number as a function of the initial membrane strain ϵ_0 , the membrane elongation Δc and the contact angle β_{contact} by

$$We = 2 \left[\epsilon_0 + \frac{\Delta c}{c} \right] \sin(\beta_{\text{contact}}). \quad (4.27)$$

Table 4.8: Membrane deflections, Weber numbers and pressure differences for three values of Young's modulus. In these cases, the membrane is not subject to pre-strain ($\epsilon_0 = 0.0$). The maximum deflections $\frac{z_{\max}}{c}$ are chosen such that the pressure difference Δp is in the 100-200 Pa range.

E (MPa)	$\frac{z_{\max}}{c}$	We ($\times 10^{-4}$)	Δp (Pa)
37	0.020	45.27	167.5
100	0.040	13.55	135.5
1000	0.060	1.70	170.4

The membrane elongation Δc and the contact angle β_{contact} are related to the maximum deflection z_{\max} . The membrane shape depends only on the Weber number and initial strain. We plot in figure 4.6 the normalized maximum deflection $\frac{z_{\max}}{c}$ as a function of the Weber number for several value of prestrain ϵ_0 . We observe that the deflections have a linear dependance to high values of the Weber number and hence the pressure loads, even without pre-strain $\epsilon_0 = 0$. With sufficient prestrain, a linearly elastic membrane could therefore be approximated with a linear behavior in the vicinity of a loaded condition.

In this comparison, we compute the deflections of a membrane with initial strains of $\epsilon_0 = 0\%$ and $\epsilon_0 = 5\%$, under the pressure difference Δp corresponding to a set of normalized maximum deflection $\frac{z_{\max}}{c}$, shown in tables 4.8 and 4.9. Because we study several material properties for the wing membrane of pterosaurs, we compare the results for three values of Young's modulus. In the case of zero initial strain, we choose values of $\frac{z_{\max}}{c}$ that yield pressure differences Δp in the range of 100-200 Pa. In the case with an initial strain $\epsilon_0 = 5\%$, we choose the pressure differences Δp that yield a maximum deflection of $\frac{z_{\max}}{c} = 0.010$.

Using the finite-element analysis, we model the two-dimensional membrane with a three-dimensional rectangular membrane. The rectangular membrane has a unit length chord (1 m) and a span of 10m, which yields an aspect ratio of 10. We compare

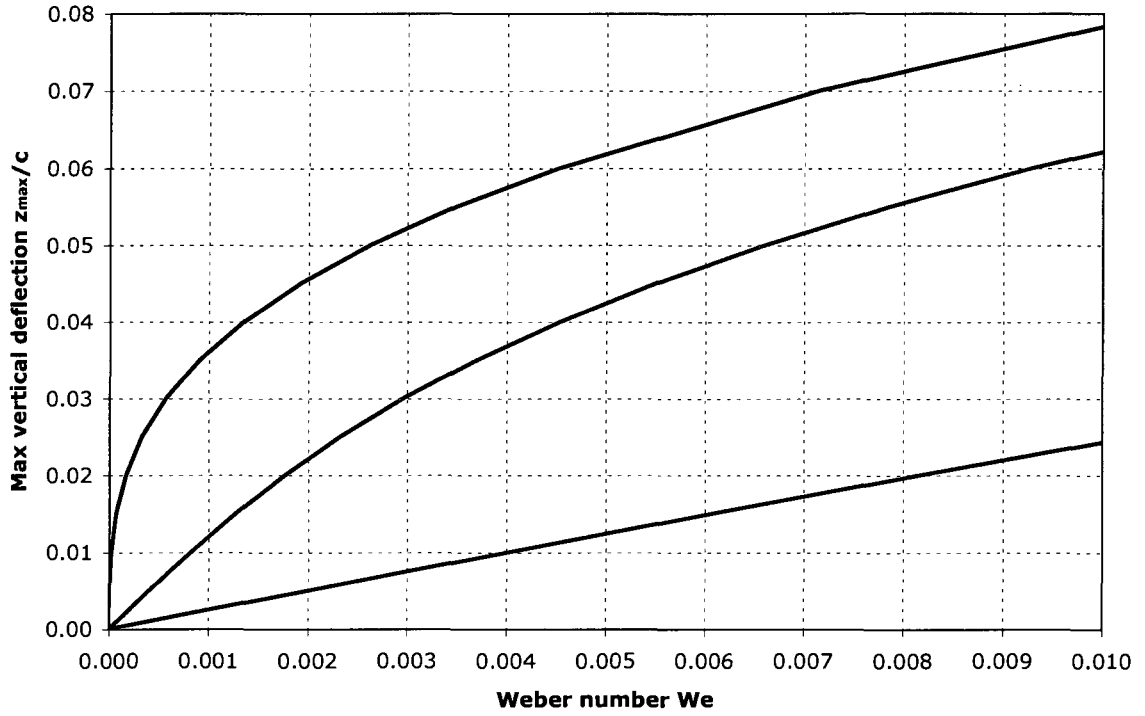


Figure 4.6: Normalized vertical displacements $\frac{z_{\max}}{c}$ of a two-dimensional membrane as a function of pressure loads in the form of the dimensionless Weber number We for four values of pre-strain ϵ_0 . The membrane is assumed of uniform thickness and with linear elastic material properties. The pressure loads are applied uniformly. The case for values of pre-strain $\epsilon_0 = 0\%$, $\epsilon_0 = 1\%$, $\epsilon_0 = 5\%$ are plotted respectively in blue, green and red lines.

Table 4.9: Membrane deflections, Weber numbers and pressure differences for three values of Young's modulus. In these cases, the membrane is subject to a pre-strain of $\epsilon_0 = 0.05$. The maximum deflections $\frac{z_{\max}}{c}$ are set at $\frac{z_{\max}}{c} = 0.010$ and the pressure difference Δp are computed accordingly from the Weber number We .

E (MPa)	$\frac{z_{\max}}{c}$	$We (\times 10^{-4})$	Δp (Pa)
37	0.010	40.20	148.8
100	0.010	40.20	402.0
1000	0.010	40.20	4020.3

Table 4.10: Computed maximum membrane deflections for three values of Young's modulus. In these cases, the membrane is not subject to pre-strain ($\epsilon_0 = 0.0$). The maximum deflections $\frac{z_{\max}}{c}$ are computed from the analytical results and the finite-element analysis (FEA).

E (MPa)	$\frac{z_{\max}}{c}$ Analytic	$\frac{z_{\max}}{c}$ FEA	Relative difference (%)
37	0.0200	0.0193	3.4
100	0.0400	0.0391	2.3
1000	0.0600	0.0587	2.1

Table 4.11: Computed maximum membrane deflections for three values of Young's modulus. In these cases, the membrane is subject to a pre-strain of $\epsilon_0 = 5\%$. The maximum deflections $\frac{z_{\max}}{c}$ are computed from the analytical results and the finite-element analysis (FEA).

E (MPa)	$\frac{z_{\max}}{c}$ Analytic	$\frac{z_{\max}}{c}$ FEA	Relative difference (%)
37	0.0100	0.0100	0.2
100	0.0100	0.0097	2.5
1000	0.0100	0.0100	0.2

the deflections computed at mid-span with the analytical results. By choosing the mid-span deflections, we eliminate the three-dimensional effects due to the border of the membrane. Because we want to compare the computed results for a relatively coarse grid, the rectangular membrane is paneled with 350 triangular elements. With this mesh, the chord is modeled by eight elements.

Tables 4.10 and 4.11 compare the value of maximum deflection between the finite-element analysis and the analytical results for different values of the Weber number We and initial strain ϵ_0 . In figure 4.7, we show the vertical deflections z in the chordwise direction at mid-span for the latter case. Although the mesh has only eight elements in the chordwise direction, we find that the computed results are within 4% of the analytical results, which is of the order of accuracy of the aerodynamic model.

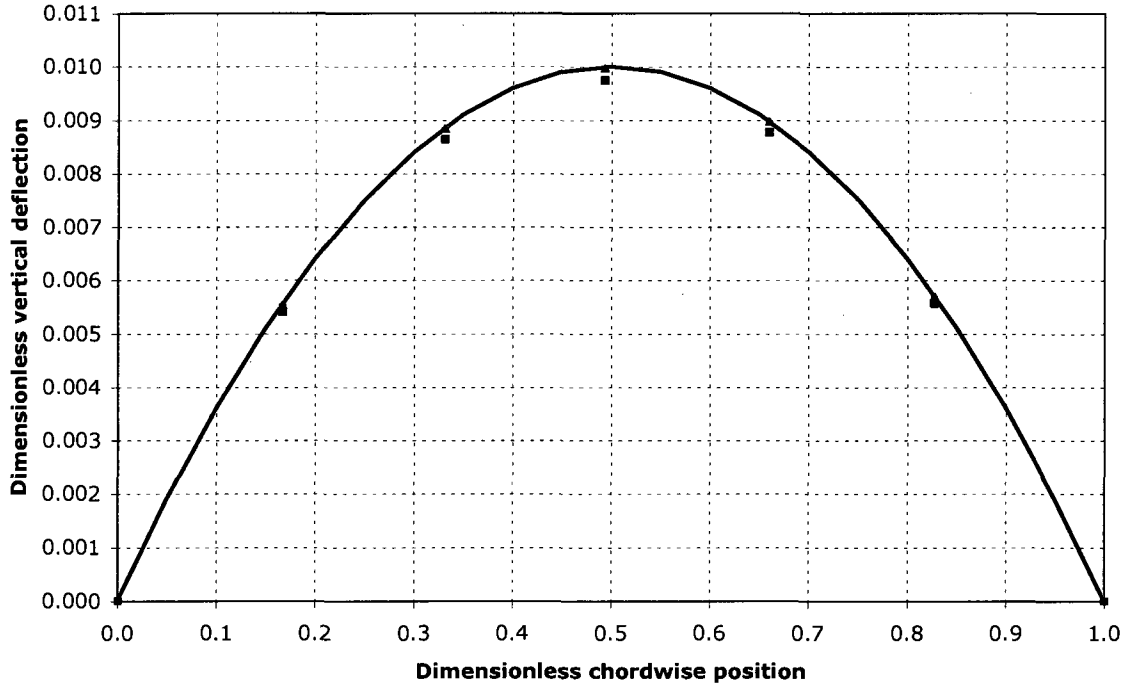


Figure 4.7: Normalized vertical displacements $\frac{z_{\max}}{c}$ as a function of chordwise position $\frac{x}{c}$ of a two-dimensional membrane for different cases of Young's modulus E with pre-strain $\epsilon_0 = 5\%$. The applied pressure is scaled with the Young's modulus to yield the same vertical displacements. The membrane is assumed of uniform thickness and with linear elastic material properties. The pressure loads are applied uniformly. The blue line represents the analytical results. The black crosses, squares and triangles represent the nodal displacements of the FEA model for the case of $E=37$ MPa, 100 MPa, 1000 MPa respectively as described in table 4.9.

4.6.3 Deflections of circular membrane subject to uniform pressure

The case of a circular membrane subject to a uniform vertical loading is known as Hencky's problem[127]. Consider a circular membrane of unit radius $R = 1$. Hencky[127] derived the stresses in the membrane as a power series, and derived a similar series for the vertical deflection z , given by

$$z(r) = q^{\frac{1}{3}} \sum_{n=0}^{\infty} a_{2n} (1 - r^{2n+2}) \quad (4.28)$$

with r the radial position such that $r \in [0.0; 1.0]$, and a_{2n} the power series coefficients. q is the dimensionless pressure given by

$$q = \frac{\Delta p R}{Eh} \quad (4.29)$$

The power series coefficients depend only on the Poisson's ratio ν and are independent of the applied loading. Fichter[128] rederived the power series to add several coefficients, and we list the first five coefficients for reference, given by

$$\begin{aligned} a_0 &= \frac{1}{b_0} \\ a_2 &= \frac{1}{2b_0^4} \\ a_4 &= \frac{5}{9b_0^7} \\ a_6 &= \frac{55}{72b_0^{10}} \\ a_8 &= \frac{7}{6b_0^{13}} \end{aligned}$$

with b_0 the first coefficient of the power series for the stresses, which was estimated at $b_0 = 1.7244$ for $\nu = 0.3$.

Fichter[128] also derived the power series solution for the uniform pressure loading case, for which the coefficients need to be solved iteratively. However, the deflections were shown to be the same in both cases for small values of dimensionless pressure $q < 0.010$. We therefore compare the analytical results for the deflections for Hencky's problem with the deflections computed by the FEA for the uniform pressure loading case, for two cases of dimensionless pressure q . Similarly to the two-dimensional case, we compute the deflections for three cases of Young's modulus considering a Poisson's ratio $\nu = 0.3$, which is typical of isotropic materials. Table 4.12 summarizes the cases of comparison.

In the finite-element analysis, we model the circular membrane with a radius of 1m. Similarly to the two-dimensional case, we want to compare the computed results for a relatively coarse grid, the membrane is paneled with 90 triangular elements. With this mesh, the diameter of the membrane is modeled by eleven elements. The pressure is applied uniformly on each element. In table 4.13, we compare the deflections computed from the FEA and the analytical results at the center of the ring. The FEA results are within 2% of the analytical results. In both cases for the two-dimensional and circular membrane, the FEA results compare within at most 3.4% to the analytical results. We therefore assume that our modeling choices in the finite-element analysis yield similar results to the membrane problem, with comparable accuracy to the aerodynamic method.

Table 4.12: Pressure differences (in Pa) for three values of Young's modulus. The values of dimensionless pressure q of $q = 0.001$ and $q = 0.010$ are chosen such that the deflections under the uniform pressure loading case are the same as under the uniform lateral loading case.

E (MPa)	$q = 0.001$	$q = 0.010$
37	37	370
100	100	1000
1000	1000	10000

Table 4.13: Dimensionless vertical deflections computed using Hencky's solution and the finite-element analysis (FEA) for three values of Young's modulus. The deflections are computed at the center of the circular ring. The values of dimensionless pressure q of $q = 0.001$ and $q = 0.010$ are chosen such that the deflections under the uniform pressure loading case are the same as under the uniform lateral loading case.

	$q = 0.001$	$q = 0.010$
Analytic solution	0.0653	0.1407
37	0.0638	0.1407
100	0.0638	0.1407
1000	0.0638	0.1407
Relative difference (%)	2.3	0.1

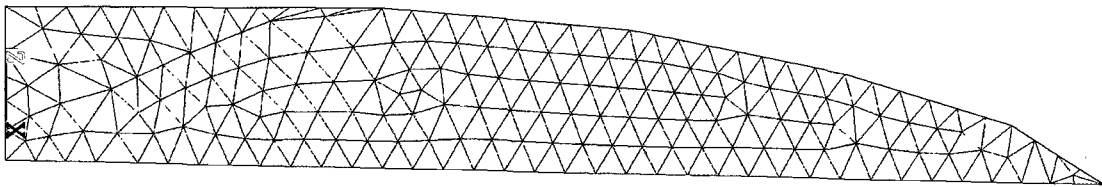
4.6.4 Comparison with automated grid

In section 4.6.1, we discussed how a structural mesh based on the aerodynamic grid, which we refer to as UVLM mesh, might be too coarse for this study. In order to quantify the errors, we compare the computed results with the grid based on UVLM with a mesh generated automatically by ANSYS using the same elements. The ANSYS mesh is chosen to be relatively coarse with 320 elements, in order to show only the effects of the element shape. From the mesh shown in figure 4.8, we note that the triangular elements of the ANSYS mesh are closer to equilateral triangles, whereas the elements in the UVLM mesh are quite narrow especially near the leading-edge and trailing-edge. We also notice that the non-linear solver requires more iterations to solve the UVLM mesh, and this is mainly due to the narrow elements.

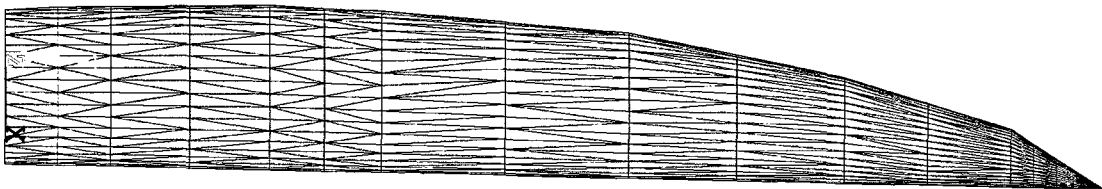
We compare in table 4.14 the maximum deflections at the trailing edge for the membrane subject to a uniform pressure of 10 Pa, for the three membrane models. We find that the deflections found with the UVLM mesh are between 4.6% and 9.6% lower than for the ANSYS mesh. This indicates that the current UVLM mesh slightly overestimates the overall stiffness of the membrane, and that this problem could be solved by adding panels in the spanwise direction. We note that these comparisons were made for the wing without pre-tensioning. In the case of pre-tensioning, these difference are expected to be reduced. A mapping technique between the structural mesh and the fluid grid would be needed to transfer the aerodynamic loads and structural displacements between the ANSYS mesh and the UVLM grid. However we do not currently have such technique in our possession. In this study we therefore use the UVLM mesh.

Table 4.14: Maximum deflections (in m) of the membrane under a uniform load of 10 Pa. The maximum deflection occurs on the trailing edge near the mid-span. The comparison is done for the three membrane models.

	Stiff membrane	Pterosaur membrane	Flexible membrane
ANSYS mesh	0.0384	0.0165	0.00173
UVLM mesh	0.0347	0.0154	0.00165
Relative difference (%)	9.64	6.67	4.62



(a) Structural mesh of the pterosaur wing generated automatically by ANSYS.



(b) Structural mesh of the pterosaur wing based on the nodal positions specified by the aerodynamic code UVLM.

Figure 4.8: Comparison of the structural mesh generated by ANSYS with the mesh created manually based on the grid of the aerodynamic code UVLM.

4.7 Aeroelastic deformations of the pterosaur wing

As discussed in section 4.2.3, we assume that pterosaurs would have controlled their wings such that the structural behaviour remains linear during the wing motion. We compute the modal decomposition for the wing subject to gliding flight loads, using the structural model of the pterosaur wing described above. The structural deformations are then computed from this reduced-order model at every time step of the wing motion. We refer to the combination of the propatagium, tenopatagium and actinopatagium as the wing membrane.

In this section, we discuss the impact of the tensioning. We then describe the computed modal decomposition, then compare the wing shape and aerodynamic forces for the wing in a steady angle of attack. We also compare the variation of lift and thrust for a given wing motion. The wing motion parameters correspond to the optimal flapping gait found for the rigid wing model considering shoulder dihedral, shoulder sweep and wrist pitch motions. This corresponds to the motion case J2 as defined in section 5.5.1. These comparison aim mainly at showing that the computed results follow the expected trends and at fine-tuning the parameters of the aeroelastic model. This step is essential before applying this model to solve the optimization problem.

Because the material properties of the membrane are unknown, we study the three membrane models described in section 4.5.2, with material properties shown in table 4.15. Finally, we discuss the effects on the modal decomposition of tensioning the membrane.

Table 4.15: Chosen values of material properties for the three membrane models considered in this study.

Membrane model	Stiff membrane	Pterosaur approximation	Flexible membrane
Young's modulus E (MPa)	1000	100	37
Poisson's ratio ν	0.3	0.3	0.3

4.7.1 Membrane tensioning from the joint motions

In section 4.6.2, we described the two-dimensional problem of a membrane attached at the leading-edge and trailing-edge subject to a uniform pressure. The maximum deflections can be significantly higher for a membrane without pre-tension than with some pre-tension. In section 4.7.2, we discuss how the vertical deflections of the trailing edge of the pterosaur wing lead to a loss in lift production. To reduce these losses, we apply tension to the membrane before applying the pressure loads. Pterosaur wing membranes were believed to be actively controlled by a layer of muscle and by the motion of the joints, and each could have been used to actively tension the membrane. In this study, we investigate only the effects of the active joint motions on the membrane tension. We do not account neither for the role of the pteroid in tensioning the propatagium, nor the role of the legs in tensioning the tenopatagium.

We operate small angular changes relative to the glide position in the active wing joints. Because we study the aeroelasticity of the planar wing, we only consider the joint motions in the plane of the geometry, which are the sweep angles ψ_i at each joint of index i . Future studies on the curved wing geometry could also investigate the effects of dihedral and pitch angles, noted ϕ_i and θ_i . We first study the stress distributions due to a one degree change in sweep at each joint. We recall that the sweep angles of the active joints are noted $\psi_1, \psi_2, \psi_3, \psi_4$ corresponding to the shoulder, elbow, wrist and knuckle respectively. We also recall that a positive change

in sweep angle leads to a forward motion relative to the joint axis. From the stress distribution computed in each case, we then choose a combination of sweep angle variations that creates tension in most parts of the wing.

Impact of separate changes relative to glide position

Figure 4.9 shows the stress patterns in the wing for each sweep change. The stress patterns shown are independent of the Young's modulus of the membrane material. The values shown correspond to the flexible membrane model, and scale accordingly with the value of Young's modulus.

We observe that shoulder sweep affects only the area between the elbow and the root, with compression occurring in front of the shoulder, and tension aft of the shoulder. The rest of the wing is relatively unaffected. Similarly, elbow sweep mostly affects the area between the elbow and the root, with same trends as for shoulder sweep.

Wrist sweep affects a larger area. The compression occurs mostly near the leading-edge of the wrist where membrane lies ahead of the fourth metacarpal. Tension occurs in the area behind the humerus from the root to the elbow.

Knuckle sweep affects mostly the outer part of the wing. Compression stresses occur near the leading-edge of the bones. Tension stresses occur on the trailing edge of most part of the wing. This motion is therefore quite effective in stretching the outer part of the wing.

Because the membrane is attached to the bones, we did not find a motion that would stretch the membrane close to the bones. It was believed that pterosaurs had other tissues along the bones, creating a streamlined transition between the bone thickness and the thin membrane. It is likely that these tissues would have created a

more rigid part of the wing, and therefore would have not resisted such compression loads.

Combined changes relative to glide position

It is likely that pterosaurs would have moved their wings to tension all parts of the wing. However such motion is hard to infer. Because of the presence of the actinofibrils, pterosaurs wings were highly anisotropical and changes in the joint positions would induce uneven stress distributions. In this study, we consider an isotropic membrane, we therefore seek to apply a uniform stress distribution. The tension applied in the y -direction has the most impact on the membrane shape in flight, because it modifies the vertical deflections of the trailing edge. For this reason, we assume that there is a combination of joint motions that yield uniform strains in the y -direction. In practice, we impose a uniform gradient of displacements of the bone elements in the y -direction. A combination of sweep changes of one degree at each joint yields a change of the span of about 0.020 m. We choose this value as the total displacement at the tip, and compute the imposed displacements at each joint proportional to its spanwise position, as shown in table 4.16.

Figure 4.10 shows the stress patterns for these displacements. We observe that all of the membrane is in tension in the y -direction, and that compression loads in the x -direction are of lesser magnitude. The membrane can therefore be considered to be stretched.

We now compare the values of stresses for each membrane model for the same displacements. In the stiff membrane model, we note that the chosen displacements lead to significant stresses, up to +1.06 MPa. In this case, the stresses due to bone tensioning are much higher than those from the glide pressure loads. The tensioning



(a) Stress distribution in the x -direction for a sweep angle change at the shoulder $\psi_1 = +1$ degrees. The values of stresses range from -8.0 kPa to +18.1 kPa.



(b) Stress distribution in the y -direction for a sweep angle change at the shoulder $\psi_1 = +1$ degrees. The values of stresses range from -35.9 kPa to +68.8 kPa.



(c) Stress distribution in the x -direction for a sweep angle change at the elbow $\psi_2 = +1$ degrees. The values of stresses range from -6.8 kPa to +5.8 kPa.



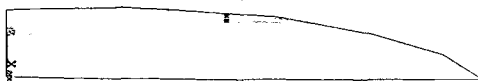
(d) Stress distribution in the y -direction for a sweep angle change at the elbow $\psi_2 = +1$ degrees. The values of stresses range from -28.5 kPa to +22.1 kPa.



(e) Stress distribution in the x -direction for a sweep angle change at the wrist $\psi_3 = +1$ degrees. The values of stresses range from -6.2 kPa to +13.5 kPa.



(f) Stress distribution in the y -direction for a sweep angle change at the wrist $\psi_3 = +1$ degrees. The values of stresses range from -20.8 kPa to +52.8 kPa.



(g) Stress distribution in the x -direction for a sweep angle change at the knuckle $\psi_4 = +1$ degrees. The values of stresses range from -2.8 kPa to +3.2 kPa.



(h) Stress distribution in the y -direction for a sweep angle change at the knuckle $\psi_4 = +1$ degrees. The values of stresses range from -7.6 kPa to +14.6 kPa.

Figure 4.9: Stress distributions of the wing membrane in the x -direction (left column) and in the y -direction (right column) for different displacements of the joints and for a uniform gradient of lateral displacements. The values of stresses correspond to the flexible membrane model ($E = 37$ MPa). In each case, we specify the range of the stress values. The dark blue color refers to the lowest value and the red color to the highest value.

due to the glide pressure loads therefore has no visible effect on the modal decomposition. In the flexible membrane model, the stresses due to the pressure loads and pre-tensioning are of the same order of magnitude. The magnitude of desired pre-tensioning is unknown at this stage, and in this study the tensioning is applied by imposing the same lateral displacements in all membrane models.

During the flapping motion, we assume that the joint angles change such that the membrane tension remains approximatively constant, leading to a linear behavior with the aerodynamic loads. Because we assume a linear structural behavior about the glide geometry, we cannot study the effects of joint motions on the membrane stresses during the flapping wing motion. Future studies could optimize the wing motion accounting for the membrane tensioning effects. This would require the complete non-linear membrane problem to be solved at each iteration using methods as described in section 4.2.2. For the optimal stress distribution and the related motions of the joints, it would also be of interest to study the amount of energy required to maintain these stress levels and whether these would be compatible with inferred musculature.

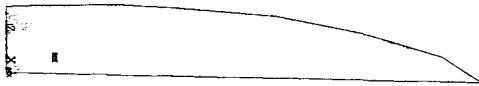
Because we don't know the shape of the wing with no initial stresses, we assume that the desired levels of tensioning are acquired in the gliding position. By making this assumption, we use the modal decomposition of the wing with the wing geometry defined for gliding flight in the aerodynamic study.

4.7.2 Modal decomposition of the tensioned wing

The modal decomposition includes the effects of the wing deformation and stress distribution due to the pressure loads and pre-tensioning. It seems unlikely that very high frequencies have a strong impact on the flapping flight of pterosaurs. We therefore limit the decomposition to the first twenty modes of the structure or to the

Table 4.16: Imposed lateral displacements (in mm) imposed at the joints. These displacements aim at applying uniform tension in the y -direction. The total displacements at the tip are chosen to be 20 mm.

Joint name	Spanwise position $\frac{y}{b_{\text{ref}}}$	Lateral displacements
Shoulder	0.00	0
Elbow	0.10	2
Wrist	0.24	5
Knuckle	0.34	7
PhI-II	0.57	11
PhII-III	0.76	15
PhIII-IV	0.91	18
Tip	1.00	20



(a) Stress distribution in the x -direction for a uniform gradient of lateral displacements. The values of stresses range from -3.1 kPa to 10.6 kPa.



(b) Stress distribution in the y -direction for a uniform gradient of lateral displacements. The values of stresses range from +21.7 kPa to +38.9 kPa.

Figure 4.10: Stress distributions of the wing membrane in the x -direction (left column) and in the y -direction (right column) for a uniform gradient of lateral displacements. The values of stresses correspond to the flexible membrane model ($E = 37$ MPa). The dark blue color refers to the lowest value and the red color to the highest value.

Table 4.17: Frequencies (in Hz) of the first five modes computed for the pterosaur wing with three membrane models.

	Stiff membrane	Pterosaur approximation	Flexible membrane
Young's modulus E (MPa)	1000	100	37
first mode	27.04	8.60	5.41
second mode	47.89	15.18	9.38
third mode	70.61	22.37	13.74
fourth mode	94.62	29.97	18.37
fifth mode	99.19	31.43	19.35

modes with frequency within 50 times the motion frequency. For the optimal wing motion of reference defined in section 4.7.2, the motion frequency is 1.9 Hz, so the upper frequency bound is 100 Hz.

The wing deformations are dominated by the membranes modes. For comparison, we computed the modal decomposition of the bones without the membrane. The first mode for the bone structure is found at 200 Hz compared to 5-22 Hz found with the membrane. However we expected some interaction with the bone structure in the higher modes, similarly to sail-mast interactions in sailing boats. This might indicate that the bone thickness estimates could be too conservative, or that the flexibility of the joints also needs to be modeled. Further studies could refine the model for the wing bones and add a model for the flexibility of the joints.

Sensitivity to Young's modulus

As we decrease the Young's modulus of the membrane, we observe that the frequencies shift to lower frequencies. Table 4.17 shows the variation of the first five frequencies with the Young's modulus.

Membrane deflections in glide loads

Having computed the modal decomposition of the pterosaur wing, we now compare the deflections and lift coefficient in the steady glide conditions, with the wing set at a constant angle of attack of $\bar{\theta} = 7.0$ degrees. In figure 4.11, we compare the vertical deflections of the trailing edge for the three membrane models. We note that the trailing edge is at $z = 0$ for the rigid wing of the aerodynamic model.

We observe that the trailing edge deflects more as the Young's modulus decreases. These deflections effectively reduce the local incidence relative to the local surface of the wing and therefore lead to a loss in lift. As shown in table 4.18, the steady-state values of lift coefficient decreases significantly with the Young's modulus. For the flexible membrane model, the steady-state lift amounts to 52% of the value for the rigid wing. This indicates that the flexibility of the membrane requires an increase in the angle of attack or an increase in the membrane tension to reduce the trailing edge deflections. We note that even for the stiff membrane model with pretension, the trailing edge deflections lead to a 6% reduction in lift. More importantly, the spanwise lift distribution is far from the ideal elliptical distribution because of the significant membrane deflections at mid-span. It is likely that the aerodynamic performance could be significantly improved by optimizing the glide position of the joints. For the preliminary study of the membrane flexibility, we do not currently optimize the glide position of the joints, but this would be an interesting problem for future studies.

Flapping motion

We now compare the performance of the membrane models in flapping flight for a given wing motion. We choose the optimal flapping gait found in section 5.5.1 for the joint motion J2, which combines shoulder flapping and sweeping and wrist pitching.

Table 4.18: Maximum trailing edge deflections z_{\max} and lift coefficients $\overline{C_L}$ in gliding flight at at set angle of attack $\overline{\theta} = 7.0$ degrees. The results are computed for the pterosaur wing with three membrane models, and with the rigid wing defined of the aerodynamic model.

	Rigid wing	Stiff membrane	Pterosaur membrane	Flexible membrane
Young's modulus E (MPa)	∞	1000	100	37
z_{\max} (mm)	0.0	2.7	14.4	20.6
$\overline{C_L}$	0.679	0.639	0.456	0.352

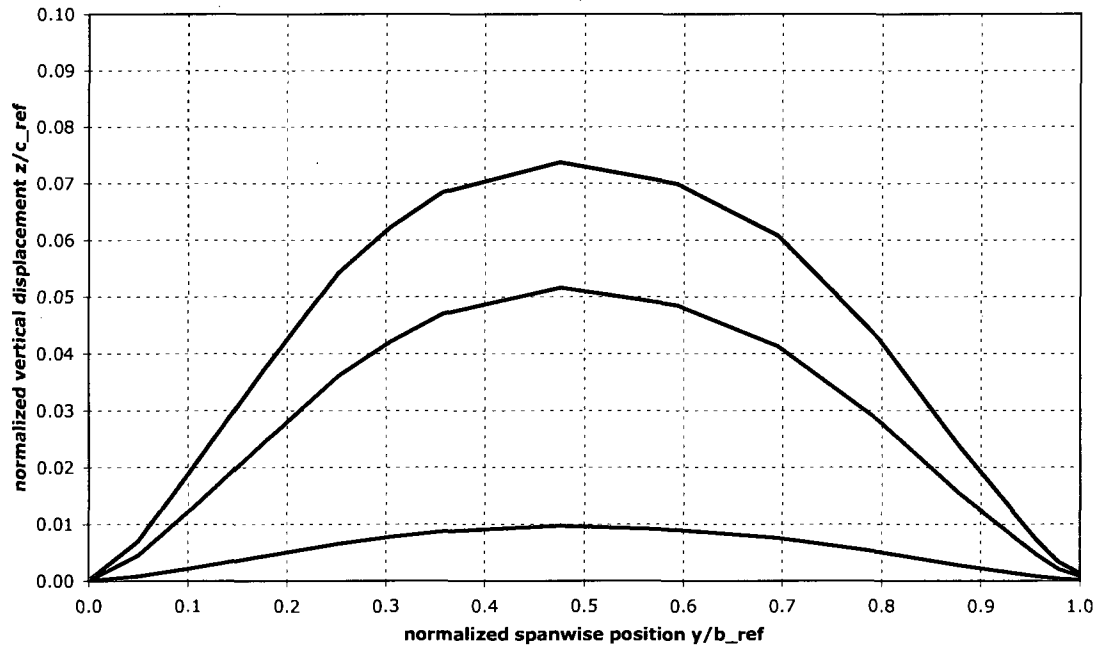


Figure 4.11: Comparison of the trailing-edge deflections in steady gliding flight for the three cases of membrane model. The vertical deflection normalized by the average chord $\frac{z}{c}$ is plotted against the spanwise position normalized by the semi span $\frac{y}{b_{\text{ref}}}$. The deflections for the stiff membrane ($E = 1000$ MPa), the pterosaur approximation ($E = 100$ MPa) and for the flexible membrane ($E = 37$ MPa) are plotted in red, green and blue respectively. The wing is held at a steady angle attack $\overline{\theta}_0 = 7$ degrees.

Table 4.19: Motion parameters for the optimized flapping gait for motion J2, which includes motions of shoulder flapping ϕ_1 , sweeping ψ_1 and wrist pitching θ_3 . All angles are expressed in degrees.

ϕ_1	14.16	U_∞ (m.s ⁻¹)	16.8
ψ_1	2.99	k	0.102
θ_3	8.44	$\bar{\theta}$	7.52
φ_{ψ_1}	210.44	f (Hz)	1.94
φ_{θ_3}	79.95		

The parameters of this motion are listed in table 4.19. Regarding the parameters of the fluid-structure interaction model, we have found that the structural deformations are identical when more than five modes are included, and that the solution converged during the second period of the motion with one hundred time steps per period. These parameters are used also in the optimization procedure.

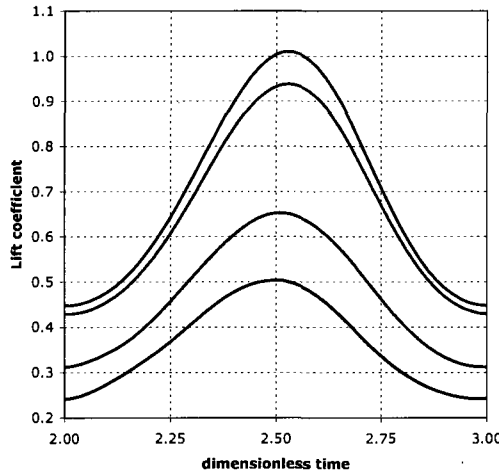
The same trends are seen for flapping flight as for gliding flight, as shown in table 4.20 and figure 4.12. Because of the reduced wing stiffness, the trailing edge deflects under the aerodynamic loads, which leads to losses in lift. The level of thrust produced also depends on the magnitude of the lift forces and hence is negatively affected by the flexibility. These results indicate that the flexibility of the wing negatively impacts the flapping performance of the wing. However, this motion does not correspond to the optimal wing motion for the membrane wing. We therefore discuss in section 5.5.7 the effect of the membrane flexibility for the respective optimal motions.

4.8 Summary

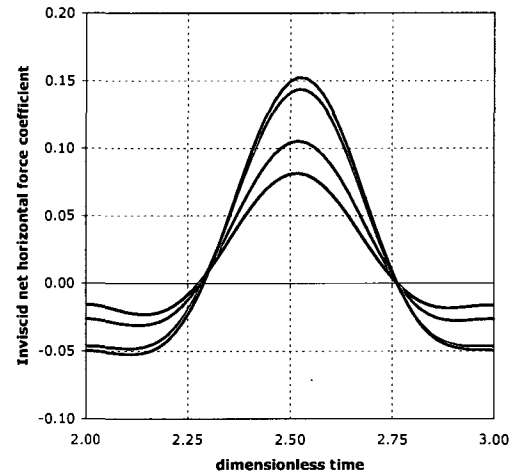
In this chapter, we have described the fluid-structure interaction model to investigate the unsteady aeroelasticity of pterosaur gliding and flapping flight. The non-linear structural behavior of the membrane is assumed linear for small deflections about the

Table 4.20: Average lift, inviscid net horizontal force and power coefficients ($\overline{C_L}$, $\overline{C_{F_{X_{inv}}}}$, $\overline{C_P}$) in flapping flight. The motion parameters are listed in table 4.19. The results are computed for the pterosaur wing with three membrane models, and with the rigid wing defined of the aerodynamic model.

	Rigid wing	Stiff membrane	Pterosaur membrane	Flexible membrane
$\overline{C_L}$	0.700	0.659	0.469	0.363
$\overline{C_{F_{X_{inv}}}}$	0.0214	0.0205	0.0175	0.0146
$\overline{C_P}$	0.0410	0.0378	0.0287	0.0229



(a) Lift coefficient C_L as a function of the dimensionless time $\frac{t}{T_{\text{period}}}$ during the second period of the motion



(b) Inviscid net horizontal force coefficient $-C_{F_{X_{inv}}}$ as a function of the dimensionless time $\frac{t}{T_{\text{period}}}$ during the second period of the motion

Figure 4.12: Comparison of the lift and inviscid net horizontal force variations in flapping flight. The motion parameters are specified in table 4.19. The forces computed in the third period are plotted. The black line represents the rigid wing of the aerodynamic model. The forces for the stiff membrane ($E = 1000$ MPa), the pterosaur approximation ($E = 100$ MPa) and for the flexible membrane ($E = 37$ MPa) are plotted in red, green and blue respectively.

equilibrium shape computed for the glide loads with tensioning from the bones. The equations of motion of the structure are solved using a time-integration scheme based on the Newmark method.

We compared the computed results with measurements for an ornithopter in free flight, and showed that the measurements should be done in a controlled environment such as a wind-tunnel to provide more insights. We detailed the approximations used in the aerolastic model of the pterosaur wing. The computational model input in the finite-element analysis required some modifications for numerical stability. We showed that these modifications do not alter the solution, by comparing results with analytical solutions.

Finally, we discussed the role of tensioning by the bones in the modal decomposition for the pterosaur wing. We investigated the impact of the flexibility of the membrane, by considering three cases of Young's modulus. We compared the deflection and aerodynamic forces for gliding and flapping flight.

Chapter 5

Optimization

5.1 Introduction

Animal flight has been the subject of numerous studies, including optimization studies by both the biological and aeronautical communities. We define the optimization problem relevant to this study, by adapting some elements of methodologies used in past studies to our questions on efficient flapping flight of pterosaurs.

In this chapter, we first motivate our choices of optimization goal. We then detail the optimization problem and formulation. The choice of adequate optimization tools is closely related to the choice of the optimization problem and we describe the two optimization methods used for our purposes. We finally present the optimization results for the aerodynamic and for the aeroelastic model.

5.2 Mechanical power as an optimization goal

In this section, we review past optimization studies on flapping flight conducted mostly for birds. We then motivate the choice of optimization goal that is most

adapted to the study of pterosaur flapping flight.

5.2.1 Optimization of vertebrate flight in biology

From the biological standpoint, explaining the choice of flapping gait and migration patterns of particular species of birds or bats are two key questions related to vertebrate flapping flight. These two problems can be expressed as optimization problems.

Rayner et al.[51] studied the flapping gait selection for different species of birds. Bird specimens were trained to fly in a wind-tunnel. The impact of the gait on the trailing wake were measured and the corresponding induced wake losses were estimated. They also discussed which gait was better suited to certain species because of their flight patterns and environmental constraints. Alerstam and Hedenstrom[63] discussed how migration patterns are related to the balance of energy expenditure and intake over the migration route. The migration speed is therefore correlated to the rate of energy expenditure in flight that maximizes the distance flown per unit of energy, and the rate of energy intake during migration stops. Using classical results of steady aerodynamics, Pennycuik[42] estimated the optimal flight speed for migratory birds by estimating the required power to overcome the drag of the animal. As discussed in section 2.4.1, because only metabolic power can be directly measured, the above studies for birds rely on the estimates of mechanical power, which are based on gliding performance.

For pterosaurs, Bramwell and Whiffeld[5], Brower[24] and Chatterjee and Templin[9] have also estimated the required flapping power based on gliding performance. However, such estimates do not include the unsteady aerodynamic effects of flapping flight. Using the unsteady code UVLM and the aerodynamic pterosaur model detailed in chapter 3, we therefore compute the mechanical power for the flapping flight. In

section 5.6.2, we compare the mechanical power computed for the gliding flight and for the flapping flight of *Coloborhynchus robustus*.

5.2.2 Optimization of flapping flight in aerodynamics

From the aerodynamic standpoint, optimization studies have been mainly focused on computing the wing motion that maximized thrust or efficiency or minimized power.

Brooks et al.[22] studied the design of a pterosaur replica based on *Quetzalcoatlus northropi*. Using a simplified quasi-steady lifting line model, the parameters of the flapping motion of the ornithopter maximized the propulsive efficiency for a set thrust level.

However, most optimization studies of flapping flight have focused on rectangular wings of high aspect ratio ($AR > 8$) or man-made ornithopter designs. Using quasi-steady results, Jones[80] studied the minimization of the energy required for a flapping wing actuated from the root. He showed that this problem is equivalent to optimizing the lift distribution by minimizing the lift-induced drag increment due to the motion. He discussed how efficiency is related to the ratio of induced velocities by the motion to the vertical velocity of the wing. His study was based on quasi-steady assumptions and therefore limited to very low reduced frequencies.

With the development of numerical methods, the optimization problems have progressively incorporated additional complexity in the motion or in the aerodynamic model. Hall and Hall[56, 85] minimized flapping power by optimizing the vorticity in the wake, by using a three-dimensional vortex-lattice model of the wake. They considered a rectangular wing with constant chord and a single airfoil along the span. The optimization method was based on constrained Lagrangians, with equality constraints on lift, thrust and drag, and an inequality constraint on the maximum

section lift coefficient. Similarly, Harada[129, 130] optimized the wake circulation for a rectangular flapping wing with a clapping motion, to maximize the average thrust subject to lift and power constraints. He studied in particular the advantage of the average dihedral angle during the motion on efficiency, and showed that the efficiency could be increased by about 3%. Willis et al.[87] used the method derived by Hall and Hall[56] to minimize the power of a rectangular wing motion subject to lift and thrust constraints, using a quasi-Newton optimization method called BFGS. They used this methodology to explore the advantages of sweep motions, an additional wing articulation at mid-span of a wing, and of an additional harmonic of motion frequency. Willis et al.[131] also used this method to investigate the effect of formation flight and ground effect of flapping flight. In particular, they minimized the power of a formation of birds by adjusting the position of the wake of each bird in the formation.

More recently, optimization studies have also investigated the airfoil shape for a specified wing motion. Tuncer and Kaya[132] optimized the heaving and pitching motion of an airfoil using an unconstrained steepest descent approach. The objective function was a linear combination of thrust and efficiency, and could be set to maximize either thrust, efficiency or a combination of both. They used an unsteady Navier-Stokes method to compute the aerodynamic forces. Kaya and Tuncer[133] later extended the study to optimize the airfoil shape and the non-sinusoidal path for a heaving and pitching airfoil.

Additionally, several studies have included the aeroelastic deformations in the optimization problem. Isogai and Harino[134] optimized the aeroelastic design of a flexible rectangular wing in flapping motion. They computed the forces with an unsteady doublet lattice method coupled to an elastic flapping wing description based on the Lagrange's equations of motion. The goal of the optimization was to optimize

the thicknesses of three sections of the wing spar and the wing motion frequency and amplitude, such that the propulsive efficiency of the flapping motion is maximized. The optimization was carried out using a gradient-free direct search method subject to constraints on the average thrust and the thicknesses. Lian et al.[135] optimized the surface shape of a flexible membrane wing for the design of a micro-air vehicle with low aspect ratio. The objective was to maximize the lift-to-drag ratio under a set of aerodynamic and geometric constraints. The forces were computed using a Navier-Stokes code coupled to a structural analysis code. They used the rigid wing model as a surrogate model of the design space coupled with a gradient-based optimizer.

5.2.3 Choice of optimization goal

If large pterosaurs were continuous flappers, they would have had to be very efficient because of their large size. In this study, we aim at finding the joint motions that contribute most to propulsive efficiency. However, the propulsive efficiency can become ill-defined. Figure 5.1 from Jones[20] show the variation of propulsive efficiency for an airfoil subject to heaving and pitching motion with respect to the amplitude and phase angle of the pitching motion. For a phase angle in the vicinity of 90 degrees, the propulsive efficiency can become ill-defined if the amplitude of the pitching motion is such that the mechanical power becomes infinitesimally small. Gradient-based optimization procedures might not converge if the objective function becomes ill-defined close to the optimum. In order to have the option of using such optimization techniques, propulsive efficiency is therefore not a good candidate of objective function in an optimization procedure.

In section 2.4.1, we defined the propulsive efficiency $\bar{\eta}$ as the ratio of the total thrust $\overline{C_T}$ to the mechanical power $\overline{C_P}$. For wing motions creating a given thrust $\overline{C_T}$,

maximizing the propulsive efficiency $\bar{\eta}$ is equivalent to minimizing the mechanical power $\overline{C_P}$. The average power $\overline{C_P}$ is usually a smooth function and therefore a better choice of objective function. In this study, we assume that, at given cruise speed and weight, the variations of average thrust required for flapping flight due to a change in the wing motion are small compared to the variations of average power around the optimum. With this assumption, by minimizing the mechanical power we therefore maximize the propulsive efficiency.

We do not know a priori if the design space of the optimization problem has a single global optimum or several local optima. We first explore the design space using evolutionary algorithms, as detailed in section 5.4.1. Although computationally inefficient, these algorithms are robust and provide some first insights on possible flapping gaits. When accounting for all the joint motions, the number of variables might be too great to ensure convergence of evolutionary algorithms. Although much more efficient, gradient-based optimizers might not converge if provided with a poor starting point. We therefore combine the two procedures by using gradient-based optimizers to find the optima from the best design points found by the evolutionary algorithms. In each case, we adapt the formulation of the optimization problem such that it is suited to each optimization method. For the gradient-based optimizer in particular, we define the constraint functions to ensure smoothness.

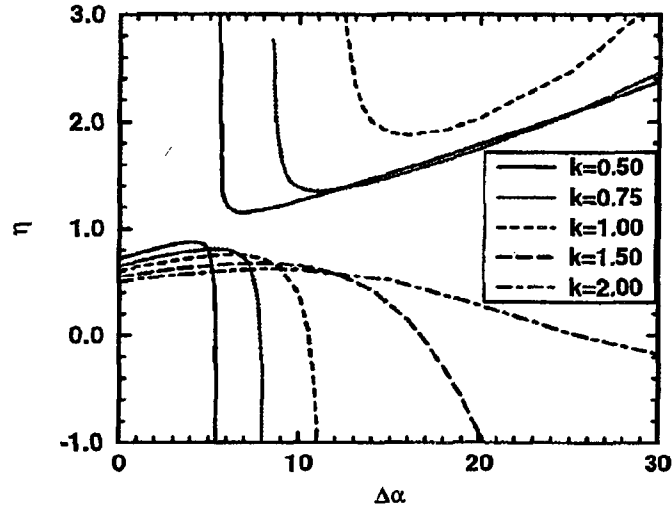


Figure 5.1: Variation of propulsive efficiency with pitching amplitude $\Delta\alpha$ at different values of reduced frequency k for the case of a heaving and pitching airfoil. Calculations used an unsteady two-dimensional panel code. Figure from Jones[20].

5.3 Formulation of the constrained optimization problem

5.3.1 Choice of optimization variables

In this section, we discuss the choice and definition of the variables relevant to the optimization of the wing motions of pterosaurs. In section 3.2, we estimated the flapping frequency of *Coloborhynchus robustus* using scaling laws. However, these scaling laws were established from observation of birds. Because of their large size, pterosaurs lie far beyond the range of sampled sizes. We therefore cannot rely on estimates made for pterosaurs based on these scaling laws and we include the flapping frequency as an optimization variable in the form of the reduced frequency k .

We impose a constraint on the average lift force, such that it matches the weight of the animal. For this purpose, we add the average angle attack of the animal $\bar{\theta}$ in

Table 5.1: Definitions of active joint motions during flapping flight

Motion	Shoulder	Elbow	Wrist	Knuckle
Dihedral	ϕ_1			
Pitch	θ_1		θ_3	
Sweep	ψ_1	ψ_2	ψ_3	ψ_4

the optimization variables.

In this study, we do not study the impact of non-sinusoidal motions nor the impact of adding harmonic frequencies to the motion. We therefore assume that all joints move sinusoidally at the same circular frequency ω , which is set by the reduced frequency k . The variables defining the wing motion are the angular amplitudes and phase angles φ of the joint motions. We recall the definitions of the joints in table 5.1. We choose the flapping motion due to shoulder flapping, noted ϕ_1 , as the reference motion, such that $\varphi_{\phi_1} = 0$. In all, the angles of the moving joints are given by

$$\begin{aligned}
\phi_1(t) &= \phi_{1\text{glide}} + \phi_1 \sin(\omega t), \\
\theta_1(t) &= \theta_{1\text{glide}} + \theta_1 \sin(\omega t + \varphi_{\theta_1}), \\
\psi_1(t) &= \psi_{1\text{glide}} + \psi_1 \sin(\omega t + \varphi_{\psi_1}), \\
\psi_2(t) &= \psi_{2\text{glide}} + \psi_2 \sin(\omega t + \varphi_{\psi_2}), \\
\theta_3(t) &= \theta_{3\text{glide}} + \theta_3 \sin(\omega t + \varphi_{\theta_3}), \\
\psi_3(t) &= \psi_{3\text{glide}} + \psi_3 \sin(\omega t + \varphi_{\psi_3}), \\
\psi_4(t) &= \psi_{4\text{glide}} + \psi_4 \sin(\omega t + \varphi_{\psi_4}), \\
\text{with } \omega &= \frac{2kU_\infty}{c}.
\end{aligned}$$

Table 5.2: The seven cases of joint motions considered in the optimization study.

Case name	J0	J1	J2	J3	J4	J5	J6
\bar{k}	x	x	x	x	x	x	x
$\bar{\theta}$	x	x	x	x	x	x	x
ϕ_1	x	x	x	x	x	x	x
ψ_1			x	x	x	x	x
ψ_2				x	x	x	
ψ_3					x	x	x
θ_3		x	x	x	x	x	x
ψ_4						x	

5.3.2 Choice of sensitivity studies

We aim at finding the joint motions that have the most impact on propulsive efficiency, hence on the required mechanical power. To explore the effect of each joint motion, the number of degrees of freedom considered is sequentially increased. As the main production of thrust will come from the flapping motion at the shoulder, we first explore the most suitable parameters for this motion with amplitudes for the other motions set to zero. We then add degrees of freedom in the order listed in table 5.2, and discuss the possible gain in performance. Table 5.2 summarizes the different cases of joint motions studied and the naming nomenclature used.

Several key parameters for *Coloborhynchus robustus* can only be roughly estimated, so we also study the sensitivity of the optimal wing motion to these parameters. These sensitivity studies, in order of results, include the impact of

- average flight speed in the form of average lift coefficient $\overline{C_L}$,
- joint angles at glide, either planar or curved wing geometry,
- membrane attachment point on the body, either at the hip or the ankle,
- mass estimate,

Table 5.3: Seven cases of average $\overline{C_L}$ conditions considered in the sensitivity study.

Average lift $\overline{C_L}$	0.5	0.6	0.7	0.8	0.9	1.0	1.1
Flight speed U_∞ (m.s ⁻¹)	19.8	18.1	16.8	15.7	14.8	14.0	13.4

Table 5.4: Three cases of animal weight considered in the sensitivity study.

Weight (N)	80	160	240
Flight speed U_∞ (m.s ⁻¹)	11.8	16.8	20.5

- body accelerations, either accounting for them or not,
- atmospheric density,
- membrane properties

The values chosen for the sensitivity studies on flight speed, weight and atmospheric density are given in tables 5.3, 5.4, 5.5. We compare the solutions to a reference motion, which is the optimal flapping gait found for the motion case J2, as listed table 5.2, considering shoulder dihedral ϕ_1 , shoulder sweep ψ_1 , and wrist pitch θ_3 . For this reference motion, the average lift coefficient $\overline{C_L}$ is fixed at 0.7, which corresponds to an average flight speed of 16.8 m.s⁻¹ for a specimen of *Coloborhynchus robustus* weighing 160 N, in air at current sea-level air density $\rho = 1.23$ kg.m⁻³. We also consider a planar wing geometry with the wing membrane attached at the hip and we do not account for the body accelerations. We choose this motion as a reference, because it yields significant savings compared to other cases, while the motion remains simple enough to draw conclusions.

Table 5.5: Five cases of atmospheric density considered in the sensitivity study. ρ

Air density ρ (kg.m ⁻³)	1.0	1.23	2.0	3.0	4.0
Flight speed U_∞ (m.s ⁻¹)	18.2	16.8	12.9	10.7	9.1

Table 5.6: List of flapping gait parameters (angles in degrees)

Input Parameters	Symbol	Range of values
Reduced frequency	k	$[0.02 ; 0.2]$
Average angle of attack	$\bar{\theta}$	$[4 ; 11]$
Shoulder	ϕ_1	$[0 ; 45]$
Shoulder	$\theta_1, \varphi_{\theta_1}$	$[0 ; 10], [-180 ; 180]$
Shoulder	ψ_1, φ_{ψ_1}	$[0 ; 25], [0 ; 360]$
Elbow	ψ_2, φ_{ψ_2}	$[0 ; 20], [0 ; 360]$
Wrist	$\theta_3, \varphi_{\theta_3}$	$[0 ; 10], [-180 ; 180]$
Wrist	ψ_3, φ_{ψ_3}	$[0 ; 15], [0 ; 360]$
Knuckle	ψ_4, φ_{ψ_4}	$[0 ; 5], [0 ; 360]$

5.3.3 Bounds of the variables

The optimization variables are varied within the allowable range of motion detailed in section 2.2.7. Table 5.6 shows a summary of input parameters and their range of allowable values. We note that the sweep phase angles are centered around 180 degrees, as we expect from bird observations a backward sweep motion as the wing moves up. Similarly, the pitch phase angles are expected to be in the vicinity of 90 degrees.

5.3.4 Definition of constraints

We focus our study on the flapping motion for a pterosaur in cruise level flight, such that its altitude, velocity and orientation remain constant on average during the motion.

We recall the nomenclature of the forces and moments defined in section 3.3.4. The forces and moments are averaged over the last period computed for the wing

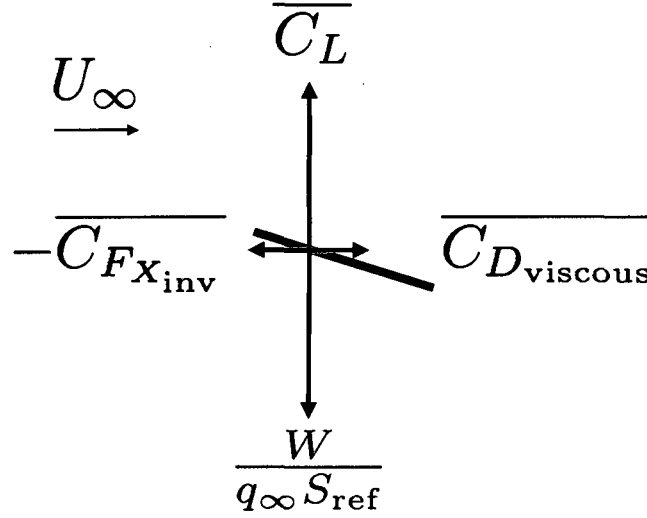


Figure 5.2: In cruise level flight, the time-averaged horizontal forces (average inviscid net horizontal force $\overline{C_{F_{X_{inv}}}}$ and average viscous drag $\overline{C_{D_{viscous}}}$) and vertical forces (average lift $\overline{C_L}$ and weight $W/(q_\infty S_{ref})$) are balanced during a period of the wing motion.

motion. $\overline{C_T}$ refers to the average total thrust, $C_{D_{total \text{ steady-state}}}$ to the total steady-state drag, $\overline{C_{F_{X_{inv}}}}$ to the average inviscid net horizontal forces, $\overline{C_{D_{viscous}}}$ to the average viscous drag, $\overline{C_L}$ to the average lift coefficient, and $C_{l_{max}}$ to the maximum section lift coefficient. C_{F_y} is the force coefficient for the side force in the y -direction. C_{M_x} and C_{M_z} are the moment coefficients about the x, y and z -axes respectively. We note $\frac{W}{q_\infty S_{ref}}$ the dimensionless weight coefficient for a given weight W . We define X_0, Y_0, Z_0 the position of the center of gravity in the inertial frame of reference, and ϕ_0, θ_0, ψ_0 the orientation of the frame attached to the body relative to the inertial frame of reference.

Average cruise conditions

For a wing in average steady cruise conditions, as shown in figure 5.2, all force coefficients are balanced on average: the average inviscid net horizontal force $\overline{C_{F_{X_{inv}}}}$ equals

the average viscous drag $\overline{C_{D_{\text{viscous}}}}$, the average lift $\overline{C_L}$ equals the weight $W/(q_\infty S_{\text{ref}})$. We recall that $\overline{C_{F_{X_{\text{inv}}}}}$ is negative if the wing motion creates thrust. For periodic motions, the state (position, orientation, velocities, forces and moments) must be the same at the beginning and the end of a period T_{period} . We assume the wing motion is symmetric about the x - z plane, so by construction, at the center of gravity, for any given time t ,

$$C_Y = 0, \quad \dot{Y}_0 = 0, \quad Y_0 = 0,$$

$$C_{Mx} = 0, \quad p_0 = 0, \quad \phi_0 = 0,$$

$$C_{Mz} = 0, \quad r_0 = 0, \quad \psi_0 = 0.$$

Periodicity conditions

If the variations of forces and moments do not affect the position and orientation of the body at the center of gravity ($Z_0(t)$ and angle of attack $\theta_0(t)$ are constant), then the periodicity conditions of the motion are met by satisfying

$$-\overline{C_{F_{X_{\text{inv}}}}} = \overline{C_{D_{\text{viscous}}}}, \quad (5.1)$$

$$\overline{C_L} = \frac{W}{q_\infty S_{\text{ref}}}, \quad (5.2)$$

$$\overline{C_{My}} = 0. \quad (5.3)$$

Additionally, consider the planar wing geometry under a flapping motion at the shoulder ($\phi_1 = 15.0$ degrees) at $k = 0.10$. During the motion, the total lift coefficient C_L reaches 0.90. However, the section lift coefficient reaches a maximum value of $C_{l_{\text{max}}} = 2.0$ near the tip. This value of section lift is excessive for our potential flow assumptions. As discussed in section 3.2, we do not account for dynamic stall effects

and we choose a limit for the section lift coefficient, set to 1.50 based on results for symmetric airfoils.

Periodicity conditions with the body accelerations

If we account for the body accelerations due to the wing motion and the variation of forces, periodicity conditions must also be considered for the body position. Because of the symmetry of the motion, we only need to verify that the altitude, velocity and pitch orientation are periodic, given by

$$\begin{aligned} Z_0(t + T_{\text{period}}) &= Z_0(t), \\ \dot{X}_0(t + T_{\text{period}}) &= \dot{X}_0(t), \\ \theta_0(t + T_{\text{period}}) &= \theta_0(t), \end{aligned}$$

We note that the periodicity condition on θ_0 is equivalent to the constraint on $\overline{C_{My}}$. In this study, we choose to check the periodicity of θ_0 .

Constraint violation functions

For a simulation over N periods, we check the periodicity conditions at $t = N$ and $t = N - 1$, and we define the functions ΔC_X , ΔC_Z , $\Delta C_{l_{\max}}$, ΔZ , $\Delta \dot{X}$, $\Delta \theta$, to measure the violation of the constraints defined above. The constraint violation function are

given by

$$\Delta C_X = \overline{C_{F_{X_{inv}}}} + \overline{C_{D_{viscous}}} \quad (5.4)$$

$$\Delta C_Z = \overline{C_L} - \frac{W}{q_\infty S_{ref}} \quad (5.5)$$

$$\Delta C_{l_{max}} = C_{l_{max}} \quad (5.6)$$

$$\Delta Z = Z_0(N) - Z_0(N-1) \quad (5.7)$$

$$\Delta \dot{X} = \dot{X}_0(N) - \dot{X}_0(N-1) \quad (5.8)$$

$$\Delta \theta = \theta_0(N) - \theta_0(N-1). \quad (5.9)$$

5.3.5 Formulation of the constrained optimization problem

Accounting for the objective function, constraints and variables defined previously, the optimization problem is formulated in the following way :

$$\begin{aligned}
& \text{minimize} && \overline{C_P} \\
& \text{with respect to} && k, \bar{\theta}, \phi_1, \theta_1, \varphi_{\theta_1}, \psi_1, \varphi_{\psi_1}, \psi_2, \varphi_{\psi_2}, \\
& && \theta_3, \varphi_{\theta_3}, \psi_3, \varphi_{\psi_3}, \psi_4, \varphi_{\psi_4} \\
& \text{such that} && -\overline{C_{F_{X_{\text{inv}}}}} = \overline{C_{D_{\text{viscous}}}}, \\
& && \overline{C_L} = \frac{W}{q_{\infty} S_{\text{ref}}}, \\
& && |C_l| < 1.50 \text{ at each spanwise section,} \\
& && Z_0(N) = Z_0(N-1), \\
& && \dot{X}_0(N) = \dot{X}_0(N-1), \\
& && \theta_0(N) = \theta_0(N-1), \\
& && \text{variables are within bounds defined in table 5.6.}
\end{aligned}$$

Using the function measuring the constraint violation, as defined in section 5.3.4,

the optimization problem is written

$$\begin{aligned}
& \text{minimize} && \overline{C_P} \\
& \text{with respect to} && k, \bar{\theta}, \phi_1, \theta_1, \varphi_{\theta_1}, \psi_1, \varphi_{\psi_1}, \psi_2, \varphi_{\psi_2}, \\
& && \theta_3, \varphi_{\theta_3}, \psi_3, \varphi_{\psi_3}, \psi_4, \varphi_{\psi_4} \\
& \text{such that} && \Delta C_X = 0, \\
& && \Delta C_Z = 0, \\
& && \Delta C_{l_{max}} < 1.50, \\
& && \Delta Z = 0, \\
& && \Delta \dot{X} = 0, \\
& && \Delta \theta = 0, \\
& && \text{variables are within bounds defined in table 5.6.}
\end{aligned}$$

5.4 Optimization algorithms used

We do not know a priori if the design space of the optimization problem has a single global optimum or several local optima. We first explore the design space using a binary genetic algorithm. Although genetic algorithms (GA) are robust, the convergence of GAs is not guaranteed if the number of variables becomes too great. When accounting for all the joint motions, our optimization problem has up to 17 variables. We therefore use gradient-based optimizers to find the optima starting from the points found by the GA. In this study, the gradient-based optimizer used is based on sequential quadratic programming (SQP).

5.4.1 Genetic algorithm

Using techniques for evolutionary optimization algorithms, as described by Kalyanmoy[136], we adapt a binary genetic algorithm from the GA toolbox[137] developed by the Illinois Genetic Algorithm Lab (IlliGAL). Although this algorithm requires a large number of function evaluations, binary GAs are a robust mean of optimization. In addition, the bounds and resolution of each variable is inherently controlled by the binary encoding of the variables. In this section, we first give a summary of the steps taken by the algorithm, then detail the formulation of the objective function and of the constraints for this algorithm.

Summary of the method for the binary genetic algorithm

The flow chart of the GA we use, shown in figure 5.3, summarizes the steps of the following optimization procedure. GAs start by initializing a sample population. The population is typically twenty to thirty times the number of variables. In our case, the population size ranges between 60 in the simplest case of wing motion, and 450 with all joint motions included. For each member of the population, the values of each design variable are initially set randomly. We then start iterating. For each iteration, the objective value for each population member is first computed, then compared to other population members to select the mating pool. It is determined by a tournament selection, such that each population member is compared to a set number of other population members. Two offsprings are produced from two parents selected in the mating pool. The genome of the offsprings are set by a random cross-over operation from the genome of the parents. The offsprings are then compared to their parents, and the best parent and best offspring or second parent are selected for the next iteration. The size of each gene is chosen to control the number of

possible values each variable can take within the defined bounds. The offsprings are also subject to random mutations. At the beginning of every iteration, the minimum objective function value over the whole population is computed, and compared to previous iterations. If this minimum objective function has not improved since a set number of iterations, then the algorithm is deemed converged.

Possible choices of penalty functions include absolute value, quadratic or logarithmic penalty functions. Logarithmic penalty functions are best suited for inequality constraints. As we do not need any gradients, the GA is insensitive to the smoothness of the objective function, so absolute value or quadratic penalty functions are both adequate for equality constraints. The absolute value penalty function enforces stricter equality than the quadratic near the equality. We therefore use absolute value penalty functions to account for the constraints. For the inequality constraint on maximum lift coefficient, the absolute penalty function is active only if the constraint is violated.

The objective function is defined as the combination of our optimization goal and constraint violations, as defined below. The objective function is computed from the values computed by UVLM for the joint motions given by the GA. As a single run of UVLM can take up to several minutes, the objective function of each population member is computed in parallel, with one CPU allocated for one population member. For this reason, the size of the population remains constant.

Objective function for the binary genetic algorithm

For the binary GA, we account for the constraints by including them in the objective function. The binary GA optimization problem then becomes an unconstrained

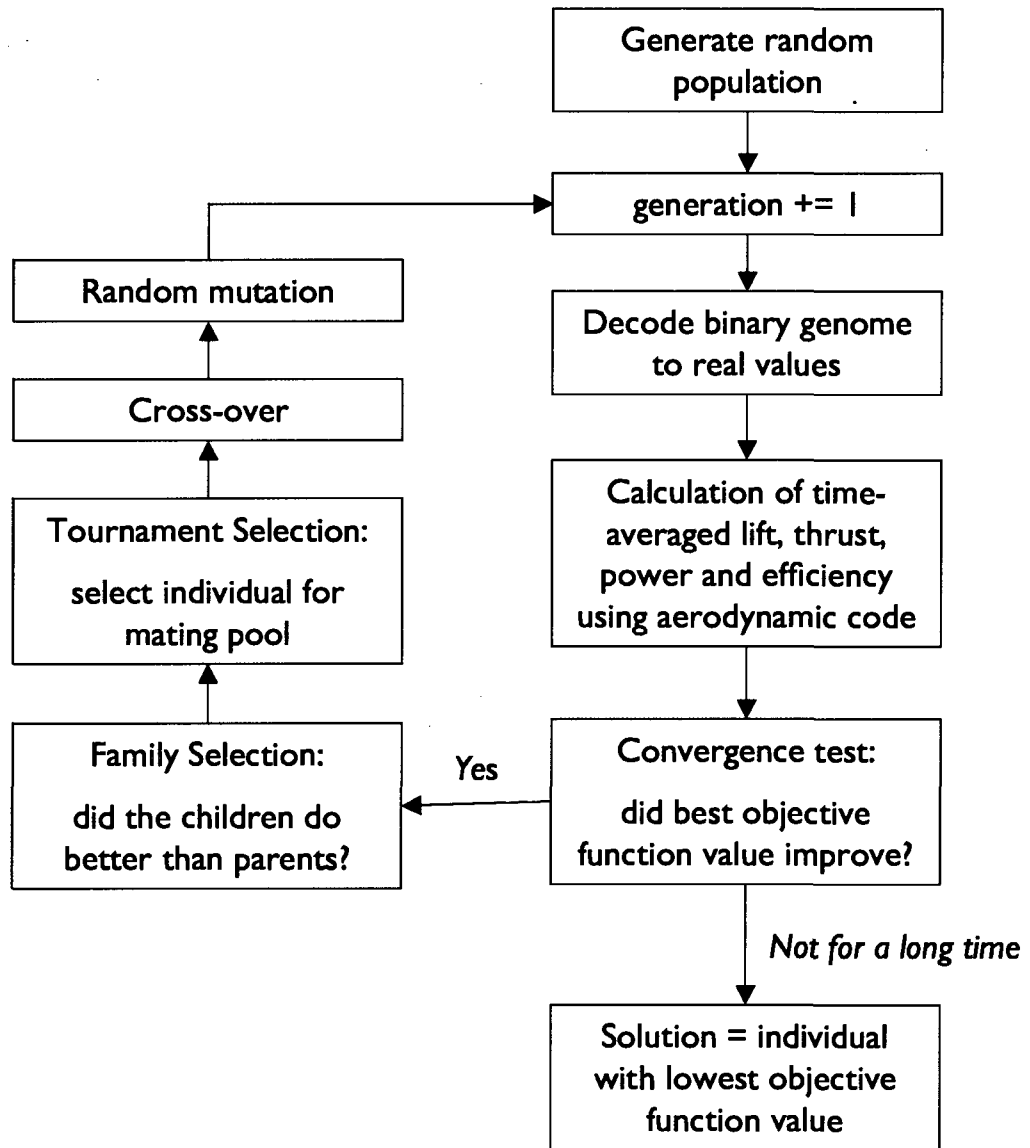


Figure 5.3: Flow chart of the binary genetic algorithm coupled to the aerodynamic code UVLM.

problem, which is easier to implement. We define the objective function J as a combination of the power coefficient and penalty functions associated with the constraints. The penalty functions are based on the absolute value of the constraint violation functions, defined in section 5.3.4. A penalty parameter ρ_i is associated with every penalty function, and the values are chosen such that all terms in J are of the same order of magnitude. This choice of penalty parameter ensures that all terms in the objective function weigh roughly equally in the objective value. The objective function used in the genetic algorithm is therefore written

$$J = \overline{C_P} + \rho_1 |\Delta C_X| + \rho_2 |\Delta C_Z| + \rho_3 |\Delta C_{l_{max}}| + \rho_4 |\Delta Z| + \rho_5 |\Delta \dot{X}| + \rho_6 |\Delta \theta|, \quad (5.10)$$

with $\rho_1 = 100$, $\rho_2 = 10$, $\rho_3 = 10$, $\rho_4 = 1$, $\rho_5 = 0.1$, $\rho_6 = 1000$. We recall that $\Delta C_{l_{max}} = 0$ if the constraint on section lift coefficient is not violated.

The optimization problem for the genetic algorithm is therefore written as the following unconstrained optimization problem

$$\begin{aligned} & \text{minimize} && J \\ & \text{with respect to} && k, \bar{\theta}, \phi_1, \theta_1, \varphi_{\theta_1}, \psi_1, \varphi_{\psi_1}, \psi_2, \varphi_{\psi_2}, \\ & && \theta_3, \varphi_{\theta_3}, \psi_3, \varphi_{\psi_3}, \psi_4, \varphi_{\psi_4} \\ & \text{such that} && \text{variables are within bounds defined in table 5.6} \end{aligned}$$

5.4.2 Sequential quadratic programming methods

Gradient-based optimization methods have been shown to be very efficient in optimizing problems, if provided with an adequate starting point. However, the choice of

method is closely linked to the formulation of the optimization problem and the properties of the functions. The optimization problem of this study has several constraints, that we expect to be smooth and non-linear with respect to all variables. Among gradient-based optimization methods, sequential quadratic programming (SQP) has been shown to be very effective in optimizing large constrained problems with smooth non-linear functions for the objective and the constraints, and therefore seems very appropriate for our study. In this study, we use SNOPT[138], developed at the Stanford Optimization Lab and UCSD, and is detailed by Gill et al.[139].

In this section, we first summarize the SQP method, then we detail the formulation of our optimization problem adapted to the formulations used in SNOPT.

Summary of the SQP method

As detailed in Gill et al.[139], SNOPT is a general-purpose system for constrained optimization. It minimizes a linear or nonlinear function subject to bounds on the variables and sparse linear or nonlinear constraints. SNOPT was developed to optimize problems defined by

$$\begin{aligned}
 & \text{minimize} && f(x) \\
 & \text{with respect to} && x \in \mathbb{R}^n \\
 & \text{subject to} && l \leq \begin{pmatrix} x \\ c(x) \\ Ax \end{pmatrix} \leq u
 \end{aligned}$$

where $f(x)$ is a linear or nonlinear objective function, $c(x)$ is a vector of nonlinear constraint functions, A is a sparse matrix of linear constraints, and l and u are vectors of lower and upper bounds. It is assumed that the nonlinear functions are smooth.

Sequential quadratic programming is an extension of the quadratic programming (QP) method, in that it solves the nonlinearly constrained problem by obtaining search directions from a sequence of quadratic programming subproblems. The basic structure of an SQP method involves major and minor iterations. The major iterations generate a sequence of iterates that converge to a final solution. At each iterate, a QP subproblem is used to generate a search direction towards the next iterate. Solving such a subproblem is itself an iterative procedure, with the minor iterations of an SQP method being the iterations of the QP method.

The constraints of each QP subproblem are linearizations of the constraints in the original problem, and the objective function of the subproblem is a quadratic approximation to the Lagrangian function. The method used to solve the QP problem involves the computation of the quasi-Newton approximations to the Hessian of the Lagrangian. The merit function for steplength control is an augmented Lagrangian merit function, and is reduced along each search direction to ensure convergence from any starting point.

SNOPT has been used for many optimization problems, which has led to the addition of many features, detailed in Gill et al.[139], that ensure it works reliably in most cases.

Definition of functions used for SNOPT

We adapt the optimization problem defined in section 5.3.5, to the formulation used in SNOPT. The vector of functions f contains the objective function, generally the first element, and the constraint functions. Using the constraint violation functions,

the element of the vector of functions f are

$$\begin{aligned}
 f[1] &= \overline{C_P}, \\
 f[2] &= \Delta C_Z, \\
 f[3] &= \Delta C_X, \\
 f[4] &= \Delta C_{l_{\max}}, \\
 f[5] &= \Delta Z, \\
 f[6] &= \Delta \theta, \\
 f[7] &= \Delta \dot{X}.
 \end{aligned}
 \tag{5.11}$$

SNOPT relies on the calculation of the gradients $g[i, j]$ with i corresponding to the variable index, and j corresponding to the function index. If the gradients are not provided by the user function, SNOPT can calculate them by finite differences. For our purposes, we calculate the gradients of the active variables by finite differences and provide them to SNOPT. This is done such that only one interface with SNOPT is required, and that SNOPT does not waste function evaluations to calculate gradients of inactive variables.

Using the definitions above, this can be written with

$$\begin{aligned}
 & \text{minimize} && f[1] \\
 & \text{with respect to} && x[i] \\
 & \text{such that} && f[2] = 0, \\
 & && f[3] = 0, \\
 & && f[4] < 1.50, \\
 & && f[5] = 0, \\
 & && f[6] = 0, \\
 & && f[7] = 0, \\
 & && \text{variables } x[i] \text{ are within bounds defined in table 5.6.}
 \end{aligned}$$

Prior to using SNOPT, we have verified the smoothness of all the objective and constraint functions $f(x)$, by doing parametric sweeps around several points of the design space. Although we did not verify the smoothness over the whole design space, we are confident, from these parametric sweeps, that the functions $f(x)$ are smooth in the vicinity of optimal flapping motions. We note that SNOPT does not converge for our optimization problem without an adequate starting point. This underlines the complementarity of the GA and the SQP methods for flapping flight optimization.

5.4.3 Combined optimization procedure

Both optimization algorithms we use have advantages and drawbacks. On the one hand, binary genetic algorithms are robust but inefficient, while SQP algorithms are extremely efficient but sensitive to the properties of the objective and constraints

functions. On the other hand, the best solution found by a genetic algorithm is likely to be close to a global optimal but the optimality conditions are not verified, while the solution found by a gradient-based algorithm is checked against the optimality conditions but might only be a local optimum and is strongly dependent on the starting point.

For our purposes, we implement an optimization strategy that combines both approaches. For each sensitivity study listed in section 5.3.2, we first explore the design space using the binary genetic algorithm, yielding a series of starting points used subsequently in SNOPT. At this time, we do not couple the optimization methods directly. The genetic algorithm has a random search behaviour by construction, and can yield solutions that are too far from satisfying the constraints. We have observed that SNOPT does not generally converge to a feasible solution with such starting points. By manually feeding the starting points to SNOPT, we have the possibility to filter such poor starting points, and start a new search with the genetic algorithm.

Exploration of the design space using the genetic algorithm

The binary genetic algorithm is used both to explore the design space and to define starting points for SNOPT. We therefore run the genetic algorithm several times in order to get at least three valid starting points for SNOPT. The best solution found by each run of the genetic algorithm is then used as starting point.

For our purposes, we have found that imposing different values of reduced frequency k , is an effective way of ensuring that the final points are not too close to each other in the design space.

Refinement of optimal solutions using the SQP algorithm

For each sensitivity study, we run SNOPT from a series of starting points. In addition to the starting points provided by the genetic algorithm, we also use other starting points. In particular, we use the solution found for the reference case, as defined in section 5.3.2. In the study of the additional joint motions, as we increase the number of degrees of freedom, we also use the solutions previously found for the cases with fewer degrees of freedom.

As we start SNOPT from multiple starting points for each case, the final solutions might differ. In that case, we compare the results and find which solution satisfy all constraints and has the lower power value. We have observed that, using adequate starting points, SNOPT converges to a single solution for the flapping motion, which we consider as a global optimum.

We have observed that, in most cases, SNOPT does not converge with the default parameters for the optimality and feasibility tolerances. However, we have observed that the solutions end up quite close together in the design space. We have found that relaxing the settings for the optimality and feasibility tolerances from 10^{-6} to 10^{-3} does not have a visible impact on the final solution. This is because these tolerances are relative to the solution value. The solutions found with SNOPT satisfy the optimality conditions and constraints within 0.1%. If SNOPT converges for only one of the specified starting points, we start the procedure over again. If SNOPT does not find a solution satisfying the constraints after several tries, we deem the problem infeasible. For a few cases, although the constraints are satisfied, the optimality conditions are not met, and we show the resulting flapping gait with lowest value of computed mechanical power.

5.5 Optimization results

Using the optimization procedure described above, we detail the results found with the aerodynamic model and with the aeroelastic model. We first present the findings for the different joint motions, and then for each sensitivity case in the order described in section 5.3.2. For each optimization case, we show only the optimal solution or the best feasible solution output by SNOPT.

As discussed in section 5.3.2, we define a reference motion for all the sensitivity studies. This motion is chosen to be the optimal flapping gait considering shoulder dihedral ϕ_1 , shoulder sweep ψ_1 , and wrist pitch θ_3 (motion case J2). For this reference motion, the average lift coefficient $\overline{C_L}$ is fixed at 0.7, which corresponds to an average flight speed of 16.8 m.s^{-1} for a specimen of *Coloborhynchus robustus* weighing 160 N, in air at current sea-level air density $\rho = 1.23 \text{ kg.m}^{-3}$. We consider a planar wing geometry with the wing membrane attached at the hip and we do not account for the body accelerations.

5.5.1 Impact of each joint motion

In this section, we refer to the optimal flapping gait for each motion studied by the name of the motion case, listed in table 5.7.

Flapping and twisting motions

We first consider the case of pure flapping motion (case J0) with variables $k, \bar{\theta}, \phi_1$. We find that SNOPT did not find a solution that satisfies the constraints. While motions can be found to satisfy the lift and thrust constraints, the constraint on maximum section lift constraint is significantly violated.

We then study the case of flapping motions with pitch rotation (case J1) with variables k , $\bar{\theta}$, ϕ_1 , θ_3 , φ_{θ_3} . This corresponds to the motion investigated in most published studies, although not applied to pterosaurs. Surprisingly, SNOPT did not find a solution that satisfies the constraints for the reference average lift coefficient $\overline{C_L}$ of 0.7. However, SNOPT did find an optimum motion J1 for an average lift coefficient $\overline{C_L}$ of 0.5. To compare with the sweeping motions, we also compute the optimum motion J2 for an average lift coefficient $\overline{C_L}$ of 0.5. For the other cases of joint motions, we compare the optimum motions found an average lift coefficient $\overline{C_L}$ of 0.7.

Subsequently, we incrementally add the sweep motions starting from the shoulder ψ_1 to the knuckle ψ_4 . Table 5.9 shows the solution for the flapping motion in each case with the corresponding objective and constraint function values. In all of these cases, SNOPT found optimal solutions. The issues encountered for the two motion cases J0 and J1 indicate that the flapping flight optimization problem we have defined is harder to satisfy with fewer degrees of freedom.

For the joint motions optimized for an average lift coefficient $\overline{C_L}$ of 0.7, we find that the reduced frequencies found are all in the vicinity of $k = 0.1 \pm 18\%$, which corresponds to a flapping frequency of about 2 Hz. The steady angle of attack $\bar{\theta}$ ranges between 7.5 and 8.1 degrees. Similarly we find that, in all cases, the pitch rotation at the wrist θ_3 has an amplitude in the range of 8-8.5 degrees, and a phase angle in the range of 80-100 degrees. The flapping amplitude ϕ_1 ranges between 12.2 and 14.2 degrees.

Sweeping motions

Pennycuik[140], Toblaske[141] and Biewener et al.[57] have observed that birds in cruise have a small sweeping motion, sweeping the wing backward on the upstroke and sweeping them forward in the downstroke. They also observed that the sweep motion amplitude increased at lower flight speed.

With the axes definition used in this study, such a sweeping motion corresponds to a phase angle of about 180 degrees. If we add the shoulder sweep motion ψ_1 (case J2), we indeed find that the optimal phase angle φ_{ψ_1} is 208 degrees. The added sweep motion reduces the required power by 7% for an average lift coefficient $\overline{C_L}$ of 0.5. If we add the elbow sweep motion (case J3), the optimization did not find a solution that improved the results compared to the case J2. If we add the wrist sweep (case J4), the average power is reduced by another 8%. If we add the knuckle sweep (case J5), the average power is reduced by another 1.4%. If we consider the case where the only sweeping occur at the shoulder and wrist (case J6), the optimization did not find a solution that improved the results compared to the case J2. This indicates that the power advantages found for the cases J4 and J5, come from the combination of the elbow and wrist sweep motions. In these cases, the sweep motion amplitudes for the elbow, wrist and knuckle have reached their respective maximum allowable value. This could indicate either that the optimal solution lies near the bounds or that these motions lead to errors in the aerodynamic model.

For these complex motions that combine motions with very different phase angles for a complex geometry, it is difficult to draw conclusions directly from the values. From animations of the motion of cases J4 and J5, we observe that the wingspan is 3% higher on average during the motion than the reference span b_{ref} . We also observe that the tip describes an ellipse with the long axis parallel to the z -axis. The

Table 5.7: Seven cases of joint motions considered in the optimization study.

Case name	J0	J1	J2	J3	J4	J5	J6
k	x	x	x	x	x	x	x
$\bar{\theta}$	x	x	x	x	x	x	x
ϕ_1	x	x	x	x	x	x	x
ψ_1			x	x	x	x	x
ψ_2				x	x	x	
ψ_3					x	x	x
θ_3		x	x	x	x	x	x
ψ_4						x	

vertical motions of the tip found for cases J4 and J5 are consistent with motions observed by Tobalske[141] for pigeons at cruise speed.

Reductions in required power

In all, we find that the sweeping motions reduces the required power by 7% from 181.4 W (case J1) to 170.0 W (case J2) for an average lift coefficient $\overline{C_L}$ of 0.5. For $\overline{C_L} = 0.7$, the required power is reduced by 9% from 155.8 W (case J2) down to 142.4 W (case J5). We estimated the range of flapping frequency, reduced frequency and flapping amplitude from scaling laws. We found that the values of frequencies are quite similar. However, the flapping amplitude ϕ_1 found by the optimization is about 30-50% lower than the values estimated from the results by Nudds et al.[69]. As the studied specimen of *Coloborhynchus robustus* is much larger than the birds they considered for their scaling law, it is not surprising that it does not seem applicable to our case.

5.5.2 Impact of average lift coefficient

Effect on average angle of attack

As shown in the results in table 5.10, we first observe that the average angle of attack $\bar{\theta}$ also increases in a roughly linear fashion as the average lift coefficient $\overline{C_L}$ is increased. This behavior is expected, as the lift coefficient has a linear dependence to the angle of attack for a flat plate airfoil in inviscid steady flow. The flapping motion induces a loss in lift and a subsequent increase in required angle of attack. This loss in lift is due mostly to the change of wing dihedral during the motion. We observe that this effect is stronger as the flapping amplitude ϕ_1 is increased.

Effect on flapping amplitude, reduced frequency and propulsive efficiency

A change in target average lift coefficient induces a notable change in reduced frequency, while the flapping amplitude ϕ_1 varies only a little. The amount of thrust and lift forces produced by the vertical motion of a wing is related to the product reduced frequency and motion amplitude, and in our case the product $k \times \phi_1$.

Figure 5.4(a) shows the increase in required average total thrust as a function of average lift coefficient. As shown in table 5.10, the increase in required thrust is due to the combined increase in zero-lift drag and lift-dependent drag. Figure 5.4(b) shows the corresponding increase of the product $k \times \phi_1$ with average lift coefficient. In the case where $\overline{C_L}$ is set at 0.5, the increase in flapping amplitude does not yield an increase in the product $k \times \phi_1$.

We observe in table 5.10 that the propulsive efficiency decreases as the average lift coefficient $\overline{C_L}$ increases, which is due to the increase in required total thrust $\overline{C_T}$ as shown in figure 5.5(a). This trend is consistent the one observed for propulsive efficiency of propellers and of two-dimensional airfoil in simple heaving motion, as

discussed by Jones et al.[20].

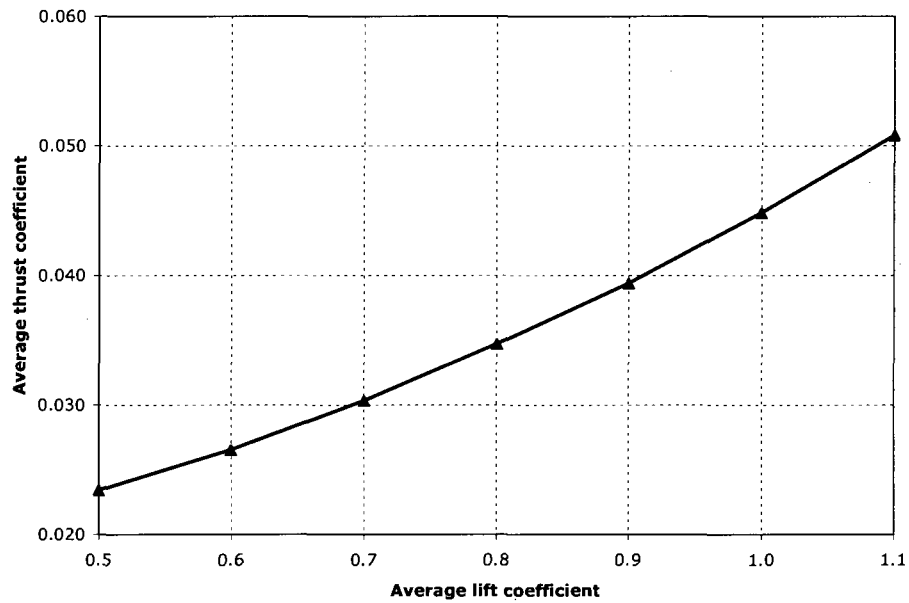
Effect on sweeping and pitching motions

An increase in the product $k \times \phi_1$ also induces an increase in peak lift forces. The amplitudes of the wrist pitch and shoulder sweep motions also need to be increased, because the limit on section lift coefficient $C_{l_{\max}}$ is kept unchanged. Pitching an airfoil, such that the pitch angle is reduced during the downstroke, helps control the maximum angle of incidence of the airfoil.

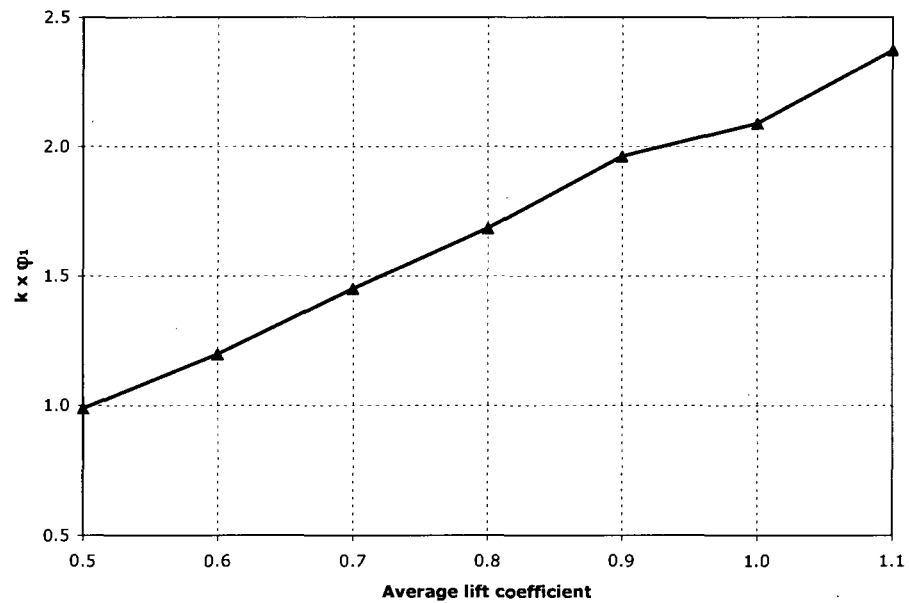
The sweeping motion also has an effect on incidence angle and on the section lift coefficient. If the wing is swept forward during the downstroke, the forward velocity is increased, which in turn reduces the angle of incidence on the wing. The additional forward velocity also reduces the section lift coefficient, because it is defined based on the local kinematic velocity. The effect of the sweeping motion is greatest at the tip where the vertical velocity would also be the greatest. The increase in sweep angles is consistent with observations by Pennycuik[140] and Tobalske[141], who observed that the sweep motion amplitude increased as the flight speed of a pigeon was reduced.

Lift coefficient for minimum power

Pennycuik[43] and Rayner[51] derived expressions of the required flight power \bar{P} of birds as a function of flight speed U_∞ as a polynomial of the third order. As shown in figure 5.5(b), we find that the variation of power \bar{P} with flight speed U_∞ follows a similar trend. We note that the curve of required power \bar{P} reaches a minimum between \bar{C}_L of 0.70 and 0.80. We estimate the minimum power, corresponding flight speed and average lift coefficient from a polynomial fit through the available data points. Using a third order polynomial fit between \bar{C}_L of 0.60 and 0.90, we estimate

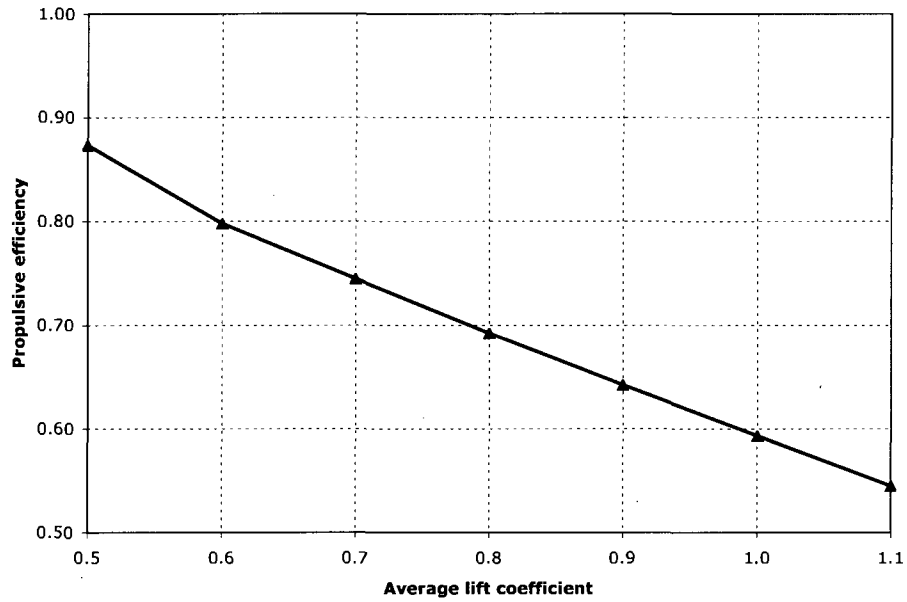


(a) Plot of the required average thrust \overline{C}_T for the optimal flapping motion as a function of average lift coefficient \overline{C}_L .

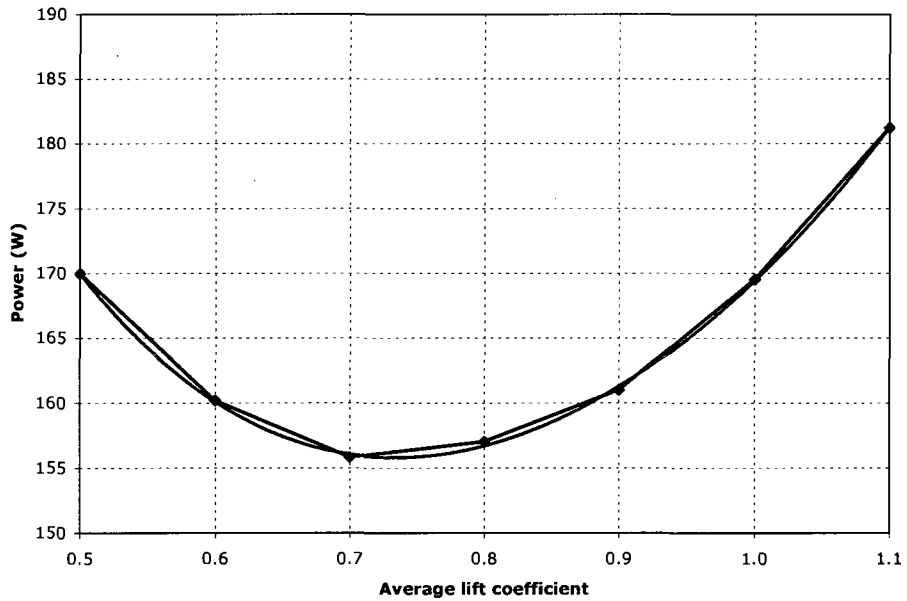


(b) Plot of the product $k \times \phi_1$ for the optimal flapping motion as a function of average lift coefficient \overline{C}_L .

Figure 5.4: Plots of the required average thrust \overline{C}_T and product $k \times \phi_1$ for the optimal wing motion as a function of average lift coefficient \overline{C}_L .



(a) Plot of the propulsive efficiency $\eta_{\text{propulsive}}$ for the optimal flapping motion as a function of average lift coefficient \overline{C}_L .



(b) Plot of the average mechanical power \overline{P} (in W) for the optimal flapping motion (blue line) as a function of average lift coefficient \overline{C}_L . The polynomial fit through the available points is shown in the red line.

Figure 5.5: Plots of the propulsive efficiency $\eta_{\text{propulsive}}$ and mechanical power \overline{P} for the optimal wing motion as a function of average lift coefficient \overline{C}_L .

that the minimum power reached is about 155.7 W at an average lift coefficient $\overline{C_L}$ of about 0.72 corresponding to a flight speed U_∞ of 16.7 m.s⁻¹. This value is very close to the power of 155.8 W found for an average lift coefficient $\overline{C_L}$ of about 0.70.

5.5.3 Impact of wing geometry

Curved and planar wing geometry

We compare the flapping gait of the curved geometry with the planar geometry. As shown in table 5.8, there is a significant decrease in average thrust and power for the curved geometry compared to the planar geometry for the same motion parameters. We therefore expect the optimization to find solutions that compensate for these decreases. As shown in table 5.11, for the curved geometry, the motion amplitudes are slightly increased by less than 1.5 degrees. The most notable difference is a 40 degrees change in phase angles for the sweep motion. However, these changes in the motion yield almost identical values of required power. Optimizing the problem for the planar geometry yields most of the information and we therefore choose the planar geometry for all the other cases with the aerodynamic model.

As discussed in section 3.5.1, the curved geometry is derived from the angles of the joints inferred from the fossil. It is likely that the wing would deform under the structural loads and future studies could investigate the advantages of the aeroelastic membrane wing with a curved bone geometry.

Hip and ankle membrane attachment point

We now study the impact of the position of the attachment point of the wing membrane. The reference area is increased by 73% from 1.3 m² to 2.1 m² for the ankle attachment. In order to maintain the same average lift coefficient, the flight speed

Table 5.8: Comparison of time-averaged quantities between the planar and curved pterosaur wing geometry. The time-averaged quantities correspond to the curved wing geometry of *Coloborhynchus robustus* with flapping motion parameters: $k = 0.10$, $\theta = 5.0$, $\phi_1 = 10.0$, $\theta_3 = 4.0$, $\varphi_{\theta_3} = 90.0$.

	Planar	Curved	Difference (%)
Average lift $\overline{C_L}$	0.4825	0.4665	4.6
Average inviscid net horizontal force $\overline{C_{F_{X_{inv}}}}$	0.0195	0.0127	35.0
Average mechanical power $\overline{C_P}$	0.0297	0.0216	27.2
Average wing parasite drag $\overline{C_{D_{wing}}}$	0.0143	0.0137	4.6
Maximum section lift $C_{l_{max}}$	1.523	1.253	17.7

is reduced from 16.8 m.s^{-1} to 13.5 m.s^{-1} , which is about 20% slower. The solution for the motion result in an increase of about +2 degrees for ϕ_1 , +3 degrees for ψ_1 , and +2 degrees for the wrist pitch θ_3 . The phase angles for sweep decreased by -14 degrees.

These changes in the motion reduce the value of required power by 11 W (-7%). By reducing the flight speed, the additional wing area changes the low-speed characteristics, which would be key for landing and take-off. If we consider the same amount of energy available for flight, the flight time is increased. However, the flying range is reduced by about 14% due to the slower flight speed. The discussion on the extent of the wing membrane relies on the low-speed characteristics of pterosaurs, which requires taking into account the role of the pteroid bone and the gait for take-off and landing. Regarding the performance during cruise flapping flight, attaching the wing membrane to the ankle yields a power advantage but also a flight range penalty. This trend is also seen in birds. Thermal soaring birds need broad wings to effectively benefit from uprising air, whereas migratory birds tend to have wings of large aspect ratio.

5.5.4 Impact of animal weight

Because the weight of pterosaurs can only be roughly estimated, we investigate the impact of the estimated weight on the optimal flapping gait. In these cases, we maintain the target average lift coefficient $\overline{C_L}$ at the reference value of 0.7. An increase in weight therefore results in an increase in average forward velocity, as shown in table 5.12.

We find that the optimal flapping gait remains almost unchanged, with the motion frequency changing by 0.4-0.5 Hz, the motion amplitudes changing slightly by 0.3-0.7 degrees, and the motion phase angles changing by 0.8-7 degrees. However these weight changes have a significant impact on the required power value with a roughly cubic trend relative to forward velocity.

With all other parameters kept constant, it seems that the optimal motion is insensitive to the animal weight, but that the required power is quite sensitive. This begs the question of how a pterosaur would best adapt its flapping gait to a change in weight due to catching a prey or due to weight loss during migration for example. It is unclear whether it would have reduced its speed, adapted its power expenditure to keep all other parameters constant and the motion the same, or whether it would have kept its power constant and adapted the motion and other parameters. Future studies could investigate this topic by modifying the formulation of the optimization problem to explore the effect of different scenarios.

5.5.5 Impact of body accelerations

As discussed in section 3.5.3, when we account for the body accelerations, we include the effects of the wing motion on the position of the center of gravity of the animal and the accelerations on the animal due to the variation of forces during the motion.

The results are listed in table 5.13. For the motion case J2, we find that the reduced frequency is increased by 30%, that the wrist pitch amplitude is increased by 3 degrees and that the phase angle of the sweep motion is reduced by 30 degrees. For the motion case J5, we find that the reduced frequency is increased by 26% and that the amplitudes and phase angles of the sweep motions are completely different. However the vertical motion of the tip is very similar to the case without the body accelerations. For this motion, the wingspan is on average the same as the reference span b_{ref} .

Most importantly, there is an increase in the required power of about 10% for the motion case J2, and 16% for the motion case J5. These estimates are consistent with published estimates. Van der Berg and Rayner[17] estimated the inertial power amounted to 11-15% of the total power in birds. Norberg et al.[142] estimated the inertial power amounted to 16% of the total power required for the bat *Plecotus auritus*.

In section 5.5.1, we found that the required power for the motion case J5 is 9% lower than for the motion case J2. Consequently, the required power for the motion case J5 accounting for the body accelerations is greater by 6% than the reference case J2 without the body accelerations.

5.5.6 Impact of atmospheric density

As discussed in section 2.2.8, it is believed that the composition of the atmosphere 150 million years ago might have been significantly different than that of today. We only study the impact of the atmospheric density ρ and do not investigate a change in chemical composition or temperature. As we change the density, we maintain the weight, the average lift coefficient constant $\overline{C_L}$ and maximum lift coefficient $C_{l_{\text{max}}}$ at the same values. We therefore adjust the forward velocity U_∞ such that the product

$\rho \times U_\infty^2$ remains constant. For comparison, at $\rho = 4.0 \text{ kg.m}^{-3}$, the flight velocity is reduced by 46% to 9.1 m.s^{-1} . The Reynolds number Re is also modified and varies from 1.78×10^5 and 3.55×10^5 compared to the reference value of 3.21×10^5 . We assume that the flow assumptions defined in section 3.2 are not affected by these changes in Reynolds number.

We observe from the results shown in table 5.14 that the resulting motions have very similar reduced frequencies, motion amplitude and phase angles as the reference case. As the density is increased fourfold, the coefficients of average viscous drag $\overline{C_{D_{\text{viscous}}}}$ and power $\overline{C_P}$ increases by 14% and 12% respectively, mainly due to the increase in Reynolds number. Although the motion parameters remain almost unchanged, the changes in frequency f and required power \overline{P} are inversely proportional to the changes in flight velocity. We observe indeed that the frequency f and required power \overline{P} found for $\rho = 4.0 \text{ kg.m}^{-3}$ are almost half of the values found for $\rho = 1.0 \text{ kg.m}^{-3}$. If pterosaurs evolved in a atmosphere four times denser than today, these results indicate that they would have required half the power to sustain continuous flapping flight for the same motion. More importantly, these results indicate the optimal flapping gaits found with the aerodynamic model are not sensitive to the atmospheric density.

5.5.7 Impact of membrane stiffness

We described in chapter 4 the aeroelastic model, which includes the linearized deformations of the wing. We recall that the membrane was tensioned prior to being subject to the flight loads. Because the properties of the wing membrane are unknown, we study the impact of the membrane properties and of the Young's modulus in particular, while the thickness is kept constant at 1 mm. We compare in table 5.15

the flapping gaits found for three different cases of Young's modulus E and for the rigid wing defined in the aerodynamic model.

We find that the flapping gait of the rigid wing and the stiff membrane ($E = 1000$ MPa) are almost identical and yield the same values of required power and efficiency. For the membrane properties that we estimated in section 4.5.2 for the pterosaur membrane ($E = 100$ MPa), the flapping gait remains also quite similar with increases in amplitudes under 2 degrees. The angle of attack $\bar{\theta}$ increases significantly by 4 degrees. Because of the reduced stiffness, the deflections of the trailing-edge induce a loss in lift, which has to be compensated by an increase in angle of attack. This change in wing stiffness leads to an increase of 10 % in required power. We note that the values of frequency and required power are consistent with the values found for $\overline{C_L} = 1.0$ ($\bar{\theta} = 11.44$) listed in table 5.10.

For the flexible membrane ($E = 37$ MPa), the angle of attack $\bar{\theta}$ is further increased to 14 degrees (+6.5 degrees), which is consistent with the increases in trailing-edge deflections. We note however that the wrist pitch amplitude θ_3 is almost zero and that the sweep amplitude ψ_1 has more than tripled. This indicates that the trailing edge deflections of the flexible membrane induce a similar effect as the pitch rotation at the wrist for the rigid wing. In this case, we even find that the small pitch rotation has a 170 degrees phase shift with the rigid wing case thereby increasing the incidence angle of the outboard wing during the downstroke. This indicates that the motion is compensating for excess lift losses during the downstroke. The required power is increased by 57%, which indicates that no wing motion was found to compensate for the inefficient wing shape. As discussed in section 4.7.2, the twist distribution of the flexible membrane wing was not optimized for gliding flight prior to applying the wing motion, which would explain such an increase in mechanical power. The

joint positions at glide should therefore be optimized to correct the twist distribution before optimizing for the joint motion.

To shed more light on the efficiency of flexible membrane wings, future studies could include an optimization of the wing shape at glide, investigate the effects of the membrane tension during the wing motion and compare the advantages of a curved wing geometry. Further studies could also investigate the advantages and drawbacks of a trailing-edge tendon as observed in bats.

5.6 Comparison with published results

5.6.1 Comparison with published results for pterosaurs

Previous published estimates on required power for flapping flight of pterosaurs were based on gliding performance. Lighthill[143, 144] contended that the horizontal speeds for the minimum power and best cruising speeds for flapping flight are closely similar to the horizontal speeds respectively for the minimum sinking speeds and the best glide ratio during glide. Similarly, he argued that the required power for flapping flight was closely similar to the power to overcome the gliding drag at these two conditions.

Bramwell and Whitfield[5] estimated the minimum average power for level flapping flight at 68 W for a 16.6 kg specimen of *Pteranodon* flying at a speed of 7.7 m.s^{-1} . We note that they estimated the minimum sinking speed using the glide polar of the Gottingen 417a airfoil for a wing area of 4.62 m^2 . The corresponding average lift coefficient $\overline{C_L}$ is 0.9.

Similarly, Brower[24] estimated the minimum average power for level flapping flight at 96 W. This estimate was made for a 14.94 kg specimen of *Pteranodon* with

Table 5.9: Optimization results for the study on the impact of the joint motions. These results apply to a 160 N specimen of *Coloborhynchus robustus* flying at an average $\overline{C_L}$ of 0.5 and 0.7. The body accelerations are not included in these cases. All angles are expressed in degrees.

Case	J1	J2	J2	J3	J4	J5	J6
k	0.060	0.052	0.102	0.102	0.101	0.111	0.102
$\overline{\theta}$	5.45	5.59	7.52	7.52	8.08	7.77	7.52
ϕ_1	17.77	19.13	14.16	14.16	13.41	12.24	14.16
ψ_1		12.60	2.99	2.99	14.82	15.42	2.99
ψ_2				0.00	20.00	20.00	
θ_3	5.09	4.31	8.44	8.44	8.28	8.16	8.44
ψ_3					15.00	15.00	0.00
ψ_4						5.00	
φ_{ψ_1}		287.62	210.44	210.44	0.00	0.38	210.44
φ_{ψ_2}				0.00	233.88	231.33	
φ_{θ_3}	81.78	95.66	79.95	79.95	99.92	92.39	79.95
φ_{ψ_3}					127.50	130.44	0.00
φ_{ψ_4}						40.31	
ΔC_Z	0.0000	0.0000	0.0000	0.0000	0.0000	0.0000	0.0000
ΔC_X	0.0000	0.0000	0.0000	0.0000	0.0000	0.0000	0.0000
$\Delta C_{l_{max}}$	1.3843	1.5000	1.5000	1.5000	1.5000	1.5000	1.5000
ΔZ							
$\Delta \theta$							
$\Delta \dot{X}$							
$\overline{C_L}$	0.5000	0.5000	0.7000	0.7000	0.7000	0.7000	0.7000
$\overline{C_{D_{viscous}}}$	0.0185	0.0183	0.0212	0.0212	0.0212	0.0212	0.0212
$\overline{C_T}$	0.0234	0.0234	0.0303	0.0303	0.0303	0.0303	0.0303
$\overline{C_P}$	0.0286	0.0268	0.0407	0.0407	0.0376	0.0372	0.0407
$\overline{\eta}$	0.8172	0.8734	0.7448	0.7448	0.8056	0.8145	0.7448
f (Hz)	1.35	1.17	1.94	1.94	1.92	2.11	1.94
\overline{P} (W)	181.4	170.0	155.8	155.8	144.0	142.4	155.8

Table 5.10: Optimization results for the study on average lift coefficient. The reference results apply to a 160 N specimen of *Coloborhynchus robustus* flying at an average $\overline{C_L}$ of 0.7, considering the motion case J2. The body accelerations are not included in these cases. All angles are expressed in degrees.

$\overline{C_L}$	0.5	0.6	0.7	0.8	0.9	1.0	1.1
U_∞ (m.s ⁻¹)	19.8	18.1	16.8	15.7	14.8	14.0	13.4
k	0.052	0.080	0.102	0.113	0.131	0.136	0.157
$\overline{\theta}$	5.59	6.42	7.52	8.80	10.14	11.44	12.94
ϕ_1	19.13	14.94	14.16	14.89	14.97	15.36	15.10
ψ_1	12.60	0.00	2.99	4.62	5.72	8.11	9.83
ψ_2							
θ_3	4.31	6.18	8.44	10.59	12.85	13.28	15.15
ψ_3							
ψ_4							
φ_{ψ_1}	287.62	151.59	210.44	186.61	177.27	171.06	168.59
φ_{ψ_2}							
φ_{θ_3}	95.66	81.09	79.95	78.93	77.45	78.67	75.71
φ_{ψ_3}							
φ_{ψ_4}							
ΔC_Z	0.0000	0.0000	0.0000	0.0000	0.0000	0.0000	-0.0008
ΔC_X	0.0000	0.0000	0.0000	0.0000	0.0000	0.0000	-0.0006
$\Delta C_{l_{max}}$	1.5000	1.5000	1.5000	1.5000	1.5000	1.5002	1.5035
ΔZ							
$\Delta \theta$							
$\Delta \dot{X}$							
$\overline{C_L}$	0.5000	0.6000	0.7000	0.8000	0.9000	1.0000	1.0993
$\overline{C_{D_{viscous}}}$	0.0183	0.0197	0.0212	0.0229	0.0249	0.0277	0.0306
$\overline{C_T}$	0.0234	0.0265	0.0303	0.0347	0.0394	0.0448	0.0508
$\overline{C_P}$	0.0268	0.0332	0.0407	0.0501	0.0613	0.0756	0.0932
$\overline{\eta}$	0.8734	0.7980	0.7448	0.6923	0.6422	0.5934	0.5449
f (Hz)	1.17	1.65	1.94	2.02	2.20	2.16	2.39
\overline{P} (W)	169.8	160.2	155.8	156.9	161.0	169.4	181.2

Table 5.11: Optimization results for the study on the impact of the curved geometry and of the wing extent. The reference results apply to a 160 N specimen of *Coloborhynchus robustus* flying at an average $\overline{C_L}$ of 0.7, considering the motion case J2, with the planar geometry. All angles are expressed in degrees.

Case	Curved	Planar with hip attachment	Ankle attachment
k	0.104	0.102	0.163
$\bar{\theta}$	7.73	7.52	8.32
ϕ_1	14.91	14.16	16.11
ψ_1	4.05	2.99	6.24
ψ_2			
θ_3	7.81	8.44	10.12
ψ_3			
ψ_4			
φ_{ψ_1}	250.00	210.44	196.33
φ_{ψ_2}			
φ_{θ_3}	82.18	79.95	79.89
φ_{ψ_3}			
φ_{ψ_4}			
ΔC_Z	0.0000	0.0000	0.0000
ΔC_X	0.0000	0.0000	0.0000
$\Delta C_{l_{max}}$	1.5000	1.5000	1.5000
ΔZ			
$\Delta \theta$			
$\Delta \dot{X}$			
$\overline{C_L}$	0.7000	0.7000	0.7000
$\overline{C_{D_{viscous}}}$	0.0208	0.0212	0.0192
$\overline{C_T}$	0.0315	0.0303	0.0328
$\overline{C_P}$	0.0408	0.0407	0.0471
$\bar{\eta}$	0.7729	0.7448	0.6966
f (Hz)	1.91	1.94	2.50
\overline{P} (W)	151.3	155.8	144.7

Table 5.12: Optimization results for the study on the impact of the animal weight. The reference results apply to a 160 N specimen of *Coloborhynchus robustus* flying at an average $\overline{C_L}$ of 0.7, considering the motion case J2, without body accelerations. All angles are expressed in degrees.

Weight W (N)	80	160	240
U_∞ (m.s ⁻¹)	11.8	16.8	20.5
k	0.107	0.102	0.102
$\bar{\theta}$	7.54	7.52	7.50
ϕ_1	14.14	14.16	13.83
ψ_1	3.03	2.99	2.71
ψ_2			
θ_3	8.92	8.44	8.27
ψ_3			
ψ_4			
φ_{ψ_1}	204.24	210.44	211.21
φ_{ψ_2}			
φ_{θ_3}	79.56	79.95	80.33
φ_{ψ_3}			
φ_{ψ_4}			
ΔC_Z	0.0000	0.0000	0.0000
ΔC_X	0.0000	0.0000	0.0000
$\Delta C_{l_{max}}$	1.5000	1.5000	1.5000
ΔZ			
$\Delta \theta$			
$\Delta \dot{X}$			
$\overline{C_L}$	0.7000	0.7000	0.7000
$\overline{C_{D_{viscous}}}$	0.0228	0.0212	0.0204
$\overline{C_T}$	0.0319	0.0303	0.0295
$\overline{C_P}$	0.0433	0.0407	0.0392
$\bar{\eta}$	0.7356	0.7448	0.7526
f (Hz)	1.43	1.94	2.38
\overline{P} (W)	58.7	155.8	275.5

Table 5.13: Optimization results for the study on the impact of the body accelerations. The reference results apply to a 160 N specimen of *Coloborhynchus robustus* flying at an average $\overline{C_L}$ of 0.7, considering the motion case J2. The body accelerations are not included unless specified. All angles are expressed in degrees. We abbreviate body accelerations with body acc.

Case	J2	J2 with body acc.	J5	J5 with body acc.
k	0.102	0.132	0.111	0.140
$\bar{\theta}$	7.52	8.34	7.76	8.00
ϕ_1	14.16	14.89	12.24	12.38
ψ_1	2.99	2.53	15.42	1.58
ψ_2			20.00	7.09
θ_3	8.44	11.15	8.16	8.26
ψ_3			15.00	0.10
ψ_4			5.00	3.86
φ_{ψ_1}	210.44	181.76	0.38	64.09
φ_{ψ_2}			231.33	221.68
φ_{θ_3}	79.95	83.59	92.39	82.58
φ_{ψ_3}			130.43	341.40
φ_{ψ_4}			40.32	59.58
ΔC_Z	0.0000	0.0000	0.0000	0.0000
ΔC_X	0.0000	0.0000	0.0000	0.0000
$\Delta C_{l_{max}}$	1.5000	1.5000	1.5000	1.5000
ΔZ		0.0000		0.0000
$\Delta \theta$		0.0000		0.0000
$\Delta \dot{X}$		0.0000		0.0000
$\overline{C_L}$	0.7000	0.7000	0.7000	0.7000
$\overline{C_{D_{viscous}}}$	0.0212	0.0210	0.0212	0.0211
$\overline{C_T}$	0.0303	0.0303	0.0303	0.0303
$\overline{C_P}$	0.0407	0.0448	0.0372	0.0431
$\bar{\eta}$	0.7448	0.6759	0.8145	0.7038
f (Hz)	1.94	2.52	2.11	2.66
\overline{P} (W)	155.8	171.6	142.4	164.8

Table 5.14: Optimization results for the study on the impact of the atmospheric density. The reference results apply to a 160 N specimen of *Coloborhynchus robustus* flying at an average $\overline{C_L}$ of 0.7, considering the motion case J2, without body accelerations, with the atmospheric density taken at sea level ($\rho=1.23 \text{ kg.m}^{-3}$). All angles are expressed in degrees.

Density ρ (kg.m^{-3})	1.0	1.23	2.0	3.0	4.0
U_∞ (m.s^{-1})	18.2	16.8	12.9	10.7	9.1
Re ($\times 10^5$)	3.55	3.21	2.51	2.05	1.78
k	0.102	0.102	0.106	0.107	0.105
$\bar{\theta}$	7.52	7.52	7.53	7.55	7.58
ϕ_1	14.08	14.16	14.05	14.26	14.69
ψ_1	2.83	2.99	3.00	3.02	3.24
ψ_2					
θ_3	8.38	8.44	8.81	9.07	9.25
ψ_3					
ψ_4					
φ_{ψ_1}	209.13	210.44	206.49	200.75	200.1
φ_{ψ_2}					
φ_{θ_3}	80.54	79.95	79.32	80.06	80.16
φ_{ψ_3}					
φ_{ψ_4}					
ΔC_Z	0.0000	0.0000	0.0000	0.0000	0.0000
ΔC_X	0.0000	0.0000	0.0000	0.0000	0.0000
$\Delta C_{l_{max}}$	1.5000	1.5000	1.5000	1.5000	1.5000
ΔZ					
$\Delta \theta$					
$\Delta \dot{X}$					
$\overline{C_L}$	0.7000	0.7000	0.7000	0.7000	0.7000
$\overline{C_{D_{viscous}}}$	0.0209	0.0212	0.0224	0.0233	0.0241
$\overline{C_T}$	0.0300	0.0303	0.0314	0.0323	0.0331
$\overline{C_P}$	0.0401	0.0407	0.0427	0.0441	0.0454
$\bar{\eta}$	0.7476	0.7448	0.7363	0.7326	0.7288
f (Hz)	2.14	1.94	1.58	1.30	1.11
\overline{P} (W)	169.8	155.8	127.9	107.9	96.1

Table 5.15: Optimization results for the study on the impact of the membrane flexibility. These results apply to a 160 N specimen of *Coloborhynchus robustus* flying at an average $\overline{C_L}$ of 0.7. The body accelerations are not included in these cases. All angles are expressed in degrees.

Case	Rigid wing	E = 1000 MPa	E = 100 MPa	E = 37 MPa
k	0.102	0.102	0.112	0.103
$\overline{\theta}$	7.52	8.00	11.35	13.97
ϕ_1	14.16	14.35	15.49	15.50
ψ_1	2.99	3.19	4.15	13.92
ψ_2				
θ_3	8.44	8.44	9.65	0.32
ψ_3				
ψ_4				
φ_{ψ_1}	210.44	210.42	188.73	190.82
φ_{ψ_2}				
φ_{θ_3}	79.95	79.97	81.74	-89.65
φ_{ψ_3}				
φ_{ψ_4}				
ΔC_Z	0.0000	0.0000	0.0000	0.0000
ΔC_X	0.0000	0.0000	0.0000	0.0000
$\Delta C_{l_{max}}$	1.5000	1.5000	1.5000	1.5000
ΔZ				
$\Delta \theta$				
$\Delta \dot{X}$				
$\overline{C_L}$	0.7000	0.7000	0.7000	0.7000
$\overline{C_{D_{viscous}}}$	0.0212	0.0212	0.0214	0.0232
$\overline{C_T}$	0.0303	0.0303	0.0303	0.0303
$\overline{C_P}$	0.0407	0.0408	0.0447	0.0640
$\overline{\eta}$	0.7448	0.7428	0.6785	0.4737
f (Hz)	1.94	1.94	2.13	1.96
\overline{P} (W)	155.8	156.2	171.1	245.0

a wing area of 2.53 m^2 using a Sailvane 2 wing drag polar. The corresponding flight speed was 8.53 m.s^{-1} and the average lift coefficient $\overline{C_L}$ was 1.3.

More recently, Chatterjee and Templin[9] estimated the flight speeds and minimum required power for level flapping flight of *Pteranodon longiceps* and *Coloborhynchus robustus*, then named *Anhanguera piscator*, using a momentum stream tube model. For a specimen of *Pteranodon longiceps* weighing 162.9 N and with a wing area of 2.65 m^2 , the minimum average power was estimated at 53 W for a flight speed of 9.30 m.s^{-1} . The corresponding average lift coefficients $\overline{C_L}$ was 1.16. For a specimen of *Coloborhynchus robustus* weighing 74.4 N with a wing area of 2.12 m^2 , they estimated the minimum average power at 25 W corresponding to a flight speed of 8.6 m.s^{-1} . The corresponding average lift coefficients $\overline{C_L}$ was 0.78.

Because the estimated wing area for these results was at least 2.0 m^2 , we compare these results with those for the ankle attachment, as summarized in table 5.16. We note that our estimates of wing area and weight compare well with values for *Pteranodon* given by Brower[24] and Chatterjee and Templin[9]. We therefore compare our estimates for *Coloborhynchus robustus* with these two studies of *Pteranodon*. We first note the differences in the flight speeds and average lift coefficients. The minimum sinking speed computed for glide depends on the choice of airfoil, and Brower[24] and Chatterjee and Templin[9] reported flight speed corresponding to average lift coefficients between 1.3 and 1.2 respectively, which are respectively 31 and 37% slower than our estimates. We also note that our power estimates differ by 39% and 63% respectively. This level of discrepancy is expected because these two studies consider a propulsive efficiency of 100%.

For this reason, we also compare our estimates with results computed by de Laurier[23], who estimated the required power for the 18 kg (40 lbs) QN replica

of *Quetzalcoatlus northropi* described by Brooks et al.[22]. Using an unsteady three-dimensional aerodynamic code, he explored the most suited twisting motion of the wing for a set flight speed of 13.4 m.s^{-1} (44 ft.s^{-1}) and root flapping amplitude ϕ_1 of 20 degrees. The twisting motion had a 90 phase angle relative the root flapping motion and the twist angle varied linearly with the span. The wing had a Liebeck LPT 110A airfoil along the span. The average chord c_{ref} was estimated at 0.41m (16.05") and the wing area S_{ref} at 2.24 m^2 . At this flight speed, the required steady angle of attack $\bar{\theta}$ to achieve enough lift amounted to 7.5 degrees and the wing motion had a frequency of 1.2 Hz. The corresponding average lift coefficient $\overline{C_L}$ and reduced frequency k were estimated at 0.72 and 0.12 respectively. The maximum propulsive efficiency of 0.42 was found for a twisting amplitudes of $7.4 \text{ degrees.m}^{-1}$ ($2.25 \text{ degrees.ft}^{-1}$) over the 5.5m (18ft) span. The corresponding twist amplitude at mid-span and at the tip were about 10 degrees and 20 degrees respectively. The corresponding average power \overline{P} was estimated at roughly 170 W.

Although the wing area and weight are a little bit different with our model, we note that our results are generally quite similar. The average lift coefficient $\overline{C_L}$ is 0.70 instead of 0.72 and the average angle of attack $\bar{\theta}$ is slightly higher by 0.6 degrees. However the reduced frequency k is 30% higher and the shoulder flapping amplitude ϕ_1 is smaller by 4 degrees. The twist amplitude at mid-span (10 degrees) is the same as the wrist pitch amplitude θ_3 , although the phase angles differ by 10 degrees. The minimum required average power is smaller by 15% (145 W compared to 170 W), which is larger than between the motions J1 and J2 (-7%). This is probably due to the differences in wing area and mass between the QN replica and our estimates for *Coloborhynchus robustus*.

In all, the estimates from this study agree quite well with the results reported

Table 5.16: Published estimates for minimum flapping power of pterosaurs of similar size and weight to *Coloborhynchus robustus*. Our estimates are for a 160 N specimen of *Coloborhynchus robustus* with the wing membrane attached to the ankle, flying at an average $\overline{C_L}$ of 0.7, considering the motion case J2, without body accelerations, with the atmospheric density taken at sea level ($\rho = 1.23 \text{ kg.m}^{-3}$). *Coloborhynchus robustus*, Average and Minimum are abbreviated *Colobor.*, Ave. and Min. respectively.

Reference	Species	Weight (N)	Wing area (m ²)	Flight speed (m.s ⁻¹)	Ave. lift $\overline{C_L}$	Min. power (W)
Bramwell & Whitfield[5]	<i>Pteranodon</i>	162.9	4.62	7.7	0.9	68
Brower[24]	<i>Pteranodon</i>	146.6	2.53	8.5	1.3	96
Chatterjee & Templin[9]	<i>Pteranodon</i>	162.9	2.65	9.3	1.16	53
Chatterjee & Templin[9]	<i>Colobor.</i>	74.4	2.12	8.6	0.78	25
de Laurier[23]	QN replica	176.6	2.24	13.4	0.72	170
Reference geometry	<i>Colobor.</i>	160.0	1.33	16.8	0.70	156
with ankle attachment	<i>Colobor.</i>	160.0	2.04	13.5	0.70	145

by de Laurier[23], while there are large differences with other published results. We therefore discuss in the next section the differences between power estimated for a flapping wing and for a fixed wing.

5.6.2 Comparison with estimates computed with 100% propulsive efficiency

As discussed above, most published results on the flapping flight of pterosaurs estimated the required flapping power as the product $D_{\text{total steady-state}} \times U_{\infty}$ of the total steady-state drag $D_{\text{total steady-state}}$ and the flight velocity U_{∞} . This corresponds to the power of a flapping motion with a propulsive efficiency of 100%. We therefore compare such values of power with the computed power for the optimal flapping motion with the reference motion J2 over a range of average lift coefficient $\overline{C_L}$ ($0.5 < \overline{C_L} < 1.1$).

Average lift coefficient

In the case of flapping flight, the motion of the wing induces significant changes in the angle of incidence, especially near the tip, and hence in the section lift coefficient. The optimization results in section 5.5 show that the constraint on maximum section lift coefficient has been met for all solution. This indicates that the section lift coefficient has reached the maximum allowed value during at least one time step of the motion, and this although the optimal average lift coefficient for the flapping flight of pterosaurs corresponds to an average lift coefficient around 0.7. If the animal flew at the minimum sinking speed, it would therefore have been limited in its ability to vary the lift coefficient and to produce thrust without stalling the wing.

Required flapping power

Figure 5.6(a) and table 5.17 compare the power estimates for the optimal flapping motion and for 100% efficiency at different values of lift coefficients $\overline{C_L}$. We find that there are significant differences ranging between 13% to 46% in the power estimates. This indicates that typical flapping motion can be far from being 100% efficient and estimates of required power should account for the efficiency losses occurring during the wing motion.

Propulsive efficiency

Figure 5.6(b) shows the variation of propulsive efficiency as a function of required thrust. We observe that the propulsive efficiency increases from 54% to 87% as the required thrust coefficient decreases, which corresponds to an increase in average flight speed. This suggest that to achieve high propulsive efficiency, a flying animal, such as a migratory bird, would fly as fast as possible within its biological constraints, and

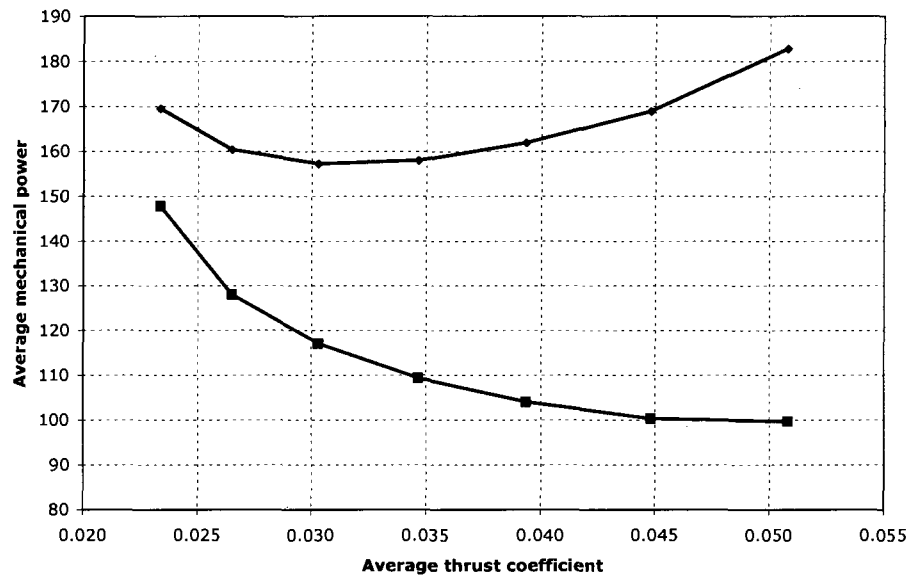
Table 5.17: Comparison of required mechanical power at different values of average lift coefficient $\overline{C_L}$ estimated for the optimal flapping motion and for 100% efficiency. We also list the propulsive efficiency $\overline{\eta}$ calculated for the optimal wing motion. The reference results apply to a 160 N specimen of *Coloborhynchus robustus* flying at an average $\overline{C_L}$ of 0.7, considering the motion case J2, without body accelerations, with the atmospheric density taken at sea level ($\rho = 1.23 \text{ kg.m}^{-3}$). All angles are expressed in degrees.

$\overline{C_L}$	Optimal Flapping			Gliding	
	C_P	P (W)	$\overline{\eta}$	$C_{D_{\text{total steady-state}}}$	$D_{\text{total steady-state}} \times U_{\infty}$ (W)
0.5	0.0268	169.8	0.8734	0.0234	147.8
0.6	0.0332	160.2	0.7980	0.0265	128.0
0.7	0.0407	155.8	0.7448	0.0303	117.0
0.8	0.0501	156.9	0.6923	0.0347	109.3
0.9	0.0613	161.0	0.6422	0.0394	103.9
1.0	0.0756	169.4	0.5934	0.0448	100.2
1.1	0.0932	181.2	0.5449	0.0508	99.6

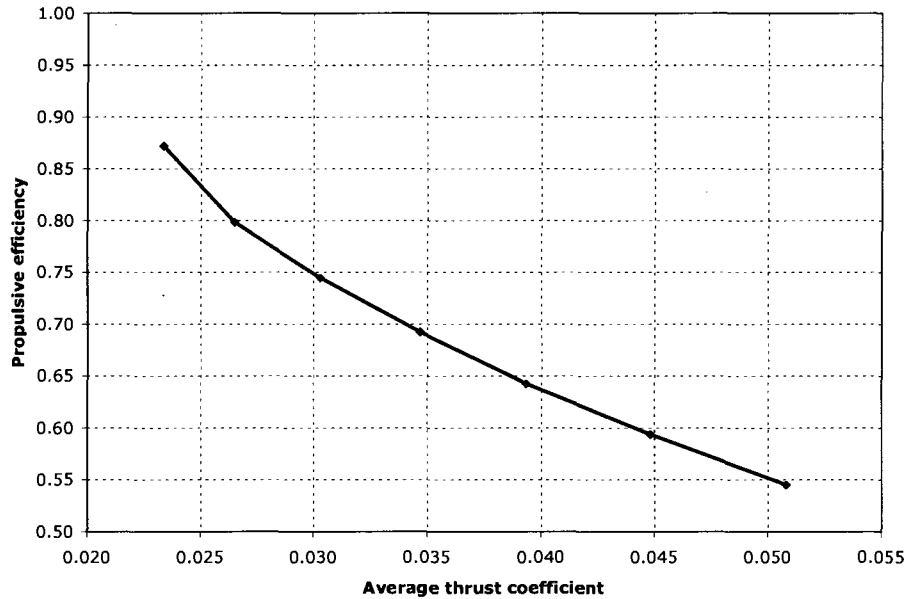
therefore would have wings with high aspect ratio and wing loadings.

In section 2.4.4, we estimated the propulsive efficiency for the European Starling. The estimated propulsive efficiencies ranged between 47% and 56% at the speed for minimum drag, while the computed propulsive efficiency for *Coloborhynchus robustus* is 74% at the speed for minimum required power. This last value of propulsive efficiency is computed in the pure aerodynamic case without accounting for the inertial or structural effects. Future studies on migratory birds could focus on estimating the propulsive efficiency for species with extraordinary migration patterns such as the Bar-Tailed Godwit and the Great Knot.

For comparison purposes, the propulsive efficiency of a propeller producing the same amount of thrust at the flight speed considered for *Coloborhynchus robustus* would be in the range of 80-90%. Using XROTOR[145], Parks[146] proposed several propeller designs that would achieve propulsive efficiencies of 86-89% at the design point considered ($\overline{T} = 7 \text{ N}$, $U_{\infty} = 16.8 \text{ m.s}^{-1}$).



(a) Comparison of the average mechanical power \bar{P} (in W) for the optimal flapping motion (blue line) and for 100% efficiency (green line) as a function of average thrust coefficient \bar{C}_T .



(b) Propulsive efficiency for the optimal flapping motion as a function of the average required thrust \bar{C}_T .

Figure 5.6: Mechanical power and propulsive efficiency for the optimal flapping motion as a function of average thrust coefficient.

5.7 Summary

In this chapter, we have described the optimization problem used to find the most relevant joint motions for propulsive efficiency. We have detailed the variables taken into account and the required constraints. We have then presented the two optimization algorithms we have used, and the strategy we have used to combine the advantages of both algorithms. We start by exploring the design space using a binary genetic algorithm, and then use the best design points found by GA as starting points for a sequentially quadratic programming algorithm. From these starting points, we have observed that the optimization has found in most cases only one optimal solution.

We have shown the results of the optimization using the aerodynamic and the aeroelastic models of the pterosaur wing. Using the aerodynamic model, we have investigated the role of the joint motions and studied the sensitivity of the reference case to the flight speed, wing geometry, weight estimate, atmospheric density and the impact of body accelerations. Using the aeroelastic model, we have investigated the impact of the choice of membrane properties on the optimal wing motion.

Our results from the aerodynamic problem have shown that the sweep motion at the shoulder provides a significant reduction of 11% in minimum power compared to the usual flapping and twisting motion of the wing. The combined motions of the other joints also provide a significant reduction of 9% in minimum power. In both cases, the flapping gaits were consistent with observations made for birds. The flight speed in the form of the average lift coefficient has a big influence on the wing motion and flapping performance. We show that the minimum required power is reached for a flight speed corresponding to an average lift coefficient of $\overline{C_L} = 0.7$. The point of attachment of the membrane, hence the wing area, reduces the flight speed by 20% and the required power by 7%. Accounting for the body accelerations leads to significant

changes in the motion and leads to an increase of 10% to 16% in required power. A variation in weight and atmospheric density does not yield a change in motion but has an impact on the required power. Increasing the atmospheric density by a factor of four can almost halve the required power. We also investigated the aeroelastic effects during flapping flight for three cases of stiffness of the wing membrane. We found that the flapping gait and required power are very similar for a stiff wing and the rigid wing defined in the aerodynamic model. As the stiffness of the membrane is reduced, the trailing-edge deflections induce losses that are compensated by an increase in angle of attack and sweep motion amplitude. We found that the required power increased by 10% and 57% respectively for the properties inferred for the pterosaur membrane and for a flexible membrane. This indicates that the optimization did not find a wing motion that corrected the aerodynamic inefficiencies due to the membrane deformations.

Finally, the flapping gait, optimal speed and required power compare well with published results for similar wing motions. The optimal speed is found to be 31% to 37% faster than previous estimates based on glide performance. Some previous estimates of required power assumed a propulsive efficiency of 100%, whereas the propulsive efficiency computed for *Colobrhynchus robustus* ranges between 54% and 87%.

Chapter 6

Conclusion

6.1 Summary of results

In this study, we first described the available information on a specimen of *Coloborhynchus robustus* and estimated the missing information relevant to flapping flight. We estimated the mass distribution in the wing by accounting for the mass of the bones, the membrane and the muscle tissue. The mass distribution of the muscle tissue was inferred by comparison with the inertial properties of the wings measured for birds and bats. We then estimated the total mass of the animal by adding the mass of the head, neck, torso and legs, which were calculated using techniques described in previous pterosaur studies. We also motivated the choice of propulsive efficiency as a relevant optimization objective and estimated the propulsive efficiencies for one species of migratory birds.

The propulsive efficiency is computed from the aerodynamic forces created during the flapping gait. These forces were computed by the unsteady three-dimensional code, referred to as UVLM, that we developed based on the vortex-lattice method.

We showed that UVLM compares well with published results for unsteady motions of rectangular wings. In the aerodynamic model of the pterosaur wing, we assumed a rigid outer wing and therefore defined the wing geometry by the position of the bones.

We then accounted for the fluid-structure interactions using a loose coupling scheme. We compared the results computed using this scheme with experiments for an ornithopter in free flight. Because of key missing information during the flights, the comparisons were inconclusive which underlines the difficulty of such comparisons. In the aeroelastic model of the pterosaur wing, we added the flexibility of the bones and of the wing membrane. We showed that the finite-element method used to model the wing compared well with analytical results for a two-dimensional membrane and a circular membrane under uniform pressure. We assumed that the nonlinear structural behavior of the membrane was linear assuming small deflections about the reference wing geometry, which was computed for the membrane subject to glide loads and pretension from the wing joint positions. The structural behavior of the wing was reduced using a modal decomposition and we showed that the first five modes accounted for most of the deformations during flapping flight.

The flapping gait was optimized in a two-stage procedure. We discussed why the mechanical power was a better objective function for the optimization without significantly changing the optimization problem. We applied this procedure to investigate the advantage of each joint motion by minimizing the mechanical power required to satisfy the constraints defined for cruise level flapping flight. By combining the advantages of a binary GA and of a SQP method, we successfully optimized the wing motion. We found that the optimal motions were in agreement with previous results

for simple wing motions. The addition of the shoulder sweep motion reduced the required power by 7%. If all the joint motions were considered, the required power was reduced by another 9% and the vertical motion of the tip was similar to measurements for birds.

Because of the large uncertainties for some estimates, we also investigated the sensitivity of the optimized flapping gait to several key parameters. The optimal motions were sensitive mainly to flight speed, body accelerations, and to the material properties of the wing membrane. The optimal flight speed was found to correspond to an average lift coefficient of $\overline{C_L} = 0.7$, which is about 31% to 37% faster than previous estimates based on glide performance. When the body accelerations were included, the required power was increased by 10% to 16%. When the aeroelastic effects were included, the optimal flapping gait was only slightly modified to accommodate for the deflections of stiff membranes. For a flexible membrane, the motion was significantly modified and the power increased by up to 57%.

Finally, the flapping gait and required power compared well with published results for similar pterosaur wing motions. Some previous estimates of required power assumed a propulsive efficiency of 100%, whereas the propulsive efficiency computed for *Coloborhynchus robustus* ranged between 54% and 87%.

6.2 Discussion of the methods and results

6.2.1 Mass estimates

We estimated the total mass using methodologies of previous studies. These studies estimated the body volume and calculated the mass by assuming a tissue density. However the estimates can greatly vary depending on the volume estimated from the

fossils and the chosen tissue density. We estimated the mass distribution in the wing from inertial considerations observed in birds. We do not know a priori if pterosaurs would have exhibited similar trends in inertia distribution as birds. Similarly to birds, the wing of pterosaurs is supported by a single digit unlike bats. Furthermore, birds are generally bigger than bats. A comparison with birds was therefore deemed the most reasonable. Only a detailed study of the required musculature in the wing could provide better estimates in both the total mass and mass distribution.

6.2.2 Aerodynamic model

In the aerodynamic model, we assumed a simplified wing geometry of *Coloborhynchus robustus*. We assumed a thin membrane wing, whereas the inner wing is believed to feature airsacks and significant tissue volume. Because thrust is mainly produced by the motion of the outer wing, this simplification does not affect the optimal wing motion. We also simplified the airfoil shapes along the wing considering flat plate airfoils, because the precise airfoil shape could not be inferred with the current paleontological knowledge. A flat plate approximation captures the main aerodynamic effects of an airfoil. These approximations therefore seem reasonable to study the relative advantage of each joint motions.

To compute the average thrust necessary to overcome the viscous drag forces, we computed the drag using a turbulent flat plate model. Although this approximation seems reasonable to calculate the drag on the wing, we approximated the head, neck and torso of the pterosaur as an elongated ellipse. The steady value of the body drag could be refined using high-fidelity methods once the shape of the body can be more precisely inferred.

6.2.3 Aeroelastic model

In the aeroelastic model, we first modeled the bone structure with geometric simplifications and by assuming stiff joints. Although we expected the membrane deflections to dominate the deformations, we also expected some visible interactions with the bones. The chosen values for the bone thickness could have been overestimated. However the measurements for the specimen we considered were not available and could only be estimated from values available for pterosaurs of similar sizes. The flexibility of the joints has been observed and simulated. However joint models are very complex and the flexibility cannot easily be reduced to a simple model unless derived from experimental measurements. We simplified the complex membrane structure of pterosaurs to an isotropic membrane model with a uniform thickness distribution. It is likely that the anisotropic properties and the variation of thickness would have played an important role. However, in light of the uncertainties in the material properties of the wing membrane, a sensitivity study using our model provides an important first step in understanding the structural effects during the optimal wing motion. Additionally, we assume that the membrane maintained a linear behavior during the wing motion. There is no current argument for or against such an assumption for pterosaurs. The membrane wing behavior is still being studied for the flapping flight of bats and such studies could provide better insights on the role of large joint motions during the flapping gait.

6.2.4 Optimization convergence

The optimization procedure did not always converge to an optimal solution, although a feasible solution was usually found. Although the quantities computed by UVLM appeared to be smooth in the parametric sweep, these functions might not be smooth

enough for SNOPT in all cases. In particular, we recall that the maximum section lift coefficient $C_{l_{\max}}$ computed during the motion is in fact the maximum absolute value of the section lift coefficient. The derivatives are computed by SNOPT by finite differences. Because of the relatively coarse grid used in UVLM, two slightly different motions might have values of $C_{l_{\max}}$ that are sufficiently different to create large gradients. This problem could be resolved by increasing the number of spanwise panels on the wing or by calculating the derivatives directly in UVLM to ensure smoother gradients.

6.2.5 Results

The connecting tissue of a joint - muscle, ligaments, cartilages and tendons - limits its possible range of motion. The ranges of joint motions were inferred from the bone fossils, and could therefore be beyond the actual values. However, the amplitudes of motion found for the optimal flapping gaits are well within the bounds except for the case where all the joint motions are considered. In this case, the wingspan is slightly increased. This indicates that the optimization might have found an error in the aerodynamic model or that a constraint on the average wingspan should be added. The results for the joint motions suggest that the large range of motion could have been used for extreme cases like take-off and landing.

We found that the optimal flapping gaits showed similar trends with motions observed in birds, in particular for the vertical motion of the tip. However, the variations in the spanwise position of the tip were not as large as seen in birds. This would indicate an effect linked to having such large span. However, most of the motions published in unsteady aerodynamic studies have not yet investigated the sweep motions, and the results we have found could therefore not be compared.

Similarly, the trends observed in the sensitivity studies were in line with expectations, but could not be compared with more detail. Future studies of flapping flight with unsteady methods could provide more insights on the validity of our results.

6.3 Future work

6.3.1 Model of the pterosaur wing

Bone geometry and joint flexibility

We modeled the wing bones as tubes of constant cross-section and assumed that these were stiffly connected at the joints. Consequently, the wing bones acted as stiff structures in our model. However the flexibility of the joints play an important role in animal locomotion. Further studies could first refine the model of the wing structure by refining the mechanical properties using the detailed shape and thickness distribution of the preserved fossils. A dynamic model of the flexibility of each joint could then be added to investigate the structural interactions between the bones and the membrane.

Wing musculature

Among the features found on fossils, ligament and tendon scars on the bones can yield important information on muscle attachments. It is believed that archosaurs may be close evolutionary relatives of pterosaurs and therefore muscle functions and morphology could show some similarities. These studies depend on the quality of the fossils and the difficulty of interpretation relies on the correct identification of ligament and tendon scars. The study of flapping motion is connected to the study of musculature in the wing. A proposed flapping motion can yield interesting insights

on required muscle motion, power, and volume. Inversely musculature inferred from the fossils can impose constraints on the possible flapping motions. A relevant topic for future studies would be to couple our methodology with a detailed analysis of required power and muscle volume at each active joint, such as the one described by Delp and Loan[147]. In turn, from the volume of muscles, we could refine the estimates of mass distribution and the aerodynamic shape of the wing near the wing bones.

Membrane model

In this study, we conducted a preliminary study of the membrane effects in flapping flight. Future studies could include an optimization of the wing shape at glide and investigate the performance of a curved wing geometry.

Future findings could shed new light on the detailed structure of the membrane by characterizing the material properties found in fossil fragments of the membrane. Future studies could investigate the role of the orientation of the actinofibrils observed in the fossil remains. It would be also of interest to simultaneously study the role of inflatable sacks along the wing bones.

If pterosaurs had muscle in the wing membrane skin, it is likely that these would have been used to actively control the shape of the membrane. Studying the impact of actively changing the stress distribution in the wing would therefore be key in assessing the size, distribution, and energy expenditure of such muscles.

Hair on the wing

Several pterosaur fossil remains exhibited imprints of hair on the body. Although the morphology of pterosaur hair seems quite different from mammals, these findings raise

the question of the extent of the hair coverage, and consequently of its function. These findings suggest that pterosaurs could regulate their body temperature similarly to warm-blooded animals. It is not clear whether hair was present on the wings. If it had been the case, it is likely that the hair would be concentrated near the bones and muscles, and to assume that the density of the hair coverage would not undermine the aerodynamic performance of the wing. Using advanced CFD methods and a refined wing shape, a future study could investigate the aerodynamic effects of hair density and location on the wing and inform on reasonable hair coverage on the wing.

6.3.2 Other flight conditions

Take-off and landing gaits

In this study, we focused only the level flapping flight of pterosaurs and did not investigate the other stage of flight such as take-off, landing, and turns. Because of their large size and hence their considerable weight, the take-off and landing speeds of derived pterosaurs would have been significantly higher than current flying vertebrates in today's atmosphere. Although landing tracks attributed to pterosaurs have been found for smaller pterosaurs, the question remains whether larger pterosaurs could have slowed down prior to landing such that the landing impact forces could be sustained by their lower limb structure. Because they are believed to be quadrupedal on the ground, the take-off gait remains a source of numerous theories. An unsteady aerodynamic study using advanced CFD methods appropriate for unsteady high-lift conditions could test these different flight conditions and investigate the impact of the atmospheric density and weight.

Stability and control

Many questions remain open for the flight controls of pterosaurs during turns and in response to gusts. The uropatagium is too small and too close to the body to create moments, which would provide significant control authority in typical cruise flight conditions. A pterosaur is essentially a flying wing with all the flights controls operated on the wing. Although it is understood how pterosaurs would have moved their wings in a general sense using classical aerodynamic results, it is still unclear how they would have moved their joints to create such changes in the membrane shape. Pterosaurs would have had to move its joints in order to taylor the stress distribution, controlling the wing shape and hence indirectly creating the desired moments. The flight stability and control problem of pterosaurs could therefore be investigated in an optimization problem. Modeling the fully nonlinear deformations on the membrane would probably be required to optimize the motions of the wing joints, the pteroid bone and of the legs to create desired moments while maintaining sufficient lift.

Role of the head motion

Derived pterosaurs also had a large head placed in front of a long neck. During flight, the pressure forces on the head could create yawing moments, that perturb the flight stability of the animal. It is likely that the head would have moved actively during flight to reduce these adverse yawing moments. However, it is believed that pterosaurs like *Coloborhynchus robustus* would have caught their preys while flying, and this raises the question of how they would have achieved these maneuvers while maintaining their flight path.

6.3.3 High-fidelity refinements

We have shown that the methods used in this study capture the main aerodynamic and structural effects of flapping flight. Refining the structural model of the membrane could be key in understanding the joint motions during the flapping gait. If the nonlinear effects are not too severe, the modal decomposition of the wing could be computed for a set of flight conditions. The modal decomposition at a given time could then be interpolated using matrix interpolation techniques such as the one described by Amsallem and Farhat[116]. Otherwise, an unsteady nonlinear membrane model would have to be considered.

Future studies could also refine the current results using high-fidelity methods. Multi-fidelity approaches such as the one described by Rajnarayan et al.[148] could combine the speed of our method and the accuracy of more advanced methods. Non-linear aerodynamic and structural effects could be explored with such methods. The importance of viscous effects and of dynamic stall could be measured and used to refine the assumptions we have made.

Bibliography

- [1] J. Katz and A. Plotkin, *Low-Speed Aerodynamics 2nd edition*, Cambridge University Press, 2001.
- [2] A. W. A. Kellner and Y. Tomida, “DESCRIPTION OF A NEW SPECIES OF ANHANGUERIDAE (PTERODACTYLOIDEA) WITH COMMENTS ON THE PTEROSAUR FAUNA FROM THE SANTANA FORMATION (APTIAN-ALBIAN), NORTHEASTERN BRAZIL,” *National Science Museum monographs*, vol. 17, pp. ix–137, 2000.
- [3] J. R. Cunningham, “Private Communications,” 2004-2005.
- [4] M. T. Wilkinson, “Three-dimensional geometry of a pterosaur wing skeleton, and its implications for aerial and terrestrial locomotion,” *Zoological Journal of the Linnean Society*, vol. 154, no. 1, pp. 27–69, 2008.
- [5] C. Bramwell and G. R. Whitfield, “Biomechanics of Pteranodon,” *Philosophical Transaction of Royal Society of London B*, vol. 267, pp. 503–581, 1974.
- [6] M. B. Habib, “Private Communications,” 2008.

- [7] S. C. Bennett, "The Osteology and Functional Morphology of the Late Cretaceous Pterosaur *Pteranodon*," *Palaeontographica A*, vol. 260, pp. 133–153, 2001.
- [8] P. Wellnhofer, *The Illustrated Encyclopedia of Prehistoric Flying Reptiles*, Barnes and Noble, 1991.
- [9] S. Chatterjee and R. J. Templin, "Posture, Locomotion and Paleoecology of Pterosaurs," Special Paper 376, The Geological Society of America, 2004.
- [10] C. J. Pennycuik, "FLIGHT 1.20 for Windows," <http://www.bio.bristol.ac.uk/people/pennycuik.htm>.
- [11] S. Ward, U. Moller, J. M. V. Rayner, D. M. Jackson, D. Bilo, W. Nachtigall, and J. R. Speakman, "Metabolic power, mechanical power and efficiency during wind tunnel flight by the European starling *Sturnus vulgaris*," *Journal of Experimental Biology*, vol. 204, no. 19, pp. 3311–3322, 2001.
- [12] S. Morris, "Stiff Wing Ornithopter Experiments," <http://www.ornithopter.org/forum/showthread.php?t=324>, April 2006.
- [13] C. T. Sun, *Mechanics of aircraft structures*, Wiley-Interscience, 1998.
- [14] K. A. Zittel, "Über Flugsaurier aus dem lithographischen Schiefer Bayerns," *Palaeontographica*, vol. 29, pp. 47–80, 1882.
- [15] S. C. Bennett, "Private Communications," 2004–2005.
- [16] S. C. Bennett, "Pterosaur Flight: The Role of Actinofibrils in Wing Function," *Historical Biology*, vol. 14, pp. 255–284, 2000.

- [17] C. van der Berg and J. M. V. Rayner, "The Moment of Inertia of bird Wings and the Inertial Power Requirement for Flapping Flight," *Journal of Experimental Biology*, vol. 198, pp. 1655–1664, 1995.
- [18] M. F. Neef, *Analyse des Schlagfluges durch numerische Strömungsberechnung*, Ph.D. thesis, Technische Universität Braunschweig, 2002.
- [19] K. D. Jones, B. M. Castro, O. S. Mahmoud, J. Pollard, M. F. Platzer, M. F. Neef, K. Gonet, and D. Hummel, "A Collaborative Numerical and Experimental Investigation of Flapping-Wing Propulsion," in *40th AIAA Aerospace Sciences Meeting and Exhibit, Reno, NV*, Jan. 14-17 2002.
- [20] K. D. Jones and M. F. Platzer, "Numerical Computation of Flapping-Wing Propulsion and Power Extraction," in *35th AIAA Aerospace Sciences Meeting and Exhibit, Reno, NV*, 1997.
- [21] G. Cuvier, "Mémoire sur le squelette fossile d'un Reptile volant des environs d'Aichstedt, que quelques naturalistes ont pris pour un oiseau, et donc nous formons un genre de Sauriens, sous le nom de Ptero-Dactyle," *Annales du Musée d'Histoire Naturelle Paris*, vol. 13, no. 424-437, 1809.
- [22] A. N. Brooks, P. B. MacCready, P. B. S. Lissaman, and W. R. Morgan, "Development of a wing-flapping flying replica of the largest Pterosaur," in *AIAA/SAE/ASME/ASEE 21 st Joint Propulsion Conference*, 1985.
- [23] J. D. DeLaurier, "An aerodynamic model for flapping-wing flight," *Aeronautical Journal*, vol. 97, no. 964, pp. 125–130, 1993.

- [24] J. C. Brower, "The Aerodynamics of Pteranodon and Nyctosaurus, Two Large Pterosaurs from the Upper Cretaceous of Kansas," *Journal of Vertebrate Paleontology*, pp. 84–124, 1983.
- [25] H. Jex, "MAKING PTERODACTYLS FLY As Presented By Henry Jex at TWITT Meeting July 15, 2000," <http://www.twitt.org/QNStory.html>, February 2003.
- [26] M. Gerritsen, "Stanford University - National Geographic Replica Project," <http://pterosaur.stanford.edu/>, 2004.
- [27] National Geographic Society (US) and W.H. Video, *Sky Monsters*, Number SKYM401. Warner Home Video, 2006.
- [28] D. M. Unwin, *The pterosaurs from deep time*, Pi Press, New York, 2005.
- [29] M. T. Wilkinson, D. M. Unwin, and C. P. Ellington, "High lift function of the pteroid bone and forewing of pterosaurs," *Proceedings of the Royal Society B: Biological Sciences*, vol. 273, no. 1582, pp. 119–126, 2006.
- [30] D. M. Martill and D. M. Unwin, "Exceptionally well preserved pterosaur wing membrane from the Cretaceous of Brazil," *Nature*, vol. 340, pp. 138–140, 1989.
- [31] E. Frey, H. Tischlinger, M. C. Buchy, and D. M. Martill, "New specimens of Pterosauria (Reptilia) with soft parts with implications for pterosaurian anatomy and locomotion," *Geological Society London Special Publications*, vol. 217, no. 1, pp. 233, 2003.
- [32] A. J. de Ricqlès, K. Padian, J. R. Horner, and F. Francillon-Vieillot, "Palaeohistology of the bones of pterosaurs (Reptilia: Archosauria): Anatomy, Ontogeny,

- and Biomechanical Implications,” *Zoological Journal of the Linnean Society*, vol. 129, pp. 349–385, 2000.
- [33] J. D. Currey, *Bones: structure and mechanics*, Princeton Univ Pr, 2002.
- [34] S. Chatterjee, R. J. Templin, and K. E. Campbell, “The aerodynamics of *Argentavis*, the world’s largest flying bird from the Miocene of Argentina,” *Proceedings of the National Academy of Sciences*, vol. 104, no. 30, pp. 12398, 2007.
- [35] D. A. Lawson, “Pterosaur from the latest Cretaceous of west Texas: discovery of the largest flying creature,” *Science*, vol. 187, no. 4180, pp. 947, 1975.
- [36] J. H. McMasters and R. M. Cummings, “Airplane design and the biomechanics of flight- A more completely multi-disciplinary perspective,” in *42nd AIAA Aerospace Sciences Meeting and Exhibit*, 2004.
- [37] M. I. Budyko, A. B. Ronov, and A. L. Yanshin, “The history of the atmosphere,” *Gidrometeoizdat, Leningrad*, 1985.
- [38] O. Levenspiel, T. J. Fitzgerald, and D. Pettit, “Earth’s early atmosphere,” *Chemical Innovation*, vol. 30, no. 5, pp. 47–51, 2000.
- [39] R. Dudley, “Atmospheric oxygen, giant Paleozoic insects and the evolution of aerial locomotor performance,” *Journal of Experimental Biology*, vol. 201, no. 8, pp. 1043–1050, 1998.
- [40] J. Conway, “The Structure of a Pterosaur,” <http://palaeo.jconway.co.uk/>, 2008.
- [41] M. Thollessen and U. M. Norberg, “Moments of Inertia of Bat Wings and Body,” *Journal of Experimental Biology*, vol. 158, pp. 19–35, 1991.

- [42] C. J. Pennycuick, *Bird flight performance: a practical calculation manual*, Oxford University Press Oxford, 1989.
- [43] C. J. Pennycuick, *Modelling the flying bird*, Academic Press, 2008.
- [44] S. M. Swartz, M. S. Groves, H. D. Kim, and W. R. Walsh, “Mechanical properties of bat wing membrane skin,” *Journal of Zoology*, vol. 239, no. 2, pp. 357–378, 1996.
- [45] T. J. Mueller and J. D. DeLaurier, “An overview of micro air vehicle aerodynamics,” in *Fixed and flapping wing aerodynamics for micro air vehicle applications*. 2001, vol. 195 of *Progress in Astronautics and Aeronautics*, AIAA.
- [46] U. S. Geological Survey, “Bird Completes Epic Flight Across the Pacific,” <http://www.usgs.gov/newsroom/article.asp?ID=1774>, September 2007.
- [47] V. A. Tucker, “Bird metabolism during flight: evaluation of a theory,” *Journal of experimental biology*, vol. 58, no. 3, pp. 689–709, 1973.
- [48] C. J. Pennycuick, “Mechanics of flight,” *Avian biology*, vol. 5, pp. 1–75, 1975.
- [49] U. M. Norberg, *Vertebrate flight: mechanics, physiology, morphology, ecology and evolution*, Springer-Verlag Berlin, 1990.
- [50] J. Aschoff and H. Pohl, “Der ruheumsatz von vögeln als funktion der tageszeit und der körpergrösse,” *Journal of Ornithology*, vol. 111, no. 1, pp. 38–47, 1970.
- [51] J. M. V. Rayner, “The mechanics of flight and bird migration performance,” *Bird migration*, pp. 283–299, 1990.
- [52] A. Betz, “Ein Beitrag zur Erklärung des Segeluges,” *Zeitschrift für Flugtechnik und Motorluftschiffahrt*, vol. 3, pp. 269–272, 1912.

- [53] R. Knoller, "Die Gesetze des Luftwiderstandes," *Flug- und Motortechnik*, vol. 3, no. 21, pp. 1–7, 1909.
- [54] R. Katzmayr, "Effect of periodic changes of angle of attack on behavior of airfoils," *NACA TM*, vol. 147, 1922.
- [55] I. E. Garrick, "Propulsion of a Flapping and Oscillating Airfoil," Tech. Rep. 567, NACA, 1936.
- [56] K. C. Hall and S. R. Hall, "Minimum Induced Power Requirements for Flapping Flight," *Journal of Fluid Mechanics*, vol. 323, pp. 285–315, 1996.
- [57] A. A. Biewener, K. P. Dial, and G. E. Goslow, "Pectoralis muscle force and power output during flight in the starling," *Journal of Experimental Biology*, vol. 164, no. 1, pp. 1–18, 1992.
- [58] D. J. Willis, M. Kostandov, D. K. Riskin, J. Peraire, D. H. Laidlaw, S. M. Swartz, and K. S. Breuer, "Modeling the flight of a bat," *Science*, vol. 317, no. 5846, pp. 1860, 2007.
- [59] D. J. Willis, P. O. Persson, E. R. Israeli, J. Peraire, S. M. Swartz, and K. S. Breuer, "Multifidelity Approaches for the Computational Analysis and Design of Effective Flapping Wing Vehicles," in *46th AIAA Aerospace Sciences Meeting and Exhibit, Reno, Nevada*, Jan. 7-10 2008.
- [60] C. H. Greenewalt, "The flight of birds: the significant dimensions, their departure from the requirements for dimensional similarity, and the effect on flight aerodynamics of that departure," *Transactions of the American philosophical society*, pp. 1–67, 1975.

- [61] J. M. V. Rayner, "A vortex theory of animal flight. II. The forward flight of birds," *J. Fluid Mech.*, vol. 91, pp. 731–763, 1979.
- [62] A. Lindstrom and T. Alerstam, "Optimal fat loads in migrating birds: a test of the time-minimization hypothesis," *American Naturalist*, pp. 477–491, 1992.
- [63] T. Alerstam and A. Hedenström, "The development of bird migration theory," *Journal of Avian Biology*, pp. 343–369, 1998.
- [64] C. J. Pennycuick and P. F. Battley, "Burning the engine: a time-marching computation of fat and protein consumption in a 5420-km non-stop flight by great knots, *Calidris tenuirostris*," *Oikos*, vol. 103, no. 2, pp. 323, 2003.
- [65] T. Piersma and R. E. Gill Jr, "Guts don't fly: small digestive organs in obese bar-tailed godwits," *The Auk*, pp. 196–203, 1998.
- [66] I. H. Tuncer and M. F. Platzer, "Computational study of flapping airfoil aerodynamics," *Journal of Aircraft*, vol. 37, no. 3, pp. 514–520, 2000.
- [67] M. F. Platzer, K. D. Jones, J. Young, and J. C. S. Lai, "Flapping Wing Aerodynamics- Progress and Challenges ," *AIAA Journal*, vol. 46, no. 9, September 2008.
- [68] P. B. S. MacCready Jr., "Private Communication," October 2004.
- [69] R. L. Nudds, G. K. Taylor, and A. L. R. Thomas, "Tuning of Strouhal number for high propulsive efficiency accurately predicts how wingbeat frequency and stroke amplitude relate and scale with size and flight speed in birds," *Proceedings of the Royal Society of London-B*, vol. 271, no. 1552, pp. 2071–2076, 2004.

- [70] R. Ames, O. Wong, and N. Komerath, "On the Flowfield and Forces Generated by a Flapping Rectangular Wing at Low Reynolds Number," in *Fixed and flapping wing aerodynamics for micro air vehicle applications*. 2001, vol. 195 of *Progress in Astronautics and Aeronautics*, pp. 287–306, AIAA.
- [71] I. H. Tuncer, R. Walz, and M. F. Platzer, "A computational study on the dynamic stall of a flapping airfoil," *AIAA Paper*, vol. 2519, 1998.
- [72] K. Isogai, Y. Shinmoto, and Y. Watanabe, "Effects of dynamic stall on propulsive efficiency and thrust of flapping airfoil," *AIAA Journal*, vol. 37, no. 10, pp. 1145–1151, 1999.
- [73] O. Lilienthal, *Birdflight as the Basis of Aviation*, American Aeronautical Archives, Markowski International Publishers, Hummelstown, PA, 2001.
- [74] T. Theodorsen, "General Theory of Aerodynamic Instability and the Mechanisms of Flutter," Tech. Rep. 496, NACA, 1934.
- [75] H. G. Küssner, "Zusammenfassender Bericht über den instationären Auftrieb von Flügeln," *Luftfahrtforschung*, vol. 13, no. 12, pp. 410–424, 1936.
- [76] D. S. Betteridge and R. D. Archer, "A Study of the Mechanics of Flapping Wings," *Aeronautical Quarterly*, vol. 25, no. 2, pp. 129–142, 1974.
- [77] R. D. Archer, J. Sapuppo, and D. S. Betteridge, "Propulsion characteristics of flapping wings," *Aeronautical Journal*, vol. 83, pp. 355–371, 1979.
- [78] C. E. Lan, "A Quasi-Vortex-Lattice Method in Thin Wing Theory," *Journal of Aircraft*, vol. 11, pp. 518–527, 1974.

- [79] P. J. Phlips, R. A. East, and N. H. Pratt, "An Unsteady Lifting Line Theory of Flapping Wings," *Journal of Fluid Mechanics*, vol. 112, pp. 97–125, 1981.
- [80] R. T. Jones, "Wing Flapping with Minimum Energy," *Aeronautical Journal*, vol. 84, pp. 214–217, 1980.
- [81] R. F. Larijani and J. D. DeLaurier, "A Nonlinear Aeroelastic Model for the Study of Flapping Wing Flight," *Fixed and flapping wing aerodynamics for micro air vehicle applications*, pp. 399–428, 2001.
- [82] M. S. Vest and J. Katz, "Unsteady Aerodynamic Model of Flapping Wings," *AIAA Journal*, vol. 37, no. 7, pp. 1435–1440, 1996.
- [83] M. J. C. Smith, P. J. Wilkin, and M. H. Williams, "The Advantage of an Unsteady Panel Method in Modeling the Aerodynamic Forces on Rigid Flapping Wings," *Journal of Experimental Biology*, vol. 199, pp. 1073–1083, 1996.
- [84] K. D. Jones, C. M. Dohring, and M. F. Platzer, "Experimental and computational investigation of the Knoller-Betz effect," *AIAA journal*, vol. 36, pp. 1240–1246, 1998.
- [85] K. C. Hall and S. R. Hall, "A Rational Engineering Analysis of the Efficiency of Flapping Flight," in *Fixed and Flapping Wing Aerodynamics for Micro Air Vehicles*, Mueller T. J., Ed. 2001, Progress in Astronautics and Aeronautics, pp. 249–274, AIAA.
- [86] D. J. Willis, J. Peraire, and J. K. White, "A combined pFFT-multipole tree code, unsteady panel method with vortex particle wakes," *INTERNATIONAL JOURNAL FOR NUMERICAL METHODS IN FLUIDS*, vol. 53, no. 8, pp. 1399, 2007.

- [87] D. J. Willis, J. Peraire, J. White, and M. Drela, "A Numerical Exploration of Parameter Dependence in Power Optimal Flapping Flight," in *24th AIAA Applied Aerodynamics Conference, San Francisco, California, June 5-8, 2006*, 2006.
- [88] AeroLogic Inc., *CMARC Version 6.5.1*, 2007.
- [89] M. Drela, *XFOIL Users Guide, Version 6.94*, MIT Aero. and Astro. Department, 2002.
- [90] I. Kroo, "Aircraft Design: Synthesis and Analysis," <http://adg.stanford.edu/aa241/AircraftDesign.html>, 2009.
- [91] H. Wagner, "Über die Entstehung des dynamischen Auftriebes von Tragflügeln," *ZAMM-Zeitschrift für Angewandte Mathematik und Mechanik*, vol. 5, no. 1, 1925.
- [92] T. Melin, *User's guide and reference manual for Tornado.*, 2000.
- [93] Desktop Aeronautics Inc., *LinAir Version 4.0*, Palo Alto CA, 2004.
- [94] H. J. P. Morand and R. Ohayon, *Fluid-Structure Interaction: Applied Numerical Methods*, Wiley, New York, 1995.
- [95] R. F. Larijani, *A Non-Linear Aeroelastic Model for the Study of Flapping-Wing Flight*, Ph.D. thesis, University of Toronto, 2000.
- [96] H. T. Lee and I. M. Kroo, "Computational investigation of airfoils with miniature trailing edge control surfaces," *AIAA paper*, vol. 1051, pp. 2004, 2004.
- [97] H. T. Lee, *Computational Investigation of Miniature Trailing Edge Effectors*, Ph.D. thesis, Stanford University, 2005.

- [98] Y. Lian, *Membrane and adaptively-shaped wings for micro air vehicles*, Ph.D. thesis, University of Florida, Gainesville, 2003.
- [99] C. Farhat, K. G. van der Zee, and P. Geuzaine, “Provably second-order time-accurate loosely-coupled solution algorithms for transient nonlinear computational aeroelasticity,” *Computer Methods in Applied Mechanics and Engineering*, vol. 195, no. 17-18, pp. 1973 – 2001, 2006.
- [100] C. R. Calladine, *Theory of shell structures*, Cambridge University Press, 1983.
- [101] P. Heppel, “Accuracy in sail simulation: Wrinkling and growing fast sails,” in *High Performance Yacht Design Conference*, 2002.
- [102] J. N. Nielsen, “Theory of Flexible Aerodynamic Surfaces,” *Journal of Applied Mechanics*, vol. 30, pp. 435–442, September 1963.
- [103] B. Thwaites, “The aerodynamic theory of sails. I. Two-dimensional sails,” *Proceedings of the Royal Society of London. Series A, Mathematical and Physical Sciences*, pp. 402–422, 1961.
- [104] F. M. Rogallo, “NASA research on flexible wings,” in *2nd International Congress on Subsonic Aeronautics*. 1968, vol. 154, pp. 953–961, Blackwell Publishing Ltd.
- [105] I. Kroo, *Aerodynamics, aeroelasticity, and stability of hang gliders*, Ph.D. thesis, Stanford University, 1983.
- [106] J. T. Oden and T. Sato, “Finite strains and displacements of elastic membranes by the finite element method,” *International Journal of Solids and Structures*, vol. 3, no. 4, pp. 471–488, 1967.

- [107] P. S. Jackson and G. W. Christie, "Numerical analysis of three-dimensional elastic membrane wings," *AIAA journal*, vol. 25, no. 5, pp. 676–682, 1987.
- [108] R. Smith and W. Shyy, "Computational model of flexible membrane wings in steady laminar flow," *AIAA journal*, vol. 33, no. 10, 1995.
- [109] J. Paton, H. P. Morvan, and P. Heppel, "FLUID STRUCTURE INTERACTION OF YACHT SAILS," in *INNOV'SAIL - INNOVATION IN HIGH PERFORMANCE SAILING YACHTS*, Lorient, France., May 2008.
- [110] C. H. Jenkins and J. W. Leonard, "Nonlinear dynamic response of membranes: state of the art," *Applied Mechanics Reviews*, vol. 44, pp. 319, 1991.
- [111] C. H. Jenkins, "Nonlinear dynamic response of membranes: state of the art-update," *Applied Mechanics Reviews*, vol. 49, pp. S41, 1996.
- [112] K. B. Smalley and M. L. Tinker, "Nonlinear pressurization and modal analysis procedure for dynamic modeling of inflatable structures," *Journal of spacecraft and rockets*, vol. 39, no. 5, pp. 732–739, 2002.
- [113] R. H. MacNeal et al., *The NASTRAN Theoretical Manual*, Scientific and Technical Information Office, National Aeronautics and Space Administration, Washington, DC, 1970.
- [114] R. C. Scott, R. E. Bartels, and O. A. Kandil, "An Aeroelastic Analysis of a Thin Flexible Membrane," in *48th AIAA/ASME/ASCE/AHS/ASC Structures, Structural Dynamics, and Materials Conference, Honolulu, Hawaii*, April 23-26 2007.

- [115] D. Amsallem, C. Farhat, and T. Lieu, "High-Order Interpolation of Reduced-Order Models for Near Real-Time Aeroelastic Prediction," in *International Forum on Aeroelasticity and Structural Dynamics, Stockholm, Sweden, June, 2007*, vol. Paper IF-081, pp. 18–20.
- [116] D. Amsallem and C. Farhat, "Interpolation Method for Adapting Reduced-Order Models and Application to Aeroelasticity," *AIAA Journal*, vol. 46, no. 7, pp. 1803–1813, 2008.
- [117] S. Kinkade, "HobbyTechnik - It's Flapping Flight," <http://flappingflight.com/>, 2005.
- [118] J. D. DeLaurier and J. M. Harris, "Experimental Study of Oscillating-Wing Propulsion," *Journal of Aircraft*, vol. 19, no. 5, pp. 368–377, 1982.
- [119] H. Rabiger, "Wie Ornithopter Fliegen," <http://www.ornithopter.de/>, 2009.
- [120] A. Kempf, "Truefly - révolution dans l'aéronautique," <http://www.chez.com/truefly/Images/trueflya.htm>, March 2001.
- [121] D. W. Green, J. E. Winandy, and D. E. Kretschmann, "Mechanical properties of wood," General technical report FPL GTR-113, USDA Forest Service, Forest Products Laboratory, 1999.
- [122] C.O. Dyrby and T.P. Andriacchi, "Secondary motions of the knee during weight bearing and non-weight bearing activities," *Journal of Orthopaedic Research*, vol. 22, no. 4, 2004.
- [123] A. W. A. Kellner, X. Wang, H. Tischlinger, C. D. de Almeida, D. W. Hone, and X. Meng, "The soft tissue of Jeholopterus (Pterosauria, Anurognathidae,

- Batrachognathinae) and the structure of the pterosaur wing membrane.," in *Proceedings. Biological sciences/The Royal Society*, 2009.
- [124] P. Watts, E. J. Mitchell, and S. M. Swartz, "A COMPUTATIONAL MODEL FOR ESTIMATING THE MECHANICS OF HORIZONTAL FLAPPING FLIGHT IN BATS MODEL DESCRIPTION AND VALIDATION," *Journal of Experimental Biology*, vol. 204, no. 16, pp. 2873–2898, 2001.
- [125] I. Ansys, *ANSYS user's manual*, vol. 275, ANSYS Inc., Southpointe, 2004.
- [126] A. Song, X. Tian, E. Israeli, R. Galvo, K. Bishop, S. Swartz, and K. S. Breuer, "The Aero-Mechanics of Low Aspect Ratio Compliant Membrane Wings, with Applications to Animal Flight," in *46th AIAA Aerospace Sciences Meeting and Exhibit*, 2008.
- [127] H. Hencky, "On the stress state in circular plates with vanishing bending stiffness," *Zeitschrift für Mathematik und Physik*, vol. 63, pp. 311–317, 1915.
- [128] W. B. Fichter, "Some solutions for the large deflections of uniformly loaded circular membranes," *NASA technical paper*, vol. 3658, 1997.
- [129] M. Harada, "Calculation method for optimal circulation distribution on a finite span flapping wing," in *1st Technical Conference and Workshop on Unmanned Aerospace Vehicles, Portsmouth, Virginia, May 20-23 2003*.
- [130] M. Harada, "Calculation Method for Optimal Circulation Distribution on Root Flapping Wing," in *35th AIAA Fluid Dynamics Conference and Exhibit; Toronto, Ontario, 2005*, pp. 1–10.

- [131] D. J. Willis, J. Peraire, and K. S. Breuer, "A computational Investigation of Bio-Inspired Formation Flight and Ground Effect," in *25th AIAA Applied Aerodynamics Conference, Miami, FL*, June 25-28 2007.
- [132] I. H. Tuncer and M. Kaya, "Optimization of flapping airfoils for maximum thrust and propulsive efficiency," *AIAA journal*, vol. 43, no. 11, pp. 2329–2336, 2005.
- [133] M. Kaya and I. H. Tuncer, "Nonsinusoidal Path Optimization of a Flapping Airfoil," *AIAA Journal*, vol. 45, no. 8, pp. 59, August 2007.
- [134] K. Isogai and Y. Harino, "Optimum Aeorelastic Design of a Flapping Wing," *Journal of Aircraft*, vol. 44, no. 6, pp. 2040–2048, 2007.
- [135] Y. Lian, W. Shyy, and R. T. Haftka, "Shape optimization of a membrane wing for micro air vehicles," *AIAA journal*, vol. 42, no. 2, pp. 424–426, 2004.
- [136] D. Kalyanmoy, *Multi-Objective Optimization using Evolutionary Algorithms*, Wiley, 2001.
- [137] K. Sastry, "Single and Multiobjective Genetic Algorithm Toolbox in C++," Technical Report 2007016, Illinois Genetic Algorithms Laboratory, University of Illinois at Urbana-Champaign, 117 Transportation Building, 104 S. Mathews Avenue Urbana, IL 61801, 2007.
- [138] P. E. Gill, W. Murray, and M. A. Saunders, "User's Guide for SNOPT Version 7, Software for Large Scale Nonlinear Programming, <http://www.sbsi-sol-optimize.com/manuals>," *SNOPT Manual. pdf*, 2002.

- [139] P. E. Gill, W. Murray, and M. A. Saunders, "SNOPT: An SQP algorithm for large-scale constrained optimization," *SIAM Journal on Optimization*, vol. 12, no. 4, pp. 979–1006, 2002.
- [140] C. J. Pennycuik, "Power Requirements for Horizontal Flight in the Pigeon *Columba Livia*," *Journal of Experimental Biology*, vol. 49, pp. 527–555, 1968.
- [141] B. W. Tobalske, "Biomechanics and Physiology of Gait Selection in Flying Birds," *Physiological and Biochemical Zoology*, vol. 73, no. 6, pp. 736–750, 2000.
- [142] U. M. Norberg, "Aerodynamics, kinematics, and energetics of horizontal flapping flight in the long-eared bat *Plecotus auritus*," *Journal of Experimental Biology*, vol. 65, no. 1, pp. 179–212, 1976.
- [143] M. J. Lighthill, *Aerodynamic aspects of animal flight*, British Hydromechanics Research Association, 1974.
- [144] M. J. Lighthill, "Introduction to the scaling of aerial locomotion," *Scale effects in animal locomotion*, pp. 365–404, 1977.
- [145] M. Drela, *XROTOR Propeller and Windmill Design Analysis Software*, MIT Aero. and Astro. Department.
- [146] B. Parks, "Private Communications," 2004–2009.
- [147] S. L. Delp and J. P. Loan, "A computational framework for simulating and analyzing human and animal movement," *Computing in Science & Engineering*, vol. 2, no. 5, pp. 46–55, 2000.

- [148] D. Rajnarayan, A. Haas, and I. M. Kroo, “A Multifidelity Gradient-Free Optimization Method and Application to Aerodynamic Design,” in *12th AIAA/ISSMO Multidisciplinary Analysis and Optimization Conference, Victoria, British Columbia, Canada*, Sept. 10-12 2008.